

University of Southampton Research Repository

Copyright © and Moral Rights for this thesis and, where applicable, any accompanying data are retained by the author and/or other copyright owners. A copy can be downloaded for personal non-commercial research or study, without prior permission or charge. This thesis and the accompanying data cannot be reproduced or quoted extensively from without first obtaining permission in writing from the copyright holder/s. The content of the thesis and accompanying research data (where applicable) must not be changed in any way or sold commercially in any format or medium without the formal permission of the copyright holder/s.

When referring to this thesis and any accompanying data, full bibliographic details must be given, e.g.

Thesis: Author (Year of Submission) "Full thesis title", University of Southampton, name of the University Faculty or School or Department, PhD Thesis, pagination.

Data: Author (Year) Title. URI [dataset]

University of Southampton

Faculty of Environmental and Life Sciences

School of Geography and Environmental Science

Insights into the Seasonal Dynamics of the Lake-Terminating Glacier Fjallsjökull, South-East Iceland, Inferred Using Ultra-High Resolution Repeat UAV Imagery

by

Nathaniel Ross Baurley

ORCID ID: 0000-0002-0444-8721

<https://orcid.org/0000-0002-0444-8721>

Thesis for the degree of Doctor of Philosophy

30th September 2022

University of Southampton

Abstract

Faculty of Environmental and Life Sciences
School of Geography and Environmental Science

Doctor of Philosophy

Insights into the Seasonal Dynamics of the Lake-Terminating Glacier Fjallsjökull, South-East Iceland, Inferred Using Ultra-High Resolution Repeat UAV Imagery

by

Nathaniel Ross Baurley

Proglacial lakes are becoming ubiquitous at the termini of many glaciers worldwide, leading to increased glacier mass loss and terminus retreat due to the influence of these proglacial lakes on ice dynamics. However, despite the highly dynamic nature and relative insensitivity to climate of many lake-terminating glaciers, an understanding of the key processes forcing their behaviour is lacking. As a result, it is difficult at present to accurately assess and predict how these glaciers may respond in the future. A novel method to address this difficulty, however, is through the use of repeat uncrewed aerial vehicle (UAV) imagery, which can provide high to ultra-high resolution (cm-dm scale) imagery of the ice surface at varying spatial and temporal scales, depending on the needs of the study, although its use as a tool for investigating the dynamics of lake-terminating glaciers is so far limited. This research utilised ultra-high resolution repeat UAV imagery to provide insights into the changing dynamics of Fjallsjökull, a large lake-terminating glacier in southeast Iceland, across the 2019 and 2021 summer melt seasons. The findings indicate that the overall dynamics of the glacier are controlled by the ~120 m deep bedrock channel under the study region, which is causing the glacier to flow faster as it enters deeper water, leading to increased ice acceleration, thinning and retreat, with the glacier being decoupled from the local climate as a result. Such a close correspondence between ice velocity and surface thinning suggests the implementation of the positive feedback mechanism dynamic thinning in this region of Fjallsjökull, with such heightened rates of surface thinning and frontal retreat likely to continue in the future until the glacier recedes out of the bedrock channel into shallower water. Within this overall pattern, however, more localised, short-term changes in glacier dynamics were also observed, with these likely being forced primarily by subaqueous melting at the waterline, rather than the specific bedrock topography. Finally, supraglacial lake drainage may also be important for forcing sub-daily (e.g. hourly) increases in velocity, although further work is required to quantify its influence more accurately. As a result, these findings clearly indicate the complex nature of the calving process, as well as the dynamics of calving glaciers in general, highlighting the need for continued monitoring of lake-terminating glaciers at varying spatial and temporal scales in order to better understand and predict how they may respond in future.

Table of Contents

Table of Contents	ii
Table of Tables	vii
Table of Figures	ix
Research Thesis: Declaration of Authorship	xvii
Acknowledgements	xix
Definitions and Abbreviations.....	xx
Chapter 1 INTRODUCTION	1
1.1. Background and Rationale	1
1.2. Aims and Objectives.....	5
1.3. Thesis Structure	5
Chapter 2 LITERATURE REVIEW	9
2.1 Glacier Movement	9
2.1.1 Internal Deformation	11
2.1.2 Subsole (Bed) Deformation.....	12
2.1.3 Basal Sliding	15
2.2 Glacier Hydrology.....	17
2.2.1 Subglacial Drainage Systems.....	18
2.3 Temporal Variations in Glacier Hydrology and Glacier Motion.....	20
2.4 Calving-Induced Dynamic Changes.....	27
2.4.1 Calving: Fracture Formation and Propagation.....	29
2.4.2 Processes of Calving.....	30
2.4.3 Glacier Velocity and Calving.....	38
2.4.3.1 Force Balance and Calving Glaciers.....	38
2.4.3.2 Basal Drag.....	39
2.4.3.3 Lateral Drag.....	41
2.4.3.4 Longitudinal Stress Gradients	42
2.4.4 Tidewater vs Freshwater Calving.....	44
2.5 Measurements of Glacier Velocity from Satellite Remote Sensing.....	50

2.5.1	Techniques to Derive Glacier Velocity from Satellite Imagery	52
2.5.1.1	InSAR.....	52
2.5.1.2	Offset Tracking	53
2.5.1.3	Feature Tracking.....	55
2.5.1.4	General Considerations for Implementing Offset and Feature Tracking Procedures.....	60
2.5.2	Limitations of Investigating Glacier Velocity with Satellite Remote Sensing...	62
2.5.3	New Developments in Satellite Remote Sensing	63
2.6	Repeat UAV Surveys of Glacier Velocity	65
2.6.1	Terrestrial Photogrammetry	65
2.6.2	Structure-from-Motion (SfM) Photogrammetry.....	67
2.6.2.1	Background.....	67
2.6.2.2	The SfM Workflow.....	69
2.6.2.3	Potential SfM Limitations	75
2.6.3	Integrated UAV-SfM Approach	79
2.6.4	UAVs in Glacial Research.....	80
Chapter 3	STUDY SITE and WIDER CONTEXT	87
3.1	Icelandic Glaciers.....	87
3.1.1	Study Site.....	89
3.1.1.1	Glaciological Setting	89
3.1.1.2	Climatological Setting.....	92
3.1.2	Previous Work	93
Chapter 4	METHODS	95
4.1	Repeat UAV Surveys	95
4.1.1	2019 Field Season.....	95
4.1.1.1	UAV and Camera System.....	95
4.1.1.2	Mission Planning and Survey Design.....	96
4.1.1.3	Georeferencing.....	98
4.1.2	2021 Field Season.....	101

Table of Contents

4.1.2.1	UAV and Camera System	101
4.1.2.2	Mission Planning and Survey Design	102
4.1.2.3	Georeferencing	104
4.1.3	Post-Processing of UAV Data	106
4.1.3.1	GNSS Processing (Base and Rover)	106
4.1.3.2	Image - Position Matching	108
4.2	3D Model Generation	109
4.2.1	SfM Photogrammetry	109
4.2.2	Uncertainty Analysis	112
4.2.2.1	2019 Field Season	112
4.2.2.2	2021 Field Season	117
4.2.2.3	Comparison to Previous Studies	119
4.3	Glacier Velocity (Feature Tracking).....	120
4.4	Surface Elevation Change	121
4.5	Frontal Position Change and Calving Events.....	122
4.6	Supraglacial Hydrological Mapping	123
Chapter 5	RESULTS.....	125
5.1	Glacier Velocity (Feature Tracking).....	126
5.1.1	2019 Field Season	126
5.1.2	2021 Field Season	127
5.2	Surface Elevation Change	130
5.2.1	2019 Field Season	130
5.2.2	2021 Field Season	131
5.3	Frontal Position Change and Calving Events.....	132
5.3.1	2019 Field Season	132
5.3.2	2021 Field Season	139
5.4	Supraglacial Hydrological Mapping	147
5.4.1	2019 Field Season	147
5.4.1.1	Supraglacial Lakes	147

5.4.1.2	Water-filled Crevasses.....	150
5.4.2	2021 Field Season.....	151
5.4.2.1	Supraglacial Lakes.....	151
5.4.2.2	Water-filled Crevasses.....	151
Chapter 6	INTERPRETATIONS and DISCUSSION	155
6.1	Variations in the Dynamics of Fjallsjökull.....	155
6.1.1	Large-scale Velocity Variations and Links to Basal Topography	155
6.1.2	Localised Velocity Variations and Links to Subaqueous Melt	164
6.1.3	Supraglacial Lake Drainage and Short-Term Velocity Variations.....	172
6.1.4	July 2019 and July 2021: A Comparison	181
6.1.5	Dynamics of Fjallsjökull: A Summary of Forcing Mechanisms	182
6.1.5.1	First Order Processes.....	182
6.1.5.2	Second Order Processes.....	183
6.1.5.3	Third Order Processes	185
6.2	Wider Relevance and Implications.....	186
6.2.1	Wider Climatological Perspective	186
6.2.2	Basal Topography and its Influence on Ice Dynamics	189
6.2.3	UAV Imagery as a Tool for Monitoring Lake-Terminating Glacier Dynamics.....	191
Chapter 7	CONCLUSIONS.....	199
7.1	Research Synthesis and Conclusions.....	199
7.2	Future Work	203
List of References	205

Table of Tables

TABLE 1 Details of each survey undertaken in July and September 2019.....	96
TABLE 2 Flight settings used when undertaking the UAV surveys in both July and September 2019.....	98
TABLE 3 Details of each survey undertaken in July 2021.	102
TABLE 4 Flight settings used when undertaking the UAV surveys in July 2021.	104
TABLE 5 Details of GCPs used for the processing of the UAV imagery from July and September 2019.....	111
TABLE 6 Reported and calculated errors for the GCP placement and final models for the July surveys.....	114
TABLE 7 Reported and calculated errors for the GCP placement and final models for the September surveys.	114
TABLE 8 Camera position and final model errors calculated for the July 2021 surveys.....	118
TABLE 9 Parameters used in CIAS for each time period investigated, as well as a brief description of each parameter for reference.	121
TABLE 10 Criteria used to differentiate between the different surface hydrological features observed in this research. An example of each feature is also given for the benefit of the reader.....	124
TABLE 11 Calculated terminus retreat for each time period in July and September 2019.	134
TABLE 122 Calculated terminus retreat for each time period in July 2021.....	141
TABLE 133 Summary of the key glaciological data acquired in both July 2019 and July 2021..	181

Table of Figures

FIGURE 1 Cross-section of a typical glacier illustrating the different components that make up the glacier force balance.	10
FIGURE 2 Schematic illustrating the vertical velocity distribution for the three different types of glacier motion.	11
FIGURE 3 The displacement of segmented rods placed into the till of Breiðamerkurjökull, south Iceland by Boulton and Hindmarsh (1987).	13
FIGURE 4 Schematic illustrating two of the ways in which water at the bed can influence sliding velocity.	16
FIGURE 5 Simple schematic diagrams of the main forms of efficient and inefficient subglacial drainage systems for rigid and deforming beds.	19
FIGURE 6 Idealised plan-view schematics of the two types of drainage system commonly thought to be present under temperate glaciers.	21
FIGURE 7 Sliding velocities (red) and subglacial runoff (blue) for Argentière glacier, Mont Blanc region, in response to a storm event that occurred on the 26 th August 2014 (precipitation = black line).	22
FIGURE 8 Monthly-averaged velocity data (solid grey line) for five land-terminating glaciers in southwest Greenland.	24
FIGURE 9 (a) Annual mean modelled surface melt (grey line), smoothed with a five-year moving mean (black line) for an 8,000 km ² land-terminating region of the west Greenland Ice Sheet. (b) Median ice velocities (blue line) across the same land-terminating region of the Greenland Ice Sheet, calculated using feature tracking applied to pairs of Landsat images for specific time periods.	26
FIGURE 10 Schematic illustrating how a fracture that is filled with water can propagate to a much greater depth than a 'dry' crevasse due to the weight of the water completely opposing the ice pressure that is attempting to close the crevasse.	30
FIGURE 11 Schematic illustrating how calving can result from longitudinal stretching at the ice surface.	32

Table of Figures

FIGURE 12 Schematic illustrating how calving can result from subaqueous melt at the waterline.	34
FIGURE 13 Schematic illustrating how calving can result from force imbalances at terminal ice cliffs.	36
FIGURE 14 Schematic illustrating how calving can result from buoyant forces acting on the terminus.	36
FIGURE 15 Relationship between glacier thinning, acceleration and calving retreat, resulting from effective pressure-dependent basal motion and the influence of longitudinal stretching on dynamic thinning and first-order calving.....	41
FIGURE 16 Near-global glacial lake distribution and area for the period 2015-2018.	46
FIGURE 17 Summary schematic of the processes occurring at the margin of a lake-terminating glacier, and the impact these processes have on overall ice dynamics.	48
FIGURE 18 Image illustrating how the terminus regions of lacustrine-calving glaciers are often heavily crevassed due to the longitudinal stretching of surface ice.	49
FIGURE 19 Example of a thermal notch near the base of Miage Glacier, Italian Alps, following the drainage of its proglacial lake in late summer 2004.....	50
FIGURE 20 Examples of velocity products obtained in previous studies that were derived using InSAR.	54
FIGURE 21 Examples of velocity products obtained in previous studies that were derived using offset tracking.	56
FIGURE 22 Examples of velocity products obtained in previous studies that were derived using feature tracking.	58
FIGURE 23 Comparison of velocity grids that were obtained using different feature tracking techniques.	59
FIGURE 24 Example outputs from previous studies that have compared the influence of sensor spatial resolution and the choice of matching window size on the accuracy of satellite-derived velocity products.	61
FIGURE 25 Example products from recent studies that have utilised either Sentinel-1 or Sentinel-2 imagery to derive glacier velocity.....	64

FIGURE 26 Conceptual diagram comparing typical spatial resolution against spatial extent of the most commonly used methods in glaciology for measuring glacier change.....	66
FIGURE 27 Structure-from-Motion photogrammetry, which requires multiple, overlapping photographs to be taken around the scene of interest from which 3D surface models can then be generated.	68
FIGURE 28 Typical SfM workflow for the production of georeferenced dense point clouds using image sets and ground control points.	70
FIGURE 29 Key aspects from different stages of the SfM workflow.	72
FIGURE 30 Relationship between GSD (survey image resolution) and final model RMSE (based off reported horizontal and vertical accuracies) for those studies within glaciology to date that have utilised UAV surveys.....	76
FIGURE 31 Schematic illustrating the relationship between GCP number and density and the RMSE of the final models.	78
FIGURE 32 Example of a customised UAV system for use in geomorphological research.....	79
FIGURE 33 Examples of UAV-derived velocity products obtained in previous studies and mentioned in the main text.	82
FIGURE 34 Location map of Fjallsjökull.	90
FIGURE 35 Field photograph of Fjallsjökull (along with its proglacial lake Fjallsárlón) taken from directly opposite the glacier on 7 th July 2021.	91
FIGURE 36 Annual and cumulative frontal variations measured at the land-terminating margin of Fjallsjökull for the period 1934 to 2019.....	91
FIGURE 37 Longitudinal surface and bedrock profiles of Fjallsjökull showing the location of the terminus in 2020, as well as the ~4 km long overdeepened bedrock trough through which the glacier is currently retreating.....	92
FIGURE 38 (a) Mean annual temperatures and (b) mean annual precipitation recorded at Fagurhólmýri weather station for the period 1949-2020.	93
FIGURE 39 The 3DR Solo quadcopter used to undertake the UAV surveys in July and September 2019.	95
FIGURE 40 Areal coverage of the UAV surveys undertaken in July and September 2019.	97

Table of Figures

FIGURE 41 Example of one of the 1x1 m GCPs placed in the vicinity of Fjallsjökull to georeference the glacier models to real-world coordinates.	99
FIGURE 42 GCP locations (pink circles), UAV launch site (TOL, white star) and Leica base station location (green triangle) for the 5th July (top), 7th July (middle) and 19th September (bottom) 2019.	100
FIGURE 43 The DJI Inspire 2 used to undertake the UAV surveys in July 2021.....	101
FIGURE 44 Areal coverage of the UAV surveys undertaken in July 2021.....	103
FIGURE 45 GCP locations (pink circles), UAV launch site (TOL, white star) and Leica base station location (green triangle) for the 2021 surveys.	105
FIGURE 46 Examples of a Q1 (left) and a Q2 (right) positional solution, obtained on the 6 th July 2021 for surveys one and three, respectively.	107
FIGURE 47 The SfM workflow that was utilised to process the UAV-derived imagery from 2019 and 2021 into high-resolution DEMs and orthomosaics of the ice surface.	110
FIGURE 48 Location of the stable ground areas (white boxes) that were used to determine the uncertainty of the feature tracking and DEM differencing calculations (see Section 4.4).	122
FIGURE 49 (a) Overview of Fjallsjökull, with the green and orange boxes indicating the areal coverage of the UAV surveys undertaken in 2019 and 2021 respectively.....	125
FIGURE 50 Horizontal velocity fields for select time periods in July and September 2019, calculated using feature tracking on UAV-derived orthomosaics.....	126
FIGURE 51 Horizontal velocity fields for all time periods in July 2021, calculated using feature tracking on UAV-derived orthomosaics.....	128
FIGURE 52 Change in ice surface elevation between the 5 th -9 th July, and the 19 th -21 st September 2019, calculated using DEM differencing.	130
FIGURE 53 Change in ice surface elevation between the 6 th -15 th July 2021, calculated using DEM differencing.	132
FIGURE 54 Location and areal extent of the calving events that occurred across the study area over (a) 5 th - 9 th July, and (b) 19 th -21 st September 2019.....	133
FIGURE 55 (a) Average and cumulative frontal change for July 2019, calculated using the rectilinear box method. (b) Same as (a) but for September 2019.	134

FIGURE 56 (a) Change in calving front position between the 5 th and 6 th July. Red boxes indicate areas of the ice surface which are of interest, with these presented in panels (b) and (c).	135
FIGURE 57 Total calving area (black line), maximum calving area lost in a single event (red line), and the total number of calving events (green line) per day for each time period of interest in July (a) and September (b) 2019.	136
FIGURE 58 (a) Change in calving front position between the 6 th and 9 th July. Red boxes indicate areas of the ice surface which are of interest, with these presented in panels (b) and (c).	137
FIGURE 59 (a) Change in calving front position between the 19 th and 21 st September. Red boxes indicate areas of the ice surface which are of interest, with these presented in panels (b) and (c).	138
FIGURE 60 Location and areal extent of the calving events that occurred across the study area between the 4 th and 15 th July 2021.....	140
FIGURE 61 Average and cumulative frontal change for July 2021, calculated using the rectilinear box method.	141
FIGURE 62 (a) Change in calving front position between the 4 th and 7 th July. Red boxes indicate areas of the ice surface which are of interest, with these presented in panels (b) and (c).	142
FIGURE 63 (a) Total calving area (black line), maximum calving area lost in a single event (red line), and the total number of calving events (green line) per day for each time period of interest in July 2021.	143
FIGURE 64 (a) Change in calving front position between the 7 th and 9 th July. Red boxes indicate areas of the ice surface which are of interest, with these presented in panels (b) and (c).	144
FIGURE 65 (a) Change in calving front position between the 9 th and 11 th July. Red boxes indicate areas of the ice surface which are of interest, with these presented in panels (b) and (c).	145
FIGURE 66 (a) Change in calving front position between the 11 th and 15 th July. Red boxes indicate areas of the ice surface which are of interest, with these presented in panels (b) and (c).	146
FIGURE 67 Overview figure illustrating the spatial extent of the four different example regions presented in this section, relative to the overall ice surface.....	147
FIGURE 68 Daily variations in the total number and area of supraglacial lakes and water-filled crevasses (WfC) on the ice surface in both July (a) and September (b) 2019.	148

Table of Figures

FIGURE 69 The drainage of supraglacial lakes on the ice surface between the 5 th and 6 th July 2019.	149
FIGURE 70 Example of the refilling of supraglacial lakes that occurred between the 19 th and 20 th September 2019.	150
FIGURE 71 Daily variations in the total number and area of supraglacial lakes and WfC on the ice surface in July 2021.	152
FIGURE 72 Variations in lake and WfC area on the ice surface in July 2021.....	153
FIGURE 73 (a)-(f) An example of the near-daily variations in WfC number and area that occurred in the western part of the study area between the 7 th and 12 th July 2021.....	154
FIGURE 74 Bedrock topography and surface velocity for select periods in July 2019 and 2021.	157
FIGURE 75 Location and size of the basal crevasse that was observed near the terminus of Fjallsjökull on the 7 th July 2019, relative to the study region overall.	159
FIGURE 76 Location and size of the four basal crevasses that were observed near the terminus of Fjallsjökull in September 2019, relative to the study region overall.....	160
FIGURE 77 Location and size of the four basal crevasses that were observed near the terminus of Fjallsjökull in July 2021, relative to the study region overall.....	162
FIGURE 78 Evolution of the large WfC in the lower portion of the study region that went from being partially filled with meltwater to being wholly filled with lake water between the (a) 12 th and (b) 15 th July 2021.	163
FIGURE 79 Photographs of the southern margin of Fjallsjökull acquired on the (a) 4 th July and (b) 19 th September 2019, highlighting the presence of extensive thermal erosion notches at the waterline (black arrows) in this region.	165
FIGURE 80 Photographs of the southern margin of Fjallsjökull acquired on the (a) 4 th (b) 6 th and (c) 7 th July 2021.	167
FIGURE 81 Photographs of the southern margin of Fjallsjökull acquired on the (a) 8 th (b) 10 th and (c) 12 th July 2021, illustrating the formation and growth of thermal notches at the waterline (black arrows) which occurred in the days after the 7 th (when no such features were observed).	169

FIGURE 82 Schematic illustrating the mechanism by which calving failure at Fjallsjökull can result from thermal notch erosion at the waterline, based on the observations made in this research.	170
FIGURE 83 (a) Hourly air temperature data from the meteorological station at Kvísker plotted alongside the overall change in lake number between the 5 th and 9 th July 2019.	174
FIGURE 84 (a) The southern margin of Fjallsjökull on the 19 th September, showing the presence of thermal erosion notches, which sit above the level of the lake at the time the photo was taken (red arrow). (b) Same as (a) but from the 23 rd September.....	177
FIGURE 85 (a) Hourly air temperature data from the meteorological station at Kvísker plotted alongside the overall change in lake number between the 6 th and 15 th July 2021.	178
FIGURE 86 Summary schematic of the processes occurring at the margin of Fjallsjökull and the impacts these processes are having on the overall dynamics of the glacier, based on the UAV data presented in this research.	184
FIGURE 87 Mean annual air temperatures from the weather station at Fagurhólmýri, plotted alongside the cumulative retreat of Fjallsjökull at its land- and lake-terminating margins for the period 1945-2021.....	187
FIGURE 88 Comparison between the spatial resolution of UAV and satellite imagery.	194

Research Thesis: Declaration of Authorship

Print name: Nathaniel Ross Baurley

Title of thesis: Insights into the Seasonal Dynamics of the Lake-Terminating Glacier Fjallsjökull, South-East Iceland, Inferred Using Ultra-High Resolution Repeat UAV Imagery.

I declare that this thesis and the work presented in it are my own and has been generated by me as the result of my own original research.

I confirm that:

1. This work was done wholly or mainly while in candidature for a research degree at this University;
2. Where any part of this thesis has previously been submitted for a degree or any other qualification at this University or any other institution, this has been clearly stated;
3. Where I have consulted the published work of others, this is always clearly attributed;
4. Where I have quoted from the work of others, the source is always given. With the exception of such quotations, this thesis is entirely my own work;
5. I have acknowledged all main sources of help;
6. Where the thesis is based on work done by myself jointly with others, I have made clear exactly what was done by others and what I have contributed myself;
7. None of this work has been published before submission

Signature: Date:.....

Acknowledgements

This thesis could not have been completed without the continued support of a great number of people, and I am indebted to each and every one of you for your kindness and generosity.

Firstly, I would like to thank my supervisor Professor Jane Hart, for providing endless support and advice throughout the whole PhD, for keeping me on track and for continually pushing me and developing my skills to improve me as a researcher. You have been a wonderful mentor, and I look forward to working with you in the future. I would also like to acknowledge the wider group of staff in the Department of Geography and Environmental Science who have also offered support and given advice throughout my PhD, most notably Dr Eli Lazarus and Dr Jo Nield. Thanks must also go to the laboratory technicians, but in particular, Dr David Sutherland for providing much-needed training and field support for the research trip undertaken in July 2019.

I must also thank several charitable and grant-giving organisations, in particular the James Pantyfedwen Foundation and Sir Richard Stapley Educational Trust, as well as the Royal Geographical Society, Mount Everest Foundation and Quaternary Research Association, without whom I could not have undertaken this PhD, nor have been able to conduct fieldwork.

I am also incredibly thankful for being able to undertake my PhD in such a close-knit and supportive environment, full of wonderful people, many of whom have become great friends. Mair, Charlotte, Nichola, Luke, Martin, Matt – the list could go on, but particular mention must go to Chris Tomsett, without whom I do not believe I would have been able to complete this PhD. Your support and advice, both in the field, as well as post-fieldwork during data processing, was invaluable, but you've also been a fantastic office buddy, whose jokes and humour have got me through the toughest days, and whose love of Icelandic skyr and crunchy peanut butter rivals only that of my own. I thank you wholeheartedly, and I hope we can work together in the future.

I am also indebted to my parents, whose support and belief in me and the pursuit of my goals has been unwavering. Thank you for getting me through my most challenging moments, for always being there for me and for being a source of continued inspiration. This is for you.

Finally, a special mention goes to my closest friend and fiancé Elin, who has been my biggest supporter and my rock throughout the last three and half years. You have always kept me positive, focused and most importantly, smiling, helping me through some of my toughest days even when inside I just wanted to give up, and for that I am eternally grateful. Thank you for everything you have done for me, it has helped me more than you could possibly know.

Definitions and Abbreviations

ALS	Airborne Laser Scanner
ANN.....	Approximate Nearest Neighbour
CCF-O	Cross-Correlation on Orientation Images
CMVS	Clustering View for Multi-View Stereo
COSI-Corr	Co-registration of Optically Sensed Images and Correlation
DEM	Digital Elevation Model
DTM	Digital Terrain Model
GCP	Ground Control Point
GLIMS.....	Global Land Ice Measurements from Space
GNSS	Global Navigation Satellite System
GPS.....	Global Positioning System
GSD	Ground Sampling Distance
IGS.....	Icelandic Glaciological Society
IMU	Inertial Measurement Unit
LIA	Little Ice Age
m.a.s.l.	Metres above sea level
MVS.....	Multi-View Stereo
NCC	Normalised Cross-Correlation
PMVS2.....	Patch-based Multi-View Stereo
PPK.....	Post-Processed Kinematic
PPP	Precise Point Positioning
RANSAC.....	RANdom SAmple Consensus
RIFT	Repeat-Image Feature Tracking
RINEX	Receiver Independent Exchange Format
RMSE.....	Root-Mean Square Error
RTK.....	Real-Time Kinematic

RTK-GPS.....	Real-Time Kinematic Global Positioning System
SAR	Synthetic Aperture Radar
SfM	Structure from Motion
SIFT	Scale Invariant Feature Transform
SLR.....	Sea level rise
TLS	Terrestrial Laser Scanner
TOL	Take-off and Landing
UAV	Uncrewed Aerial Vehicle
UTC.....	Coordinated Universal Time
WGMS	World Glacier Monitoring Service
WfC.....	Water-filled Crevasse

Chapter 1 INTRODUCTION

1.1. Background and Rationale

Intensive global climate warming, particularly over the last decade, is driving patterns of glacier recession and dynamics, and consequently it is now widely established that all glaciers worldwide are undergoing extensive retreat (Marzeion et al., 2014; Zemp et al., 2015, 2019; Farinotti et al., 2019). Such patterns of retreat and mass loss, exacerbated by anthropogenic warming, are forecast to continue over the coming decades (Meier et al., 2007; Gardner et al., 2013) due to the highly sensitive nature of glaciers to abrupt changes in climatic conditions (Marzeion et al., 2018). This sensitivity makes them both key indicators of recent climate change, and vulnerable to the climatic forcing they reflect (Huang and Li, 2011; Riveros et al., 2013).

This has important consequences for their meltwater contribution to global sea level rise (SLR) (Huss and Hock, 2015; Cazenave et al., 2018; Rossini et al., 2018; Zemp et al., 2019), as well as for regional hydrology due to the strong control glacier meltwater has on modulating down-glacier streamflow. This in turn affects freshwater availability, hydropower operations and sediment transport (Immerzeel et al., 2014; Huss and Hock, 2018; Shannon et al., 2019). Their future SLR contribution is of particular concern to researchers as although they only comprise a small fraction of the world's total ice volume (with the majority found in the two ice sheets), the consequences of the mass loss and SLR contribution from glaciers and ice caps are widespread and of global significance (Bach et al., 2018; Farinotti et al., 2019). Indeed, present rates of glacier mass loss are estimated to be equivalent to the sea-level contribution of the Greenland Ice Sheet over 2003-2012 (Khan et al., 2015), exceed the loss from the Antarctic Ice Sheet over 2012-2017 by 62% (IMBIE, 2018), and account for ~30% of total observed SLR over 1993-2014 (Watson et al., 2015).

Furthermore, while glaciers and ice caps have dominated cryospheric contributions to global SLR over the last century, they are forecast to contribute significantly over the coming century as well (Radić and Hock, 2011; Parkes and Marzeion, 2018; Farinotti et al., 2019). Although estimates of future contribution vary (depending on the emissions scenarios used to force future evolution), current modelling studies suggest that glaciers and ice caps could contribute between 79 ± 24 and 157 ± 31 mm to SLR, and potentially as much as 215 ± 21.3 mm, by the end of the century (Marzeion et al., 2014, 2018; Huss and Hock, 2015; Shannon et al., 2019).

To determine how glaciers may respond to climate change requires resolving patterns of glacier velocity in space and time (Riveros, et al., 2013; Vincent and Moreau, 2016). Glacier velocity, in

turn, is strongly controlled by glacier hydrology and bed deformation (Schellenberger et al., 2015; Hart et al., 2019b). Hydrological processes at the ice-bed interface are known to modulate ice-surface flow, and numerous studies, on both alpine glaciers (e.g. Hubbard and Nienow, 1997; Nienow et al., 1998; Vincent and Moreau, 2016) and Greenland outlet glaciers (e.g. van de Wal et al., 2008; Palmer et al., 2011; Bartholomew et al., 2012) among others, have demonstrated a clear relationship between surface meltwater input and increased ice flow (Zwally et al., 2002; Sundal et al., 2011).

However, despite the known importance of surface hydrology in modulating ice dynamics, it varies considerably in both space and time, and consequently it is still unclear exactly how this meltwater influences the basal hydrological system, and, therefore, overall glacier velocity at different spatial and temporal scales (Andrews et al., 2014; Ryser et al., 2014). As a result, the relationship between sub-surface glacial hydrology and ice velocity remains poorly understood. Furthermore, the present geographic reach of glacier case studies is limited: recent research has focused nearly entirely on the Antarctic and Greenland ice sheets (e.g. Palmer et al., 2011; Schroeder et al., 2013; Andrews et al., 2014; Muto et al., 2019), and on high-Arctic ice masses (e.g. Clason et al., 2012; How et al., 2017; Gong et al., 2018), meaning the dynamics of glaciers elsewhere is comparatively less well known.

This relationship between surface meltwater input and ice velocity becomes distinctly more blurred for those glaciers that terminate in water, however, be it a proglacial lake or a marine fjord. In these settings, glacier velocity (and, coincidentally, glacier retreat) is often instead controlled by an additional, and highly important mass loss mechanism termed calving (van der Veen, 2002; Howat et al., 2007; Benn and Åström, 2018). Calving is important because it can decouple the dynamic behaviour of a glacier from climate, with factors other than variations in mass balance, such as changes in water depth and glacier geometry, exerting major controls on the flow velocity and retreat rate of these glaciers (Meier and Post, 1987; Nick et al., 2009; Carrivick and Tweed, 2013). Indeed, these factors can often cause calving glaciers to flow considerably faster and retreat at a far greater rate than would otherwise be observed if their dynamic behaviour was forced solely by climate (i.e. surface ablation) (Benn et al., 2007b; Sakakibara et al., 2013; Baurley et al., 2020). This potential for calving glaciers to undergo rapid flow acceleration and terminus retreat (even during positive mass balance years), suggests they can contribute disproportionately to global sea level, further highlighting the importance of calving in controlling how such glaciers may respond in future (Benn et al., 2007b; Carrivick and Tweed, 2013; Chernos et al., 2016).

Of the two main types of waterbody that a glacier can terminate in, it is the calving dynamics of marine-terminating glaciers which have received the most attention in the literature over recent decades because the large and rapid losses often associated with these glaciers is particularly important for global SLR (Benn et al., 2007b; Trüssel et al., 2013; Truffer and Motyka, 2016). However, much less is known about the changing dynamics of, and the future contributions to SLR from, lake-terminating glacier systems, despite the number of such systems increasing worldwide in response to continued glacier retreat, with such patterns of lake formation forecast to continue in future (Schomacker, 2010; Trüssel et al., 2013; Shugar et al., 2020). Furthermore, while there has been an increase in the number of studies over recent years which have examined the changing dynamics of lake-terminating glaciers (e.g. Sakakibara and Sugiyama, 2014; Chernos et al., 2016; King et al., 2018; Tsutaki et al., 2019), the key processes which are forcing these changes are still not wholly understood, meaning further research is required so that the future dynamics and retreat patterns of these glaciers can be more accurately quantified (Carrivick et al., 2020; Shugar et al., 2020).

To date, much of our understanding of lake-terminating glacier dynamics stems from the application of satellite remote sensing, which facilitates the monitoring of these glaciers over a range of spatial (glacier-wide to regional) and temporal (days to decadal) scales with relatively low cost and effort (e.g. King et al., 2018; Dell et al., 2019; Xue et al., 2021). Furthermore, due to present constraints in our ability to access the ice-bed interface to assess basal movement directly, surface measurements of ice velocity are commonly used to improve our understanding of subglacial processes and provide insights into overall ice dynamics (e.g. Scherler et al., 2008; McNabb et al., 2012; Watson and Quincey, 2015; Sakakibara and Sugiyama, 2018). For example, Baurley et al. (2020) utilised satellite remote sensing to investigate the changing dynamics of Breiðamerkurjökull, southeast Iceland, over a 27-year period. The authors found that near-terminus surface velocities increased from $\sim 1.00 \pm 0.36 \text{ m d}^{-1}$ in 1991 to $3.50 \pm 0.25 \text{ m d}^{-1}$ in 2015, with velocities remaining elevated from ~ 2008 onwards. Furthermore, nearly 3.5 km of retreat was observed between 1982 and 2018, with $\sim 2.6 \text{ km}$ of this retreat occurring since ~ 2006 , coinciding with a 270% increase in the area of its proglacial lake, Jökulsárlón. The authors suggest that while initial retreat was instigated by rising air temperatures following the Little Ice Age, once Jökulsárlón increased to a sufficient size where it was able to start influencing frontal retreat and ice flow, then this became the dominant mechanism, resulting in the rapid retreat and increased velocities observed since the turn of the 21st century. Similar interpretations have also been reached by several other satellite remote sensing-based studies of lake-terminating glaciers, including Sakakibara et al. (2013), Dell et al. (2019) and Liu et al. (2020).

However, despite the widespread use of satellite remote sensing in cryospheric studies, the method still suffers from several important limitations (Whitehead et al., 2013; Bhardwaj et al., 2016; Śledź et al., 2021). These are primarily related to the relatively coarse spatial and temporal resolution of the currently available sensors, and to the susceptibility of the imagery to certain weather conditions (e.g. cloud cover), which can significantly affect the regularity and quality of the acquired data (Altena and Käab, 2017; Yang et al., 2020; Śledź et al., 2021). In particular, this can make it difficult to investigate the short-term changes and spatial variability in calving behaviour and ice dynamics that are occurring at these glaciers using satellite remote sensing alone, and thus their influence on overall ice dynamics remains unclear (Altena and Käab, 2017b; Wigmore and Mark, 2017; Groos et al., 2019).

The emergence of uncrewed aerial vehicles (UAVs) in cryospheric research over recent years, however, may provide a sound alternative due to their ability to offer rapid assessments of glacier surface dynamics at extremely high spatial (cm-scale) and temporal (sub-daily) resolutions (Whitehead et al., 2013; Ryan et al., 2015; Chudley et al., 2019). This method has a number of advantages, the primary one being that it is well-suited for conducting rapid repeat surveys of the ice surface due to the ability to deploy the UAV system 'on demand' (Immerzeel et al., 2014; Rossini et al., 2018), which affords glaciologists the opportunity to undertake weekly, daily or even sub-daily surveys of the ice surface at high spatial resolutions (e.g. Bash et al., 2018; Jouvét et al., 2019; Xue et al., 2021). Furthermore, because surface measurements (e.g. of ice velocity) are typically used to infer about the conditions at the bed of a glacier, it means repeat UAV surveys can provide important insights into the overall dynamic behaviour of ice masses. Consequently, the increased spatial and temporal resolution of data collected by such methods, especially when compared to traditional satellite remote sensing, will likely enhance our ability to monitor and quantify the rapidly changing glacial landscape, and how it may respond in future (e.g. Ryan et al., 2015; Benoit et al., 2019; Groos et al., 2019; Jouvét et al., 2019).

This method is particularly suited for investigating those glaciers in southeast Iceland, which are known to be highly sensitive to climate warming, with extremely rapid glacier retreat observed here in recent years as a result (Sigurðsson et al., 2007; Bradwell et al., 2013; Hannesdóttir et al., 2015). Furthermore, this retreat has also resulted in the formation and rapid growth of proglacial lakes at the termini of many of these glaciers, which are now beginning to exert a significant control on their overall dynamics (e.g. Schomacker, 2010; Dell et al., 2019; Baurley et al., 2020). However, in general there is a paucity of studies in this region that have investigated the dynamics of these glaciers, with much of the focus limited to just one glacier (Breiðamerkurjökull), despite it not being wholly representative of many of the other glaciers in the region. As such the current

and future dynamic behaviour of these lake-terminating glaciers is not well understood (Björnsson and Pálsson, 2008; Björnsson et al., 2013; Guðmundsson et al., 2019).

1.2. Aims and Objectives

Consequently, to investigate glacier velocity and ice dynamics at varying spatial and temporal resolutions, this project utilised ultra-high resolution repeat UAV imagery to measure 3D changes in ice surface and surficial patterns in ice topography at Fjallsjökull, a large lake-terminating glacier in southeast Iceland. This was achieved through the following objectives:

- 1) Undertake repeat surveys over the terminus region of Fjallsjökull at different timescales across the 2019 and 2021 ablation season using ultra-high-resolution UAV structure-from-motion (SfM) photogrammetry.
- 2) Utilise a 'feature tracking' methodology to resolve spatially heterogeneous patterns in surface velocity over different temporal intervals.
- 3) Investigate the change in ice surface elevation across each research period, and determine to what extent these changes are controlled by surface velocity and overall ice dynamics.
- 4) Examine the impact that individual calving events may have had upon glacier surface velocity, as well as overall terminus geometry, by providing a robust estimate of glacier calving over time.
- 5) Map and analyse the evolution of supraglacial lakes and water-filled crevasses on the ice surface to determine how these may have forced short-term, localised variations in surface velocity.
- 6) Compare and contrast the UAV datasets from both years to investigate how the dynamics of Fjallsjökull are evolving across different timescales (e.g. sub-seasonal to seasonal), whether these changes are being forced by glacier-specific or climate-specific factors, and what this may mean for the future response of the glacier.

1.3. Thesis Structure

Following **Chapter 1** (*Introduction*), the *Literature Review* in **Chapter 2** explores the field of ice motion, and how glacier motion can be monitored and understood. It first focuses on the basic theory behind glacier movement and glacier hydrology, with particular focus given to describing the temporal variations in ice motion that can occur in response to surface meltwater delivery to the bed. Next, glacier calving, the different calving mechanisms and the influence of these on ice motion are then explored, with the role of calving on the dynamics of lake-terminating glaciers

Chapter 1

described in particular detail due to its explicit relevance to this thesis. Following this, an overview of the use of satellite remote sensing for the monitoring of glacier dynamics is given, before the UAV-SfM methodology is introduced and described, with particular focus given to its advantages compared to traditional satellite remote sensing, and thus its suitability for this research.

Chapter 3 (*Study Area and Location*) introduces Fjallsjökull, the study glacier for this research.

Firstly, the recent climatic changes that have occurred in Iceland are outlined, particularly in regard to rising air temperatures and what this has meant for glacier mass loss. Next, detailed insights into the study glacier itself are provided, in terms of both its climatic and glaciological setting, as well as the recent changes it has undergone. Finally, an overview of the previous work undertaken at Fjallsjökull and its relevance to this thesis are discussed.

Chapter 4 (*Methods*) provides detailed information on all the methods utilised in the research, both those used while in the field, and those utilised post-fieldwork. First, the UAV system, survey set-up (e.g. mission planning) and site set up (e.g. georeferencing) used to obtain the imagery in both 2019 and 2021 is outlined. Next, the steps used to process this imagery into high-resolution 3D models (i.e. orthomosaics and DEMs) of the ice surface are then described in detail. Particular attention is given to the errors obtained in the creation of these models and how these vary between individual surveys and each research trip. Following this, the exact methods used to obtain each of the glacier-specific products, including how error was derived, are then described in turn.

Chapter 5 (*Results*) presents and describes the different glacier-specific products that were obtained from the UAV-derived 3D models. Firstly, the glacier velocity products produced at daily and multi-day intervals for both 2019 and 2021 are presented, with the overall velocity pattern of each described, as well as any localised variations that are present. Next, the changes in surface elevation across each research period are presented, with both the overall, and more localised, patterns of elevation gain and loss described in detail. Following this, the estimates of glacier calving, as well as changes in frontal position (i.e. retreat rate) for each day are then presented, before any observed variations between individual days, or indeed between the different research periods, are then described. Finally, the daily variations in surface hydrological features are then presented, with particular focus given to how these features evolve (i.e. grew or disappeared) across each of the research periods.

Chapter 6 (*Interpretation and Discussion*) suggests possible explanations, supported by the literature, for the patterns and trends presented in Chapter 5, as well as their wider relevance. The three distinct processes that are controlling the dynamics of Fjallsjökull, and the different spatial and temporal scales at which they operate, are first discussed. These are: (i) Large-scale

velocity variations and links to basal topography, (ii) Localised velocity variations and links to subaqueous melt and (iii) Supraglacial lake drainage and short-term velocity variations. A brief comparison between the data acquired in 2019 and 2021 is then outlined, with possible explanations for any differences given. Following this discussion, a summary of the three mechanisms is presented and a hierarchy is put forward, based on the relative importance of each process in controlling the dynamics of Fjallsjökull. The following section discusses the wider implications of these findings and is split into three parts. The first of these puts the findings of this research into the wider climatological context to investigate whether the observed dynamic behaviour is predominately being forced by the changing climate of the region, or by glacier-specific factors. Next, the results of this research are placed in the broader global context by providing examples from other studies to date which have shown the importance of basal topography in controlling the dynamics of lake-terminating glaciers. Finally, the third part revisits the importance of UAVs as a tool for monitoring glacier dynamics by using the data acquired in this research as supporting evidence for the relative advantages and disadvantages of the method compared to traditional satellite remote sensing. The chapter then closes by offering some thoughts as to the current suitability of the method, and how it can be best utilised to ensure the changing dynamics of glaciers at different spatial scales can be more accurately quantified.

Chapter 7 (*Conclusions*) summarises the key findings of the research, as well as those that have emerged from the previous chapter. It also briefly discusses the wider implications of these findings, in particular what they mean for both the current and future response of Fjallsjökull, as well as for the future response of other lake-terminating glaciers in Iceland and elsewhere. Finally, some potential avenues for future work are explored.

Chapter 2 LITERATURE REVIEW

2.1 Glacier Movement

One of the most fundamental characteristics of glaciers is their ability to move. Glaciers flow in response to the force of gravity pulling them vertically downwards (due to the weight of the ice), which results in the horizontal movement of the glacier (Cuffey and Paterson, 2010; Jiskoot, 2011). Generally, the rates of ice flow are dependent on the stresses acting upon the glacier, the way in which the ice can deform, and whether or not, and how, the glacier can slide over or deform its bed (Jiskoot, 2011; Dehecq et al., 2019). In the majority of cases, the flow of a glacier can be described using a *force balance* approach, which relates the gravitational driving stress (the force driving the glacier forward) to the resistive stresses (the forces resisting ice flow), and how these vary in time and space (Figure 1) (O'Neel et al., 2005; Cuffey and Paterson, 2010; Jiskoot, 2011). In their pioneering study on glacier force balance, van der Veen and Whillans (1987) were the first to define the relationship between the driving and resistive stresses and how these stresses control the flow of ice masses. What follows here is a brief description of the different components that make up the glacier force balance and how these relate to glacier flow. For further detail on the specific mathematical theory of glacier force balance, readers are referred to van der Veen and Whillans (1987), Cuffey and Paterson (2010), and references therein.

The gravitational driving stress is fundamentally determined by the thickness of the ice and the surface slope of the glacier, and thus is influenced by gains and losses of mass (van der Veen and Whillans, 1987; O'Neel et al., 2005; Dehecq et al., 2019). For example, thickening of the accumulation area and thinning in the ablation area will result in a steeper surface slope, leading to an increase in the gravitational driving stress (Cuffey and Paterson, 2010; Jiskoot, 2011). As such, glacier flow is intricately related to a glacier's surface mass balance (Benn and Evans, 2010). The resistive stresses, meanwhile, act on the base of the glacier in the form of basal drag, at the sides of the glacier in the form of lateral drag or through pushing and pulling due to longitudinal stress gradients within the ice (van der Veen and Whillans, 1987; Cuffey and Paterson, 2010). These resistive forces often result from the strength of the glacier ice, the contact between the glacier and its bed, and the composition of the bed itself (Benn and Evans, 2010; Dehecq et al., 2019).

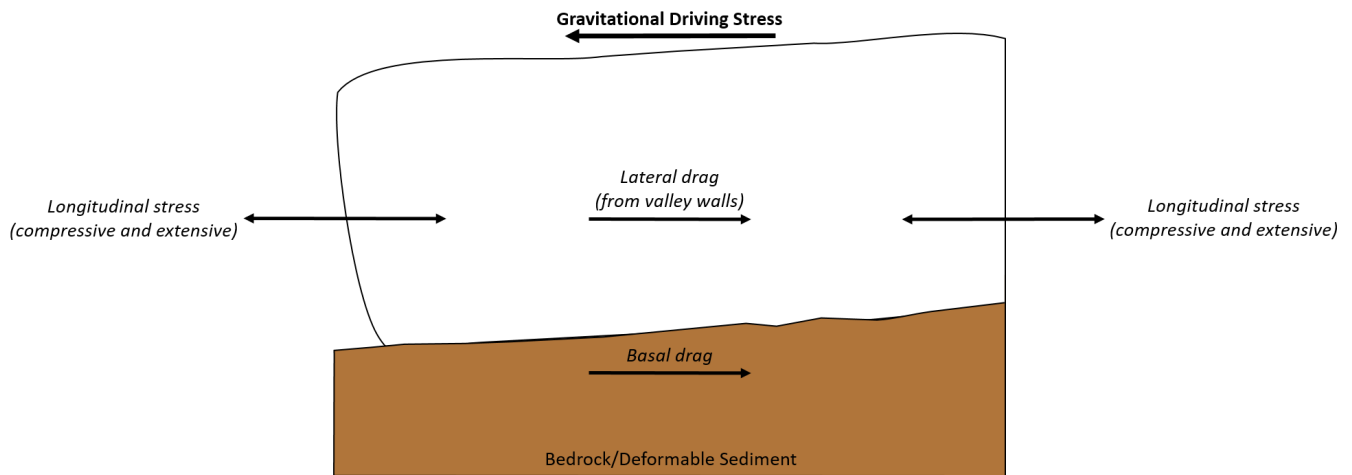


FIGURE 1 Cross-section of a typical glacier illustrating the different components that make up the glacier force balance. Driving stresses are given in bold, while the resistive stresses are given in *italics*. Ice flow direction is from right to left. Figure modified from Davies (2020).

Over extended periods of time, the driving and resistive forces are kept in natural and dynamic balance by glacier flow, with the glacier generating sufficient driving forces to overcome the resistive forces and thus balance the mass budget of the glacier (Iken and Truffer, 1997; Benn and Evans, 2010; Jiskoot, 2011). However, the resistive forces can undergo temporary and rapid changes, primarily due to variations in water input and storage at the glacier bed, which allows the glacier to speedup (or slow-down) over varying (often short) timescales (Iken and Bindshadler, 1986; Nienow et al., 1998; Benn et al., 2007b; Andrews et al., 2014; Dehecq et al., 2019).

A particularly important component of glacier movement is the concept of the *effective pressure*, which is defined as the ice overburden pressure (the weight and thickness of the overlying ice at any given point) minus the basal water pressure (the amount of pressurised water within the basal system) (Benn and Evans, 2010; Schoof, 2010). This concept is important because variations in the effective pressure control the amount of coupling between the ice and its bed (Willis, 1995; Schoof, 2010). Where basal water pressures equal zero, the effective pressure is the same as the overburden pressure and thus at its maximum, meaning no bed separation can occur and the glacier moves slowly (Shreve, 1972; Benn and Evans, 2010). Conversely, when basal water pressures equal the overburden pressure, the effective pressure is zero, meaning the ice is wholly supported by a thin layer of water and thus can be separated from its bed, leading to faster ice movement (Bindshadler, 1983; Howat et al., 2008a; Schoof, 2010). The three mechanisms by which glaciers move; internal deformation, bed deformation and basal sliding (Figure 2), are all controlled to different extents by spatial and temporal variations in the effective pressure (Creyts and Schoof, 2009). The effective pressure also exerts a strong influence on the character of sub-glacial drainage (Section 2.2.1.) and on the dynamics and stability of calving glaciers (Section

2.4.3.) indicating its significance within Glaciology (Shreve, 1972; Iken, 1981; Iken and Bindshadler, 1986; Benn and Evans, 2010; Sugiyama et al., 2011).

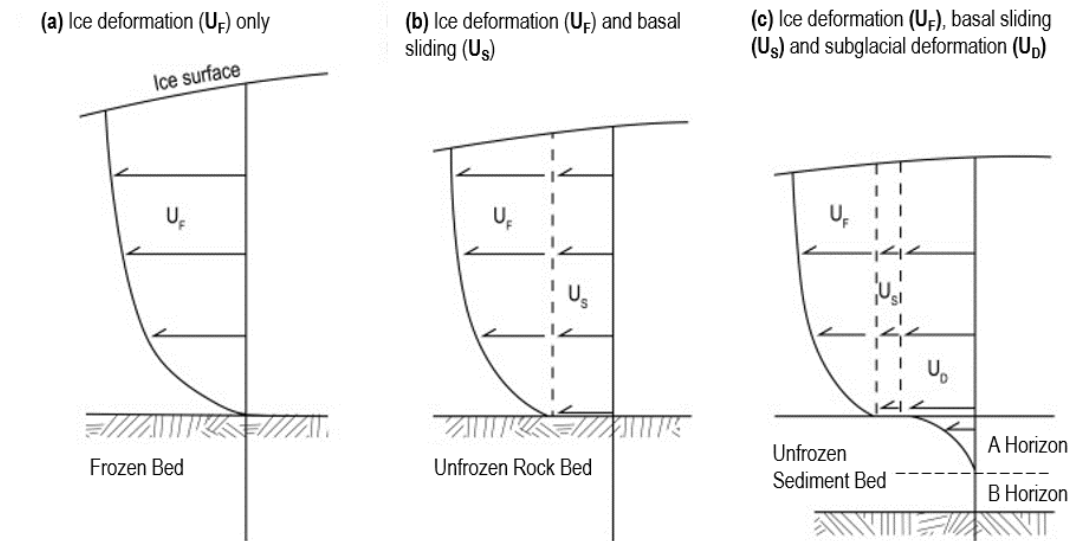


FIGURE 2 Schematic illustrating the vertical velocity distribution for the three different types of glacier motion. (a) Ice deformation only over a frozen bed (rigid or sediment); (b) Ice deformation and basal sliding over an unfrozen rigid bed and (c) Ice deformation, basal sliding and subsole deformation over unfrozen deformable sediments. Modified from Boulton (1996).

2.1.1 Internal Deformation

Ice deformation refers to the change in shape of a region of glacier ice in response to stress, and can consist of either creep or fracture (Benn and Evans, 2010; Jiskoot, 2011). Most internal ice motion is considered in terms of ice creep, which is the deformation that results from the movement within or between individual ice crystals, and thus is a consequence of several complex interrelated processes (Weertman, 1983; Alley, 1992). Movement *within* crystals may occur by gliding along cleavage planes (lines of weakness related to the molecular structure of the crystal), or through movement along crystal defects, whereas the movement *between* crystals involves changes in their shape or size through recrystallization at the grain boundaries (Nye, 1952; Benn and Evans, 2010).

The relationships describing the response of ice to stress (termed 'flow laws') have been established in numerous lab studies, with the most widely used being Glen's Law (Glen, 1955) which was first adopted for glaciers by Nye (1957):

$$\varepsilon = A\tau^n$$

Where ε is the strain rate, A and n are constants and τ is the shear stress of the ice. A decreases rapidly with ice temperature, so that the colder the ice, the less readily it deforms (Hubbard and

Glasser, 2005). This is because the creep processes are most effective when melting occurs at the grain boundaries (Benn and Evans, 2010). The flow law exponent n also varies, but is often given a value of ~ 3 (Hooke, 1981). This means that the strain rate is proportional to the cube of the shear stress, highlighting how a small increase in stress produces a large increase in strain (Nye, 1952; Benn and Evans, 2010). As a result, glacier motion due to creep is a function of the thickness of the ice and the surface slope, with thicker and steeper glaciers having a larger rate of internal deformation than thin glaciers with shallow slopes (Cuffey and Paterson, 2010; Jiskoot, 2011). However, in reality it is unrealistic to think in terms of a single flow law for ice as several processes contribute to creep, and thus their relative importance changes in space and time (Hubbard and Glasser, 2005; Benn and Evans, 2010). Therefore, any general flow law would need to be incredibly complicated, and so it is more desirable to formulate different flow laws depending on the dominant processes of creep present (Alley, 1992).

2.1.2 Subsole (Bed) Deformation

The process of subsole deformation, where the sediments underlying a glacier may undergo permanent strain in response to stresses imposed by the ice, is now widely-believed to account for a significant portion of the forward movement of a number of glaciers because the strain rates within the sediment may be equal to or greater than the peak strain rates in the ice (Boulton et al., 2001; Hubbard and Glasser, 2005; Benn and Evans, 2010). Furthermore, it is thought that up to 85% of the motion of a glacier underlain by soft sediments occurs within the sediment (till) itself, rather than the overlying ice (Boulton et al., 2001; Hart et al., 2019a). Indeed, the processes of subsole deformation have received a large amount of attention over recent decades due to the fact they may provide possible mechanisms for the fast flow of numerous outlet glaciers and ice streams (e.g. Boulton and Jones, 1979; Alley et al., 1987b; Tulaczyk et al., 2000; Bougamont et al., 2014; Hart et al., 2019a,b).

The earliest evidence of subsole deformation came from a series of experiments undertaken at Breiðamerkurjökull, Iceland by Boulton (1979), and later Boulton and Hindmarsh (1987), who inserted segmented rods into the unfrozen till layer and found that when they were recovered several days later, the rods had been displaced down-glacier, providing clear evidence for a deforming bed (Figure 3).

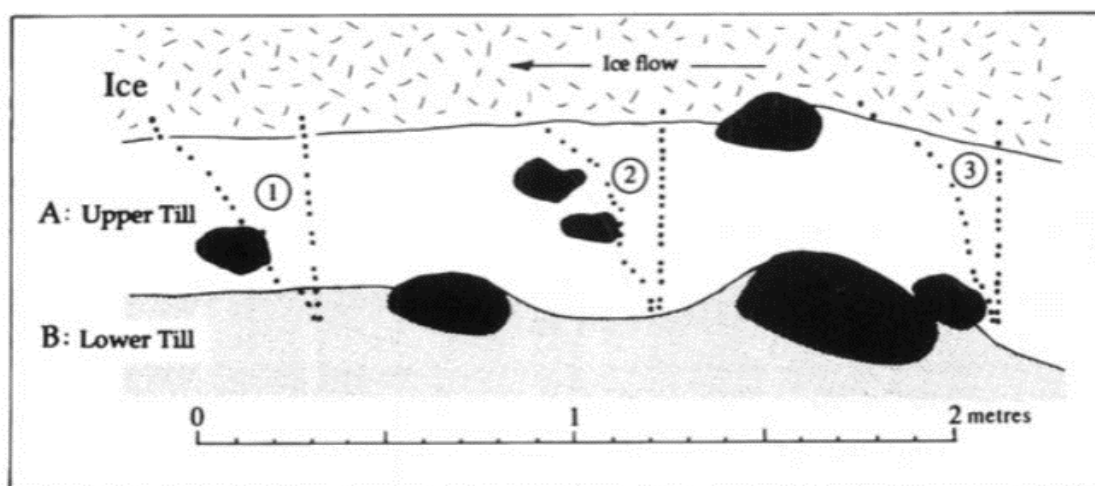


FIGURE 3 The displacement of segmented rods placed into the till of Breiðamerkurjökull, south Iceland by Boulton and Hindmarsh (1987). The initial and final positions of the three-segmented rods (labelled 1, 2 and 3) are shown. Taken from Benn (1995).

It was found that most deformation occurred by ductile flow in the upper layer of low strength till, which accounted for 80-95% of all forward movement (Boulton, 1979). The low-strength of the till was attributed to it having a low density, where only 40-45% of the total volume was occupied by mineral grains, with the rest consisting of water-filled pores (Boulton and Hindmarsh, 1987; Benn and Evans, 2010). Indeed, porewater pressures were found to be high, and tended to fluctuate daily in response to the amount of meltwater reaching the bed (Boulton, 1979). Finally, their measurements importantly showed a strong relationship between porewater pressures and strain rates in the deforming till, with peak strain rates lagging behind peaks in water pressure by several hours (Boulton, 1979; Boulton and Hindmarsh, 1987), indicating that the till water-content, strength, and deformation, as well as the rates of basal melting and glacier movement are strongly coupled together (Boulton and Hindmarsh, 1987; Clarke, 1987a; Boulton et al., 2001).

Around the same time, Alley et al. (1986, 1987a,b,c) and Alley (1989) used seismic data to argue that unfrozen deforming till underlies a large portion of Ice Stream B, West Antarctica, thus comprising an important component of overall velocity. Similarly, borehole studies at Trapridge Glacier, Yukon (Blake et al., 1992) and Storglaciären (Iverson et al., 1995) revealed complex patterns of subsole till deformation, with rates and direction of strain varying on an hourly basis. Finally, Tulaczyk et al. (2000) showed how such coupling between the till, porewater content and basal movement could explain the variation in flow regime of Ice Stream B in West Antarctica through a Coulomb model of till strength. More recently, several studies have highlighted how subglacial sediments underlie several of the major ice streams draining West Antarctica, with important implications for their stability (e.g. Schroeder et al., 2013; DeConto and Pollard, 2016).

Despite such key findings, the number of direct observations of subsole deformation occurring is still limited, and as such our current understanding and its influence on glacier movement is primarily based on theoretical modelling (Benn and Evans, 2010). Several such modelling studies have been undertaken (e.g. Boulton and Hindmarsh, 1987; Clarke, 1987b; Alley, 1989; Kamb, 1991), and although their methods of analyses differ, most agree that subglacial sediments will not undergo permanent deformation unless subjected to some threshold stress, known as the yield, or critical shear stress (Tulaczyk et al., 2000; Boulton et al., 2001; Jiskoot, 2011). The value of the critical shear stress varies with several factors, the most important being the effective pressure, exerted on the sediment by the overlying ice (Alley et al., 1986; Hubbard and Glasser, 2005; Benn and Evans, 2010). Above the critical shear stress, the sediment will deform, with the strain rates varying in a non-linear fashion with the shear stress and confining pressure (Tulaczyk et al., 2000; Benn and Evans, 2010; Jiskoot, 2011).

Within deforming sediments, the porewater pressure (i.e. the effective pressure) is an important factor in determining subglacial processes and the resulting deformation (Kjær et al., 2006; Iverson, 2010; Hart et al., 2019a). At low water contents, the porewater tension pulls grains together, increasing the normal stress and thus the frictional strength of the sediment, reducing overall ice motion (Benn and Evans, 2010). However, as the amount of water within the sediment, and thus the porewater pressure, increases, these tension forces disappear, leading to a reduction in the strength of the sediment (Iverson et al., 1999a; Cuffey and Paterson, 2010). This means that part of the weight of the overlying ice is transferred from the sediments to the porewater, leading to a reduction in effective pressure, increased deformation and thus increased ice motion (Iverson et al., 1999a; Boulton et al., 2001; Jiskoot, 2011).

Sediment deformation is also more likely to occur when the water within the sediment cannot drain away freely, leading to sustained increases in porewater pressure and thus overall increases in ice velocity (Iverson et al., 1999a; Boulton et al., 2001; Hart et al., 2019b). At very high basal water pressures, there is extensive decoupling of the ice from the till and thus a reduction in sediment deformation rates, with rapid ice flow now facilitated by efficient sliding over a well-lubricated bed (Iverson, 1990, 1999b; Kjær et al., 2006; Benn and Evans, 2010). Such a mechanism illustrates the complex and interrelated nature of the subsole deformation and basal sliding processes, while further highlighting the strong dependence of glacier motion on variations in water pressure at the glacier bed (Boulton et al., 2001; Benn and Evans, 2010; Armstrong and Anderson, 2020).

2.1.3 Basal Sliding

Basal sliding is the name given to the slip that occurs between a glacier and its bed (Hubbard and Glasser, 2005; Jiskoot, 2011). In theory, wet ice resting on smooth bedrock would lead to highly efficient sliding and thus movement would be catastrophically fast, however, in reality this rarely ever occurs, primarily due to several independent factors that increase the drag between the ice and its bed (Howat et al., 2008a; Benn and Evans, 2010). The most important factors controlling drag (and thus rates of sliding) are (i) adhesion due to freezing of ice to the bed, (ii) bed roughness, (iii) the quantity and distribution of water at the bed and (iv) the amount of rock debris at the base of the ice (e.g. Weertman, 1957; Shreve, 1984; Schweizer and Iken, 1992; Willis, 1995). Due to its relevance to this thesis, the effect of basal water pressure on sliding will be discussed in more detail below. For more detail on the other factors, interested readers are referred to Benn and Evans (2010) and references therein.

The presence of pressurised water at the glacier bed is a fundamental requirement for effective sliding to occur, and it is widely recognised that the distribution and pressure of water at glacier beds is the most important factor regulating short-term velocity fluctuations (e.g. Willis, 1995; Hubbard and Nienow, 1997; Howat et al., 2008a; Schoof, 2010; Armstrong and Anderson, 2020). Indeed, numerous studies have demonstrated a strong association between periods of increased glacier motion and elevated basal water pressure, as determined from the level of water in boreholes that have made a connection with the subglacial drainage system (e.g. Iken et al., 1983; Hooke, 1989; Hubbard et al., 1995; Jansson, 1995; Andrews et al., 2014), and thus it is unsurprising that basal water pressure forms an important component of modern glacier sliding theory (e.g. Lliboutry, 1968, 1983; Fowler, 1987; Kamb, 1987; Schweizer and Iken, 1992).

For glaciers flowing over rock beds, the presence of a thin water-film may enhance sliding by submerging minor obstacles (of the order of millimetres), effectively creating a smoother bed and thus reducing the importance of these obstacles as a limiting factor in sliding (Figure 4a) (Weertman, 1964, 1972). At larger scales, bed roughness is reduced by the presence of pressurised water in cavities (Figure 4b). Water-filled cavities will form at the leeside of obstacles on the bed when the water pressure exceeds the local effective pressure exerted by the ice (Weertman, 1964; Lliboutry, 1968; Harper et al., 2007), and can occur as isolated features or form part of a linked-cavity network connected by narrow orifices (Lliboutry, 1968, 1976). The pressure fluctuations in these networks, and the extent of their formation, generally reflects variations in the supply of meltwater from the surface, with increasing meltwater delivery to the bed leading to an increase in water pressures, further reducing bed roughness and increasing sliding (Hooke, 1989; Willis, 1995; Schoof, 2005, 2010).

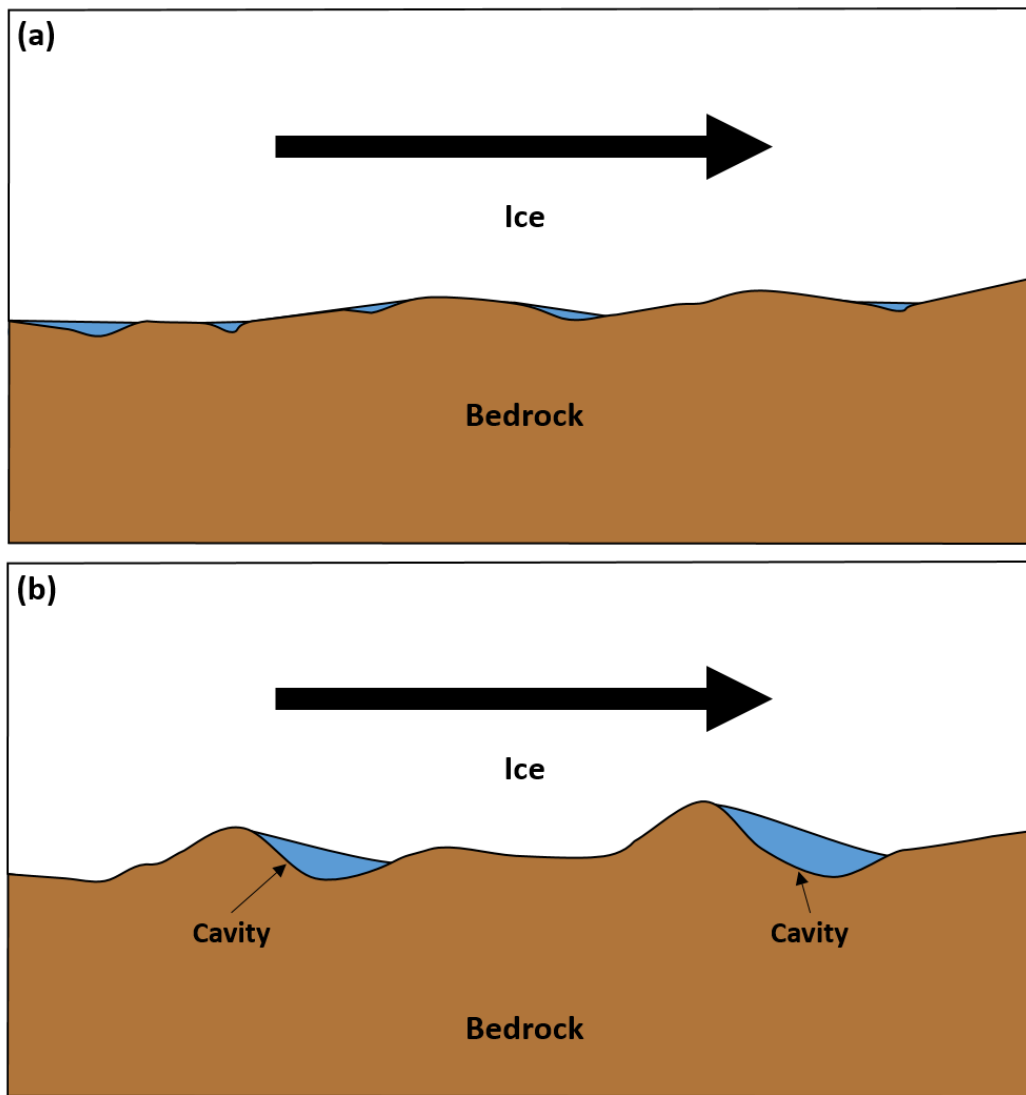


FIGURE 4 Schematic illustrating two of the ways in which water at the bed can influence sliding velocity. (a) The presence of a thin water film that submerges small bed roughness elements, creating a smoother bed. (b) Water-filled cavities that have formed in the lee of bedrock bumps, which can further reduce bed roughness.

The water pressure at which cavities begin to form is dependent on bed roughness because the size and shape of obstacles governs spatial variations in the effective pressure exerted by the ice, and thus determines the extent and magnitude of low-pressure zones in lee-side locations in which cavities may form (Iken, 1981; Bindshadler, 1983). The threshold water pressure for cavity formation is known as the separation pressure, and is high for short-wavelength, high amplitude bumps, and low for long-wavelength, low amplitude bumps (Iken, 1981; Schweizer and Iken, 1992), meaning sliding rates will be more sensitive to rising water pressures on smooth beds than on rougher ones (Benn and Evans, 2010).

Enhanced sliding caused by increasing cavity water pressure generates additional meltwater at the bed because of the increased generation of viscous heat and pressure melting (Iken, 1981).

Once a certain threshold is reached, this process creates a positive feedback loop by increasing the water pressure in cavities, thus further increasing the sliding rate, which in turn leads to the generation of more meltwater and so on (Iken and Bindschadler, 1986; Schweizer and Iken, 1992). This process can, therefore, lead to unstable, accelerating sliding of the glacier with the velocity increasing catastrophically until the subglacial drainage system 'switches' to a more efficient channelised system, evacuating the excess water and leading to a reduction in the areal extent and pressure of water at the bed, and thus a reduction in sliding velocities to more sustainable levels (Iken and Bindschadler, 1986; Schoof, 2005, 2010; Benn and Evans, 2010). The point at which sliding becomes unstable is termed the critical pressure, and it is widely thought that the transition from stable to unstable sliding as water pressures cross the critical pressure can account for the rapidly accelerating ice flow during glacier surges, and for the short-term seasonal velocity increases observed on numerous glaciers (e.g. Kamb, 1987; Willis, 1995; Sugiyama et al., 2011; Vincent and Moreau, 2016).

Although several different equations exist which can explain the sliding behaviour of glaciers, they are often difficult to apply in practice (Benn and Evans, 2010). Instead, it is often preferable to use simpler empirical sliding relations, which describe relationships between basal water pressure and sliding velocity (e.g. Budd et al., 1979; Pattyn, 2002). Importantly, these relations indicate that sliding rates increase with basal shear stress while being inversely proportional to the effective pressure, i.e. sliding increases with water pressure (Bindschadler, 1983; Schoof, 2010). This exponential relationship between sliding and effective pressure indicates that small changes in sliding will occur when water pressures are low, and large changes in sliding will occur when water pressures are high (Hubbard and Glasser, 2005; Jiskoot, 2011). However, the clear complexity of the sliding process means that an all-purpose sliding law remains elusive (Schoof, 2005, 2010; Benn and Evans, 2010).

2.2 Glacier Hydrology

Meltwater, produced through surface ablation (and, to a lesser extent, basal melting), is an important component of the glacier system. For example, meltwater has a profound influence on the overall motion of glaciers, as well as on the erosion, transportation and deposition of glacial sediments and the landform assemblages they can produce (Hubbard and Glasser, 2005; Schoof, 2005; Benn and Evans, 2010). Glacier meltwater is also important for human livelihoods, providing seasonal irrigation to farmers and renewable energy for millions through hydroelectric power generation (Huss and Hock, 2018; Shannon et al., 2019). However, it can also be a serious hazard, with the sudden (and often catastrophic) drainage of stored meltwater (e.g. in proglacial lakes)

forming a recurring and potentially fatal threat in glaciated regions such as the High Andes, Himalaya, and Iceland (Schomacker, 2010; Carrivick and Tweed, 2013; Nie et al., 2017). Of relevance to this thesis, however, is the role (subglacial) meltwater has in controlling overall glacier motion. Indeed, it is widely agreed that the single most important factor controlling variations in glacier motion is the distribution and pressure of water at the glacier bed (Willis, 1995; Hubbard and Nienow, 1997; Howat et al., 2008a; Hart et al., 2019a,b).

2.2.1 Subglacial Drainage Systems

An understanding of the configuration and dynamics of subglacial drainage systems is important for understanding the role subglacial hydrology has on glacier dynamics, both via subglacial sediment deformation (e.g. Boulton and Hindmarsh, 1987; Clarke, 1987b; Iverson et al., 1995), and basal sliding (e.g. Iken, 1981; Iken and Bindshadler, 1986; Schoof, 2010). Several field-based studies, allied with conceptual and numerical models have provided evidence for the existence of a variety of subglacial drainage systems, the distribution of which depends on water discharge, the temperature distribution at the ice-bed interface and the permeability, topography and rigidity of the bed (Hubbard and Nienow, 1997; Fountain and Walder, 1998; Benn and Evans, 2010).

A fundamental distinction is made between channelised (discrete) or distributed systems of drainage (Figure 5). The former is often composed of channels incised upwards into the ice (e.g. Röthlisberger, 1972; Hooke et al., 1990), or downward into the bedrock (Nye, 1973), which form efficient linked networks with the capacity to drain large amounts of meltwater rapidly from the bed (Fountain, 1994; Hubbard et al., 1995; Vincent and Moreau, 2016). The existence of such channels has been confirmed by dye-tracing studies since the late 1960s (e.g. Stenborg, 1969; Behrens et al., 1975; Seaberg et al., 1988; Nienow, 1994). Such studies have shown that the dye emerges as a single concentrated peak, indicating little dispersal during flow and no storage in side channels, with reported transit velocities suggesting that meltwaters are transported at some tens of centimetres a second, providing strong evidence for efficient channelised drainage systems (Iken and Bindshadler, 1986; Willis et al., 1990; Hubbard and Nienow, 1997).

In comparison, distributed systems drain extensive areas of the bed at lower flow rates, leading to inefficient, poorly connected networks, which may occur via meltwater films (Weertman, 1957, 1972), linked-cavity networks over bedrock (Lliboutry, 1968; Walder, 1986), permeable subglacial sediments (Boulton, 1974) or through 'canals' above these sediments (Walder and Fowler, 1994). Individual flow pathways are commonly spatially distributed, taking the form of small, anastomosing passages, where water pressures scale positively with discharge, preventing down-

glacier evolution into a small number of major channels (Hubbard and Nienow, 1997; Fountain and Walder, 1998).

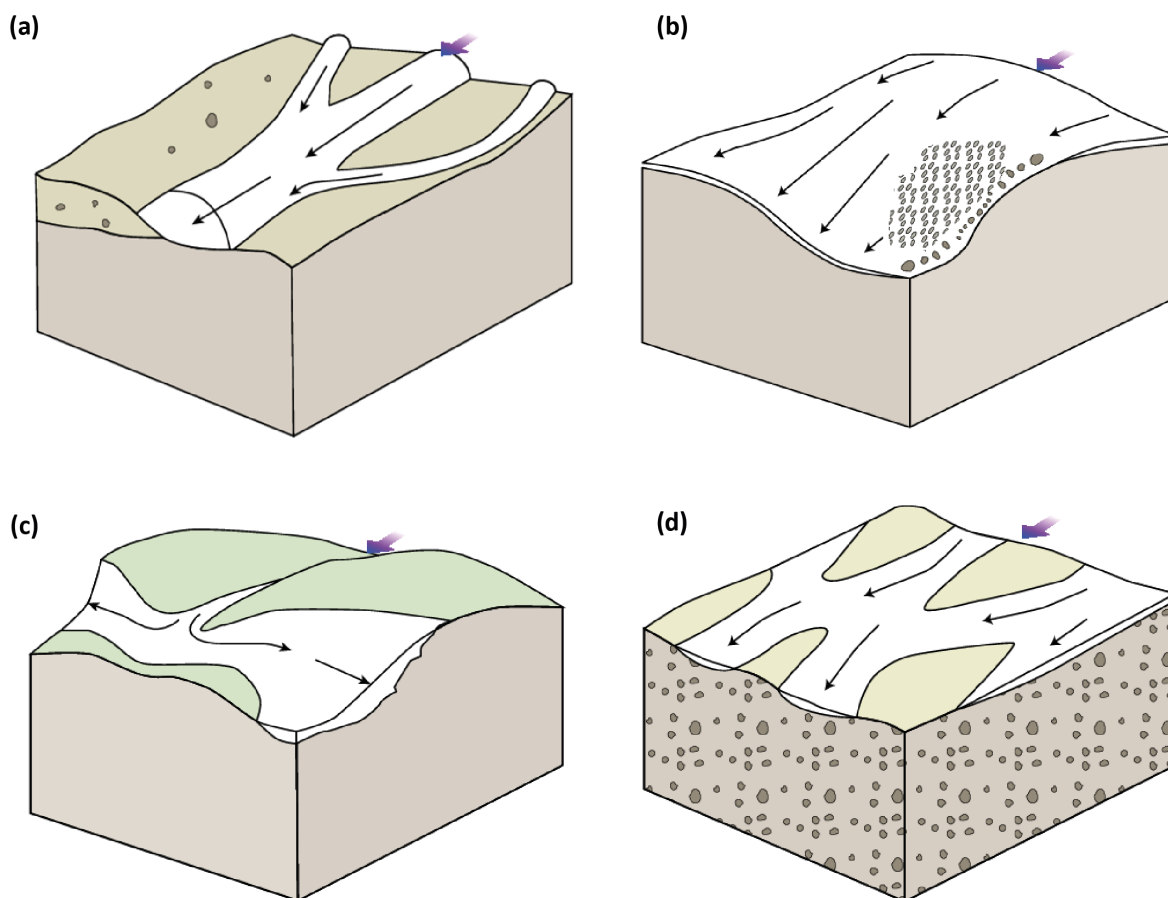


FIGURE 5 Simple schematic diagrams of the main forms of efficient and inefficient subglacial drainage systems for rigid and deforming beds. (a) Channelised network; (b) thin water film; (c) linked-cavity network and (d) braided canal system. Type (a) is an efficient system, while (b), (c) and (d) are forms of inefficient drainage. Purple and black arrows denote ice flow and subglacial water flow direction, respectively. Figure adapted and modified from Benn and Evans (2010) and Rossman (2015).

Again, dye-tracing studies have confirmed the presence of such inefficient systems, whereby rather than the dye emerging from the glacier as one single, sharp peak, where inefficient systems are present the dye will emerge as a diffuse, multi-peaked pattern (Willis et al., 1990; Benn and Evans, 2010). This indicates the splitting and re-joining of different flow paths, as well as the temporary storage of water within the drainage network (Lliboutry, 1976, 1979; Benn and Evans, 2010), with studies indicating that the transit velocity within such networks is an order of magnitude less than those found for channelised systems (e.g. Kamb et al., 1985). The different hydraulic efficiencies of the two drainage configurations is significant as it controls water pressure conditions at the glacier bed, and thus, overall ice motion (Walder, 1986; Hubbard and Nienow, 1997; Benn and Evans, 2010; Jiskoot, 2011).

2.3 Temporal Variations in Glacier Hydrology and Glacier Motion

As the foregoing discussion illustrates, the single most important control on temporal variations in glacier motion is the distribution and pressure of water at the bed (Willis, 1995; Howat et al., 2008a; Schoof, 2010; Armstrong and Anderson, 2020). This is because elevated water pressures serve to both increase the rate of strain in layers of subglacial deforming sediment, owing to the reduction in frictional strength, and to increase basal sliding rates by increasing the spatial extent of water-filled cavities and thus the likelihood of separation (Iken and Bindshadler, 1986; Boulton and Hindmarsh, 1987; Schweizer and Iken, 1992; Willis, 1995).

Increased water pressures, however, do not directly affect ice creep rates as these are mainly controlled by shear stress and ice temperature (Benn and Evans, 2010). That said, creep rates may be indirectly influenced by water pressures because water pressure-controlled variations in sliding rates on one part of a glacier will alter the longitudinal stresses elsewhere, leading to greater rates of internal deformation (van der Veen and Whillans, 1989; Hutter, 2017). Therefore, because most velocity fluctuations are dependent on variations in subsole deformation and basal sliding, cold-based glaciers which are frozen to their beds will tend to flow at constant rates (e.g. Boulton, 1979; Echelmeyer and Wang, 1987; Chinn, 1988). As such, the remainder of this section will focus on the temporal changes occurring at warm-based (temperate) glaciers due to their relevance to this thesis.

As the supply of meltwater due to basal melting does not vary significantly over short timescales on most glaciers, most fluctuations in basal water pressure and thus glacier motion are mainly due to variations in the supply of meltwater from the surface and the reorganisation (or switching) of the subglacial drainage system from a high pressure, inefficient system at the onset of the ablation season to a low pressure, efficient one by the time the ablation season ends (Figure 6) (Hubbard et al., 1995; Nienow et al., 1998; Schoof, 2010; Pimentel and Flowers, 2011).

A relationship between increased rates of surface ablation and increased surface velocities during the summer ablation season has been observed on numerous Alpine and Arctic glaciers since the 1980s and 1990s, including Unteraargletscher (Iken et al., 1983); Findelengletscher (Iken and Bindshadler, 1986) and Haut Glacier d'Arolla (Hubbard et al., 1995; Nienow et al., 1998) in Switzerland as well as Storglaciären in Sweden (Hooke et al., 1983, 1989a) and Columbia Glacier, Alaska (Meier et al., 1994). Velocities only reduce towards the end of the ablation season after the subglacial drainage system 'switches' to a more efficient configuration which can rapidly remove water from the bed, lowering basal water pressures and basal sliding rates as a result

(Schoof, 2010; Pimentel and Flowers, 2011; Vincent and Moreau, 2016). Short-term (e.g. diurnal) peaks in ablation and velocity can also occur within the normal ablation season cycle, often as a result of transient weather events such as long periods of clear-sky conditions or heavy rainfall which can produce significant volumes of meltwater (Figure 7) (Howat et al., 2008a; Benn and Evans, 2010; Vincent and Moreau, 2016).

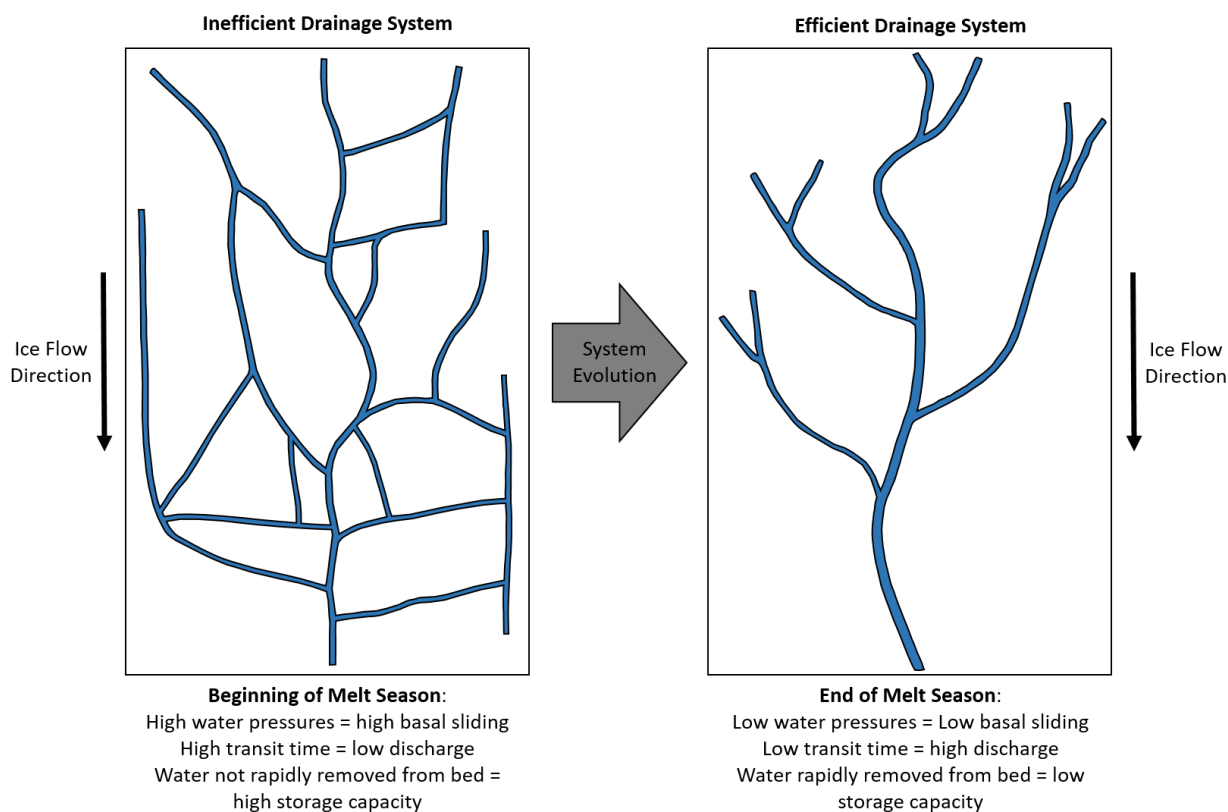


FIGURE 6 Idealised plan-view schematics of the two types of drainage system commonly thought to be present under temperate glaciers. (Left) an inefficient drainage system composed of linked cavities or braided canals, and (right) an efficient drainage system composed of a small number of large channels. Specific characteristics related to both systems are also summarised for convenience. Figure adapted and modified from Fountain and Walder (1998).

The supply of meltwater to the bed can also influence glacier velocity by increasing the amount of water temporarily stored in the distributed subglacial drainage network, such as in linked-cavity systems, braided canal systems and till porewater (Iken, 1981; Creyts and Schoof, 2009; Hart et al., 2019a). In these inefficient systems there is a positive correlation between discharge and water pressure, so that increased supply to the system results in elevated pressures, however, once meltwater drains from the system faster than it can be recharged, water pressures fall and sliding velocities are reduced (Hubbard et al., 1995; Willis, 1995; Howat et al., 2008a).

Evidence in support of this has been provided by Iken and Bindshadler (1986), who observed that periods of enhanced water pressure and sliding velocity on Findelengletscher were accompanied

by temporary uplift of the ice surface, interpreted as the 'jacking' effect of pressurised water in cavities. The glacier surface would only subside when basal water pressures and sliding velocities reduced to lower levels, indicating closure of the cavities and removal of water from storage, with this effect being observed on several other glaciers since (e.g. Naruse et al., 1992; Nienow et al., 1998; Hart et al., 2019a). In comparison, variations in discharge in efficient systems, such as R-channels, are not thought to influence glacier motion to as greater an extent, as water is confined to a small proportion of the bed and because transit times are low even when discharges are high (Hubbard and Nienow, 1997; Schoof, 2005, 2010; Jiskoot, 2011). This means that water pressures over much of the bed, and thus sliding rates, can remain low due to the ability of these channels to rapidly evacuate meltwater (Iken and Bindshadler, 1986; Fountain and Walder, 1998; Schoof, 2010; Sundal et al., 2011).

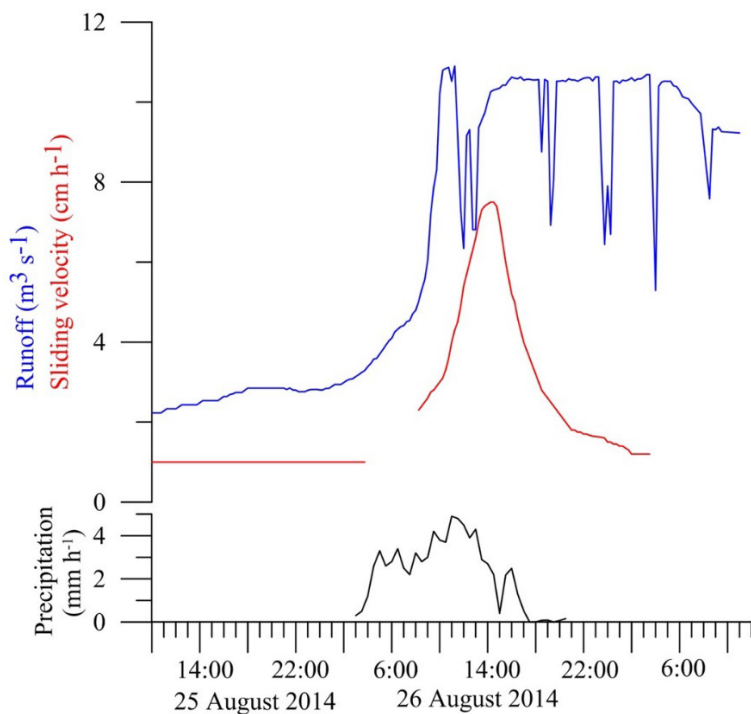


FIGURE 7 Sliding velocities (red) and subglacial runoff (blue) for Argentière glacier, Mont Blanc region, in response to a storm event that occurred on the 26th August 2014 (precipitation = black line). This illustrates how such events can lead to short-term (diurnal) increases in sliding velocity. Figure reproduced from Vincent and Moreau (2016).

More recently, this relationship between increased rates of summer ablation and enhanced glacier flow has been observed on several hard- and soft-bedded land- and marine-terminating glaciers in Greenland (e.g. Zwally et al., 2002; Shepard et al., 2009; Bartholomew et al., 2012; Shannon et al., 2013; Everett et al., 2016) and Antarctica (e.g. Schroeder et al., 2013; Joughin et al., 2014; Gomez et al., 2019). Ice acceleration occurs when the meltwater input from the surface to the bed via moulins exceeds the hydraulic capacity of the subglacial system, causing a drop in

effective pressure at the bed and, therefore, a reduction in basal friction. This then facilitates rapid ice acceleration to occur through higher rates of basal sliding (Bartholomew et al., 2010; Sundal et al., 2011; Andrews et al., 2014). It was thought originally that such a mechanism could lead to a rapid increase in future mass loss from the Greenland Ice Sheet under enhanced climate warming (Zwally et al., 2002; Parizek and Alley, 2004). However, subsequent studies in the late 2000s instead found the opposite was likely to be occurring (van de Wal et al., 2008; Sundal et al., 2011).

As the flux of water to the bed continues to increase over the melt season, inefficient conduits at the bed start to enlarge due to rapid melting of their walls, allowing an efficient channelised system to develop (Röthlisberger, 1972; Schoof, 2010; Chandler et al., 2013). This system relieves water pressures and decreases overall ice velocity by efficiently routing surface meltwater to the glacier terminus (Bartholomew et al., 2012; Andrews et al., 2014; Stevens et al., 2016). Therefore, ice velocity should decrease over the course of the melt season as drainage efficiency increases in line with the amount of meltwater routed from the surface to the bed, and there are numerous observations to support this theory (e.g. Bartholomew et al., 2010; Chandler et al., 2013; Tedstone et al., 2013; Ryser et al., 2014). However, this relationship is much more complicated than described due to the spatially variable and highly unsteady nature of the subglacial drainage system (Schoof, 2010; Sole et al., 2013; Stevens et al., 2016).

Some authors, e.g. Sundal et al. (2011) and Bartholomew et al. (2012) argue that in high melt years the switch to a more efficient drainage system occurs quicker due to a larger volume of water reaching the bed earlier in the melt season, which suppresses the magnitude of the early-summer speed up (Figure 8). Consequently, they argue that short-term pulses of meltwater delivered to the bed are much more important as they can cause rapid sliding episodes to occur, even when the drainage system is fully channelised (Schoof, 2010; Bartholomew et al., 2012). This is because the channels of the efficient drainage system can only grow in response to increased melt delivery over several days, whereas rapid routing of large volumes of meltwater can occur in hours (Hoffman et al., 2011; Bartholomew et al., 2012). As such, the drainage system is unable to accommodate such large volumes of water except by increasing the hydraulic gradient, which raises the water pressure while conversely lowering the effective pressure, leading to short-term rapid sliding events (Schoof, 2010). Such high volumes of water can be sourced from days of particularly intense surface melt and rainfall, or from the drainage of surface lakes (e.g. Das et al., 2008; van de Wal et al., 2008; Hoffman et al., 2011).

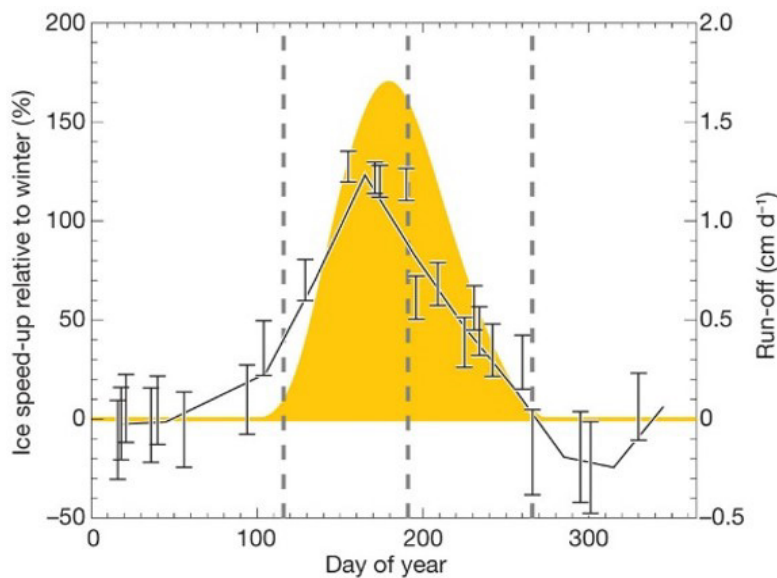


FIGURE 8 Monthly averaged velocity data (solid grey line) for five land-terminating glaciers in southwest Greenland. The plot illustrates how in high melt years velocities increase rapidly at the beginning of the melt season but then decrease equally as rapidly in response to the earlier switch from an inefficient to an efficient drainage system, which suppresses the magnitude of this speed up. Also shown are the model estimates of daily surface runoff for the study area during high melt years (orange) and the error bars for the velocity point measurements. Figure adapted from Sundal et al. (2011).

Indeed, it has been shown in several studies that the rapid drainage of supraglacial lakes are important for facilitating large increases in velocity over timescales of days or less (e.g. Das et al., 2008; Bartholomew et al., 2010; Hoffman et al., 2011). For example, Das et al. (2008) observed a lake on the western margin of the ice sheet that was >2 km in diameter and which drained rapidly in ~2 hours, with the corresponding increase in velocity >100 times the background value.

Bartholomew et al. (2012) meanwhile observed the drainage of a large lake (also on the western margin of the ice sheet), which coincided with a 400% increase in velocity over less than 24 hours. In the days following these events, velocities have been shown to slowly return to their pre-lake drainage levels, indicating that their overall influence on seasonal or annual velocities is likely to be limited (Das et al., 2008; Hoffman et al., 2011). However, it does provide further evidence that an efficient system of drainage must have been present at the base of these glaciers to allow velocities to quickly return to baseline levels following these events (Hoffman et al., 2011; Pimentel and Flowers, 2011).

Conversely, later in the melt season the observed slow-down in velocities can only occur once there is a stabilisation or decline in meltwater input relative to the capacity of the drainage system (Sundal et al., 2011; Bartholomew et al., 2012). It has been argued, therefore, that it is the variability in the rate, rather than the absolute volume, of meltwater delivered to the bed that

exerts the greatest control on the velocity patterns of these glaciers (Schoof, 2010; Hoffman et al., 2011; Bartholomew et al., 2012). Other authors have taken these observations further and argued that in the future summer velocities will increase due to both longer melt seasons and more prevalent unsteady conditions in the subglacial system. These warmer and longer melt seasons will likely cause longer periods of consistently increasing surface melt to occur, challenging the subglacial drainage system to constantly evolve to evacuate larger and larger quantities of water, regardless of whether an efficient system were in place, causing summer velocities to continuously remain high (Meierbachtol et al., 2013; Sole et al., 2013).

In contrast to these studies, more recent research has suggested that it is the complex interconnectivity and spatial extent of the glacier-wide subglacial drainage system that exerts the strongest control on ice motion, not drainage system evolution (e.g. Andrews et al., 2014; Tedstone et al., 2015; Hoffman et al., 2016). For example, Andrews et al. (2014) and Hoffman et al. (2016) have both shown that subglacial drainage systems are not just made up of one single component, but several, and that a change in extent of one at the expense of the other (e.g. by increasing the extent of the interconnected channelised system at the expense of the isolated distributed system) would result in a larger portion of the bed at lower water pressures, increasing basal traction and consequently decreasing flow velocities at the end of the melt season, without requiring a change in the efficiency of the channelised system.

Furthermore, several studies have indicated that long-term annual velocities for several land-terminating glaciers in Greenland are decreasing, despite seasonal increases in velocity, and such trends are also thought to be due to the change in connectivity between different regions of the glacier bed (Figure 9) (Cowton et al., 2013; Tedstone et al., 2015). These studies suggest that following high-melt summers, a higher capacity and more extensive channelised system has evolved which has the ability to evacuate notably more water from surrounding linked but unchannelised regions of the bed, causing more widespread dewatering of the ice-bed interface, despite annual increases in melt runoff (Sole et al., 2013; Tedstone et al., 2015). Therefore, if increases in drainage efficiency occur annually, then the gradual net drainage of water stored in the unchannelised regions of the bed will result in reduced basal lubrication and net ice slowdown over annual and even decadal timescales (Cowton et al., 2013; Tedstone et al., 2015; Stevens et al., 2016).

However, recent research by Hart et al. (2019a) at Skálafellsjökull, a soft-bedded outlet glacier in south Iceland, suggests that the widely observed seasonal evolution of the subglacial drainage system may not be as widely applicable as first thought. Data from subglacial probes inserted into the till and boreholes drilled to the bed indicated that during the melt season porewater

pressures were continually high, with no diurnal variations, and as such meltwater input was approximately equivalent to the capacity of the drainage network, and thus could easily adapt to changing inputs (Hart et al., 2019a). This led the authors to suggest that during the summer a distributed drainage system was present, dominated by wide anastomosing broad flat channels and thin water sheets (e.g. Creyts and Schoof, 2009), with this being corroborated by GPR mapping of the site by Hart et al. (2015) which suggested the presence of a braided subglacial system (Hart et al., 2019a).

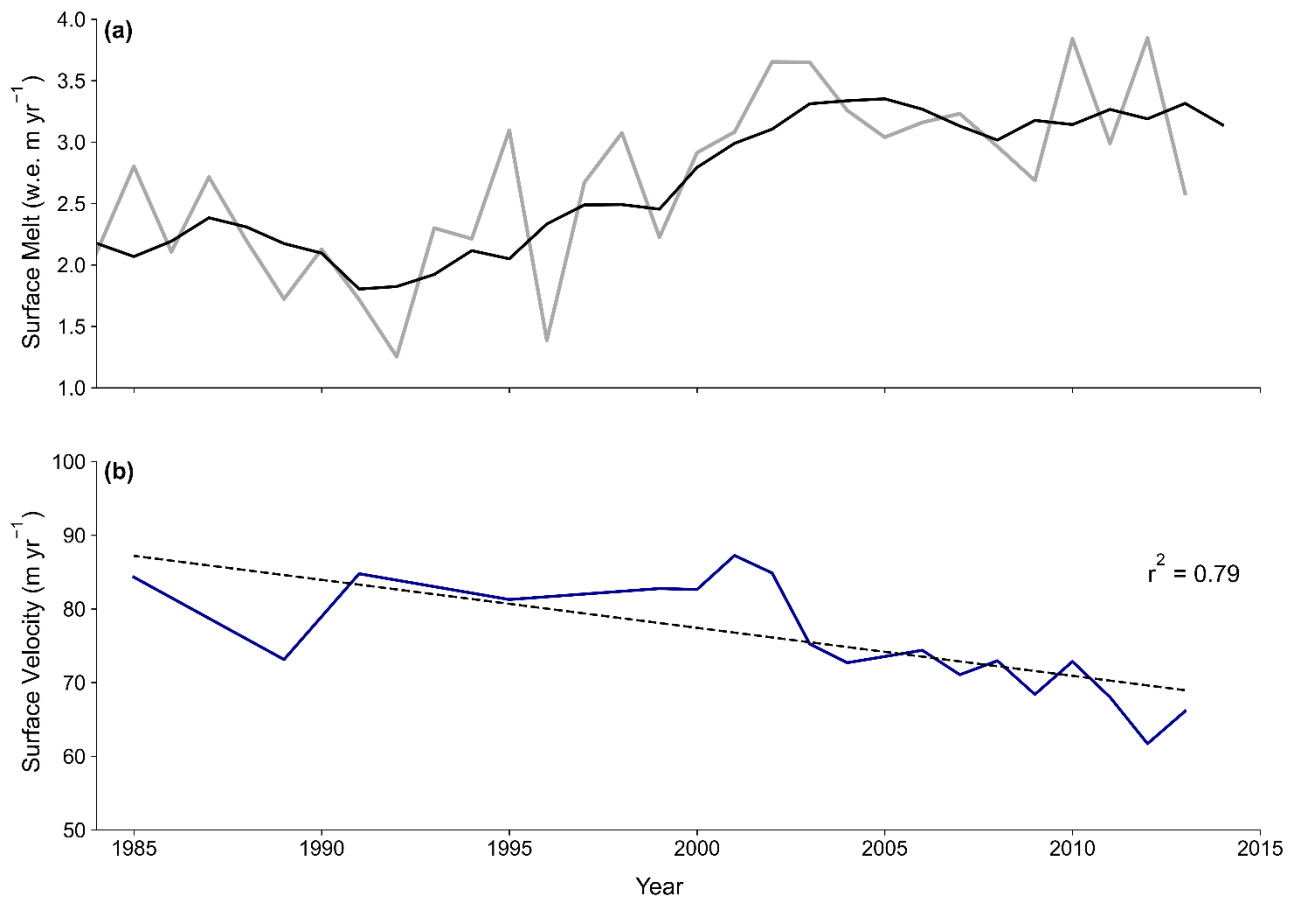


FIGURE 9 (a) Annual mean modelled surface melt (grey line), smoothed with a five-year moving mean (black line) for an 8,000 km² land-terminating region of the west Greenland Ice Sheet. (b) Median ice velocities (blue line) across the same land-terminating region of the Greenland Ice Sheet, calculated using feature tracking applied to pairs of Landsat images for specific time periods. The plot illustrates that despite an increase in surface melt production since the early 1980s, annual velocities across this portion of the ice sheet have decreased over the same period. Plot reproduced from data provided by Tedstone et al. (2015).

Importantly, the authors found no drop in subglacial water pressures towards the end of the melt season reflecting the 'switch' to a more efficient system, with their data instead indicating that water pressures were generally lower during the winter when efficient channels may develop in the till to remove meltwater released from storage or route water to the bed during days of high

melt (Hart et al., 2019b). These findings are the opposite of those observed during the 1980s and 1990s for Alpine and Arctic glaciers, and more recently in Greenland, and highlight the complexity of the subglacial drainage system and indeed its implications for glacier motion (e.g. Bougamont et al., 2014; Vincent and Moreau, 2016; Hart et al., 2019a,b). Furthermore, the majority of the above studies that have illustrated such a relationship between meltwater input and increased flow have been limited to land-terminating glaciers. Water-terminating glaciers (either marine- or lake-terminating) have received far less attention, despite the fact that many have been observed to be accelerating over recent years, with such increases in velocity likely to be fundamentally controlled by the processes of glacier calving, rather than solely the input of meltwater to the bed (e.g. Howat et al., 2010; Sugiyama et al., 2011; Tsutaki et al., 2013; Baurley et al., 2020).

2.4 Calving-Induced Dynamic Changes

It is widely recognised that the recent patterns of mass loss and retreat observed at numerous land-terminating glaciers worldwide have been driven by widespread surface ablation (i.e. melt), in response to climate warming (Marzeion et al., 2014; Huss and Hock, 2018; Zemp et al., 2019). However, this relationship between surface ablation, retreat and climate warming is much more complicated for those glaciers which terminate in water (either lake- or marine-terminating) due to the implementation of an additional, and highly important mass loss mechanism, termed calving (Warren and Kirkbride, 2003; Boyce et al., 2007; Chernos et al., 2016). Glacier calving, otherwise known as frontal ablation, refers to the mass loss that can result from both the mechanical 'break off' of blocks of ice from the terminus, as well as from the direct melting of the terminus face through subaqueous melt (Truffer and Motyka, 2016; Carrivick et al., 2020; Mallalieu et al., 2020). Although these processes are spatially and temporally complex, calving can result in greater rates of mass loss than would otherwise be possible through surface ablation alone, and thus as a result glacier calving comprises an important component of the mass budget of many glacier systems worldwide (Benn et al., 2007b; Boyce et al., 2007; Dykes et al., 2011; Chernos et al., 2016). It accounts for practically all of the mass loss from the Antarctic Ice Sheet, and contributes at present to ~60% of the total losses from the Greenland Ice Sheet (Rignot et al., 2013; Truffer and Motyka, 2016; van den Broeke et al., 2017; Shepard et al., 2018).

Calving is also contributing significantly to mass loss in many other high- to mid-latitude regions, such as Alaska (e.g. O'Neel et al., 2005; Boyce et al., 2007; Trüssel et al., 2013), Iceland (e.g. Schomacker, 2010; Dell et al., 2019; Guðmundsson et al., 2019), The Himalaya (e.g. Nie et al., 2017; King et al., 2018; Watson et al., 2020), Patagonia (e.g. Warren et al., 2001; Sugiyama et al., 2011; Sakakibara and Sugiyama, 2014) and New Zealand (e.g. Warren and Kirkbride, 2003; Dykes

et al., 2011; Robertson et al., 2012). However, its relative contribution to total mass loss (i.e. from both calving and surface ablation), and thus its overall impact on glacier mass balance does vary between individual glaciers and regions (Sakakibara and Sugiyama, 2014; King et al., 2018; Guðmundsson et al., 2019). For example, calving was found to account for ~40% of the total mass loss for Glaciar Perito Moreno, Patagonia (Stuefer et al., 2007), and for up to 49% for Bridge Glacier, British Columbia in individual seasons (Chernos et al., 2016). Conversely in Alaska, calving was found to account for only ~4% and ~16.8% of the total losses from the Mendenhall and Yakult Glaciers, respectively (Boyce et al., 2007; Trüssel et al., 2013), highlighting the heterogenic nature of the calving process. For the majority of glacier systems worldwide, however, comprehensive data relating to the calving flux, rate of surface ablation, and to overall mass balance, are severely lacking (Benn et al., 2007b; Trüssel et al., 2013). This makes it difficult at present to fully assess the relative importance of calving as opposed to surface ablation for all calving glaciers worldwide, which raises important questions for our understanding of the future response of these ice masses (Benn et al., 2007b; Boyce et al., 2007; Carrivick et al., 2020). Finally, it is also important to note that calving processes likely played a key role in the stability of the Quaternary Ice Sheets during the Last Glacial Maximum (Pollard, 1984; Benn et al., 2007b; Carrivick et al., 2020). Indeed, many of the Northern Hemisphere ice sheets terminated in the sea and/or in large proglacial lakes, and as a result glacier calving is believed to have exerted a significant control on ice stream onset and dynamics, as well as being the likely driver behind the relatively rapid destabilisation and disappearance of these ice sheets during this time (Hughes, 2002; Stokes and Clark, 2004; Perkins and Brennand, 2015).

The past and present extent of calving glaciers is of importance because their dynamic behaviour is at least partly decoupled from climate, with factors other than variations in glacier mass balance, such as water depth and fjord geometry, exerting major controls on the position, and on the rate of advance and retreat, of calving margins (Meier and Post, 1987; Benn et al., 2007b; Howat et al., 2007; Carrivick and Tweed, 2013; Watson et al., 2020). Indeed, these factors can often cause calving glaciers to undergo significantly greater rates of retreat than would otherwise be observed if they lost mass by surface ablation alone (Warren and Kirkbride, 2003; Howat et al., 2008b; Trüssel et al., 2013), and thus it is no surprise that in recent years many calving glaciers worldwide have undergone dramatic acceleration and retreat (e.g. Thomas, 2004; Howat et al., 2005; Sakakibara et al., 2013; Baurley et al., 2020). This indicates that calving glaciers display a highly non-linear response to an initial climatic forcing, and as such they have the potential to contribute disproportionately to global SLR (Rignot et al., 2003; Benn et al., 2007a,b; Chernos et al., 2016; Carrivick et al., 2020). Furthermore, the formation of proglacial lakes in the basal depressions left by mountain glaciers as they recede has also led to the onset of calving at these

formerly land-based termini, which has dramatically transformed their dynamics and climatic sensitivity (e.g. Warren and Kirkbride, 2003; Diolaiuti et al., 2006; Tsutaki et al., 2013; King et al., 2018), sometimes with hazardous results (e.g. Haeberli et al., 2016; Nie et al., 2017). An understanding of the different calving processes is, therefore, crucial for the accurate prediction of cryospheric response to both future climate change and global SLR (Benn et al., 2007b; Sakakibara et al., 2013; Truffer and Motyka, 2016; Benn and Åström, 2018).

2.4.1 Calving: Fracture Formation and Propagation

Fractures (crevasses) play a primary role in the magnitude and frequency of calving events, and consequently, the stability and dynamics of calving glaciers (Benn et al., 2007a; Gong et al., 2018). This is because all calving events are a consequence of the propagation of crevasses in response to stresses acting on the ice surface (Benn et al., 2007a; Benn and Åström, 2018). Calving then occurs when pre-existing or new crevasses propagate downwards sufficiently to isolate blocks of ice from the main glacier mass, which can then fall or float away from the terminus (Diolaiuti et al., 2006; Benn et al., 2007b). Thus, the location, magnitude and timing of calving events are preconditioned by the propagation of crevasses, and the position and form of calving margins reflects the distribution and orientation of former crevasses (Benn et al., 2007b).

Although dry crevasses will typically only penetrate to a depth where the tensile strain rate opening the crevasse is exactly balanced by the rate of creep closure from ice overburden (Nye, 1957; van der Veen, 2007), the presence of water within a crevasse can exert a further control on the penetration depth, and thus calving rate (Figure 10) (van der Veen, 1998a, 2007; Nick et al., 2010). This is because the weight of the water can overcome the lithostatic stresses in the ice due to its greater density, thus allowing propagation to greater depths (van der Veen, 1998a,b; Benn et al., 2007b). Furthermore, as long as the crevasse remains water-filled, then the water pressure will compensate for the majority of the lithostatic stress trying to close it, potentially allowing the crevasse to penetrate through the entire ice thickness (Fountain and Walder, 1998; van der Veen, 2007). Sustained water input into crevasses can occur in response to surface melt, supraglacial ponds or if a free connection exists with the proglacial water body, which is most likely to occur if the crevasse is located close to the margin (Das et al., 2008; Sugiyama et al., 2011; Danielson and Sharp, 2013), and thus this mechanism provides an additional control on the frequency and magnitude of calving events (van der Veen, 2007; Benn and Åström, 2018).

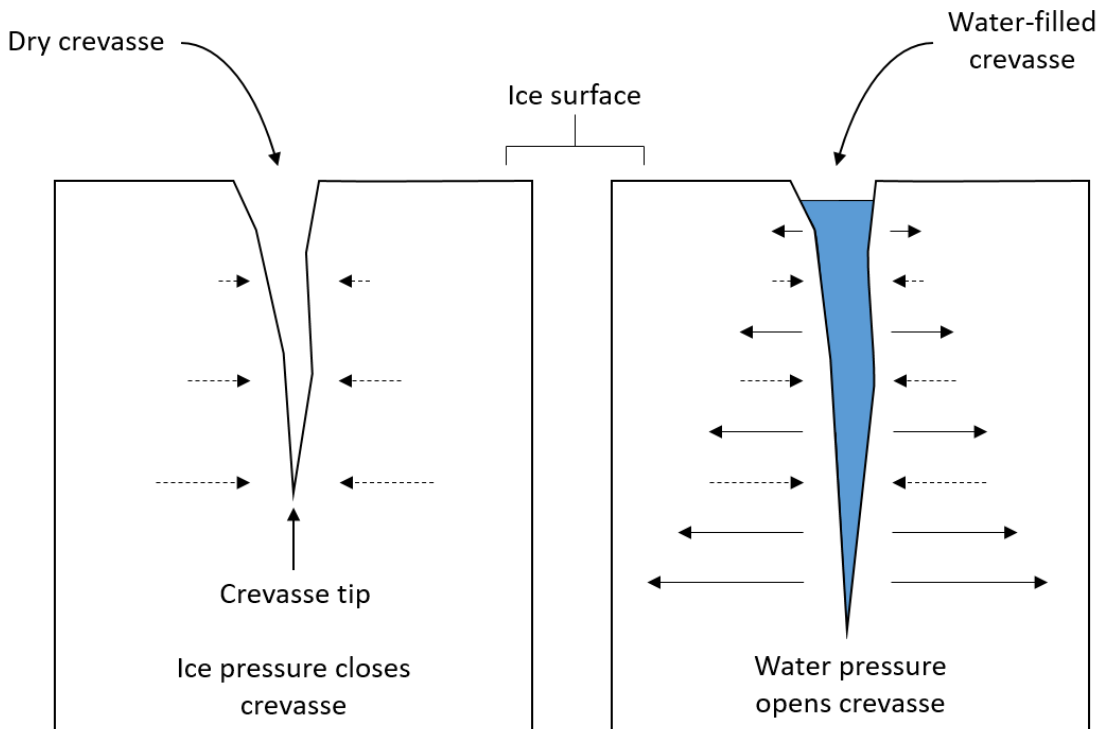


FIGURE 10 Schematic illustrating how a fracture that is filled with water can propagate to a much greater depth than a 'dry' crevasse due to the weight of the water completely opposing the ice pressure that is attempting to close the crevasse. Modified from Benn and Evans (2010).

2.4.2 Processes of Calving

Glacier calving cannot be defined as one single process, rather, it consists of several interrelated processes that can often take place in wide variety of calving environments (Benn et al., 2007b; Truffer and Motyka, 2016; Benn and Åström, 2018). Generally, the termini of calving glaciers can either be grounded or floating, although in reality this distinction is far more complicated, for example where parts of the grounded terminus of a calving glacier can become locally buoyant (Boyce et al., 2007; Pritchard et al., 2009; Dykes et al., 2011; Sakakibara and Sugiyama, 2014). Calving glaciers can also flow relatively slowly (10s to 100s m a⁻¹) or extremely rapidly (1 to 10 km a⁻¹), and can be found in a wide variety of climatic environments, such as arid polar, temperate alpine and monsoonal sub-tropical mountains (e.g. Naruse and Skvarca, 2000; Howat et al., 2008b; Trüssel et al., 2013; Nie et al., 2017). Furthermore, the proglacial water body in which they terminate can either be freshwater (lacustrine) or saltwater (tidewater), with the various water body properties, such as temperature, salinity and circulation patterns, not only varying between the two different types of water body, but also between the same type of water body in different glaciated regions (e.g. Skvarca et al., 2002; Röhl, 2006; Howat et al., 2010; Schild et al., 2018). As a result, it is unsurprising that such a large number of different calving environments have been observed in nature (Warren and Kirkbride, 2003; Benn et al., 2007b). That said, several situations

have been identified where surface stresses are often high enough to allow fractures to propagate down through the ice, triggering calving events (Benn et al., 2007b; Benn and Åström, 2018). These are: (i) where spatial gradients in the velocity of the glacier cause the ice surface to stretch and fracture; (ii) where submarine melt at or below the waterline can cause undercutting and failure of the calving face; (iii) as a result of force imbalances in the vicinity of subaerial ice cliffs; and (iv) where torque is introduced by buoyant forces acting on the terminus.

For glaciers and ice shelves, the close correspondence between glacier velocity and the stresses associated with *longitudinal stretching* are commonly sufficient to initiate crevasse formation at the ice surface (Figure 11) (van der Veen and Whillans, 1989; van der Veen, 2007; Mottram and Benn, 2009). Such a close correspondence suggests that crevasses which have opened in response to velocity gradients at the glacier scale provide a first-order control on the geometry and overall position of calving termini by providing preferential lines of weakness near the margin (van der Veen, 1996; Hanson and Hooke, 2000; Benn et al., 2007b). For those glaciers with grounded calving margins, ice velocities typically increase towards the terminus which allows the formation of large fields of transverse crevasses where longitudinal strain rates are sufficiently high (Meier and Post, 1987; Joughin et al., 2008a; Tsutaki et al., 2013; Sakakibara and Sugiyama, 2018).

Particularly large increases in velocity near the glacier terminus can often be attributed to a reduction in the effective pressure at the glacier bed, and therefore, basal drag, as the glacier approaches floatation (Vieli et al., 2000; O'Neel et al., 2005; Tsutaki et al., 2011). Furthermore, because basal water pressures are consistently close to ice overburden near the termini of calving glaciers, this means that any slight change in water pressure (e.g. from the changing level of the water body) or in overburden pressure (from a change in ice thickness) can lead to extremely large changes in ice velocity and thus calving (Howat et al., 2007; Sugiyama et al., 2011; Sakakibara et al., 2013). It is important to note, however, that velocity gradients on some calving glaciers have been observed to decrease towards the terminus, suggesting that in these cases other processes are more important in forcing calving behaviour (e.g. Krimmel, 2001; O'Neel et al., 2001; Dykes et al., 2011; Trüssel et al., 2013).

In the longitudinal stretching mechanism, therefore, if surface velocity gradients constitute the only factor controlling fracture propagation, then calving will occur where such gradients are sufficiently high to allow surface crevasses to penetrate through the entire ice thickness (Diolaiuti et al., 2006; Mottram and Benn, 2009; Benn and Åström, 2018). Indeed, given that water-filled crevasses can often propagate downwards without limit (by overcoming the lithostatic stress in the ice) (Fountain and Walder, 1998; van der Veen, 2007), the calving margin itself will be located approximately where these crevasses reach the lake or sea level, assuming of course that there is

a free connection between the crevasse and sea or lake (Alley et al., 2005; Benn et al., 2007b; Sugiyama et al., 2011).

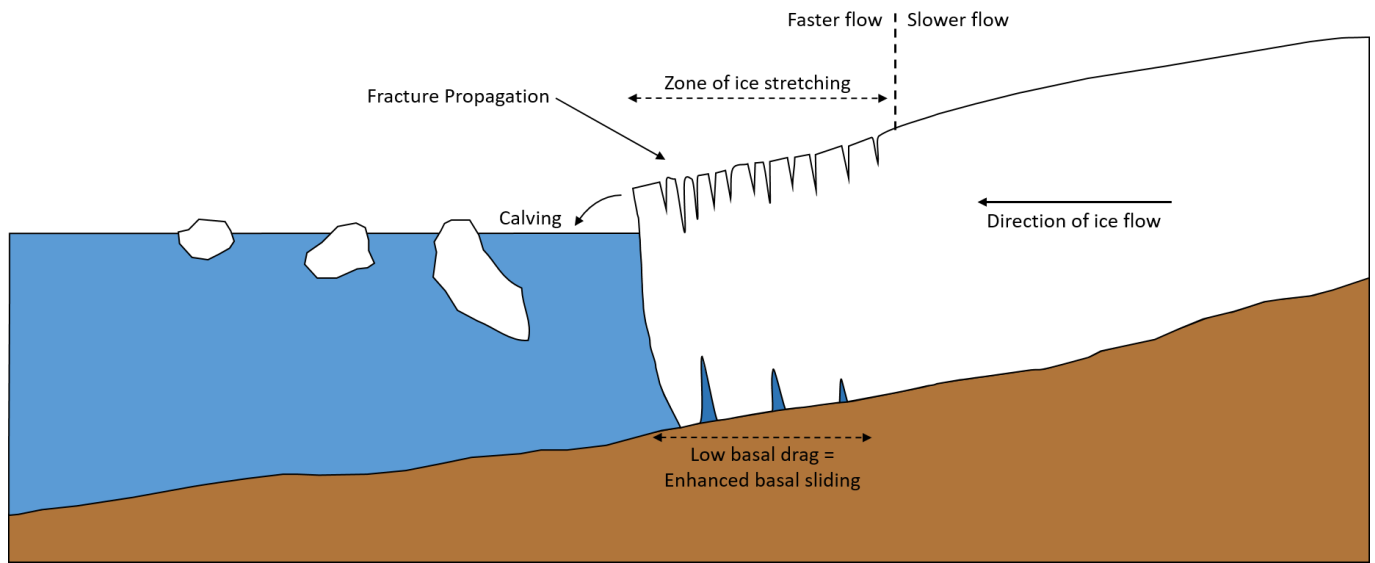


FIGURE 11 Schematic illustrating how calving can result from longitudinal stretching at the ice surface. At the glacier margin, low basal drag leads to enhanced sliding and thus increased ice flow, which stretches the ice surface allowing crevasses to form. If the stresses are particularly high, then these crevasses can propagate through to the waterline causing calving to occur. Modified from Bendle (2020).

As such, the position of the calving margin is determined by the velocity distribution across the ice surface (which controls crevasse depth) (van der Veen and Whillans, 1989; Benn et al., 2007b; Mottram and Benn, 2009) and the height of the ice above the sea or lake level (which determines whether a crevasse of a given depth will reach the waterline) (Benn et al., 2007a; Mottram and Benn, 2009; Nick et al., 2010). Therefore, calving is controlled by those factors that determine the ice velocity (e.g. the driving and resisting stresses) and the ice thickness (e.g. the surface mass balance and ice flux) (Meier and Post, 1987; Benn et al., 2007b; Joughin et al., 2008a; Sugiyama et al., 2011; Tsutaki et al., 2013).

Subaqueous melting at calving termini plays an important role in controlling both the calving rate and the stability of calving glaciers in both lacustrine and tidewater settings (Benn et al., 2007b; Minowa et al., 2017; Benn and Åström, 2018). Indeed, it is now recognised as a highly significant process, particularly in those environments where relatively warm water is brought into contact with the glacier termini, including fjords in Alaska and Svalbard, and lakes in Greenland and New Zealand (e.g. Motyka et al., 2003; Dykes et al., 2011; Schild et al., 2018; Mallalieu et al., 2020). Subaqueous melting can impact calving rates directly, for example through processes occurring in the proglacial water body that melt the terminus face directly, leading to mass loss (e.g. Motyka et al., 2003; Schild et al., 2018), or indirectly, where melt at the waterline can cause subaerial ice

cliffs to form, which can then be progressively undercut until calving occurs (e.g. Röhl, 2006; Robertson et al., 2012). Due to its importance in helping control calving rates, as well as its relevance to this thesis, the latter mechanism will be the primary focus here. For more detail on the role of subaqueous melt as an ablative mechanism on calving glaciers, the reader is referred to the recent review by Truffer and Motyka (2016).

Where melt rates at or below the waterline exceed those above, the face of the calving front will be progressively undercut, increasing force imbalances at the margin and ultimately encouraging calving failure (Figure 12) (Robertson et al., 2012; Minowa et al., 2017; Benn and Åström, 2018). The location and timing of calving above waterline notches, as well as the precise geometry of the failure surface, is strongly influenced by the presence of pre-existing lines of weakness such as crevasses or debris bands (Hanson and Hooke, 2000; Benn et al., 2007b), with high magnitude calving events often occurring as a result where these lines of weakness are already present (Benn et al., 2017). In this mechanism, where subaqueous melting at or below the waterline is the primary control on calving, the long-term calving rate will equal the rate at which the subaerial part of the terminal cliff is undercut (Warren and Kirkbride, 2003; Benn et al., 2007b).

The calving rate will, therefore, be a function of water body properties such as temperature, density structure and circulation patterns (King et al., 2018; Schild et al., 2018), with the rate at which the terminus is undercut not simply being a function of total ice melt, but also by how that melt is focused at the terminus (Röhl, 2006; Benn et al., 2007b). A given amount of melt distributed over a narrower elevation range at the terminus will be more effective at undercutting the calving face than the same amount focused over a broader range (Röhl, 2006; Schild et al., 2018). This distribution, in turn, will depend on water-level fluctuations, circulation patterns and other factors (Schild et al., 2018). Therefore, long-term changes in terminus position will be driven by the maximum subaqueous melt rate and the ice velocity, analogous to the following mechanism (Benn et al., 2007b, 2017).

Reeh (1968), in what was one of the earliest models of calving processes, showed that a *force imbalance* exists near the terminus of a floating glacier or ice shelf. Above the waterline, the cryostatic pressure at the terminal face is unopposed by atmospheric pressure, while below the waterline it is always greater than the pressure exerted by the water column, except that is, at the base (Reeh, 1968; Benn et al., 2007b). This outwardly acting force is unevenly distributed and is at its maximum at the waterline (Hanson and Hooke, 2000; Benn and Åström, 2018).

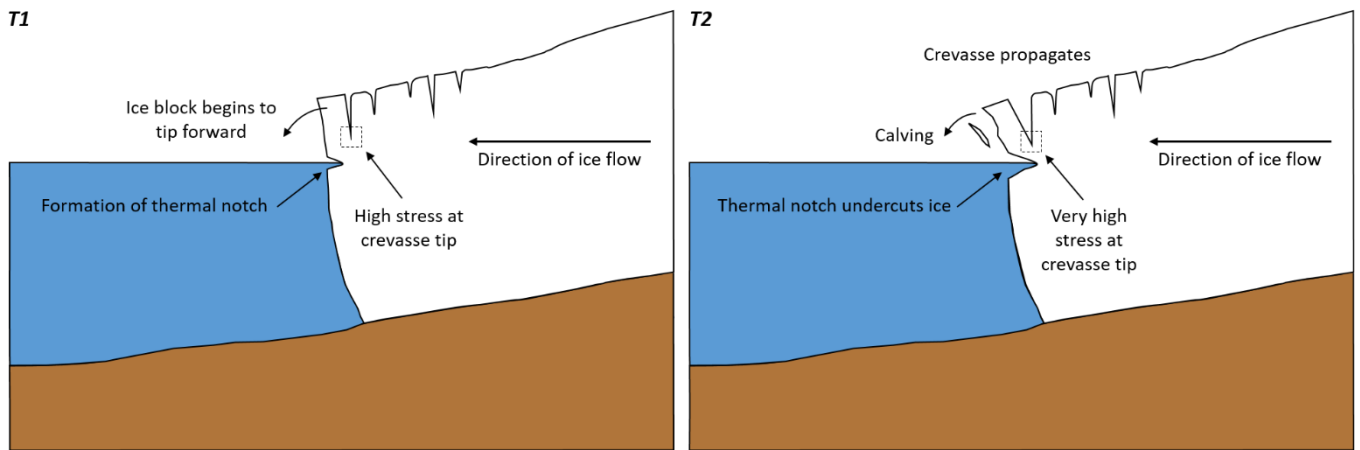


FIGURE 12 Schematic illustrating how calving can result from subaqueous melt at the waterline.

Melting at or below the waterline can erode a notch into the terminal calving face (T1). Over time, the notch erodes further into the terminal face, undercutting the ice above it and causing it to become increasingly unstable until calving occurs. Modified from Bendle (2020).

Here, an eccentrically applied stress results in a bending movement or torque, giving a tendency for the terminal face to bulge outward and to rotate downward at this locality (Hanson and Hooke, 2003; Benn et al., 2007b). This results in a zone of high tensile and shear stresses at the surface, found at a distance from the front roughly equal to the ice thickness (Benn and Evans, 2010), with it being argued by Reeh (1968) that surface fractures will then develop in this region, promoting calving (Figure 13) (Benn et al., 2007b; Benn and Åström, 2018). When both the tensile and shear stresses are considered the threshold for calving failure is ~ 1 MPa, which based on modelling work and recent observations implies an upper-bound on ice-cliff height of no more than ~ 110 m (Hanson and Hooke, 2003; Ma et al., 2017). This is because an ice cliff that is higher than this will be subject to extremely high stresses and consequently will calve rapidly in an attempt to reduce the imbalance (Hanson and Hooke, 2003; Benn et al., 2007b).

In this mechanism, where fractures are generated and propagate entirely in response to unbalanced stresses at subaerial and/or subaqueous ice cliffs, it is the geometry of the glacier terminus and the ice rheology that control the calving rate (Benn et al., 2007b). It is a cyclical process, where unbalanced stresses drive geometric changes at the ice margin, culminating in calving failure, which in turn reinstates a condition of unbalanced stresses at the new marginal ice cliff (Reeh, 1968; Hughes, 1998, 2002). Calving frequency, therefore, is determined by fracture propagation rates, the rate at which the terminus geometry evolves and the feedbacks that ensue between geometric changes and the fracturing process (Benn et al., 2007b). Consequently, any change in the position of the ice margin will be determined by the magnitude of the individual calving events and the calving cycle which drive ice cliff retreat, and the ice velocity, which carries the ice cliff forward (Benn et al., 2007b; Benn and Evans, 2010).

Fracture propagation and calving failure resulting from *buoyant forces at the terminus* can occur via two mechanisms, the most important being where surface melting can cause the terminal zones of previously grounded glaciers to become buoyant, which can lead to calving when these buoyant forces become sufficiently high (Warren et al., 2001; Benn et al., 2007b). Buoyancy-driven calving is a particularly important process at lake-terminating glaciers; where it can occur in response to ice-surface lowering through surface melt, retreat into deeper water or by a rise in lake level (e.g. Warren et al., 2001; Boyce et al., 2007; Chernos et al., 2016). Recent research has also indicated that buoyancy-driven calving may also be an important process on fast-flowing tidewater glaciers in Greenland, which can cause the release of large icebergs in dramatic calving events (e.g. James et al., 2014; Murray et al., 2015; Wagner et al., 2016).

The termini of grounded glaciers can become buoyant when surface melting thins the ice below what is known as the floatation thickness (e.g. Lingle et al., 1993; Warren et al., 2001; Boyce et al., 2007). To maintain equilibrium as a result, the surface and basal gradients of a buoyant ice front must maintain a constant ratio (Benn et al., 2007b; Benn and Åström, 2018). However, if this condition is not met (for example through a change in the ice overburden pressure or in the depth of the proglacial water body), then the torque arising from buoyant forces will increase until a threshold is met at which point the glacier terminus can no longer remain grounded (Dykes et al., 2011; Benn and Åström, 2018).

As this mechanism proceeds, the glacier terminus becomes increasingly out of buoyant equilibrium, producing large upward-directed bending forces near the junction with non-buoyant ice (Warren et al., 2001; Boyce et al., 2007). Any pre-existing crevasses in this region will determine the precise location of failure through the effect of stress concentrations at the ice surface, producing large tabular bergs often several hundreds of metres in size (Figure 14) (Warren et al., 2001; Benn et al., 2007b; James et al., 2014). In this mechanism, the long-term calving rate will be primarily controlled by the rate of grounding line retreat, as determined by changes in ice thickness relative to water depth (e.g. Vieli et al., 2001; van der Veen, 2002). Thinning of the ice surface can occur by surface and basal melting, or by longitudinal or transverse extension (dynamic thinning), and as such this type of buoyant calving will be influenced by both climatic and dynamical factors (e.g. Warren et al., 2001; Howat et al., 2005; Nick et al., 2010).

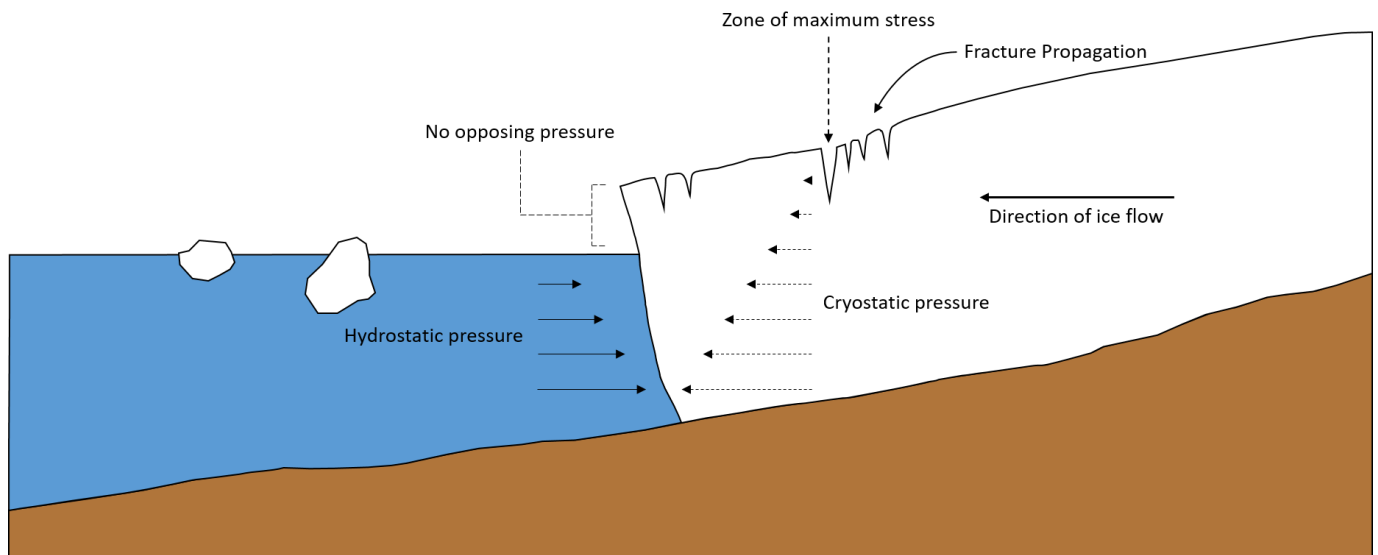


FIGURE 13 Schematic illustrating how calving can result from force imbalances at terminal ice cliffs. Below the waterline, the outwardly directed cryostatic pressure is partly opposed by the inwardly directed hydrostatic pressure of the water body. However, above the waterline this cryostatic pressure is completely unopposed by atmospheric pressure, allowing high stresses to act on the terminal face which can then result in calving. Modified from Bendle (2020).

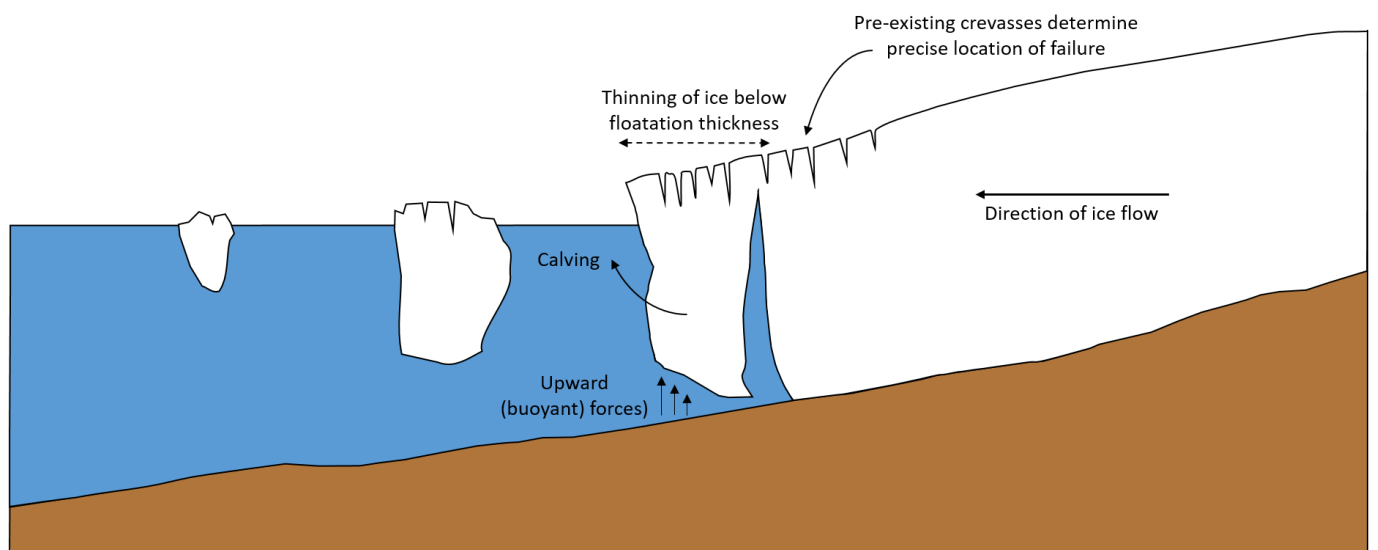


FIGURE 14 Schematic illustrating how calving can result from buoyant forces acting on the terminus. Thinning of the ice surface below the floatation thickness can cause large bending forces to occur at the grounding line as the terminus region becomes buoyant. The mechanism will proceed until calving failure occurs, releasing large tabular icebergs in the process. Modified from Bendle (2020).

From the preceding discussion, it is clear that several different factors control the frequency and magnitude of calving events, and that these factors are highly dependent on the relative importance of the four calving processes (Benn et al., 2007b; Benn and Åström, 2018). However,

in reality calving events often involve a combination of the above processes, and furthermore different processes can occur on different parts of the same calving front at any one time (e.g. Dykes et al., 2011; Medrzycka et al., 2016; Dell et al., 2019), highlighting the inherent complexity of the calving process. As a result, it was suggested by Benn et al. (2007b) that a hierarchy of calving processes should be identified, with each individual process subjected to various extrinsic and intrinsic controls.

Longitudinal stretching can be regarded as the first-order control on calving because it is entirely associated with the large-scale velocity structure of the glacier (van der Veen, 1996; Hanson and Hooke, 2000; Benn et al., 2007b; Sakakibara and Sugiyama, 2018). This is because such velocity gradients determine the penetration depth of crevasses, and as a result, they also determine whether crevasses will reach the waterline as the terminus approaches floatation (Diolaiuti et al., 2006; Mottram and Benn, 2009). Where velocity gradients are high near the grounding line, crevasses will more likely reach water level and initiate calving, in which case the glacier will terminate in a grounded ice cliff (Benn et al. 2007b; Nick et al., 2007a; Shapero et al., 2016). On the other hand, where velocity gradients are small near the grounding line, crevasses will only propagate to shallow depths which will allow the terminus to become buoyant and form a floating ice tongue for a lake-terminating glacier, or an ice shelf for a tidewater glacier (e.g. Warren et al., 2001; Boyce et al., 2007; Trüssel et al., 2013; James et al., 2014). Therefore, velocity gradients, combined with the ice thickness relative to water depth, will determine the maximum possible extent of the calving glacier terminus and how this extent changes in both time and space (Alley et al., 2005; Benn et al., 2007a; Nick et al., 2010; Shapero et al., 2016).

Subaqueous melt, force imbalances at terminal ice cliffs and torque arising from buoyancy can be classed as second order processes, which are often superimposed on the first order mechanism of longitudinal stretching (Benn et al., 2007b). This does not mean that these processes are any less important, instead, it simply implies that they tend to operate within the limits imposed by dynamical changes occurring at the glacier-wide scale (Hughes, 2002; Carrivick and Tweed, 2013). Indeed, although longitudinal strain rates determine the maximum possible position the glacier terminus can attain, second order processes can cause the terminus to have a more limited extent by further eroding the calving front (e.g. Motyka et al., 2003; Truffer and Motyka, 2016; Schild et al., 2018). Furthermore, on those glaciers where longitudinal strain rates, and thus velocity gradients are small, second order processes are likely to be the primary control on calving rate (Warren and Kirkbride, 2003; Benn et al., 2007b; Benn and Åström, 2018). Such a scenario is particularly likely to be present where the proglacial water body is shallow and relatively warm, in which case subaqueous melting will be the primary control (e.g. Motyka et al., 2003; Robertson et al., 2012; Mallalieu et al., 2020), or where surface melting thins the glacier below the floatation

thickness and/or lake levels rise, in which case buoyancy-driven calving will be the primary driver (Warren et al., 2001; Boyce et al., 2007; Dykes et al., 2011). Regardless of the exact processes occurring at calving termini, however, it is clear that glacier velocity exerts a first-order control on both the position of the calving margin and the overall calving rate in the majority of calving glacier settings (Benn et al., 2007b; Mottram and Benn, 2009; Carrivick and Tweed, 2013; Tsutaki et al., 2019).

2.4.3 Glacier Velocity and Calving

Glacier velocity exerts a fundamental control on the calving rate in two ways. Firstly, the ice velocity at the terminus is usually much larger than the rate of change in terminus position, meaning a good correlation is to be expected between calving rate and glacier velocity (Hanson and Hooke, 2000; van der Veen, 2002), except during times of rapid terminus retreat (van der Veen, 1996). Secondly, longitudinal and transverse velocity gradients determine both the depth of surface crevasses and the rate of dynamic thickness change, and are, therefore, primary controls on calving processes (Howat et al., 2005; Mottram and Benn, 2009). As a result, the behaviour of calving glaciers depends critically on glacier velocity and its variations in space and time (Meier and Post, 1987; Benn et al., 2007b), with basal motion in particular being a prerequisite for fast flow and high longitudinal strain rates (Naruse et al., 1997; Howat et al., 2010; Sugiyama et al., 2011).

2.4.3.1 Force Balance and Calving Glaciers

Glacier velocity and its derivatives depend on the magnitude of the driving stress (the forces driving the glacier forward), the basal drag, lateral drag and the longitudinal stress gradients (the forces resisting ice flow), and how these vary in time and space (Benn et al. 2007b; Cuffey and Paterson, 2010). The force balance approach developed by van der Veen and Whillans (1987) first defined the relationship between the driving and resistive stresses, based on the traditional theory that for a steady-state glacier (calving or non-calving) both these forces must be in equilibrium (Cuffey and Paterson, 2010). More detail on the mathematical theory of the glacier force balance can be found in van der Veen and Whillans (1987), Cuffey and Paterson (2010) and references therein. Temporal fluctuations in the velocity of calving glaciers that occur over short timescales largely reflect variations in the resisting stresses because significant changes in driving stress require large adjustments to glacier geometry (Benn et al., 2007b). Changes in calving glacier velocity occurring over longer timescales, however, can reflect variations in either the resistive stress or the driving stress (Iken and Truffer, 1997; Jiskoot, 2011), and thus as a result it is often useful to consider the role of each resistive stress individually (Benn et al., 2007b). Although

the relative importance of each of the three resistive stresses in influencing calving glacier velocity will be detailed below, it is worth noting that this discussion will focus predominately on the role that basal drag has in controlling the velocity of calving glaciers, due to its known importance in regulating the dynamics of Fjallsjökull, the glacier of interest here (e.g. Dell et al., 2019).

2.4.3.2 Basal Drag

As we have seen previously (Section 2.1.) the effective pressure is the difference between ice overburden pressure and the water pressure at the glacier bed (Iken and Bindshadler, 1986; Sugiyama et al., 2011), with a change in effective pressure determining the amount of resistance to flow offered by basal drag (Schoof, 2010; Tsutaki et al., 2013). For calving glaciers, the presence of a water body at the terminus of these glaciers causes an increase in basal water pressure at these locations (Tsutaki et al., 2011; Carrivick and Tweed, 2013). These high basal water pressures tend to arise due to the up-ice propagation of lake- or fjord-water, and because high basal water pressures are often required to be able to evacuate basal water from the glacier against the outward pressure of the water body (Sugiyama et al., 2011; Liu et al., 2020). This maintains high basal water pressures close to ice overburden (i.e., close to, or at, zero), meaning basal drag is practically negligible and velocities are high as a result (Tsutaki et al., 2013; Carrivick et al., 2020). Furthermore, the hydraulic head within calving glaciers is also often much higher than that of the proglacial water body, due to the up-ice propagation of lake or fjord water (Meier and Post, 1987; Sugiyama et al., 2011). This means that any slight change in water pressure (e.g. from the changing level of the water body), or in ice overburden pressure (from a change in ice thickness), can lead to large changes in ice velocity and thus calving rate (Howat et al., 2007; Carrivick and Tweed, 2013; Sakakibara et al., 2013). It is this change in overburden which is particularly important for calving glaciers as it indicates that ice velocities and longitudinal strain rates increase rapidly as ice approaches floatation due to the fact that for any given water depth the effective pressure decreases as the ice thins (O’Neel et al., 2005; Benn et al., 2007b; Howat et al., 2008b; Tsutaki et al., 2013).

This has two important implications, which can account for the majority of the observed behaviour of calving glaciers (Benn et al., 2007b). Firstly, any *spatial* gradients in ice thickness relative to the depth of the proglacial water body will lead to increased sliding velocities and longitudinal strain rates as the ice becomes thinner, particularly near the terminus (Meier and Post, 1987; Benn et al., 2007a). As high rates of stretching near the terminus lead to deeper crevasses, any concurrent flow acceleration resulting from loss of basal drag (due to low effective pressure) will encourage calving to occur (O’Neel et al., 2005; Howat et al., 2008b; King et al., 2018). Indeed, the high longitudinal strain rates observed near the termini of two tidewater

glaciers, Columbia Glacier and LeConte Glacier, appear to be largely attributable to this process (Venteris et al., 1997; O'Neel et al., 2001; Benn et al., 2007a).

Secondly, any *temporal* reductions in ice thickness relative to water depth will result in flow acceleration and increasing longitudinal stretching rates through time. Here, an imposed thinning (for example due to surface melt) will lead to a reduction in effective pressure at the bed (due to the reduction in ice overburden relative to basal water pressure caused by surface thinning), and consequently, basal drag (Howat et al., 2007; Joughin et al., 2008a; King et al., 2018). This causes the glacier to speed up while also increasing longitudinal strain rates, leading to calving (Benn et al., 2007a; Howat et al., 2010). This is because longitudinal strain rates exert a first order control on crevasse depth, so, high strain rates equate to deeper crevasses, and because thinning reduces the freeboard level (the height of the glacier above the water level), increasing the likelihood that crevasses will penetrate to the waterline (Benn et al., 2007a; Mottram and Benn, 2009; King et al., 2018). Importantly, this process can trigger a positive feedback between ice acceleration, thinning, and calving retreat to occur, termed 'dynamic thinning', because longitudinal extension also results in thinning in the vertical direction (Vieli et al., 2001; Trüssel et al., 2013; Sakakibara and Sugiyama, 2018; Tsutaki et al., 2019). As a result, initial thinning resulting from increased surface melting will lead to flow acceleration and longitudinal stretching, which will lead to further thinning, and so on (Figure 15) (Howat et al., 2005; Benn et al., 2007b; Tsutaki et al., 2013).

Such a response is important for several reasons. First, it further highlights how changes in the position, and in particular the thickness of the calving front exert a first-order control on the sensitivity and stability of calving glaciers (Thomas, 2004; Nick et al., 2009). Second, dynamic thinning will greatly increase the calving rate (for the reasons described above), and as a result will trigger terminus retreat when increased calving losses outweigh the effects of flow acceleration, which may partly explain the observed rapid retreat of calving glaciers in Greenland and elsewhere (e.g. Vieli et al., 2000; Nick et al., 2007b; Joughin et al., 2008b; Pritchard et al., 2009; Sakakibara and Sugiyama, 2018). Third, it illustrates how climatic conditions and calving glacier behaviour are linked, whereby an initial forcing (e.g. surface melt) can result in a large-scale dynamic response, providing a direct link between environmental forcing and glacier mass balance (Benn et al., 2007b; Howat et al., 2010; Minowa et al., 2017). Indeed, it has been shown for several Greenlandic outlet glaciers that an initial forcing at the front occurring over several days can result in acceleration and retreat that is sustained over much longer time periods as the glacier dynamically responds to the perturbations at the front (Joughin et al., 2008c; Nick et al., 2009; Howat et al., 2010). Finally, it can also help to explain the widely observed correlation between calving rates and water depth (e.g. Pelto and Warren, 1991; Warren and Kirkbride, 2003;

Sakakibara et al., 2013). The very definition of calving rate means there will be a strong correlation with ice velocity (except during times of rapid retreat), meaning faster glaciers will have higher calving rates (van der Veen 1996; Benn et al., 2007b). As discussed previously, an inverse relationship exists between effective pressure and basal drag, which means that glaciers will flow faster when they enter deeper water due to lower effective pressure, so that calving rates can be expected to be larger for glaciers grounded in deeper water (van der Veen, 2002; Benn et al., 2007b; Carrivick and Tweed, 2013). This will be discussed in more detail in Section 2.4.4.

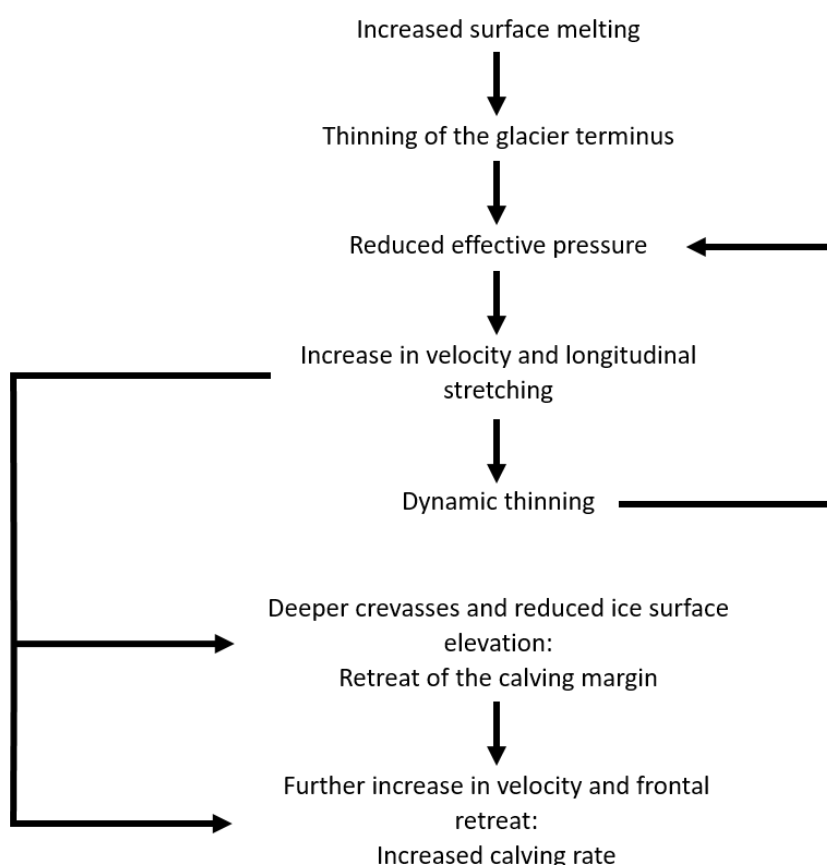


FIGURE 15 Relationship between glacier thinning, acceleration and calving retreat, resulting from effective pressure-dependent basal motion and the influence of longitudinal stretching on dynamic thinning and first-order calving. Modified from Benn et al. (2007b).

2.4.3.3 *Lateral Drag*

For many outlet glaciers, ice streams and ice shelves, but particularly those that sit within steep-sided glacial valleys or which flow through narrow fjords, the driving stress can also be opposed by drag at the glacier margin, although its relative importance varies in both time and space (Benn et al., 2007b; Cuffey and Paterson, 2010). In Greenland for example, many tidewater glaciers sit within narrow fjord systems, suggesting that lateral drag is likely to provide a greater proportion

of the total resistance to ice flow, and as a result, any reductions in basal drag will have relatively little impact on ice speed (Joughin et al, 2008b; Shapero et al., 2016). Conversely, Naruse et al. (1997) suggested that Glacier Upsala, Patagonia, was moving entirely by basal sliding due to water being present at both the bed and the lateral margins, greatly reducing their resistive potential. Finally, force balance reconstructions undertaken by O’Neel et al. (2005) for the retreating Columbia Glacier indicated that lateral drag was generally less important than basal drag, except during times of rapid retreat when it became more important (Benn et al., 2007b).

In those instances where lateral drag does provide a significant proportion of the overall flow resistance, glacier velocity is independent of both the ice thickness and the effective pressure, and is instead proportional to both the ice surface gradient and the width of the ice front (Benn et al., 2007b). As a result, ice velocity will not increase as ice thickness decreases, so that flow acceleration may not necessarily occur even if the ice tends towards floatation (as it does for basal drag) (Thomas, 2004; Benn et al., 2007a). Importantly, this strong dependence of glacier velocity on the width of the ice front explains the widely observed tendency for calving margins to be located at widenings in fjords or other embayments (Warren, 1991; Thomas, 2004; Howat et al., 2008b).

In these locations, even a small increase in terminus width beyond the fjord walls will result in a large increase in velocity, and as a result longitudinal strain rates are also likely to be high (Benn et al., 2007b; Joughin et al., 2008b). As discussed previously, the margin of a calving glacier will be located at the point where the longitudinal strain rates are high enough to allow crevasses to penetrate to the waterline and thus trigger calving (van der Veen, 1996; Diolaiuti et al., 2006; Mottram and Benn, 2009). In this instance, therefore, the calving margin will be located where the terminus width is large, but the ice thickness is small (Benn et al., 2007b). Conversely, when the glacier is positioned at a narrowing within the fjord system the glacier terminus is far more stable due to longitudinal compression, which results in reduced ice velocities and strain rates (Howat et al., 2005; Shapero et al., 2016; King et al., 2018). However, while lateral drag is an important component of the force balance of many glaciers worldwide, at Fjallsjökull its overall influence, particularly since the turn of the century, is likely to be limited (Dell et al., 2019), and as result its control on velocity will not be discussed here in any further detail.

2.4.3.4 *Longitudinal Stress Gradients*

At the vertical terminal face of a calving glacier, the outward-directed cryostatic pressure is greater than the backward-directed hydrostatic pressure so that for equilibrium, viscous stretching is required to balance this gradient in longitudinal stress (Cuffey and Paterson, 2010; Shapero et al., 2016). If there are additional forces resisting glacier flow, however, such as drag at

the ice margins or at localised grounded zones (termed 'pinning points'), this can partially or wholly offset the imbalance between cryostatic and hydrostatic pressures at the point of attachment, reducing velocities (Benn et al., 2007b; Tsutaki et al., 2013; Shapero et al., 2016). This backward-acting pressure is known as *backstress*, and is defined on the grounded part of a calving glacier as the effects of non-local basal and lateral drag transmitted up-glacier via longitudinal stresses (van der Veen, 1997; Howat et al., 2007; Nick et al., 2009). Although backstress is often provided by bedrock bumps or rises (topographic 'pinning points') (e.g. Nick et al., 2009; Sakakibara et al., 2013; Tsutaki et al., 2013), it can also be provided by other obstructions to glacier flow, such as fjord narrowing's, ice melange and terminal moraines (e.g. Thomas, 2004; Howat et al., 2005; Joughin et al., 2008a; Liu et al., 2020).

The role of longitudinal stresses in controlling the overall flow and dynamics of calving glaciers has been demonstrated in a number of studies for both lacustrine and tidewater glaciers. For example, Boyce et al. (2007) attributed the rapid retreat of Mendenhall Glacier, Alaska, to the loss of support following initial retreat from a bedrock ridge near the eastern margin, while Tsutaki et al. (2019) suggested that the recently observed retreat and thinning of Thorthormi Glacier in the Bhutanese Himalaya was due to its detachment from its terminal moraine. Meanwhile, for three of the largest outlet glaciers of the Southern Patagonia Icefield, Sakakibara and Sugiyama (2014) proposed that the observed rapid retreat and increase in flow velocities may have been caused by a significant backstress reduction following terminus thinning. Similarly, for several outlet glaciers in Greenland, initial terminus retreat has been observed to have caused a substantial reduction in the buttressing resistance provided by the ice tongue, leading to rapid flow acceleration and surface thinning as these glaciers have then attempted to restore force balance (Howat et al., 2007; Joughin et al., 2008a; Shapero et al., 2016).

At Helheim Glacier, Joughin et al. (2004) found that after the glacier retreated 2.1 km (reducing the longitudinal stress), the driving stress increased by ~20% within the first 12.5 km of the terminus, driving the subsequent 45-60% increase in ice velocity that was observed (Howat et al., 2005; Nick et al., 2009). Finally, at Columbia Glacier, Alaska, longitudinal stress gradients have also been found to be important for opposing the driving stress, particularly up-glacier of where the glacier trough narrows (Meier and Post, 1987; O'Neel et al., 2005). It was concluded that ice acceleration likely did occur when the glacier retreated from these 'pinning points' (O'Neel et al., 2005). However, while longitudinal stress gradients are an important component of the force balance on numerous glaciers worldwide, including for Fjallsjökull (e.g. Dell et al., 2019), it is difficult to discern its influence on the overall dynamics of the glacier based on available data, and as such the role of basal drag will be the primary focus for the remainder of this thesis.

2.4.4 Tidewater vs Freshwater Calving

Traditionally, calving in freshwater settings received little attention in glaciological studies because the majority of pioneering work on calving was undertaken on Alaskan tidewater glaciers, most notably Columbia Glacier (Sikonia, 1982; van der Veen, 1996; Krimmel, 2001). Despite this, studies of glaciers calving into hydropower storage lakes in the European Alps around the same time showed that the calving rate in freshwater settings also exhibited a good correlation with ice velocity (Bindschadler, 1980; Funk and Röthlisberger, 1989). However, despite these similarities, it was importantly shown that calving rates in freshwater were lower than those in tidewater (e.g. Bindschadler, 1980; Funk and Röthlisberger, 1989; Hooke et al., 1989b; Laumann and Wold, 1992), which led Warren (1991) to suggest that freshwater-calving glaciers may occupy an intermediate position on the 'climatic sensitivity' spectrum between non-calving and tidewater glaciers (Warren and Kirkbride, 2003; Benn et al., 2007b). Subsequent studies in Alaska, New Zealand, Norway and Patagonia added further support for this by showing that rates of freshwater calving were consistently an order of magnitude lower than rates for tidewater glaciers for any given water depth (e.g. Pelto and Warren, 1991; Kennet et al., 1997; Skvarca et al., 2002; Motyka et al., 2003; Warren and Kirkbride, 2003; Haresign, 2004). Many calving glaciers are highly dynamic and are currently undergoing widespread retreat, and as such an understanding of the processes that influence glacier behaviour in both tidewater and freshwater settings will allow us to better predict their future response and stability (e.g. Howat et al., 2008b, 2010; Nick et al., 2009; Hart et al., 2011; Sakakibara et al., 2013; Baurley et al., 2020). However, only the processes occurring at freshwater calving glaciers will be discussed in detail below due to their particular relevance to this thesis.

Proglacial lakes are becoming ubiquitous at the termini of many glaciers worldwide due to continued climate warming and glacier retreat, with this forecast to continue as precipitation and temperature changes in these regions also continue (Haeberli et al., 2016; King et al., 2018). Indeed, over recent decades there has been a rapid increase in the number and size of proglacial lakes globally, with the latest estimates indicating a 53% and 51% increase respectively between 1990-1999 and 2015-2018 (Figure 16) (Shugar et al., 2020). At a regional scale, particularly large increases in proglacial lake number and area have been observed for areas such as Iceland, The Himalaya, the European Alps, Patagonia and New Zealand (e.g. Diolaiuti et al., 2006; Schomacker, 2010; Dykes et al., 2011; Minowa et al., 2017; Nie et al., 2017), and recent research has even shown an increase in lake-terminating glaciers on the western flank of the Greenland Ice Sheet (e.g. Carrivick and Quincey, 2014), although the rate and extent of change varies between regions. For example, in Iceland the number of proglacial lakes increased from 32 to 106 between the period 1990-1999 and 2015-2018, while proglacial lake area increased from 54.83 km² to 132.42

km² over the same period, equating to an overall increase of 231% and 142%, respectively (Shugar et al., 2020). Meanwhile in Patagonia, where a number of very large lakes are observed, the rate of change is slightly less rapid, with lake number and area increasing by 121% and 97% respectively over the same period (Shugar et al., 2020). Despite such regional variations, however, it is highly likely that the number and size of proglacial lakes worldwide will continue to increase over the coming decades, which will greatly impact the overall dynamics of the glaciers that terminate into them (Carrivick et al., 2020; Shugar et al., 2020).

As is the case for tidewater glaciers, once a glacier undergoes the transition from land- to lake-terminating, then other factors which are independent of climate (e.g. water depth, glacier geometry), can cause large-scale-changes in glacier dynamics to occur (Warren and Kirkbride, 2003; Carrivick and Tweed, 2013; Chernos et al., 2016). However, unlike at tidewater glaciers, which terminate in a water body of a certain depth and size that remains fairly consistent over time, the lakes at the termini of lake-terminating glaciers can continually grow and evolve over decades in response to glacier retreat and the infilling of meltwater into the lake system (Sakai et al., 2009; Carrivick and Tweed, 2013). In this way, the formation, evolution, character and behaviour of proglacial lakes is intrinsically linked to climate through the surface energy balance and to wider geologic systems through glacier dynamics, meltwater and sediment fluxes (Larsen et al., 2011; Carrivick and Tweed, 2013).

Many proglacial lakes form in overdeepened bedrock troughs which were fashioned by glacier erosion during the advance cycle, but have since then been infilled with meltwater as they have become exposed during glacier retreat, and as such they are common in mountainous regions and at ice cap fringes (Schomacker, 2010; Trüssel et al., 2013; Tsutaki et al., 2013). Furthermore, as lake-terminating glaciers begin to recede into these overdeepened bedrock troughs, the rate of retreat often accelerates due to enhanced calving, which in turn causes additional lake expansion and therefore, further calving and retreat (Schomacker, 2010; Carrivick and Tweed, 2013; Baurley et al., 2020). Indeed, proglacial lakes usually grow rapidly once glacier calving begins as this increases the meltwater input to the system over that of glacier surface melt alone, leading to further dynamic effects (Fujita et al., 2009; Sakai et al., 2009; Carrivick et al., 2020).

The growth of proglacial lakes exerts a strong control on the velocity, mass balance and longitudinal stress regime of the glacier that calves into it, and the interactions between these lakes and the dynamics of lake-terminating glaciers have been measured in several studies (e.g. Diolaiuti et al., 2006; Schomacker, 2010; Dykes et al., 2011; Sakakibara et al., 2013; King et al., 2018).

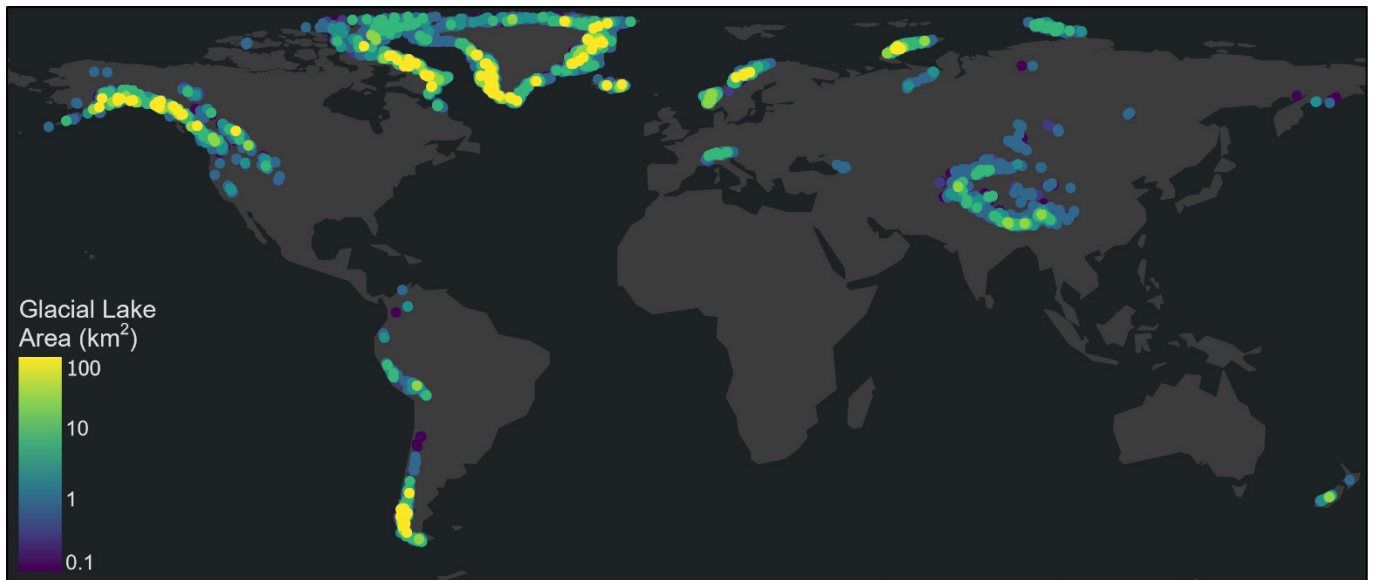


FIGURE 16 Near-global glacial lake distribution and area for the period 2015-2018. All lakes with areas $>0.05 \text{ km}^2$ and $<200 \text{ km}^2$ are included, with each circle representing an individual lake. Insufficient data was available for three Arctic regions (Svalbard, Jan Mayen and Franz Josef Land) and for Antarctica, and thus lakes in these regions were not included in the global database. Map reproduced from data provided by Shugar et al. (2020), while the base map was provided by ESRI.

Although several factors can influence the dynamics of lake-terminating glaciers (Figure 17), the most important of these is the water depth (Warren and Kirkbride, 2003; Boyce et al., 2007; Carrivick and Tweed, 2013). The depth of the proglacial lake at the ice margin determines: (i) the distance up-ice that water propagates (Sugiyama et al., 2011), (ii) the vertical extension of the basal hydrological system (Harper et al., 2010), via basal water pressures (Tsutaki et al., 2011), and (iii) the calving rate (Carrivick and Tweed, 2013). All three factors encourage faster ice velocities and, therefore, increased longitudinal stretching, and as a result the terminal regions of many lacustrine-calving glaciers are heavily crevassed (Figure 18) (Diolaiuti et al., 2006; Benn et al., 2007b; Tsutaki et al., 2013). This increases the likelihood of surface crevasses propagating to the waterline, allowing calving to occur and thus consequently leading to enhanced rates of mass loss and retreat (Mottram and Benn, 2009; Minowa et al., 2017; King et al., 2018). The water depth at the terminus also has an important control on the subglacial drainage configuration as where marginal water depths are greatest the subglacial conduit system is most unstable, which favours the development of an inefficient distributed system (Fyfe, 1990; Benn et al., 2007b). As such, the water pressures at the bed are high, leading to faster ice velocities due to the inverse relationship that exists between the effective pressure and basal drag, leading to further calving and retreat (Sugiyama et al., 2011; Carrivick and Tweed, 2013).

Furthermore, where large volumes of water are able to persist at the bed and even propagate up into the interior of lake-terminating glaciers, the high basal water pressures will not only promote

sliding (Harper et al., 2010; Tsutaki et al., 2011), but could also result in hydro-fracturing and basal crevasse development, leading to increased calving (van der Veen, 1998a; 2007). Therefore, as proglacial lakes increase in size and mass loss via calving increases due to the increase in water depth, the glacier surface must steepen, increasing the driving stress and, therefore, glacier velocity, leading to a positive feedback mechanism between water depth, ice velocity, thinning, calving and retreat (Benn et al., 2007b; Schomacker, 2010; Carrivick and Tweed, 2013). This relationship between water depth and an increase in mass loss has been observed for several lake-terminating glaciers in Iceland, The Himalaya, Patagonia and New Zealand over recent years (e.g. Warren and Kirkbride, 2003; Sakakibara et al., 2013; King et al., 2018; Dell et al., 2019) and consequently its influence for the dynamics of glaciers in these regions has become extremely significant (e.g. Carrivick and Tweed, 2013; Sakakibara et al., 2013; Tsutaki et al., 2019; Baurley et al., 2020).

The mass loss from, and the velocity of, lake-terminating glaciers can also be further augmented by thermally induced melting through lake water delivering heat to the glacier terminus (Sakai et al., 2009; Carrivick and Tweed, 2013; Nie et al., 2017), although this often occurs at a smaller scale than at tidewater glaciers due to cooler temperatures and reduced circulation (e.g. Fried et al., 2015; Truffer and Motyka, 2016; Schild et al., 2018). Nevertheless, this thermally induced melt can cause notches to develop at the waterline, which may then begin to undercut the terminus face and in some cases, control the rate of calving (Diolaiuti et al., 2006; Röhl, 2006; Mallalieu et al., 2020). Such thermal notches tend to be relatively small in vertical extent (several metres) and form via wave action and warm water which erode the terminus face at the waterline (Figure 19) (Röhl, 2006; Truffer and Motyka, 2016; King et al., 2018). Importantly, the rate at which these notches erode the terminus face is not simply a function of total ice melt, but also by how that melt is focused at the terminus (Röhl, 2006; Benn et al., 2007b).

Indeed, a given amount of melt that is distributed over a narrower area of the terminus will be more effective at undercutting the calving face than the same amount focused over a much broader range (Röhl, 2006), leading to an increase in force imbalances at these locations and ultimately resulting in high magnitude calving events (Benn et al., 2017). Although direct measurements of notch erosion at lacustrine calving margins are rare, the available data suggests that fairly significant rates of erosion are possible (Mallalieu et al., 2020). For example, rates of 0.2 to 0.3 m d⁻¹ have been recorded for Miage (Diolaiuti et al., 2006) and Tasman (Röhl, 2006) glaciers, while Haresign and Warren (2005) reported rates of up to 0.8 m d⁻¹ for Glaciar Leon. More recently, it has been suggested that such rates of notch erosion may be present at the termini of Glaciar Perito Moreno, Patagonia and Russel Glacier, Greenland by Minowa et al.

(2017) and Mallalieu et al. (2020) respectively, although neither study were able to provide direct measurements.

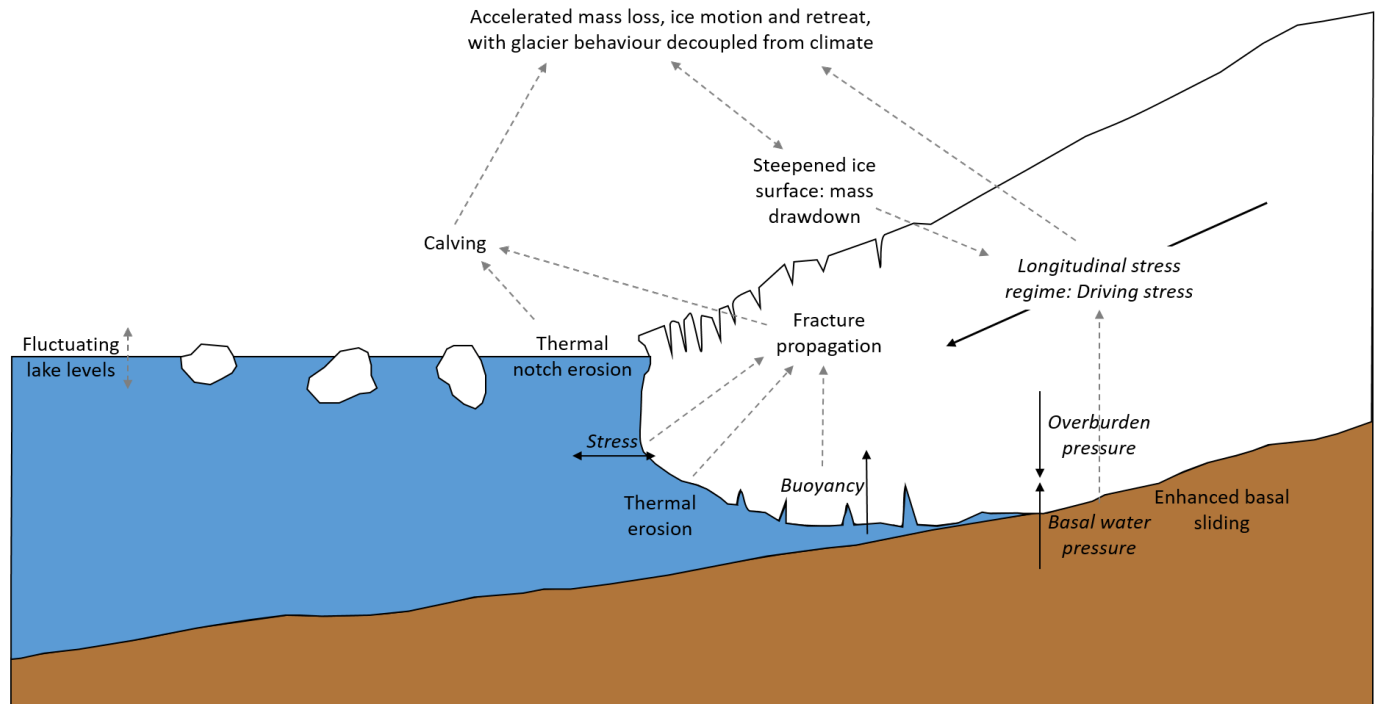


FIGURE 17 Summary schematic of the processes occurring at the margin of a lake-terminating glacier, and the impact these processes have on overall ice dynamics. Forces are shown in italicised text with thick black arrows, while processes are given with black text and dashed dark grey lines to denote interactions. Modified from Carrivick and Tweed (2013).

The role of thermally induced melt notches is particularly important for slow-moving glaciers, such as those in New Zealand, where compressive flow regimes can often cause slow velocities and limited crevassing, meaning calving for these lake-terminating glaciers tends to be driven by subaqueous melt at the waterline (Warren and Kirkbride, 2003; Röhl, 2006; Dykes et al., 2011). Thermal erosion notches can also cause unstable overhanging ice cliffs to form, which calve and retreat rapidly leading to the development of subaqueous 'ice feet' below the waterline (Warren and Kirkbride, 2003; Robertson et al., 2012). As a result, thermal erosion notches are a relatively common occurrence on many lake-terminating glaciers, and thus comprise an important component of overall frontal ablation (e.g. Röhl, 2006; Dykes et al., 2012; Minowa et al., 2017; Mallalieu et al., 2020). In addition to these thermal erosion notches, the heat delivered from proglacial lakes to the termini of lake-terminating glaciers can also control thermal erosion far beyond the immediate extent of the lake itself by producing ponded meltwater beneath and within a glacier, for example within crevasses (Carrivick and Tweed, 2013).



FIGURE 18 Image illustrating how the terminus regions of lacustrine-calving glaciers are often heavily crevassed due to the longitudinal stretching of surface ice. The glacier in this image is Grey Glacier, Chilean Patagonia, and was acquired in June 2007. Scale bar is approximate. Image source: NASA Earth Observatory (2007).

Therefore, while the above examples highlight the important control water depth and subaqueous melt have on the dynamics and stability of lake-terminating glaciers, they also importantly show that the rapid retreat and highly dynamic changes occurring at lake-terminating glaciers worldwide cannot be solely attributed to climatic forcing, and that in some cases, such changes can occur completely independent of any climatic influences (e.g. Rignot et al., 2003; Sugiyama et al., 2011; Carrivick and Tweed, 2013; Chernos et al., 2016; Watson et al., 2020).

Due to the highly dynamic nature and relative insensitivity to climate of many calving glaciers, further research is needed into their likely future response and stability over the coming years, whether this is forced by climate or by geometric changes within the glacier itself (Boyce et al., 2007; Howat et al., 2010; Carrivick and Tweed, 2013; Truffer and Motyka, 2016). Such predictive work can be carried out through modelling studies (e.g. Benn et al., 2007a; Nick et al., 2009, 2010), however, due to the highly complex nature of glacier calving it is still challenging to model the future evolution of calving glaciers (Nick et al., 2010; Joughin et al., 2012; Lemos et al., 2018a). As a result, comprehensive, frequent and systematic monitoring of such highly dynamic glaciers (calving and non-calving) using remote sensing techniques (e.g. satellite imagery and UAV

surveys) is required to further understand and quantify the processes governing their dynamical stability and contribution to future SLR (Paul et al., 2015; Ryan et al., 2015; Wigmore and Mark, 2017; Lemos et al., 2018a; Robson et al., 2018; Jouvét et al., 2019).



FIGURE 19 Example of a thermal notch near the base of Miage Glacier, Italian Alps, following the drainage of its proglacial lake in late summer 2004. The surveyor to the right of the image is positioned on the lake floor and is for scale. White line represents the vertical profile of the notch. The black arrows highlight the location of the notch and the extent of thermal undercutting. Image modified and annotated from Diolaiuti et al. (2006).

2.5 Measurements of Glacier Velocity from Satellite Remote Sensing

Increases in the availability and quality of remotely sensed satellite datasets have allowed substantial progress to be made in glaciological research over recent years (Berthier et al., 2003; Redpath et al., 2013; Rieg et al., 2018). For example, the advent of freely available satellite data (e.g. Pope et al., 2014) has allowed numerous glacier-related products, such as glacier outlines, ice thickness estimates and flow velocities to be derived using well-established algorithms (e.g. Raup et al., 2006; Gjermundsen et al., 2011; Malenovsky et al., 2012; Paul et al., 2017; Farinotti et al., 2017). These products provide key information about global glacier distribution and changes in length, area and mass balance, which in turn provide a strong indicator for the current state of

the cryosphere, regional trends in water resources, glacier dynamics and the impacts of climate change (Vaughan et al., 2013; Paul et al., 2015, 2017; Millan et al., 2019). Traditionally, the data which informs such products would be collected using field surveys, which although can provide extremely high-resolution point measurements, are fundamentally limited in mountainous regions by the harsh climate, poor accessibility and limited manpower (König et al., 2001; Bhardwaj et al., 2015). The key advantage of satellite remote sensing, however, is that it can obtain a regionally more complete picture of glacier changes by extending the number of glaciers measured, the time period covered and the parameters that can be assessed, thus facilitating year-round glacier monitoring while simultaneously complementing traditional field measurements (Bhardwaj et al., 2015; Paul et al., 2015, 2017).

One of the most important products that can be efficiently derived from satellite remote sensing is glacier velocity (Scherler et al., 2008; Tiwari et al., 2014; Ruiz et al., 2015). To date, it has been used for: (i) studying glacier dynamics and related processes (e.g. Leprince et al., 2008; Paul et al., 2015), (ii) detecting advance and retreat cycles (e.g. Herman et al., 2011), (iii) calculating ice thickness and modelling bed topography (e.g. McNabb et al., 2012) and (iv) observing glacial response to climate change (e.g. Berthier et al., 2003; Scherler et al., 2011). Although these velocities can be measured directly on the glacier surface by monitoring the position of stakes using dGPS, observations over long periods (i.e. over multiple seasons) involve frequent revisits to the site which can be costly and logistically challenging, while the stakes themselves can only be located in accessible regions, which results in sparse spatial coverage (Scherler et al., 2008; Tiwari et al., 2014; Rieg et al., 2018). In contrast, the large number of archived and upcoming satellite data mean it is now possible to map and measure ice velocity on a nearly global scale, providing the opportunity to achieve large and possibly complete spatial coverage, even in very remote areas (Scherler et al., 2008; Paul et al., 2015). This has facilitated the accurate monitoring and derivation of ice velocity for numerous glaciers simultaneously without the effort and costs associated with field-based measurements (Karpilo, 2009; Gjermundsen et al., 2011). It is unsurprising, therefore, that the use of satellite data to derive velocity information has become commonplace in glacial research over recent years.

For example, Copland et al. (2009) provided velocity fields on a regional scale for all central Karakoram Glaciers between 2006 and 2007, with the technique also subsequently applied to the Everest region by both Luckman et al. (2007) and Quincey et al. (2009), and to Mont Blanc Glaciers by Fallourd et al. (2011). Heid and Käab (2012b) utilised the long-time span of Landsat data to investigate the link between variations in mass balance and velocity for six glaciated regions across the globe between 1985 and 2011. Velocity variations were also shown by Willis et al. (2011) for the entire Northern Patagonian Icefield for the period 2000-2011 and by Burgess et

al. (2013) for Alaska Range Glaciers between 2007 and 2010. More recently, glacier velocities have also been provided for Svalbard (Schellenberger et al., 2015), the Antarctic Peninsula (Fieber et al., 2018), northwest Greenland (Sakakibara and Sugiyama, 2018) and High Mountain Asia (Dehecq et al., 2019), among many others.

At the very basic level, simple 2D measurements of glacier velocity can be made from satellite imagery by monitoring the movement of glacier surface features through time (e.g. Harrison et al., 1992; Berthier et al., 2005). However, this only works if the features on the ice surface can be identified in two consecutive images, but if this is the case then the method is limited only by the spatial resolution of the sensor (Hubbard and Glasser, 2005, Kääb, 2005; Paul et al., 2015).

Traditionally, this monitoring of features was undertaken manually (e.g. Lucchitta and Ferguson, 1986). However, technological advances over recent decades, particularly in regard to computer processing power, has meant that novel image mapping techniques, when applied to pairs of satellite images, can automatically map and measure the resulting displacements at high accuracy with very little user input (Debella-Gilo and Kääb, 2012; Heid and Kääb, 2012a; Redpath et al., 2013). At present, surface velocities can be derived from satellite imagery using three main techniques: SAR interferometry (InSAR) (e.g. Rignot et al., 1997; Strozzi et al., 2002), offset tracking on SAR images (e.g. Riveros et al., 2013; Nagler et al., 2015) or through feature tracking applied to optical images (e.g. Scherler et al., 2008; Dehecq et al., 2015). Each method has its own relative advantages and disadvantages, and these will be detailed in the following section.

2.5.1 Techniques to Derive Glacier Velocity from Satellite Imagery

2.5.1.1 *InSAR*

InSAR is a widely used method for surface deformation and velocity mapping (e.g. Kääb, 2005; Luckman et al., 2007), which can provide highly accurate displacements (mm-cm scale) over timescales of several days or less (Scherler et al., 2008; Quincey et al., 2009; Sam et al., 2016). InSAR has been used in recent years to investigate velocity variations on glaciers in Svalbard, the Himalaya, Canadian Arctic and in Greenland, among others, at extremely high spatial and temporal resolutions (e.g. Rignot et al., 1997, 2000, Quincey et al., 2009; Schneevoigt et al., 2012; Sánchez-Gómez and Navarro, 2017; Pavelka et al., 2018) (Figure 20).

The method works by taking two complex SAR images acquired from slightly different orbit configurations and time periods, which are then combined to exploit the phase difference of the signals within both images, which corresponds to surface displacement (Strozzi et al., 2002; Quincey and Luckman, 2009). However, the method requires that coherence between the images

is not lost due to modification of the glacier surface, which can occur through surface melt, snowfall, or surface deformation (Strozzi et al., 2002; Riveros et al., 2013). As such, the method cannot be used on fast-flowing glaciers where the surface deforms very quickly, or for assessing velocity variations that occur over time spans of weeks or longer (Tiwari et al., 2014; Sánchez-Gómez and Navarro, 2017; Pavelka et al., 2018). This means that InSAR-derived velocity measurements are typically constrained to time spans of one, three or six days (Joughin et al., 1996; Scherler et al., 2008) for the clean-ice areas of relatively slow-moving glaciers to ensure that coherence is well maintained (Quincey et al., 2009; Paul et al., 2015). Furthermore, the velocity information obtained from InSAR is often only representative of the observation period as extrapolation of the data to annual velocities is difficult (Scherler et al., 2008). As a result, InSAR is generally unsuitable for global-scale application (Paul et al., 2015).

2.5.1.2 *Offset Tracking*

In lieu of the limitations present within the InSAR methodology, offset tracking procedures are now largely adopted in glacial research when investigating long-term velocity variations using SAR imagery (e.g. Gray et al., 1998; Strozzi et al., 2002; Quincey et al., 2009; Nagler et al., 2015). Offset tracking estimates the movement of the ice surface between two time-separated acquisitions through cross-correlation on selected ground control points in coregistered images (master and slave) in both the slant-range and azimuth direction (Paul et al., 2015; Fahnestock et al., 2016; Lal et al., 2018). The movement velocity is then computed based on the offsets estimated by the cross-correlation, with these values then interpolated to create a map of glacier velocity (Scherler et al., 2008; Burgess et al., 2013; Serco Italia 2018). The method is particularly advantageous because it is less sensitive to loss of coherence between images, making it a highly efficient alternative to InSAR (Nagler et al., 2015; Sánchez-Gómez and Navarro, 2017; Lal et al., 2018).

Furthermore, as the images themselves are captured using an active microwave sensor, it means they are not impacted by the persistent cloud cover often present in glaciated regions that can partially or completely obscure the area of interest (Schneevoigt et al., 2012; Schellenberger et al., 2015; Winsvold et al., 2018). This means it is particularly useful for analysing rapidly flowing glaciers over time periods spanning several weeks to months (and potentially longer), where InSAR methods suffer due to loss of coherence (Luckman et al., 2007; Riveros et al., 2013; Nagler et al., 2015) (Figure 21). For example, Strozzi et al. (2002) utilised sixteen ERS-1/2 SAR images acquired between 1992 and 1996 to investigate the 1994 surge of Monacobreen in Northern Svalbard. Lemos et al. (2018a) meanwhile utilised the 6-day repeat interval of Sentinel-1 SAR data to map the complex flow patterns of four rapidly flowing outlet glaciers of the Greenland Ice Sheet between 2015 and 2017. Finally, complete velocity maps of the Greenland Ice Sheet since

~2009, generated using SAR offset tracking, have recently been released by the Greenland Ice Mapping Project, providing key insights into its dynamics ranging from the individual glacier scale to the entirety of the ice sheet, at monthly to decadal time scales (Joughin et al., 2018).

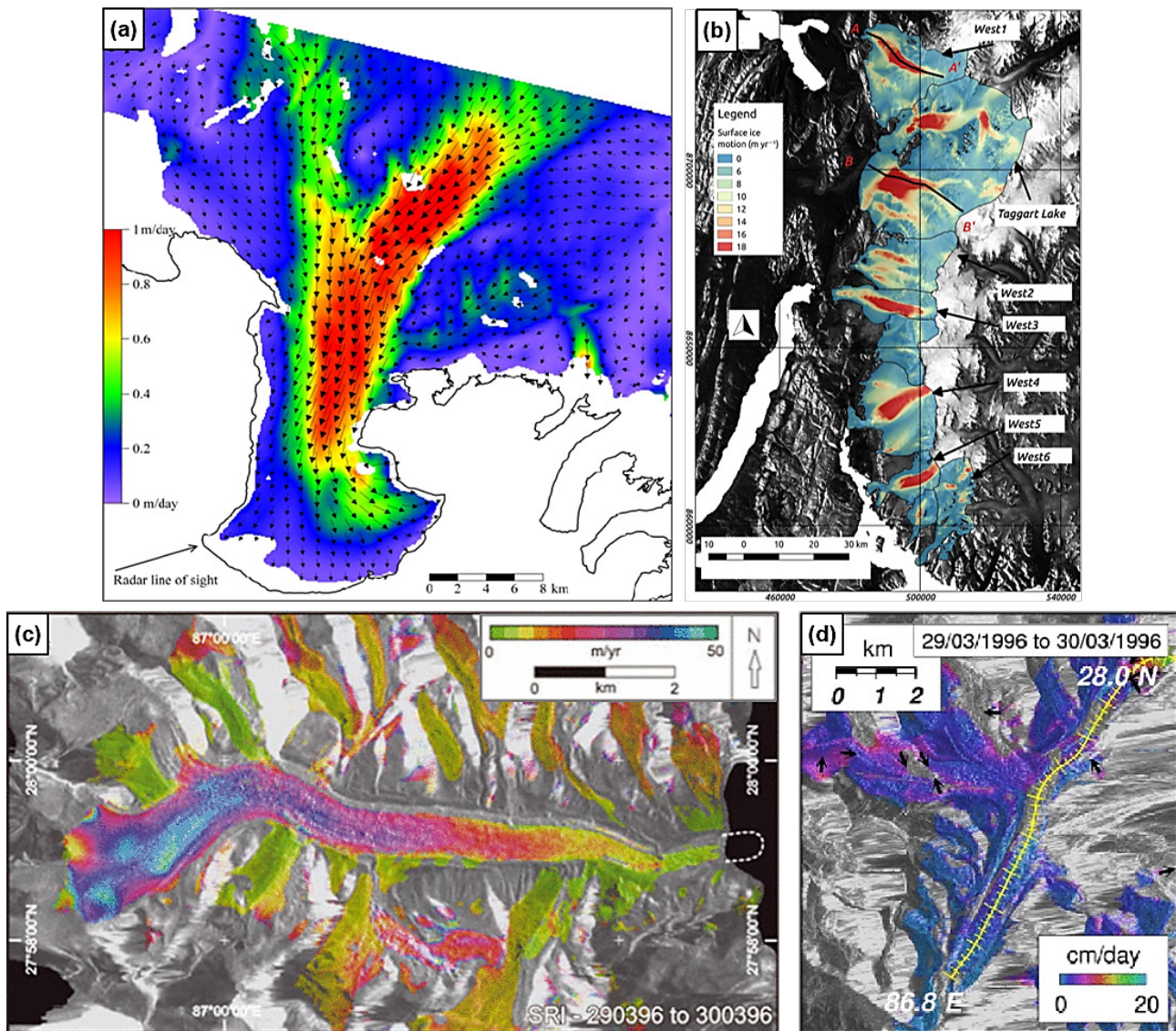


FIGURE 20 Examples of velocity products obtained in previous studies that were derived using InSAR. (a) Speed-up of Skeiðarárjökull, Iceland between 27/03 - 28/03/1996, following the jökulhlaup that occurred that same month (Magnússon et al., 2006); (b) Western glaciers of the Prince of Wales Icefield, Canadian Arctic for the period 10/02 - 17/02/2016 (Sánchez-Gómez and Navarro, 2017); (c) Khangshun Glacier, Everest Region, for the period 29/03 - 30/03/1996 (Quincey et al., 2009) and (d) Khumbu Glacier, Everest Region, for the period 29/03 - 30/03/1996 (Luckman et al., 2007).

However, a key general limitation of the offset tracking methodology is that when analysing glaciers in steep mountainous terrain, the high incidence angle of the SAR sensor can inhibit visibility of the target glacier (due to shadowing and the effect of increased layover), leading to large errors unless a DEM of sufficiently high accuracy is used to correctly orthorectify the

measurements (Trouvé et al., 2007; Bhardwaj et al., 2015; Winsvold et al., 2018). Additionally, the images acquired by the SAR sensors utilised in offset tracking are highly sensitive to changes in the ice surface conditions over time (e.g. Paul et al., 2015), as well to ionospheric noise (e.g. Wegmüller et al., 2006).

In regard to the former, this can occur through changes in illumination conditions or a shift in surface features between the two acquisitions, with SAR sensors showing a particular sensitivity to the presence of liquid water on the ice surface, which can significantly reduce the quality of the results (Paul et al., 2015, 2017). In terms of the latter, ionospheric noise can cause shifts in azimuth position, and tend to be especially prevalent at higher latitudes while being strongly dependent on solar activity (Wegmüller et al., 2006; Nagler et al., 2015). Such shifts tend to lead to higher relative errors when measuring slower-moving areas of ice, potentially highlighting the limited capacity of offset tracking in resolving particularly small displacements, such as in the ice sheet interior (Nagler et al., 2015; Schellenberger et al., 2015). Further errors can also result from sub-pixel geometric sensor noise level (which is usually larger than the precision of the offset tracking algorithm), and from the relative lack of a robust post-processing procedure that can eliminate measurement noise and mismatches (Paul et al., 2015).

2.5.1.3 *Feature Tracking*

With the continued improvement of the spectral and spatial characteristics of satellite sensors, however, optical image correlation algorithms, otherwise known as feature tracking, has become a hugely popular and efficient method in glaciology for deriving surface velocity measurements at low costs (Heid and Kääb, 2012a; Bhardwaj et al., 2015; Sam et al., 2016). At a general level, feature tracking works by tracking distinct surface features (e.g. crevasses) through cross-correlation of image patterns between two repeat pairs of images, which are then used to calculate the displacement with sub-pixel ($1/10^{\text{th}}$) precision (Luckman et al., 2007; Heid and Kääb, 2012a; Tiwari et al., 2014). The method was first undertaken automatically on glaciers by Bindschadler and Scambos (1991) using simple image correlation algorithms based on work done by Bernstein (1983). In recent years, however, several additional methods have been developed and applied in glaciology (Heid and Kääb, 2012a; Bhardwaj et al., 2015). These include: (i) normalised cross-correlation in the spatial domain (NCC) (e.g. Scambos et al., 1992; Berthier et al., 2003), (ii) cross correlation in the Fourier domain (e.g. Rolstad et al., 1997), (iii) sub-pixel phase correlation (COSI-Corr) (e.g. Leprince et al., 2007; Herman et al., 2011), (iv) orientation correlation (CCF-O) (Haug et al., 2010) and (v) repeat-image feature tracking (RIFT) (e.g. Ahn and Howat, 2011). In combination with these, several open-source software packages have also been developed over recent years which utilise the above principles, with the most widely-used

including: (i) IMCORR (Scambos et al., 1992), (ii) CIAS (Kääb and Vollmer, 2000), (iii) COSI-Corr (Leprince et al., 2007) and (iv) ImGRAFT (Messerli and Grinsted, 2015).

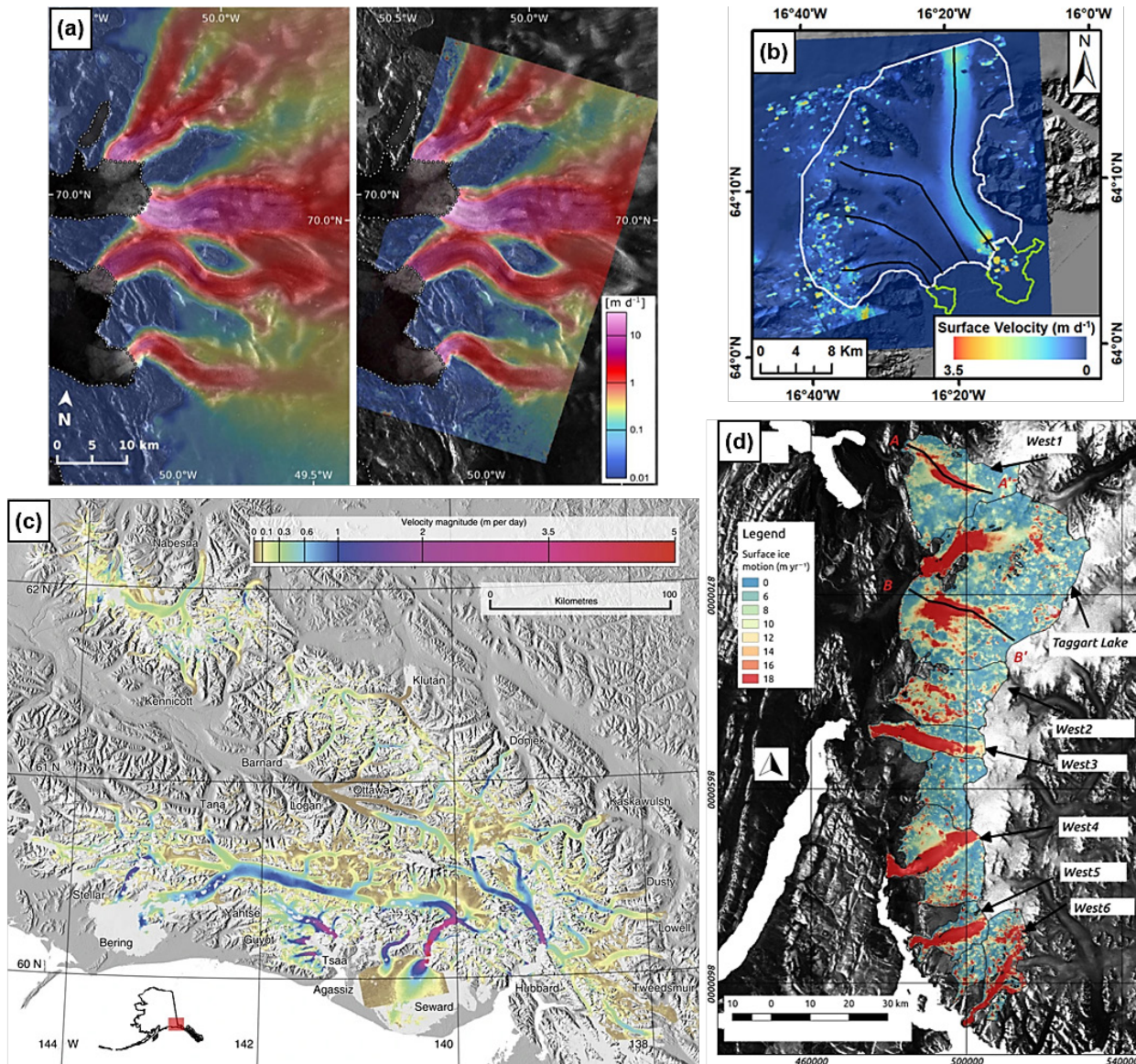


FIGURE 21 Examples of velocity products obtained in previous studies that were derived using offset tracking. (a) Northern Disko Bugt outlet glaciers, Greenland Ice Sheet, for the period 03/01 - 15/01/2015 (left) and 09/09 - 20/09/2014 (right) derived using Sentinel-1 and TerraSAR-X imagery respectively (Nagler et al., 2015); (b) Breiðamerkurjökull, Iceland, for the period 26/07 - 17/08/2012 (Baurley et al., 2020); (c) Wrangell and St Elias Ranges, Alaska, between 2007 and 2010 (Burgess et al., 2013) and (d) Western glaciers of the Prince of Wales Icefield, Canadian Arctic for the period 10/02 - 17/02/2016 (Sánchez-Gómez and Navarro, 2017). Note that this is the same glaciated region as shown in Figure 20b, but in this instance the high velocities observed in the terminus region of all the glaciers present within this portion of the Icefield have been accurately mapped using the offset tracking technique. This demonstrates how offset tracking is better suited for deriving velocities over faster moving areas of ice (e.g. near the terminus) where InSAR often fails due to loss of coherence.

Due to the variety of feature tracking algorithms and software packages now available to glaciologists, it is no surprise that it has become one of the most widely used techniques for measuring glacier velocity in recent years (Figure 22). For example, NCC has been used to investigate the velocity of ice streams in Antarctica (Scambos et al., 1992), as well as for mountain glaciers in the European Alps (e.g. Kääb, 2002; Berthier et al., 2005). Meanwhile, CCF-O and COSI-Corr have been utilised in numerous studies to investigate the velocity variations of glaciers in both the Himalaya (e.g. Scherler et al., 2008; Robson et al., 2018) and New Zealand (e.g. Herman et al., 2011; Redpath et al., 2013), amongst many others. However, despite there being several different feature tracking algorithms available, only a few studies to date have actually compared and assessed how these different algorithms perform in a variety of glacial environments (Paul et al., 2015) (Figure 23). For example, NCC has been shown to return a larger number of successful matches in comparison to other techniques over areas of high visual contrast (e.g. ablation areas), where large velocity gradients are present and over smaller glaciers when using small window sizes (Heid and Kääb, 2012a; Paul et al., 2015).

However, it is less effective at returning matches over areas of low contrast (e.g. snow-covered accumulation areas), or where there are large spatial gradients in image intensity, such as between bright snow and dark ice (Heid and Kääb, 2012a). In comparison, both CCF-O and COSI-Corr have been shown to be far less sensitive to image noise, and tend to outperform almost all other techniques in areas of high and low visual contrast, making them a far more robust method overall (Heid and Kääb, 2012a). As a result, this led both Heid and Kääb (2012a) and Paul et al. (2015) to suggest that overall no single algorithm is clearly better suited for velocity estimation in all glacial environments and circumstances, and that instead a set of two feature tracking techniques (e.g. NCC and CCF-O) should be used and combined depending on image conditions and the characteristics of the glacier being investigated.

When using optical satellite imagery and feature tracking algorithms to derive glacier velocity, several conditions must be met in order to obtain accurate displacements. Firstly, measurements of displacements using feature tracking are highly reliant on the accurate coregistration between image pairs (Kääb, 2005; Scherler et al., 2008), as well as the removal of geometric distortions from each image by means of precise orthorectification (Redpath et al., 2013; Paul et al., 2015). For the former, this is often the most important (and difficult) step, and can lead to inaccuracies in the final displacements in the order of one pixel (e.g. 15 m for ASTER images, Kääb, 2005; Scherler et al., 2008). In regard to the latter, a level of spatial uncertainty accompanies the orthorectification process, which in turn governs the accuracy with which the glacier surface displacements can be measured (Scherler et al., 2008; Redpath et al., 2013). Typically, orthorectification errors of ± 1 pixel are often sought across the two images, however, much

higher errors may arise if inaccurate DEMs are used in this process, further limiting the accuracy with which the resulting displacements can be measured (Redpath et al., 2013; Paul et al., 2015).

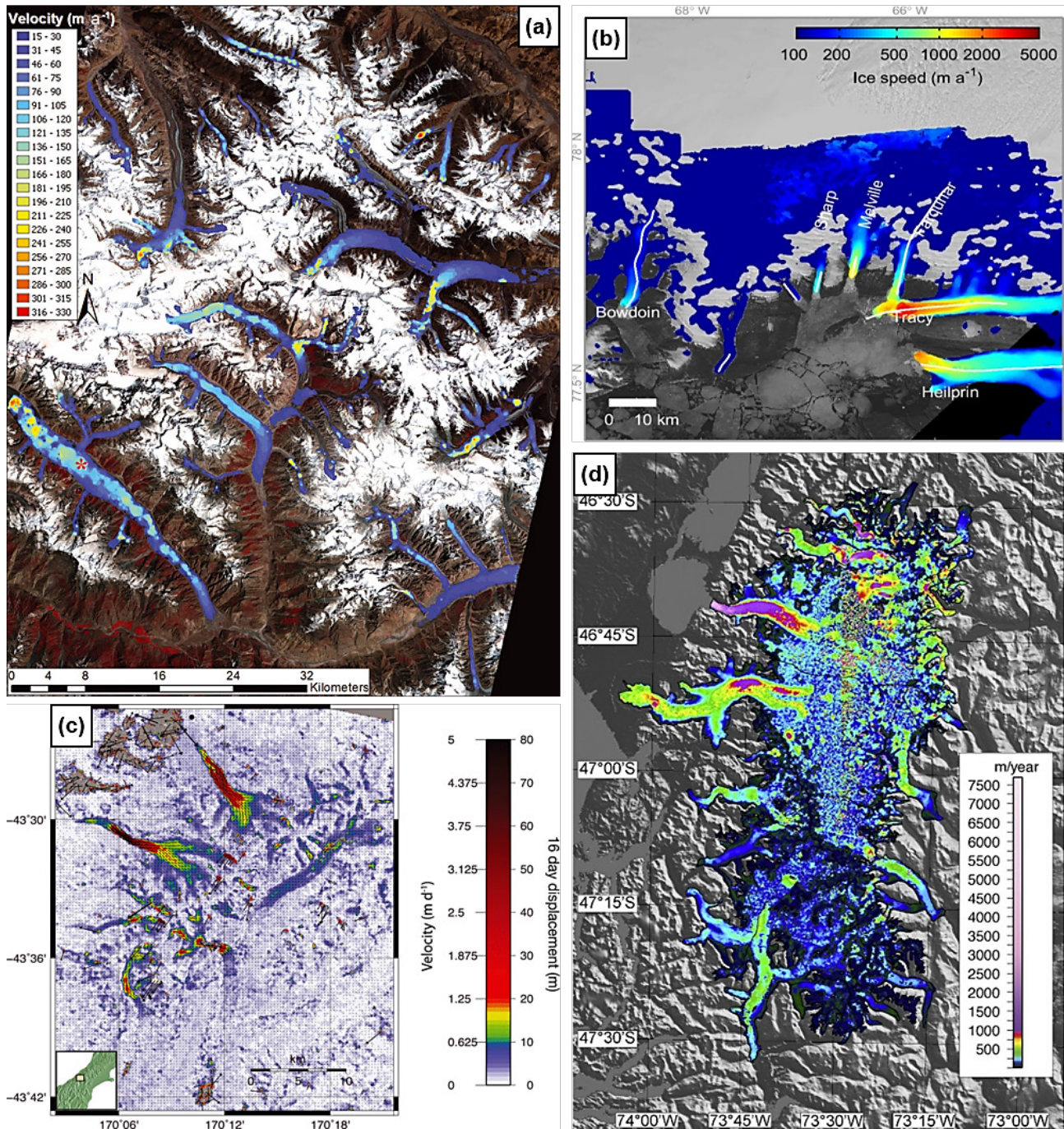


FIGURE 22 Examples of velocity products obtained in previous studies that were derived using feature tracking. (a) Central Karakoram glaciers for the period 26/07/2006 - 27/06/2007 (Copland et al., 2009); (b) Eastern glaciers of Prudhoe Land, Greenland Ice Sheet in 2014 (Sakakibara and Sugiyama, 2018); (c) Glaciers of the Southern Alps of New Zealand for the period 29/01 - 14/02/2002 (Herman et al., 2011) and (d) Composite velocity field for the Northern Patagonian Icefield, Chile, between 2000 and 2011 (Willis et al., 2011).

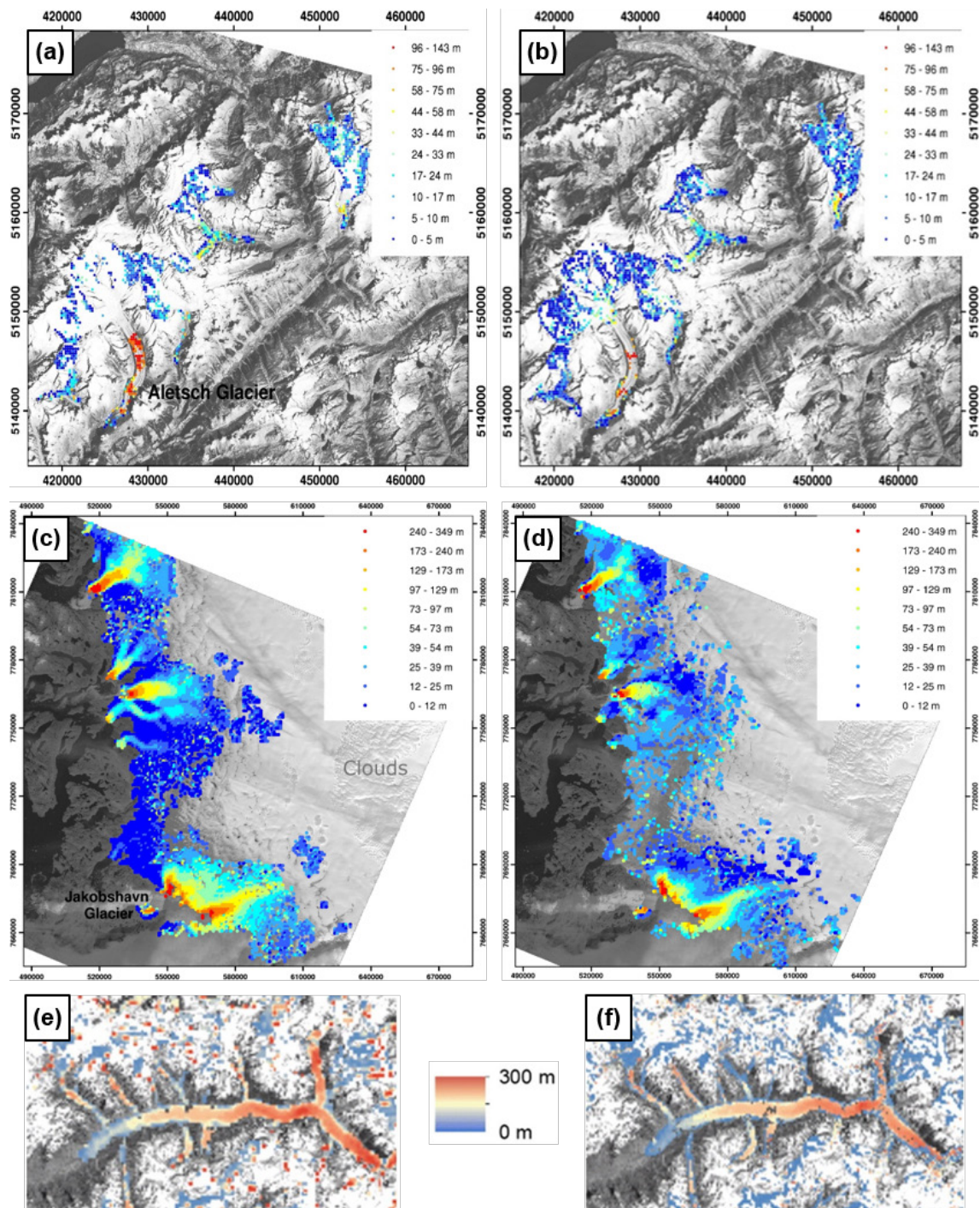


FIGURE 23 Comparison of velocity grids that were obtained using different feature tracking techniques. (a) Section of the European Alps measured using NCC for the period 12/08/2000 - 30/07/2001 (Heid and Käab, 2012a); (b) Same as (a) but using COSI-Corr (ibid); (c) Southwest section of the Greenland Ice Sheet measured using COSI-Corr for the period 07/08 - 08/08/2001 (ibid); (d) Same as (c) but using CCF-O (ibid); (e) Baltoro Glacier, Karakoram measured using NCC (no date given) (Paul et al., 2015) and (f) Same as (e), but using CCF-O (ibid). Max displacement in both (e) and (f) is 300 m a^{-1} .

Secondly, surface features have to be detectable in at least two of the repeat images in order for them to be tracked (Käab, 2005). Generally, feature tracking works best when distinct features

are present for tracking with regard to the size of the matching window and the spatial resolution of the images (Paul et al., 2017). However, the appearance of observable features may have degraded from one image to the next, which can influence the quality of the image matching correlations (Altena and Kääb, 2017a; Rieg et al., 2018). For example, such features can be changed by ice melt or surface deformation (Altena and Kääb, 2017a). In addition, fresh snowfall or cloud cover present in one image can reduce the precision of the matching process (Scherler et al., 2008; Paul et al., 2017), while fresh snow, along with shadowing, can also complicate the matching process by changing the illumination conditions between images (Altena and Kääb, 2017a; Paul et al., 2017). To address this, when velocities are high, short time spans between images (e.g. weeks to months) will often lead to better results (as it reduces the chance of surface features deforming), while when velocities are low a longer time span should be utilised (e.g. months to years) (Scherler et al., 2008; Ruiz et al., 2015). However, despite these considerations, feature tracking does provide glaciologists with a quick and efficient method for measuring glacier surface velocities at sub-pixel precision over a variety of spatial and temporal scales (Scherler et al., 2008; Redpath et al., 2013; Paul et al., 2015).

2.5.1.4 General Considerations for Implementing Offset and Feature Tracking Procedures

While offset and feature tracking both have their own sensor-specific limitations, there are also several more general considerations that are shared between the two techniques. Firstly, the spatial resolution of the sensor must be finer than the measured displacement between the two images in order for the results to be statistically significant (Kääb, 2005; Altena and Kääb, 2017a). Often, the most accurate results are obtained when using high-resolution sensors as this allows for a greater number of successful displacements to be made, both where large velocity gradients are present (e.g. near the terminus of fast-flowing glaciers), as well as over the slowest-moving areas of ice (Dehecq et al., 2015; Nagler et al., 2015; Ruiz et al., 2015) (Figure 24a and 24d). In comparison, coarser resolution sensors would most likely underestimate the measured velocity in these areas, or potentially fail to resolve any displacement measurements at all (Heid and Kääb, 2012a; Nagler et al., 2015). A final important consideration when analysing glacier velocity using either technique is that the specific algorithms used in both the offset tracking and feature tracking procedure only provide displacement estimations for the time period between image acquisitions (Strozzi et al., 2002; Paul et al., 2017). This means that the derived velocities represent the averaged value over the observation period, and as a result they cannot account for any velocity variations that occur between the dates the images were acquired, such as short-term speed up events (Quincey and Luckman, 2009; Paul et al., 2017).

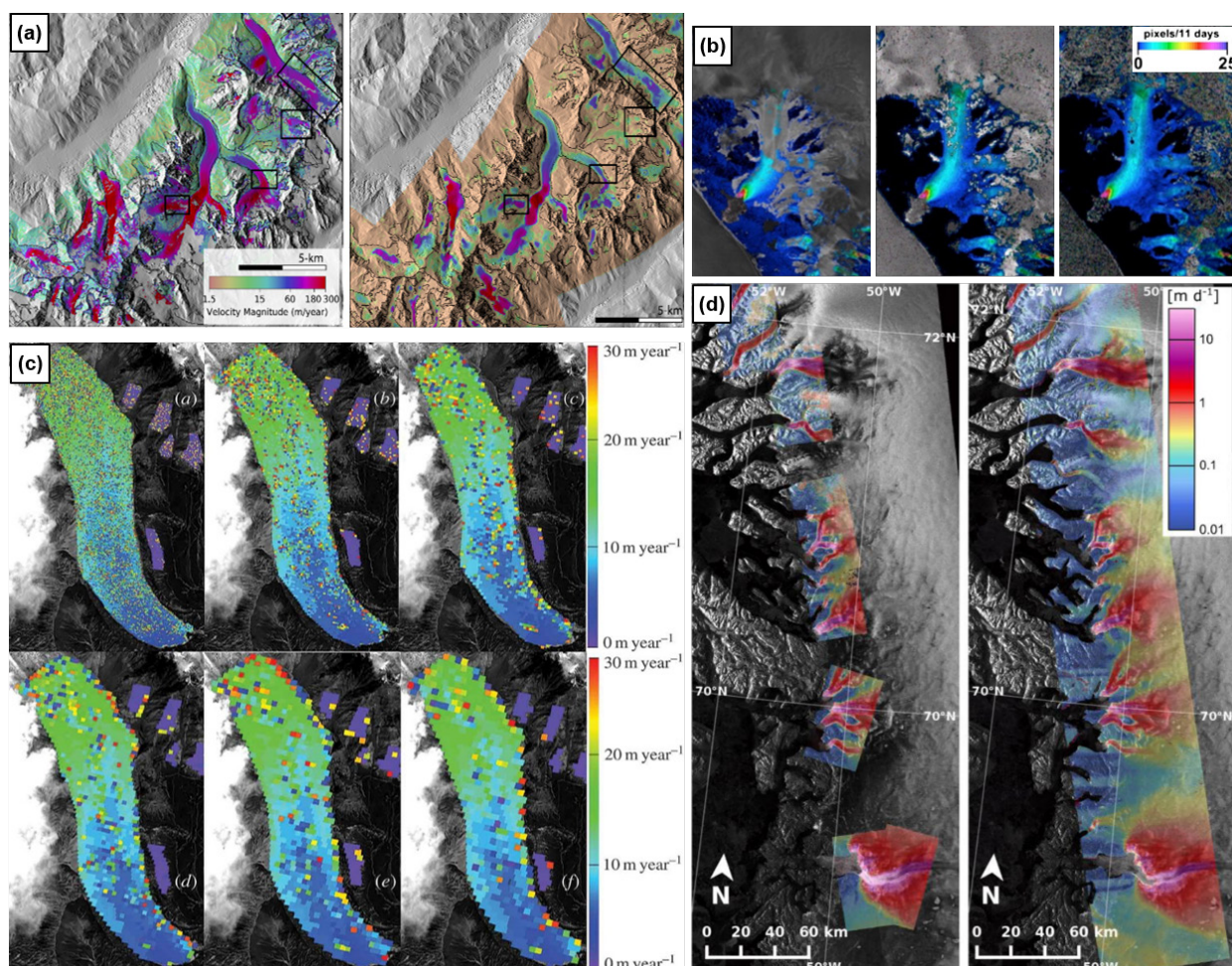


FIGURE 24 Example outputs from previous studies that have compared the influence of sensor spatial resolution and the choice of matching window size on the accuracy of satellite-derived velocity products. (a) Mont-Blanc Massif, European Alps, captured using 0.5 m resolution Pleiades imagery for summer 2018 (left), and 15 m resolution Landsat-8 imagery averaged for the period 2017-2018 (right) (Millan et al., 2019); (b) Breiðamerkurjökull, Iceland (no date), captured using different window sizes (from left to right) of 128 x 128, 64 x 64 and 44 x 40 on the same pair of TerraSAR-X images (Paul et al., 2015); (c) Keqikaer Baxi Glacier, China, for the period 09/05/2007 - 09/06/2008, captured using different window sizes on the same pair of ALOS PRISM images. The different window sizes from left to right (top row) are 10 x 10, 20 x 20 and 30 x 30, and (bottom row) 40 x 40, 50 x 50 and 60 x 60 (Huang and Li, 2011) and (d) Outlet glaciers of the west coast of Greenland, captured using 2 m resolution TerraSAR-X imagery from different epochs in December 2014 and February 2015 (left) and ~7 m resolution ALOS PALSAR imagery for the period 20/11/2009 - 05/01/2010 (Nagler et al., 2015).

2.5.2 Limitations of Investigating Glacier Velocity with Satellite Remote Sensing

However, despite the large number of satellite constellations and tracking techniques that are now available for measuring glacier velocity, several key limitations remain in the use of satellite remote sensing for the monitoring of glacier dynamics more generally. In particular, the resolution of the satellite used in a study has a direct effect on the accuracy of the final products (e.g. Nagler et al., 2015; Ruiz et al., 2015; Lemos et al., 2018b). It has been shown by Heid and Kääb (2012a) that differences in spatial resolution can enhance or suppress the features tracked in each image, meaning that displacements of different magnitudes can often result from sensors of different resolutions, even when imaging the same area. For example, where sharp velocity gradients are present, such as at the terminus or shear margins of rapidly flowing glaciers, higher-resolution sensors will be able to track such changes, whereas coarser-resolution sensors will tend to smooth these over, masking the overall signal (Joughin et al., 2018; Baurley et al., 2020). Furthermore, by utilising sub-metre resolution imagery provided by some satellite sensors such as Pleiades, researchers can often obtain highly precise velocity grids that are derived from images acquired days or weeks apart, allowing the velocities of even the slowest-moving areas of ice to be accurately quantified (Ruiz et al., 2015; Millan et al., 2019).

Indeed, while it may seem sensible, therefore, to only utilise high-resolution sensors in studies of glacier velocity, such imagery is often not freely available (e.g. TerraSAR-X, Pleiades), and as such large costs are often incurred, even for data covering a small period, which means their use in large-scale glacier monitoring is limited (Quincey and Luckman, 2009; Whitehead et al., 2013; Ruiz et al., 2015). A further limitation on the capability of satellite remote sensing for investigating glacier dynamics is that image acquisition depends on the revisit time of the satellite (its temporal resolution), which means researchers cannot expect data to be acquired on specific dates at specific times (Bhardwaj et al., 2016; Altena and Kääb, 2017b). The majority of freely available satellite sensors that are available currently have revisit times of around one week to a month (Altena and Kääb, 2017b). This means that short-term (i.e. sub-daily to daily) changes in velocity, for example those that follow supraglacial lake drainage or calving events, cannot be detected using satellite remote sensing alone (Das et al., 2008; Quincey and Luckman, 2009; Altena and Kääb, 2017b). Additional limitations stem from the fact that very few remote sensing platforms currently offer stereo-viewing capabilities. This is important for two reasons: Firstly, optical stereo images can be combined to create accurate DEMs of the glacier, and these DEMs can then be used for the precise orthorectification and coregistration of optical images acquired from different viewing angles, allowing more accurate displacements to be derived (Redpath et al.,

2013; Bhardwaj et al., 2015). Secondly, these DEMs can then also be used to obtain accurate information on geodetic mass balances, which in turn provides important information on the current dynamics of a glacier (Bhardwaj et al., 2015; Paul et al., 2015). Clearly, therefore, there is a need for publically available, high-resolution sensors to be developed for use in glaciological studies that can capture images at continuous temporal intervals to allow velocity variations to be accurately mapped at various scales (Bhardwaj et al., 2015; Millan et al., 2019; Groos et al., 2019; Bhushan et al., 2021).

2.5.3 New Developments in Satellite Remote Sensing

In recent years there has been a shift in optical remote sensing from the use of a few scenes from individual satellites towards exploitation of full constellations, which can sense the cryosphere at ever-shorter revisit times (Altena and Kääb, 2017b; Bhushan et al., 2021). In glaciology, the use of short temporal sampling times provides several opportunities, with the most important being the exploration of short-term changes in glacier flow (Fahnestock et al., 2016). To date, many studies have often utilised targeted acquisitions to focus on a specific glacier over the course of an individual season (e.g. Berthier et al., 2005; Riveros et al., 2013; Armstrong et al., 2016). However, several newly launched public and commercial earth observation constellations have been designed to source almost continuously in a non-discriminate fashion (Nagler et al., 2015; Altena and Kääb, 2017a). For example, as part of the Copernicus constellation, the Sentinel-1A and 1B SAR satellites were launched in 2014 and 2016 respectively, followed by the Sentinel-2A and 2B optical satellites in 2015 and 2017 as part of the same constellation (Kääb et al., 2016; Mouginot et al., 2017). These public satellites now provide freely available and high resolution (10 m) SAR and optical satellite data with near global spatial coverage (Kääb et al., 2016; Millan et al., 2019). Importantly, both constellations systematically acquire data at 12-day repeat intervals, and in some regions, every six days (such as toward the Poles), which has afforded more wide-scale and high resolution monitoring of glacier and ice sheet dynamics to be undertaken (e.g. Mouginot et al., 2017; Lemos et al., 2018a; Joughin et al., 2018; Millan et al., 2019) (Figure 25).

Similarly, the recent proliferation of low-cost, small imaging satellites (termed 'CubeSats') has revolutionised earth observation, with commercial constellations of inexpensive satellites now offering greater operational capacity and reduced revisit intervals than were possible previously (Bhushan et al., 2021). For example, the new Dove constellation from Planet, which consists of ~140 small satellites, has been designed to acquire world-wide high resolution (3 m) optical imagery at a near-daily basis (Altena and Kääb, 2017a,b; Planet Team, 2017; Marta, 2019). Although only a limited number of studies to date have utilised Planet imagery to derive glacier velocities (e.g. Altena and Kääb, 2017a; Steiner et al., 2018; Millan et al., 2019), the high spatial

and temporal resolution of the sensor means it can provide unique insights into short-term ice dynamical changes, such as the speed-up events that often follow complex spatial-temporal phenomena like glacier calving (Altena and Kääb, 2017a,b).

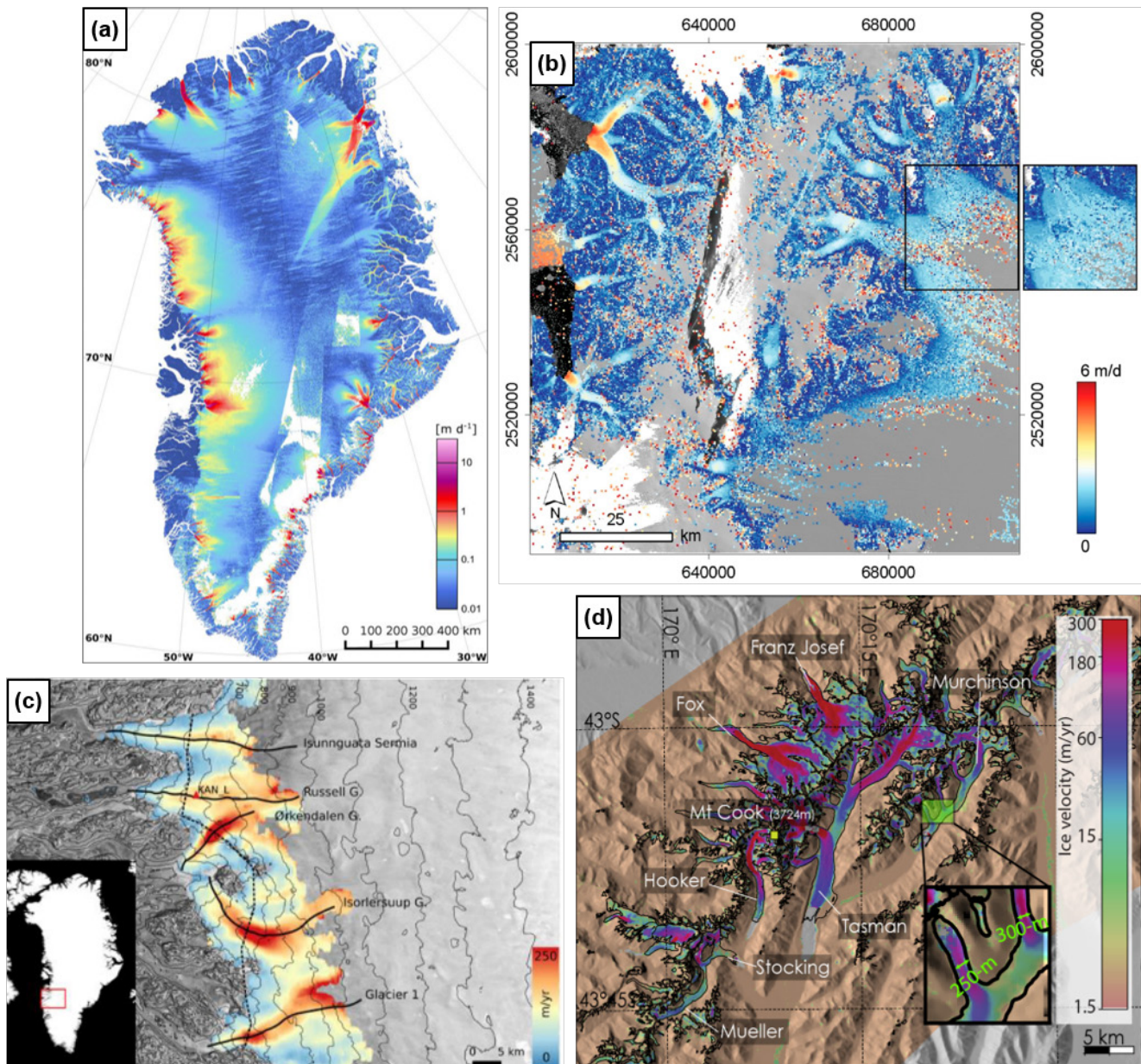


FIGURE 25 Example products from recent studies that have utilised either Sentinel-1 or Sentinel-2 imagery to derive glacier velocity. (a) Velocity map of the Greenland Ice Sheet between January and March 2015, measured using Sentinel-1A SAR imagery (Nagler et al., 2015); (b) Section of the Antarctic Peninsula (Larsen C Ice Shelf to the right of image) for the period 08/01 - 18/01/2016, measured using Sentinel-2A optical imagery (Kääb et al., 2016); (c) Average summer velocities (May-July) for the glaciers of central west Greenland between 2016 and 2017, measured using Sentinel-1 imagery (Lemos et al., 2018b) and (d) Glaciers of the Southern Alps of New Zealand between 2016-2018, measured using Sentinel-2 imagery (Millan et al., 2019).

However, the large number of satellites in orbit means that repeat imagery of the same area is very often acquired at different viewing angles, which require the use of sufficiently high resolution DEMs for accurate image orthorectification (Millan et al., 2019; Bhushan et al., 2021). Only then can high-quality glacier velocity maps be produced using this imagery (Millan et al., 2019). Furthermore, despite being captured at daily intervals, extensive cloud cover in glaciated regions can inhibit the use of many images, potentially resulting in a time series of imagery with a highly inconsistent temporal repeat interval (Altena and Kääb, 2017b). Although these limitations are important to consider, commercial constellations like Planet do show clear potential in glacial research for glacier velocity mapping, and when combined with large-scale acquisitions like Sentinel-2 can supplement records of glacier dynamics at even finer spatial and temporal scales (Millan et al., 2019; Bhushan et al., 2021).

Overall, however, several challenges remain in the use of satellite remote sensing for the systematic monitoring of many glaciers worldwide (Whitehead et al., 2013; Bhardwaj et al., 2015; Millan et al., 2019). These relate to the current availability of public and commercial satellites for glaciological research, the spatial resolution of the sensor in question and the temporal baseline between image acquisitions (Bhardwaj et al., 2016; Altena and Kääb, 2017a; Yang et al., 2020). As a result, satellite remote sensing is, at present, unable to fully provide accurate, complete and in-depth information on the complex dynamic changes currently underway at many calving and non-calving glaciers worldwide, which are occurring in response to both climatic, and non-climatic forcing (Berthier and Vincent, 2012; Ryan et al., 2015; Wigmore and Mark, 2017; Groos et al., 2019).

2.6 Repeat UAV Surveys of Glacier Velocity

2.6.1 Terrestrial Photogrammetry

While satellite remote sensing suffers from the drawbacks related to the coarse spatial resolution of its sensors, and to the varying repeat intervals that lead to uncertainties over temporal resolution, there is a need to develop and employ other methods with which to accurately measure and monitor glacier change and dynamics (Bhardwaj et al., 2016; Rossini et al., 2018; Juvet et al., 2020) (Figure 26). Laser scanning methods, such as terrestrial (TLS) and airborne (ALS) laser scanning provide high resolution 3D glacier surface changes over a wide range of spatial scales at high spatial resolutions (Brasington et al., 2012; Piermattei et al., 2015). However, both methods suffer from high operational costs, while TLS in particular requires specific training to be utilised correctly, and incurs substantial logistical costs when measuring in remote and hard

to access regions (Westoby et al., 2012; Cook, 2017). As such, this limits their usage and makes them an unattractive and unfeasible option for those studies undertaking research in mountainous and remote areas.

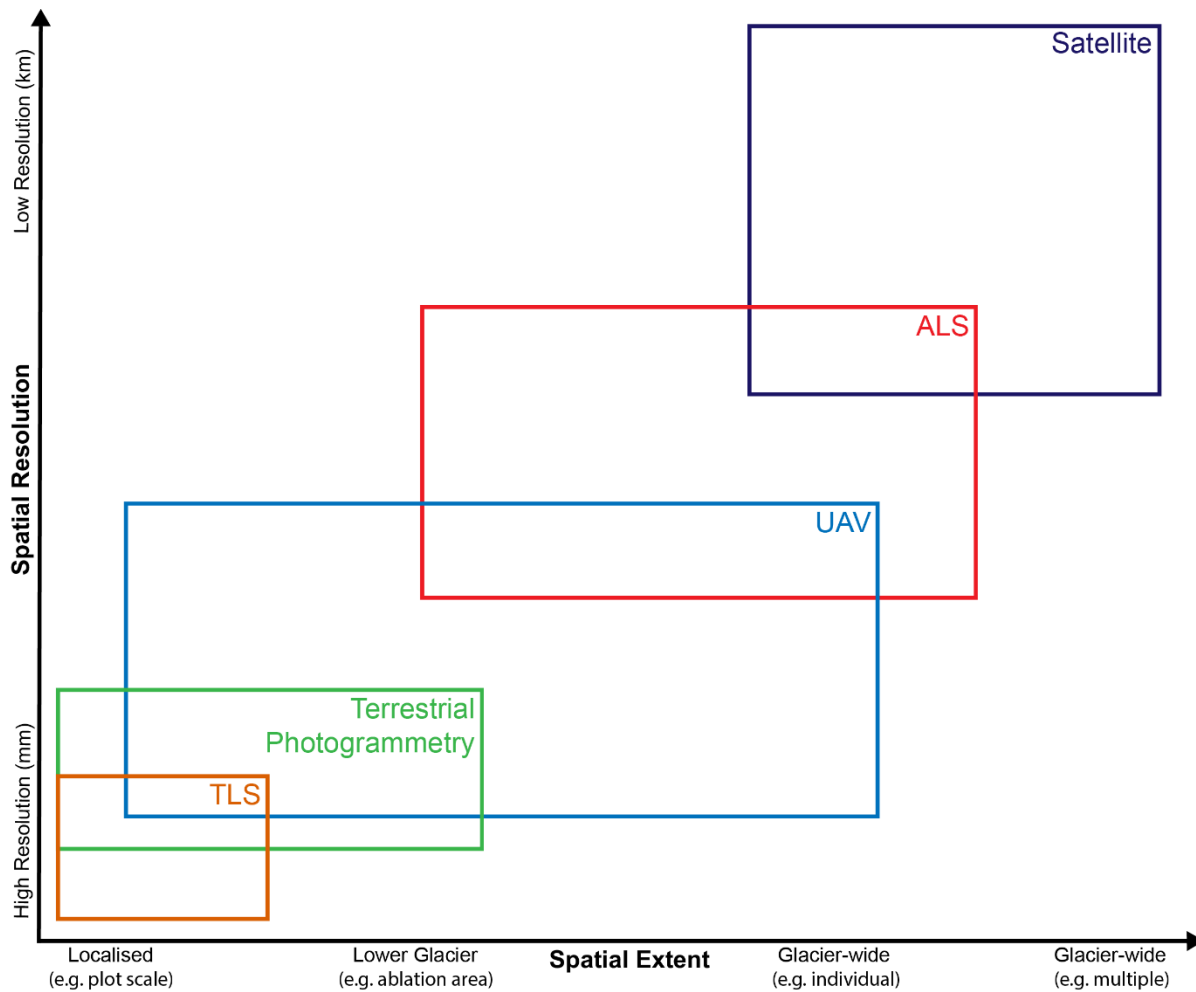


FIGURE 26 Conceptual diagram comparing typical spatial resolution against spatial extent of the most commonly used methods in glaciology for measuring glacier change. The plot was inspired by a similar concept developed in Figure 2 of Tomsett and Leyland (2019).

An alternate methodology that can accurately measure glacier surface change is ground-based photogrammetry, a multi-image technique that extracts 3D geometry from a 2D static scene, which can then be used to create high quality surface models (Eltner et al., 2015; Piermattei et al., 2015). Although extensively applied in several geomorphological studies in the 1980s and 1990s (e.g. Welch et al., 1984; Lane et al., 1993; Kääb and Funk, 1999), such traditional photogrammetric techniques required specialised training and equipment for the creation of these detailed surface models (Karpilo, 2009), which limited their use for non-specialists (Piermattei et al., 2015).

Over the last 15 years, however, there has been a resurgence in the use of terrestrial photogrammetry due to a number of technological advances in the field (Kaufmann and Seier, 2016; Fugazza et al., 2018). The slow and manual data acquisition phase has now become fully

automated, meaning digital photogrammetry has become a powerful and widely used tool for the generation of high resolution datasets and digital elevation models (DEMs) (Westoby et al., 2012; Irvine-Fynn et al., 2014; Fugazza et al., 2018). These advances have been aided by improvements in the cost and quality of compact and single lens reflex cameras with ever-increasing resolution (Heng et al., 2010; Irvine-Fynn et al., 2014), as well as in the development of automated camera calibration software which have simplified the extraction of relevant parameters that describe the internal camera geometries, which is needed for accurate data acquisition (Fryer et al., 2007; Sanz-Ablanedo et al., 2012). These factors combined have facilitated the development of Structure-from-Motion photogrammetry (SfM), a high-quality approach that is ideally suited for low-budget research and application in remote areas (James and Robson, 2012; Piermattei et al., 2015).

2.6.2 Structure-from-Motion (SfM) Photogrammetry

2.6.2.1 Background

SfM is a low cost, non-selective and non-specialist survey method which allows the automated production of high-resolution topographic reconstructions from multiple overlapping photographs which are captured by consumer-grade cameras moving around a scene of interest (Fisher et al., 2013; Piermattei et al., 2015) (Figure 27). Although 360° coverage is not always necessary, it is recommended as it leads to much higher resolution outputs (Smith et al., 2016). As such, photos are often taken horizontally and obliquely, as well as with >60% overlap between consecutive images to maximise accurate 3D reconstruction (Favalli et al., 2012; Westoby et al., 2012). The technique has its origins in the computer vision community (e.g. Spetsakis and Aloimonos, 1991; Boufama et al., 1993), and in the development of automatic feature-matching algorithms the decade prior (e.g. Förstner, 1986). Indeed, as discussed previously, SfM operates under the same basic principles as traditional stereoscopic photogrammetry through the need for multiple overlapping images for scene reconstruction (Westoby et al., 2012; Micheletti et al., 2015). However, it differs fundamentally from traditional methods in that the scene geometry, camera positions and orientations are solved automatically without the need to specify a priori of target networks with known 3D positions (Westoby et al., 2012; Smith et al., 2016).

Instead, by utilising a highly redundant, iterative bundle adjustment procedure, which is based on a database of features automatically extracted from a set of multiple overlapping images, this information can be solved quickly and simultaneously (Lowe, 2004; Snavely, 2008; Westoby et al., 2012). This then allows image-mapping algorithms to calculate and create a high quality, 3D point cloud of the surveyed object or scene, which is given in an arbitrary coordinate system by default

(Javernick et al., 2014; Piermattei et al., 2015; Kraaijenbrink et al., 2016). From this, high resolution orthomosaics and DEMs can be generated which are of similar quality (cm-dm scale) to those outputs obtained from other surface reconstruction techniques such as LiDAR and TLS (Doneus et al., 2011; Tonkin et al., 2014).

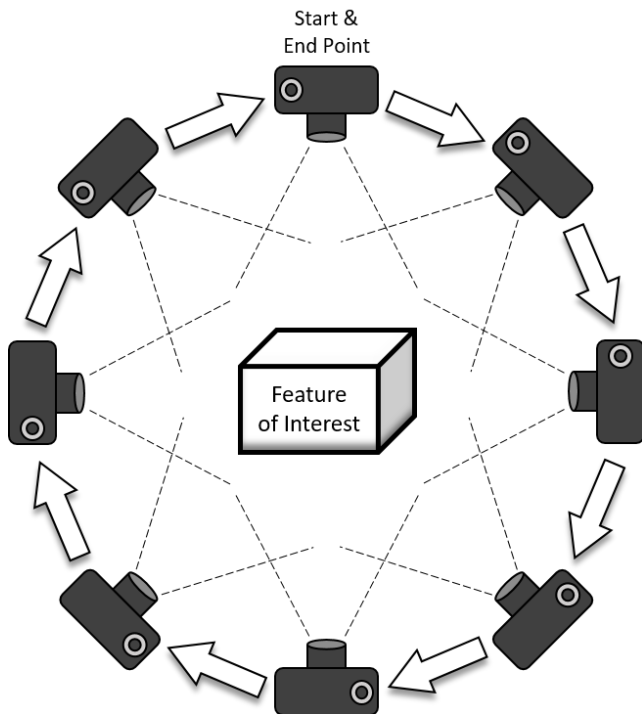


FIGURE 27 Structure-from-Motion photogrammetry, which requires multiple, overlapping photographs to be taken around the scene of interest from which 3D surface models can then be generated. Reproduced from Westoby et al. (2012).

The SfM processing workflow has been particularly popularised in recent years due to the development of a range of user-friendly and relatively low-cost cloud-processing software engines such as Microsoft Photosynth and Agisoft Metashape (previously Agisoft PhotoScan), which automatically solve the SfM algorithms for the user (Micheletti et al., 2015; Piermattei et al., 2015). Furthermore, because consumer-grade cameras are utilised to collect the data, it provides users with a high degree of choice when it comes to survey design, depending on their budget, study area and required survey resolution. For example, data can be collected by walking around a scene of interest and taking photos by hand (e.g. Smith et al., 2014; Piermattei et al., 2015), by attaching the camera to a blimp or kite (e.g. Verhoeven et al., 2009; Vericat et al., 2009) or by using UAV platforms which can carry additional payloads in addition to a high-quality camera (e.g. Tonkin et al., 2014; Rippin et al., 2015; Cook, 2017). As such geomorphologists have been quick to adopt SfM in their research, which is highlighted by the ever-increasing number of studies over recent years that have utilised this methodology (e.g. James and Robson, 2012; Lucieer et al., 2014; Javernick et al., 2014; Frankl et al., 2015). Due to the high level of automation involved in

the SfM processing stages, it is not unusual for SfM users to not have a full or clear understanding of the individual workflow stages, nor the overall workflow itself (Smith et al., 2016). Indeed, a key advantage of the SfM methodology over similar methods such as TLS is that it enables non-specialists to produce highly accurate DEMs and orthomosaics, without requiring any prior knowledge of photogrammetric techniques (James and Robson, 2012; Eltner et al., 2015). However, that said, an understanding of the full SfM workflow is particularly useful for physical geographers as it allows them to be able to identify and minimise potential sources of error in the resulting topographic data (Smith et al., 2016). As a result, the typical SfM workflow will be detailed in the following section.

2.6.2.2 *The SfM Workflow*

The typical SfM workflow utilised by many software packages is outlined and summarised in Figure 28. Although the exact specifics of the workflow will evidently vary between the different software packages, a distinct commonality does exist between them (Smith et al., 2016). As such, each step of the SfM workflow will be presented in detail below, with particular emphasis on identifying and removing potential error sources at each stage of the processing chain. For more detail regarding the mathematical operations applied during these processes, readers are directed towards sources such as Lowe (2004), Snavely (2008) and Szeliski (2010).

1) Feature Detection

The first stage in the process is the identification of key features or 'keypoints' in the images, which may then be used for image correspondence (Westoby et al., 2012). Although a number of feature detection algorithms exists (e.g. Bay et al., 2008; Morel and Yu, 2009), the most widely used is the Scale Invariant Feature Transform (SIFT) object recognition system (Lowe, 1999, 2004; Snavely, 2008). This method identifies features in every image, regardless of the image scaling and rotation, while also being partially invariant to changes in 3D camera viewpoint and illumination conditions (Lowe, 2004; Westoby et al., 2012; Smith et al., 2016). Such keypoints are identified automatically over all scales and locations in each of the images, before a unique feature descriptor is assigned which is computed through the transformation of local image gradients into a visual representation that is largely insensitive to changeable illumination conditions and orientation (Lowe, 2004; Westoby et al., 2012). The number of keypoints identified during this process is primarily controlled by the image texture and resolution, so that often the most complex images at the highest (original) resolution will return the most results (Westoby et al., 2012).

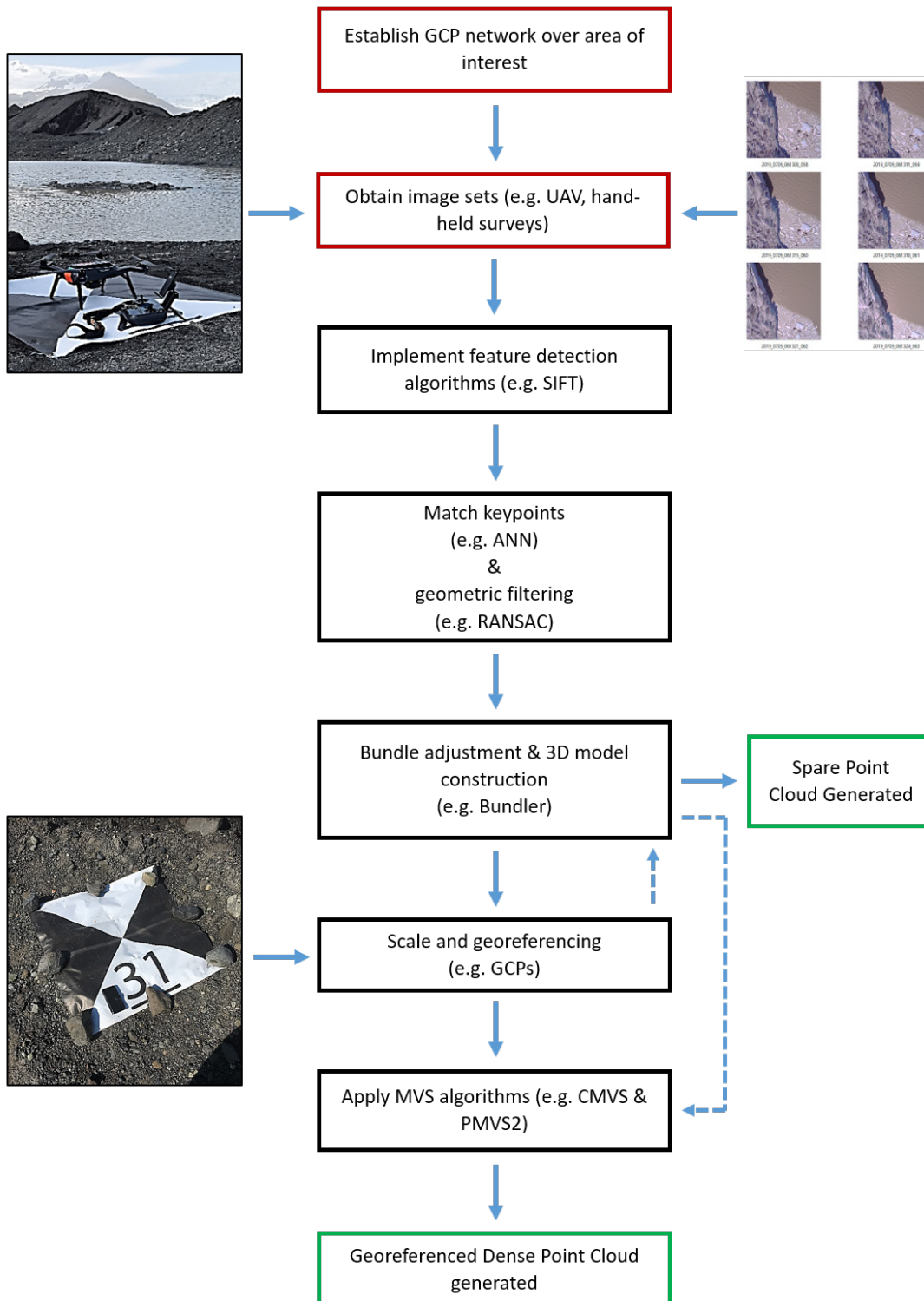


FIGURE 28 Typical SfM workflow for the production of georeferenced dense point clouds using image sets and ground control points. Red boxes represent inputs required for SfM, black boxes represent different stages of the SfM workflow whilst green boxes represent model outputs.

Therefore, the resolution of the resulting point cloud will be determined by the density, sharpness and resolution of the images, as well as the range of textures present in the natural scene being imaged (James and Robson, 2012; Westoby et al., 2012). Usually, features such as edges or other highly textured, geometrical similarities in the images are detected by the SIFT algorithms

particularly well (Verhoeven, 2011). As such, it is advisable to ensure the scene being photographed is sufficiently textured to ensure the highest number of identified keypoints, and to take a large number of photographs of the scene to ensure a high number of keypoints matches to give the best results (Westoby et al., 2012). Not doing so can result in poor model construction and system redundancy.

2) Keypoint Correspondence and Geometric Filtering

The next step is to identify and match keypoints that appear within multiple images, and, because there is no guarantee that each keypoint will be present in each image, the computer software applies a threshold with which to identify matches (Smith et al., 2016) (Figure 29a). This increases the chance of all keypoint matches being successfully identified in all the images (Snavely, 2008). Such a process would be computationally demanding, however, so the Approximate Nearest Neighbour (ANN) algorithm is applied as an efficient and approximate solution to this problem, reducing computational time whilst still obtaining a high number of keypoint matches (Arya et al., 1998; Smith et al., 2016). This process does also filter out some erroneous matches from the overall dataset, increasing final output quality.

Following application of the ANN algorithm, a further filtering stage is then applied to attempt to identify and remove any remaining erroneous matches. Taking any image pair with matching keypoints, a fundamental matrix (F-matrix) can be calculated using the Eight Point algorithm (Longuet-Higgins, 1981). The F-matrix specifies the relationship between the images while also reconstructing the scene up to a projective transformation where all points lying on a single line should remain aligned in this way (Smith et al., 2016). Following this, the RANdom SAmple Consensus (RANSAC) algorithm is used to evaluate all the F-matrices (Fischler and Bolles, 1981). This algorithm randomly samples the keypoints used in the construction of the F-matrix and calculates the difference between the returned F-matrix and that returned by the other sampled keypoints (Smith et al., 2016). Beyond a set threshold, the returned keypoint is considered an outlier and is not considered part of the model fit. Following subsequent sampling and refinement of each F-matrix, all outliers are removed (Smith et al., 2016). Using such a method means that transient features, such as people moving across the scene of interest, are automatically removed from a dataset before 3D model construction begins, ensuring the final outputs are of sufficient quality (Snavely et al., 2008; Westoby et al., 2012).

3) Structure-from-Motion (Bundle Adjustment)

Following the feature matching and filtering stages, SfM utilises and applies an iterative bundle adjustment procedure named Bundler to the dataset (Ullman, 1979; Snavely et al., 2008). This is

carried out in three stages. Firstly, the camera extrinsic parameters (i.e. the position of the camera at the time of image acquisition) are calculated automatically using a similarity transform (Verhoeven, 2011; Westoby et al., 2012) (Figure 29b). Secondly, the internal camera parameters (i.e. focal length, lens distortion and principal point) are also calculated automatically (Verhoeven, 2011; Javernick et al., 2014). Finally, triangulation is utilised to estimate the 3D point positions and incrementally reconstruct scene geometry resulting in the creation of a sparse point cloud representing the 3D structure or geometry of the scene, fixed into a relative coordinate system (Verhoeven, 2011; Westoby et al., 2012; Javernick et al., 2014) (Figure 29c).

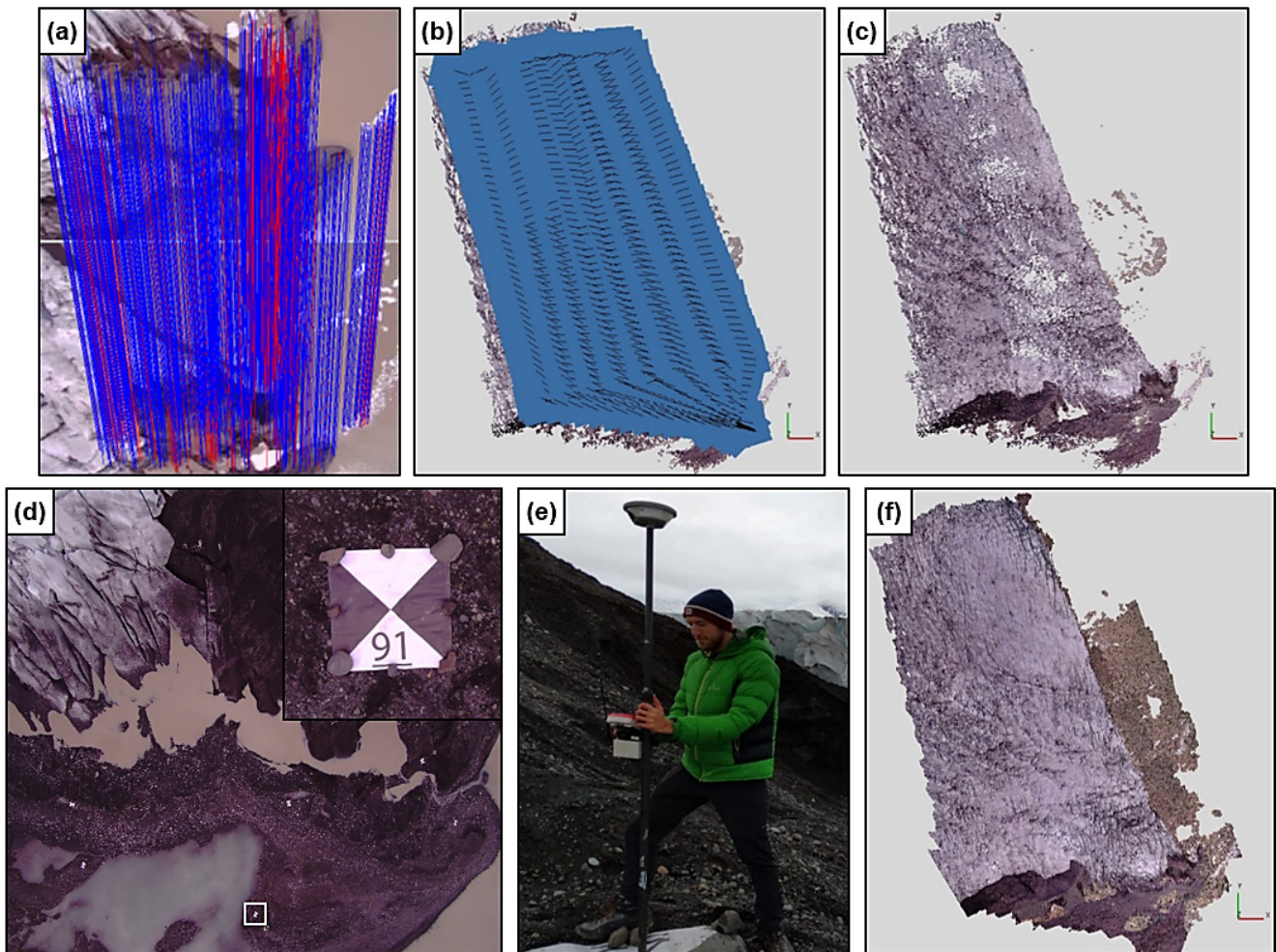


FIGURE 29 Key aspects from different stages of the SfM workflow. (a) Example of the successful (blue) and unsuccessful (red) matches identified during Stage 2 of the SfM workflow for two UAV images acquired 7th July 2019. (b) Estimated camera positions calculated by the Bundler algorithm during Step 3 of the SfM workflow. Background is the sparse point cloud from 7th July 2019. (c) Sparse point cloud created during Stage 3 of the SfM workflow for 7th July 2019. (d) UAV image from 19th September 2019 showing several GCPs spread over a portion of the study area for use in Stage 4 of the SfM workflow. Inset shows a close-up of one of these GCPs, which is 1x1 m in size. (e) Measuring the position of one of the GCPs in the field using dGPS. (f) Dense point cloud from 7th July 2019 produced using MVS image mapping algorithms in Stage 5 of the SfM workflow.

Although errors are present in this process, for example those errors resulting from the projection of individual image features in the object space (re-projection errors) (Szeliski, 2010), these are generally minimised by utilising a least-squares solution (Szeliski and Kang, 1994; Westoby et al., 2012). Full automation of the bundle adjustment procedure, from keypoint extraction to accurate scene reconstruction, is a key advantage of the SfM methodology over traditional photogrammetric techniques (Westoby et al., 2012). A further key advantage of the process is that SfM does not require the 3D location or orientation of the camera at image capture, nor the 3D location of control points to be known prior to scene reconstruction (Verhoeven et al., 2012; Javernick et al., 2014; Smith et al., 2016), allowing the rapid production of high-quality 3D reconstructions (Westoby et al., 2012; Smith et al., 2016).

4) Scale and Georeferencing using Ground Control Points

The resulting point cloud is presented in an unscaled arbitrary coordinate system, so to align this output to absolute real-world coordinates, a 3D seven parameter linear similarity transform is used (three translation, three rotation, one scaling) (James and Robson, 2012; Dandois and Ellis, 2013). This similarity transform is based upon a small number of ground control points (GCPs) with known coordinates (Doneus et al., 2011; Westoby et al., 2012). GCPs are fixed markers clearly identifiable and well-represented between the different images, the accurate locations of which are often obtained by ground survey using dGPS (Westoby et al., 2012; Javernick et al., 2014; Micheletti et al., 2015) (Figure 29d and 29e). These can either be high contrast physical markers placed in the field with a clearly defined centroid or clear, static features in the scene of interest which are sampled ad-hoc, after confirming their presence in the resulting point cloud, such as large boulders (Westoby et al., 2012; Smith et al., 2016).

At least three GCPs are required to scale and georeference the SfM-derived point cloud, however, a much larger number is recommended, and in practice the GCPs should cover the whole extent of the survey area (James and Robson, 2012; Javernick et al., 2014) and be well distributed throughout it (James and Robson, 2012; Smith et al., 2016). Not doing so will likely negatively influence final model quality as more, well distributed GCPs provide a more robust solution which is less sensitive to error on any one point (James and Robson, 2012; Westoby, et al., 2012). Conversely, if the GCPs are only placed covering a sub-section of the entire scene, then georeferencing errors will increase across the reconstruction with distance from the GCP locations (James and Robson, 2012; Micheletti et al., 2015).

Nonetheless, the identification of GCPs and the input of their coordinates is a key step as it provides important additional information of the 3D scene geometry (Westoby et al., 2012; Javernick et al., 2014). This can be used to further refine estimates of the intrinsic camera

parameters as well as the reconstructed scene geometry (Smith et al., 2016). Furthermore, the GCP coordinates (and estimates of their point error) provide an additional source of error in the minimisation of the non-linear cost function during the bundle adjustment step, as outlined in stage 3 (Smith et al. 2016). Consequently, with this new information now included in the model, the bundle adjustment procedure can be re-run to optimise the image alignment based upon the GCP coordinates (Javernick et al., 2014). In this process, the sum of the re-projection error and the georeferencing error can now be minimised in the new output, assuming the GCPs were set up in a well-distributed manner across the whole survey area (Smith et al., 2016). If this was not the case, then the effectiveness of this re-alignment process will be reduced (James and Robson, 2012; Micheletti et al., 2015).

5) Dense Point Cloud Generation

Up to this stage, the bundle adjustment package used in Bundler (Lourakis and Argyros, 2009) has produced a sparse point cloud (Westoby et al., 2012). To obtain an enhanced density point cloud, however, Multi-View stereo (MVS) image mapping algorithms need to be applied to the now georeferenced and scaled 3D output (Smith et al., 2016) (Figure 29f). The MVS process usually increases the density of the point cloud by at least, but often in excess of, two orders of magnitude (Westoby et al., 2012; Smith et al., 2016). A dense point cloud can be derived by applying the Clustering View for Multi-View Stereo (CMVS) (Furukawa and Ponce, 2009), followed by the Patch-based Multi-View Stereo (PMVS2) algorithms (Furukawa et al., 2010). In this stage, the camera positions derived from Bundler are used as an input to the dense point cloud creation. Next, the CMVS algorithm decomposes overlapping input images into clusters or subsets of manageable sizes that are then run through the dense reconstruction separately (Furukawa et al., 2010; Westoby et al., 2012). This reduces overall computational time while also permitting a larger number of images to be processed within a given run time (Dietrich, 2016; Smith et al., 2016). The PMVS2 algorithm is then applied to independently reconstruct the 3D data from each of the individual clusters (Furukawa and Ponce, 2009; Westoby et al., 2012). The PMVS2 algorithm is a commonly applied method in physical geography, and, when compared to other MVS algorithms, performs very well (Ahmadabadian et al., 2013; Smith et al., 2016). Importantly, feature matching using PMVS2 requires reliable textural information, and if this is not present then this may result in gaps in the final model (Smith et al., 2016). Once features are matched, patches are then grown around the identified matches before visibility constraints are then utilised to filter out any outlier patches (Furukawa and Ponce, 2009; Smith et al., 2016).

The resulting dense point cloud can then be exported for analysis or indeed processed further in a number of SfM software packages to obtain a dense surface reconstruction called a mesh

(Javernick et al., 2014). From this textured mesh, high resolution DEMs and orthomosaics of the surface of interest can also be generated, which are often the desired output as they provide geomorphologists with additional information which can be beneficial in a number of applications (Smith et al., 2016).

2.6.2.3 *Potential SfM Limitations*

However, despite the clear advantage of using SfM in geomorphological applications over traditional photogrammetric methods, the quality of the final output, whether that be a dense point cloud or DEM, is strongly dependent on a variety of factors present at the time of image acquisition (Bash et al., 2018; Fugazza et al., 2018). These may be determined by the environment itself, for example smooth surfaces, lack of texture and shadowing, or they may be user controlled, for example through the survey design or the GCP number, location and distribution. A number of these key factors and their influence upon the quality of the final SfM-derived 3D outputs will be discussed in detail below.

In SfM photogrammetry, the quality of the generated point cloud is primarily controlled by the texture, sharpness and resolution of the input images, which influence the performance of the dense matching algorithms (Dall'Asta, et al., 2015; Fugazza, et al., 2018). Image texture in particular is the most important control on the density and quality of the generated point clouds (Westoby et al., 2012; Smith et al., 2016). This is because deriving 3D information from images depends on the ability of the SfM algorithms to identify common features present in multiple images taken of the same scene (James and Robson, 2012). Unsurprisingly, this process is influenced by the presence of distinctly detectable features in the surveyed object and the captured images, i.e. how textured the object is and how well this texture is displayed in the images (Fonstad et al., 2013; Piermattei et al., 2015).

According to the SfM technique, images that exhibit enhanced texture enable the extraction of reliable features and, therefore, the detection of numerous matching points, which in turn creates better camera alignment and higher spatial coverage of the reconstructed model (Verhoeven, 2011; Piermattei et al., 2015). Studies by Bemis et al. (2014) and Gómez-Gutiérrez et al. (2014) have shown the negative influence that poor or variable image texture, as well as shadowing and surface reflection, can have on the 3D quality and accuracy of SfM models. Examples of texturally poor surfaces include fresh snow cover (Irvine-Fynn et al., 2014; Tonkin et al., 2014), fine debris (Piermattei et al., 2015; Cook, 2017), clean ice (Smith et al., 2016; Gindraux et al., 2017), and sparse vegetation (Cook, 2017). It is, therefore, highly advisable to ensure the object or scene being photographed has sufficient texture to ensure the highest possible quality of model output (James and Robson, 2012).

A further control on point cloud quality is the resolution of the captured imagery, otherwise known as the ground sampling distance (GSD), which is controlled by the distance between the camera and the feature of interest (Gindraux et al., 2017; Bash et al., 2018). A low or small GSD will lead to an increase in the spatial resolution of the acquired imagery, which in turn will enhance the spatial density and resolution of the final point cloud while simultaneously reducing the error (Westoby et al., 2012; Gindraux et al., 2017; Sanz-Ablanedo et al., 2018) (Figure 30).

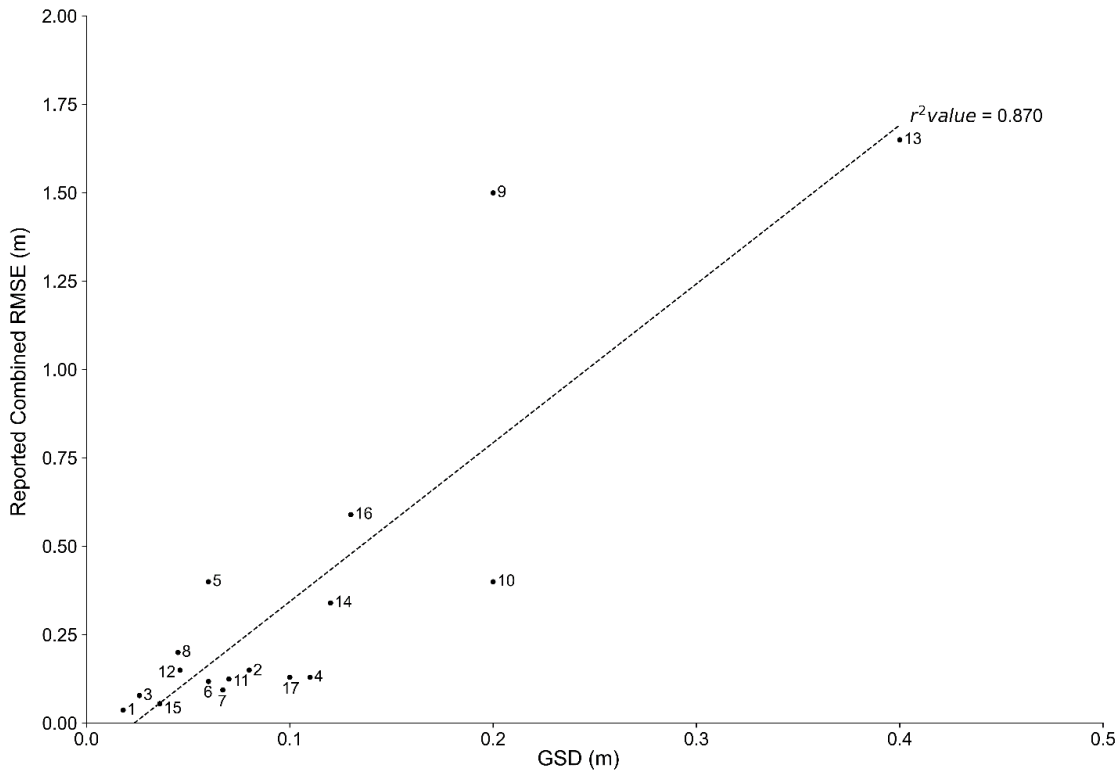


FIGURE 30 Relationship between GSD (survey image resolution) and final model RMSE (based off reported horizontal and vertical accuracies) for those studies within glaciology to date that have utilised UAV surveys. The numbers alongside the data points refer to the publications from which data were extracted for the plot. Although the majority of studies undertook multiple surveys, only the mean of the GSD and RMSE values they report are plotted here, as these values did not vary significantly between the multiple surveys undertaken in each individual study. The exception to this is the study of Juvet et al. (2019) which report large differences between their surveys due to the inclusion of accurate RTK positioning: 1. Bash et al. (2018); 2. Benoit et al. (2019); 3. Chandler et al. (2020); 4. Chudley et al. (2019); 5. Fugazza et al. (2018); 6. Gindraux et al. (2017); 7. Groos et al. (2019); 8. Immerzeel et al. (2014); 9. Juvet et al. (2019) no RTK; 10. Juvet et al. (2019) with RTK; 11. Kraaijenbrink et al. (2016); 12. Rossini et al. (2018); 13. Ryan et al. (2015); 14. Whitehead et al. (2013); 15. Wigmore and Mark (2017); 16. Xue et al. (2021); Yang et al. (2020). Note only those studies that utilised accurate ground control are plotted here: some studies utilised a low GSD but no ground control, resulting in RMSEs of >2 m which when plotted alongside the other data points here negatively skewed the linear correlation.

GSD is particularly important when acquiring images from an airborne platform, such as via UAV or a small plane, as a lower flying height will lead to a smaller GSD which can improve automatic tie-point location in the SfM process and decrease errors in manually locating GCP target centres (Wigmore and Mark, 2017; Bash et al., 2018). This can result in point clouds of an extremely high accuracy, particularly in the vertical dimension. For example, Bash et al. (2018) obtained vertical accuracies of a few centimetres with a GSD of ~ 0.018 m, resulting in high quality final models, illustrating the importance of GSD in the SfM process. However, in the majority of studies when designing a survey, it is often preferable to fly at a higher GSD to obtain greater spatial coverage and horizontal resolution at the expense of the vertical (Ryan et al., 2015; Bash et al., 2018). Even so, many studies have still obtained dm-scale vertical accuracies, despite flying at a higher GSD (e.g. Javernick et al., 2014; Jouvét et al., 2019; Yang et al., 2020). Therefore, although desirable, implementing a low GSD during survey design is not a fundamental requirement for the generation of high-resolution 3D models.

The accuracy of the 3D models generated through the SfM workflow are strongly controlled by the number and the distribution of the GCPs used to georeference the acquired imagery (Kääb et al., 2014; Gindraux et al., 2017). As mentioned previously, GCP number and distribution is important for determining final model quality, whereby a large number of GCPs well distributed across the survey area should be utilised (James and Robson, 2012; Smith et al., 2016; Yang et al., 2020). Numerous studies have demonstrated that DEMs georeferenced in this way are much more accurate than those DEMs georeferenced by few GCPs that are clustered together (Tahar et al., 2012; Tonkin et al., 2014; Shahbazi et al., 2015; Gindraux et al., 2017) (Figure 31). This is because a greater number of GCPs allows for a reduction in the bundle adjustment error, allowing for more robust georeferencing (James and Robson, 2012; Gindraux et al., 2017). However, it is worth noting that increasing the number of GCPs will only increase DEM accuracy up to a certain point, after which no further increase in accuracy is observed (Tonkin et al., 2014; Gindraux et al., 2017).

Furthermore, GCPs should be placed towards the edges of the survey region so that the coordinate transformations are not extrapolated outside the volume encompassed by the control, which can result in doming or 'fishbowling' of the DEM to occur (James and Robson, 2014; Wigmore and Mark, 2017). Finally, GCPs should also cover a good range of values in each spatial dimension (Smith et al., 2016). Unsurprisingly, undertaking photogrammetric surveys using a small number of GCPs in a clustered network is not recommended as it can lead to DEMs of insufficient quality (Sanz-Ablanedo et al., 2018).

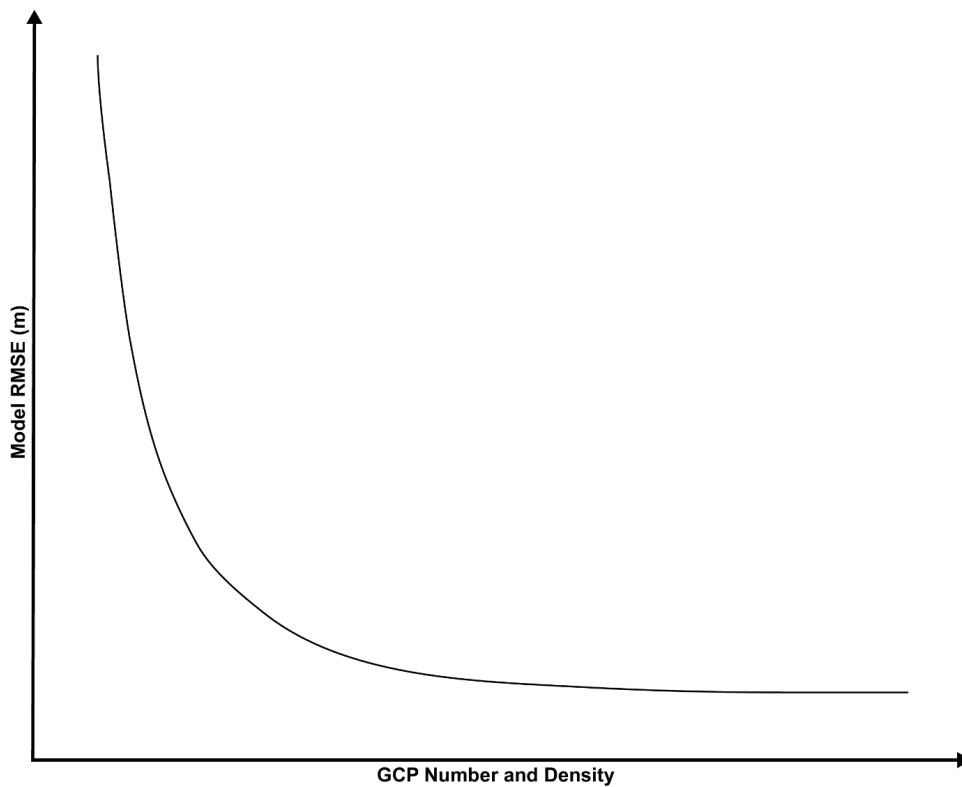


FIGURE 31 Schematic illustrating the relationship between GCP number and density and the RMSE of the final models. Generally speaking, a model georeferenced using a larger number of GCPs placed in dense network will result in a much lower RMSE than if only a few, sparsely located GCPs are used. However, this relationship only occurs up to a certain point, after which increasing GCP number will have no further impact on model RMSE. The point at which this occurs varies between specific studies, but is represented here by the levelling out of the black line above the x-axis. This schematic was produced based off data presented in Tahar et al. (2012), Gindraux et al. (2017) and Sanz-Ablanedo et al. (2018).

For example, James and Robson (2012) reported an increase in the Root Mean Square Error (RMSE) of their models when their GCPs were not distributed throughout the survey area. Similarly, Javernick et al. (2014) described an increase in RMSE from 0.23 m to 0.27 m when the study reach was extended beyond the area covered by their GCPs. Smith et al. (2014) reported an even greater increase, from 0.14 m to 0.47 m, in their reconstruction of flash flood magnitude. Indeed, a lack of GCPs in the processing stages altogether can result in metre-level geolocation errors and substantial deformation of the final DEMs (James and Robson, 2012; Benoit et al., 2019). Therefore, when designing such surveys, and where possible, a large number of GCPs should be placed as evenly as possible across the survey area to avoid introducing large errors into the final surface models, due to the key control GCP number and distribution has on final model accuracy (Westoby et al., 2012; Smith et al., 2016; Wigmore and Mark, 2017).

2.6.3 Integrated UAV-SfM Approach

In recent years, the development of the SfM methodology as a means of rapidly and accurately reconstructing topographic and morphological information has been simultaneously accompanied by technological advances in the development of low-cost, reliable and efficient UAV platforms for geomorphological applications (Eltner et al., 2015; Smith et al., 2016; Cook, 2017). These recent advances have resolved previous issues that were prevalent within the UAV systems, for example by allowing greater image stability and increasing battery life (Hardin and Hardin, 2010; Smith et al., 2016). Furthermore, many UAVs are now equipped with on-board GPS and Inertial Measurement Units (IMU) which allow for organised flight planning using user-friendly software packages (Eltner et al., 2015; Ryan et al., 2015). Such on-board GPS systems can be used to increase the accuracy of methods that determine the camera position coordinates directly, which would avoid the need for target-based georeferencing, for example by using real-time kinematic GPS (RTK-GPS), although such systems are at-present expensive to purchase (Smith et al., 2016; Tomsett and Leyland, 2019; Yang et al., 2020). Additionally, UAV systems are highly customisable, and thus can carry a number of different sensors and payloads, ranging from consumer grade cameras to thermal and hydro-spectral cameras, as well as small laser scanners (Colomina and Molina, 2014; Eltner et al., 2015) (Figure 32).



FIGURE 32 Example of a customised UAV system for use in geomorphological research. In this instance, the UAV is a DJI M600 which has been equipped with a velodyne VLP-16 laser scanner for surface height measurements (carried under the UAV) as well an on-board IMU to allow for much greater positional accuracy than given by traditional GPS receivers.

Finally, the ease of set up and data collection makes it an ideal tool for repeat surveying, allowing data to be collected by non-specialists over specific, often short, time intervals (Tomsett and Leyland, 2019). As a result, such UAV systems, when combined with the SfM methodology, have greatly enhanced our ability to monitor and quantify rapidly changing landscapes and landscape features at extremely high spatial and temporal resolution (Cook, 2017; Tomsett and Leyland, 2019; Jouvét et al., 2020). It is unsurprising then that the number of geomorphological studies utilising this integrated UAV-SfM approach have increased over the last decade, with recent applications including topographic reconstructions of river corridors (Cook, 2017), soil erosion (Eltner et al., 2015) glacier dynamics (Immerzeel et al., 2014; Ryan et al., 2015; Jouvét et al., 2019) and the reconstruction of glacier surfaces and related features (Piermattei et al., 2015; Rippin et al., 2015; Bash et al., 2018).

2.6.4 UAVs in Glacial Research

Although the integrated UAV-SfM approach is still in its relative infancy, the method is becoming an increasingly attractive option in glaciological research due to its ability to offer rapid assessment of glacier surface dynamics and evolution at extremely high spatial and temporal resolutions (Whitehead et al., 2013; Immerzeel et al., 2014; Jouvét et al., 2019). Indeed, the number of studies utilising this integrated methodology has steadily increased over the last decade (Bhardwaj et al., 2016; Fugazza et al., 2018; Groos et al., 2019). To date, UAVs have been utilised in glaciological research to investigate: the surface motion of mountain glaciers (e.g. Immerzeel et al., 2014; Wigmore and Mark, 2017; Groos et al., 2019), the dynamics and calving behaviour of tidewater glaciers (Ryan et al., 2015; Chudley et al., 2019; Jouvét et al., 2017, 2019), glacier surface structures (Ely et al., 2017; Jones et al., 2018), supraglacial drainage networks (Rippin et al., 2015), patterns of surface melt (Bash et al., 2018; Rossini et al., 2018) and surface albedo (Ryan et al., 2017, 2018), and the distribution of organic matter (Hodson et al., 2007; Stibal et al., 2017).

The integrated UAV-SfM approach is attractive to researchers undertaking studies in glacial environments for a number of reasons (Rossini et al., 2018; Benoit et al., 2019; Jouvét et al., 2019). First, UAVs are a highly cost-effective method for undertaking glacier surface assessments when compared with traditional, more expensive surveying techniques such as LiDAR and TLS, which often require manned aircraft to complete the surveys (Immerzeel et al., 2014; Ryan et al., 2017; Jouvét et al., 2019). A second advantage over more traditional methods is that UAV systems tend to be particularly lightweight due to the fact they are equipped with consumer-grade cameras (Immerzeel et al., 2014; Ryan et al., 2015; Groos et al., 2019). This, combined with continued technological advances that have increased the endurance of many battery-powered

UAV systems, mean it is now possible to survey particularly large (10 km^2) areas on one set of batteries (Fugazza et al., 2018; Jouvét et al., 2019). Third, as mentioned previously, UAV systems can be equipped with a variety of customisable sensors, including optical and multi-spectral cameras, SAR sensors and laser scanners, which allows researchers to investigate a wider variety of glacier surface characteristics and how these evolve through time (Rippin et al., 2015; Benoit et al., 2019).

Fourth, UAVs are able to acquire imagery at sub-dm scale resolution (depending on the camera model used and the survey set up), which allows glacier surface features to be picked out with extreme clarity, resulting in orthomosaics and DEMs with a final resolution and quality proposed to be on par with, or even better than LiDAR (Tonkin et al., 2014; Ely et al., 2017; Bash et al., 2018; Yang et al., 2020). Fifth, the highly automated workflow found in many SfM processing packages in recent years means that non-specialists can now more-easily process UAV-acquired imagery to produce high resolution orthomosaics and DEMs, making the method far more accessible to a wider number of researchers (Tonkin et al., 2014; Piermattei et al., 2015; Ryan et al., 2015; Groos et al., 2019). Finally, and perhaps most importantly, UAVs are particularly well-suited for conducting rapid repeat surveys of the ice surface at short temporal intervals due to the ability to deploy the UAV system 'on demand' (Immerzeel et al., 2014; Rossini et al., 2018). This affords researchers the opportunity to complete weekly, daily and even sub-daily surveys of the ice surface at high spatial resolutions, enhancing our ability to monitor and quantify the rapidly changing glacial landscape by providing unique insights into glacial processes that would be nearly impossible to obtain using more traditional techniques (Ryan et al., 2015; Jouvét et al., 2017; Wigmore and Mark, 2017). As a result of the above, UAVs are particularly suited for undertaking research in highly dynamic, yet remote and relatively inaccessible environments, such as on the Greenland Ice Sheet, in Iceland and in The Himalaya, where expensive logistics constrain the use and availability of both ground-based and airborne TLS and LiDAR surveys (Piermattei et al., 2015; Fugazza et al., 2018; Jouvét et al., 2019; Yang et al., 2020).

Of the many applications of UAVs in glacial research, it is their use in investigating the dynamics of glaciers, both land- and water-terminating, that has garnered the most attention in recent studies (Figure 33). For example, several studies have investigated the dynamics of debris-covered glaciers, both in the Himalaya (e.g. Immerzeel et al., 2014; Kraaijenbrink et al., 2016) and in the Cordillera Blanca, Peru (Wigmore and Mark, 2017). Immerzeel et al. (2014) found spatially variable velocity patterns at Lirung Glacier, Nepal Himalaya, with velocities of up to 2.5 m a^{-1} obtained in the upper reaches, yet at the debris-covered terminus, velocities were near stagnant. This led the authors to suggest that the UAV imagery allowed for the detailed analysis of glacier surface velocity at a resolution and accuracy that could not have been met by satellite-derived

products, concluding that UAVs have a key role to play in future glaciological studies. Similar spatial patterns in velocity were also observed at the calving Llaca Glacier in the Peruvian Cordillera Blanca by Wigmore and Mark (2017), where velocities of up to 27 m a^{-1} were found in the upper reaches, yet at the calving front where there was a thick layer of surface debris, surface velocities dropped to $\sim 4 \text{ m a}^{-1}$.

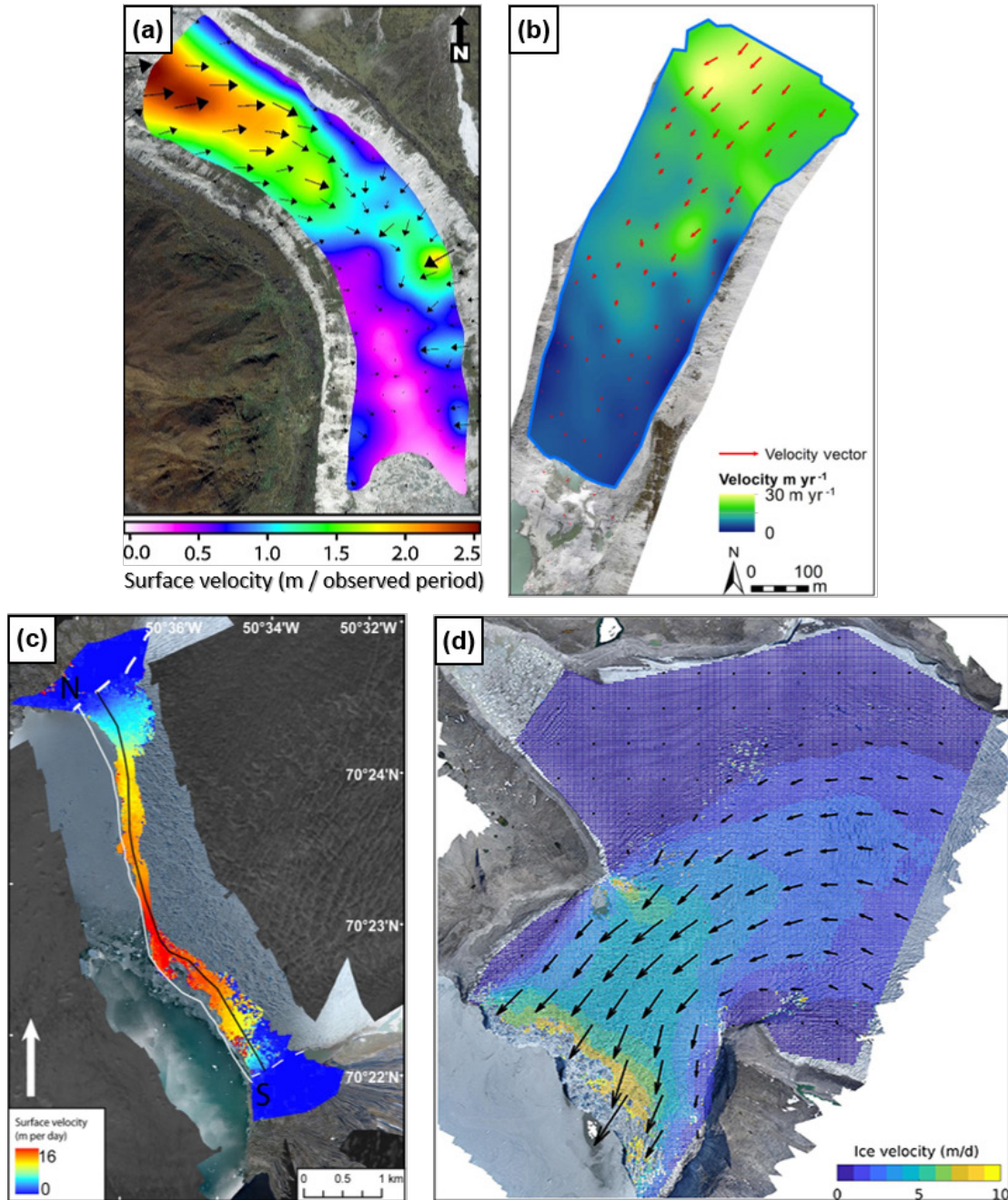


FIGURE 33 Examples of UAV-derived velocity products obtained in previous studies and mentioned in the main text. (a) Lirung Glacier, Nepal, between May and October 2013 (Immerzeel et al. (2014); (b) LLaca Glacier, Cordillera Blanca between 2014 and 2015 (Wigmore and Mark, 2017); (c) Calving front of Store Glacier, Greenland over a 24-hour period in July 2013 (Ryan et al., 2015) and (d) Eqip Sermia, Greenland, over a three-day period in July 2018 (Jouvet et al., 2019).

At a much larger scale, several recent studies have been undertaken to investigate the dynamics of large calving glaciers on the Greenland Ice Sheet (e.g. Ryan et al., 2015; Chudley et al., 2019; Jouvét et al., 2019). For example, Ryan et al. (2015) flew several sorties over Store Glacier, a major tidewater glacier, finding that the near-terminus region of the glacier was a complex system, with large variations in crevasse patterns, surface velocities, calving activity, surface elevation and frontal position occurring at daily and seasonal timescales. The authors found that during the summer the surface velocity varied widely across the terminus, reaching peaks of 16 m d^{-1} near the centreline where ice depth was greatest, but near the lateral margins velocities dropped to as low as 2.5 m d^{-1} , leading the authors to suggest that primary resistance to the driving stress was provided by lateral drag, which may cause ice flux to increase in future as the glacier retreats into a wider trough (Ryan et al., 2015). Meanwhile, Jouvét et al. (2019) investigated the dynamics and calving behaviour of several tidewater glaciers in western Greenland, finding complex and spatially variable patterns in velocity, ranging from 3.1 m d^{-1} for the smallest and up to 10 m d^{-1} for the largest glacier. Using their custom-built UAV system, they were also able to undertake repeat surveys of the largest glacier, Equip Sermia, at a temporal separation of 105 minutes, providing extremely detailed insights into the dynamic and highly changeable nature of its calving front. Such insights may be useful in furthering our understanding of calving processes, and to their knowledge is the shortest time period of glacial motion captured by UAV photogrammetry (Jouvét et al., 2019).

However, despite the numerous applications of UAVs in glacial research, and its advantages compared to other techniques, the method still suffers from several key practical and technical limitations (Whitehead et al., 2013; Jouvét et al., 2019). For example, despite recent technical improvements in UAV weight and battery power, the maximum possible survey area is still fundamentally linked to the flight time given by the UAV battery, meaning it may not always be possible to survey the desired area of interest (Whitehead et al., 2013; Wigmore and Mark, 2017). Battery performance can also be deteriorated further when undertaking research in particularly cold ($<10^\circ$) temperatures (Jouvét et al., 2019). Furthermore, adverse weather conditions, such as strong winds, precipitation and low cloud, which are common in high mountain glacial environments, can haze the camera lens and effect the internal UAV electronics, further hindering data collection (Bhardwaj et al., 2016; Ely et al., 2017). In addition, further issues may arise when undertaking research in remote and inaccessible regions, such as high mountain or extreme Polar environments (Groos et al. 2019; Jouvét et al., 2019), where access to fly the UAV may be logistically challenging and dangerous (Immerzeel et al., 2014). Similarly, the placement of control points around the study area, and the recovery of the UAV in case of technical failure will be

made far more difficult if the area of interest is a glacier calving front for example (Ryan et al., 2015; Jouvét et al., 2019).

Indeed, the dependency of the UAV-SfM methodology on GCPs is a key limitation of the method, yet it is a necessity in order to scale and georeference the resulting 3D models to real world coordinates (James and Robson, 2014; Chudley et al., 2019). Previous geomorphological studies have shown that the quantity and distribution of GCPs can have a significant impact on the accuracy of the final models (e.g. James and Robson, 2014; Shahbazi et al., 2015; Sanz-Ablanedo et al., 2018). Accuracy assessments performed specifically for glaciological environments meanwhile have reported that the optimal GCP distribution density (beyond which no improvement in accuracy occurs) is 7 GCPs km⁻² and 17 GCPs km⁻² for the horizontal and vertical accuracy respectively (Gindraux et al., 2017). However, producing a GCP network of this density in glacial environments is often impractical, logistically expensive to collect and highly unfeasible (Chudley et al., 2019; Yang et al., 2020). The use of GCPs also limits one of the fundamental advantages of using UAVs to measure surface change: the ability to remotely and accurately observe terrain that is difficult and hazardous to access on the ground (Chudley et al., 2019). Due to the practical difficulties in producing such networks, several applied glaciological studies have only been able to install their own GCPs on the sides of the valley near the glacier's lateral margin (e.g. Immerzeel et al., 2014; Ryan et al., 2015). Although on-ice GCPs can be utilised, they require repeat surveying due to the continuous movement of the ice surface, which on fast-flowing glaciers is highly unfeasible (Chudley et al., 2019). Due to such limitations, therefore, reported errors in the majority of glaciological studies to date have been systematically larger than what is theoretically possible with this technique (Chudley et al., 2019; Jouvét et al., 2019).

Nevertheless, continued technological advances mean that several of the above limitations may be addressed in future. For example, it has already been mentioned how UAV systems are constantly improving, leading to longer flying times due to increased battery life and more resistance to adverse weather conditions (Ely et al., 2017). Coupled with this, recent developments in lightweight, low-cost GNSS technology have allowed for the proliferation of a new technique whereby differential carrier-phase GNSS positioning can be used to accurately georeference each image mid-flight (Chudley et al., 2019; Yang et al., 2020). This technique has been shown to result in cm-scale accuracy without the need for a network of ground-based GCPs, resulting in highly accurate 3D models (Benassi et al., 2017; van der Sluijs et al., 2018).

Applications of this technique, termed 'direct georeferencing', are so far limited in glacial research, with only a small number of studies utilising it to date (e.g. Chudley et al., 2019; Jouvét et al., 2019; Yang et al., 2020). However, the results of these studies are promising, with Chudley et al. (2019) obtaining horizontal and vertical errors of 0.12 m and 0.14 m respectively over the

5.2 km long calving front of Store Glacier, Greenland, at a flying height (GSD) of 450 m (11 cm). Similar accuracies were also found by Jouvét et al. (2019) and Yang et al. (2020). However, at present commercial off-the-shelf UAV systems with direct georeferencing capabilities remain highly expensive, often in excess of £20,000, which can make them an unfeasible option in many cryospheric studies (Chudley et al. 2019; Groos et al., 2019). This has led to an increase in the number of studies utilising customised UAV systems which can be modified and fine-tuned to best suit the environment in which the system is to be deployed (e.g. Ryan et al., 2015; 2017). Such custom-built systems can be equipped with several different payloads, including the lightweight differential carrier phase GNSS receivers mentioned above, which come at a fraction of the cost when compared to off-the-shelf UAV systems (e.g. Chudley et al., 2019; Groos et al., 2019; Jouvét et al., 2019).

In the majority of studies, however, such highly customised UAV systems are not available, nor appropriate (due to financial constraints, lack of expertise and access restrictions), meaning at present it is impractical to solely use UAVs to investigate the large-scale and long-term changes in ice dynamics that are occurring at the glacier-wide scale (Immerzeel et al., 2014; Bhardwaj et al., 2016; Groos et al., 2019). Instead, in this instance a combination of both UAV surveys, and satellite remote sensing, would be desirable to allow for more accurate monitoring of these glaciers to be undertaken (Immerzeel et al., 2014; Bhardwaj et al., 2016; Fugazza et al., 2018). Yet despite the above, the UAV-SfM approach is still particularly well-suited for investigating those short-term changes in ice dynamics that can often occur over spatial (e.g. localised) and temporal (e.g. daily) scales that could never be captured using satellite remote sensing alone (Ryan et al., 2015; Rossini et al., 2018; Jouvét et al., 2019). Indeed, such short-term changes in dynamics can often occur at lake-terminating glaciers, for example those in south Iceland, and as a result it is this integrated UAV-SfM approach that forms the basis of this research.

Chapter 3 STUDY SITE and WIDER CONTEXT

3.1 Icelandic Glaciers

Iceland is situated in what is recognised as a climatically important region of the North Atlantic, due to its location at the boundary of the polar and mid-latitude atmospheric circulation cells, converging warm and cold ocean currents, and because it lies directly in the path of cyclonic westerlies that are driven by the North Atlantic oscillation (Flowers et al., 2005; Björnsson et al., 2013; Dell et al., 2019). In particular, the warm Irminger Current, which travels from the southwest to the northern coast of Iceland, directly contributes to its maritime climate, which is characterised by small seasonal variations in temperature and high rates of precipitation (Björnsson and Pálsson, 2008; Hannesdóttir et al., 2015). As a result, Iceland's glaciers are highly sensitive climatic indicators, responding rapidly to climatic fluctuations (Flowers et al., 2005; Björnsson and Pálsson, 2008). At present, ~10% of Iceland is covered by glaciers and ice caps (equating to an area of ~11,000 km²), with ~90% of this permanent ice cover found in the country's six major ice caps (Foresta et al., 2016; Wittman et al., 2017).

The majority of Iceland's ice masses have been retreating since the mid-1990s in response to warming temperatures in the region (Björnsson and Pálsson, 2008; Hannesdóttir et al., 2015), with many of these glaciers and ice caps displaying a particularly heightened rate of retreat since the turn of the century (Bradwell et al., 2013; Foresta et al., 2016). This response can be attributed to a 1°C increase in mean annual air temperatures since ~2000, which is three to four times higher than the Northern Hemisphere average over the same period (Jones et al., 2012; Hannesdóttir et al., 2015). This increased warming is in itself linked to a shift in atmospheric and oceanic circulation patterns around Iceland, which may have been induced by a weakening of the North Atlantic subpolar gyre (Björnsson et al., 2013; Foresta et al., 2016). This has contributed to the loss of $\sim 240 \pm 20$ Gt of ice in the period 1994-95 to 2018-19 (9.6 ± 0.8 Gt a⁻¹) (Aðalgeirsdóttir et al., 2020), with the most rapid mass loss occurring between 2003-2010, where $\sim 11.6 \pm 0.8$ Gt a⁻¹ of ice was lost (Foresta et al., 2016). Overall, Icelandic glaciers and ice caps contributed $\sim 0.03 \pm 0.004$ mm a⁻¹ to global SLR between 1995 and 2010, and $\sim 0.02 \pm 0.01$ mm a⁻¹ between 2010 and 2015 (Björnsson et al., 2013; Hannesdóttir et al., 2015; Zemp et al., 2019). This contribution is over twice that of Scandinavian glaciers for 2006-2015, and is comparable to the contribution of Svalbard glaciers over the same period, signifying Icelandic glaciers contribute at present one of the highest rates of meltwater input to the North Atlantic (Björnsson et al., 2013; Foresta et al., 2016).

However, while the overall trend is one of increasing mass loss, there is significant interannual variability within this overall pattern, with rates of mass loss since 1995 varying by between 2 to 25 Gt a⁻¹ (Foresta et al., 2016). Such differences may partly represent the variability in tephra deposition on the ice surface, which can change the surface albedo and thus enhance melt, but it is likely such differences predominately reflect the high sensitivity of Iceland's glaciers to any slight change in temperature or precipitation (de Woul and Hock, 2005; Björnsson et al., 2013; Wittman et al., 2017). For example, since 2010 the mass loss rate in Iceland has been ~50% lower relative to the preceding 15 years, primarily due to cooler oceanic conditions around Iceland during this time (Aðalgeirsdóttir et al., 2020). These conditions cooled the atmosphere, and meant that the mass balance year 2014-15 was characterised by a winter of continuous low-pressure systems bringing large amounts of precipitation followed by a summer of cooler temperatures with little melt, resulting in positive mass balances for all of Iceland's glaciers (Foresta et al., 2016; Aðalgeirsdóttir et al., 2020). Conversely, one of the most negative mass balance years on record occurred in 2018-19 (-15 ± 1.6 Gt a⁻¹), which was due to the persistence of anti-cyclonic conditions over Iceland during the summer of 2019. This resulted in warm and sunny conditions from early spring and thus the earlier exposure of low-albedo ice surfaces in the ablation areas of its ice masses, leading to enhanced melting (Aðalgeirsdóttir et al., 2020). Such variability in the recent trends of mass loss further highlights how the mass balance and retreat patterns of the majority of Iceland's glaciers are strongly governed by, and highly sensitive to, any slight change in summer temperature and precipitation (Björnsson et al., 2013; Hannesdóttir et al., 2015; Belart et al., 2020).

Recent research has shown, however, that non-surface mass balance processes, such as geothermal melting, volcanic eruptions and glacier calving, have also contributed significantly to the recently observed patterns of mass loss (Aðalgeirsdóttir et al., 2020; Jóhannesson et al., 2020). For example, such processes are thought to account for ~1/5th of the total mass loss since 1994, with some ice caps, like Vatnajökull, losing as much as 38% of their mass in response to these processes (Jóhannesson et al., 2020). A particularly important component of this recent mass loss has been glacier calving, which although insignificant during the first half of the 20th century, has become a gradually increasing contributor over recent years in response to the ongoing retreat of outlet glaciers through, and the resultant formation of proglacial lakes in, overdeepened bedrock troughs (Hannesdóttir et al., 2015; Aðalgeirsdóttir et al., 2020). Indeed, many of the southerly-flowing outlets of Vatnajökull are underlain by deep bedrock troughs (100-300 m), and have thus seen the development and growth of proglacial lakes at their margins since the mid-1990s (Guðmundsson et al., 2019; Jóhannesson et al., 2020), which have caused accelerated terminus retreat (Schomacker, 2010; Dell et al., 2019). As a result, these outlets are

particularly sensitive, not just to continued climate warming, but also to accelerated mass loss as a result of calving processes, with the latter forecast to considerably impact their dynamics and future retreat patterns in particular (Schomacker, 2010; Hannesdóttir et al., 2015). One of the most dynamic and rapidly changing glaciers in this region is Fjallsjökull, yet despite its recent trends of mass loss it is little studied, and consequently it is this glacier that forms the focus of this research.

3.1.1 Study Site

3.1.1.1 *Glaciological Setting*

Fjallsjökull (64°01'N, 16°25'W) is a piedmont outlet lobe of the Öræfajökull ice cap, situated on the southern side of the Vatnajökull Ice Cap, in southeast Iceland (Figure 34) (Evans and Twigg, 2002; Dell et al., 2019). The glacier flows out eastwards from the Öræfi caldera, descending rapidly over a series of ice falls before terminating in the low-elevation foreland at ~30 m a.s.l. (Figure 35) (Hannesdóttir et al., 2015; Chandler et al., 2020). Like many glaciers in Iceland, however, Fjallsjökull has been losing mass since the Little Ice Age (LIA), with a ~23% reduction in area, a ~35% reduction in volume and over 2.2 km of retreat observed between ~1890 and 2010 (Hannesdóttir et al., 2015; Chandler et al., 2020). As a result, in 2010 Fjallsjökull covered an area of ~44.6 km², had a volume of 7.0 km³ and was ~12.9 km long (Hannesdóttir et al., 2015). The frontal variations of Fjallsjökull have been routinely monitored since ~1934 and compiled by the Icelandic Glaciological Society (IGS) (Sigurðsson et al., 2007; Hannesdóttir et al., 2015). Measurements at the land-terminating southern margin indicate that ~1.7 km of retreat occurred between 1934 and 2019 (Figure 36) (WGMS, 2020), with a particularly heightened rate of retreat observed since the early 2000s (Dell et al., 2019; Chandler et al., 2020).

As with many of the southerly flowing outlets of Vatnajökull, the ongoing retreat of Fjallsjökull has revealed a substantial overdeepening, which attains a maximum depth of ~206 m and is ~3 km wide and ~4 km long (Figure 34d and 37) (Magnússon et al., 2012; Dell et al., 2019). The emergence of this overdeepening has led to the development of the large proglacial lake Fjallsárlón, the third largest in southeast Iceland, into which the glacier currently terminates (Dell et al., 2019; Chandler et al., 2020). Although Fjallsárlón first formed in ~1938, it has grown particularly rapidly since the mid-1990s, at a rate of ~0.1 km² a⁻¹ in the period 1994-2018 (compared to ~0.02 km² a⁻¹ for 1938-1994) (Guðmundsson et al., 2019). In 2018 the area of Fjallsárlón was ~3.7 km², with radio echo soundings of the water depth obtained around this time indicating the volume of the lake was ~170x10⁶ m³ and that near the middle of the calving front the maximum depth reached >100 m (Guðmundsson et al. 2019; Dell et al., 2019).

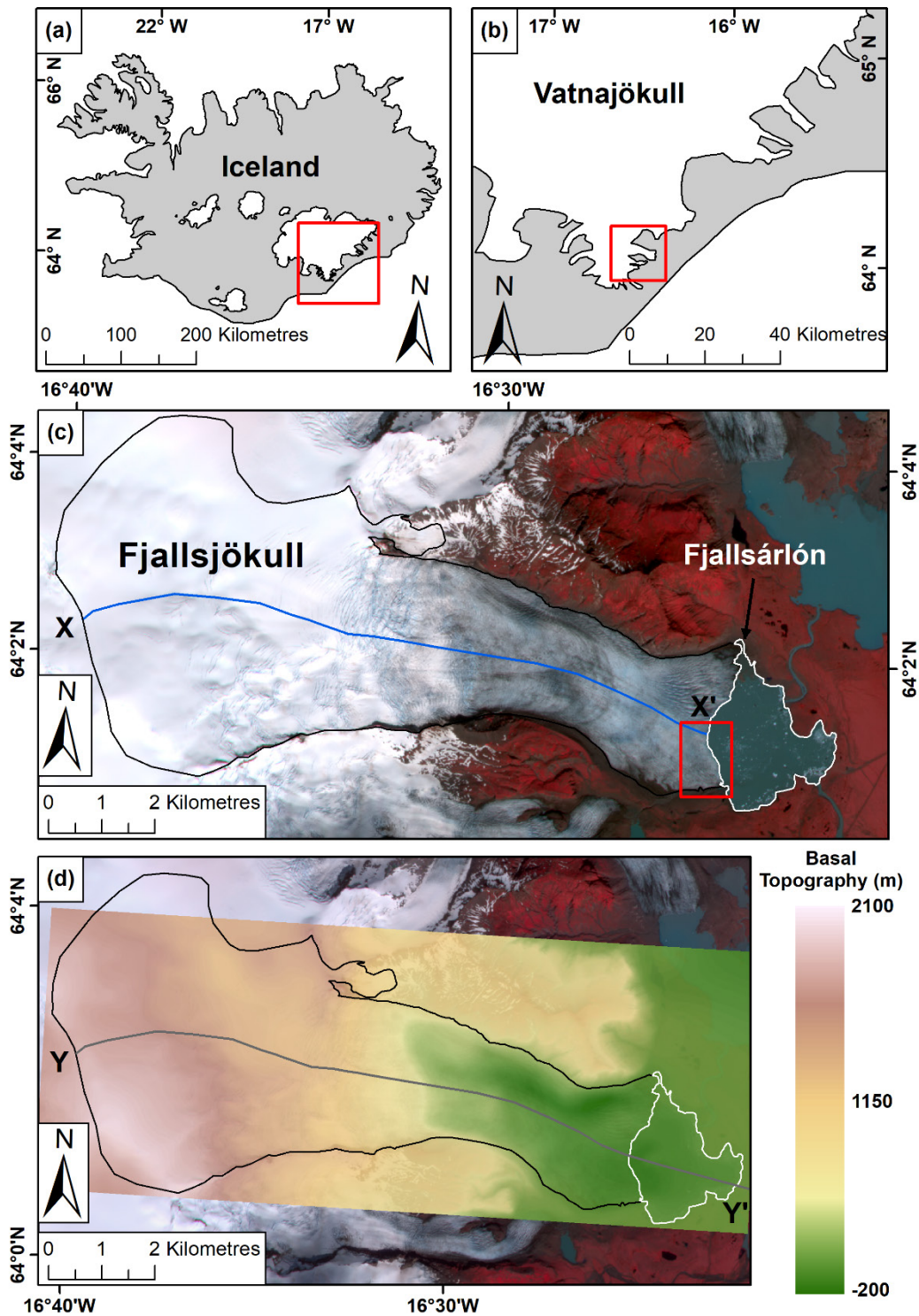


FIGURE 34 Location map of Fjallsjökull. (a) Location of Fjallsjökull within Iceland, and (b) within the Vatnajökull Ice Cap. (c) Area of Fjallsjökull and Fjallsárlón as of July 2021. Red box delineates the areal coverage of the UAV surveys undertaken in this research. Glacier outline obtained from the GLIMS database. (d) Bedrock topography of Fjallsjökull, which extends down to ~206 m below sea level at its deepest (dark green). Interpolated from data provided to the author by E. Magnússon. Lake area and glacier outline as before. Longitudinal flowlines X-X' and Y-Y' are shown in Figure 36. Background image is a 4-band false-colour PlanetScope acquisition from 07/07/2021.



FIGURE 35 Field photograph of Fjallsjökull (along with its proglacial lake Fjallsárlón) taken from directly opposite the glacier on 7th July 2021. In this image, the glacier descends rapidly over a series of icefalls before terminating in a ~2.3 km wide calving front.

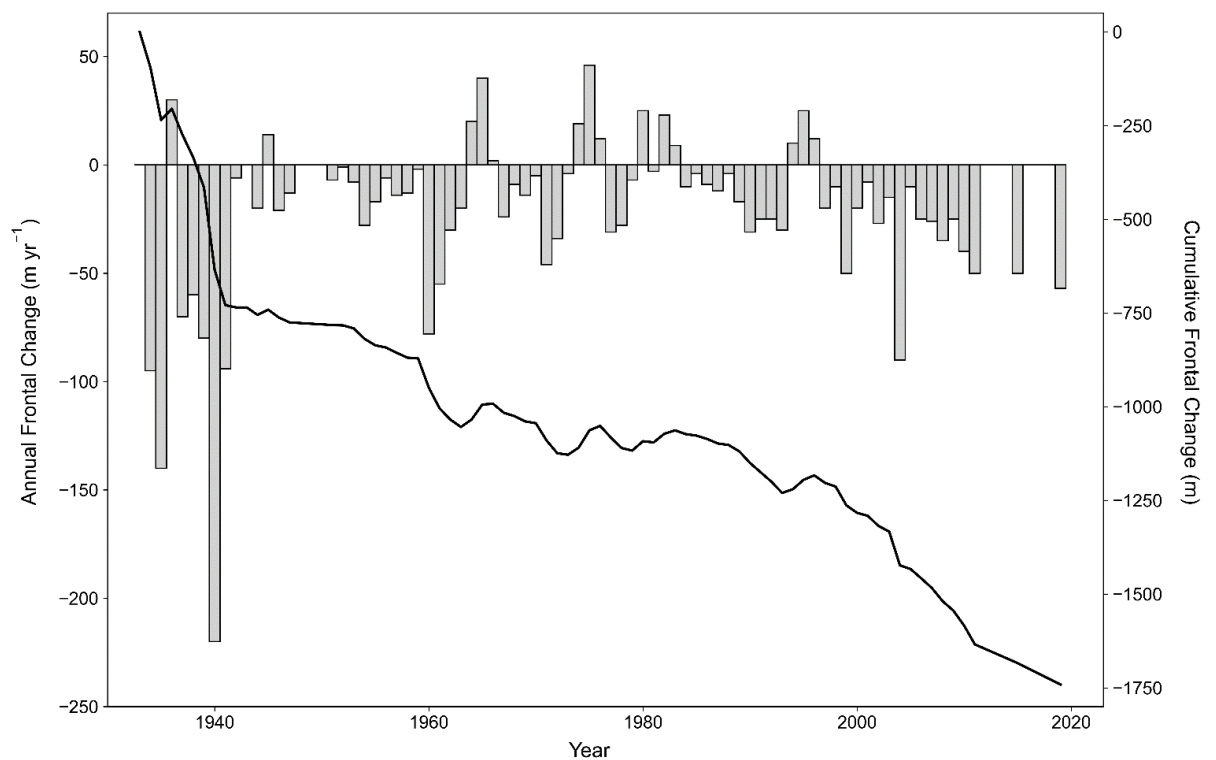


FIGURE 36 Annual and cumulative frontal variations measured at the land-terminating margin of Fjallsjökull for the period 1934 to 2019. Data obtained from WGMS (2020) and the IGS (<http://spordakost.jorfi.is/>).

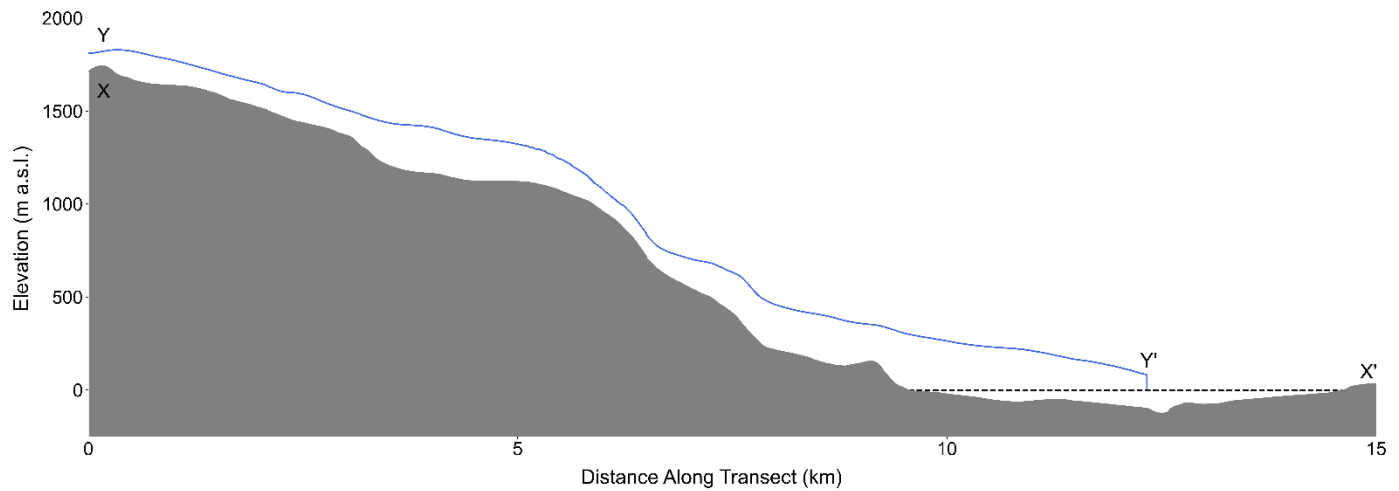


FIGURE 37 Longitudinal surface and bedrock profiles of Fjallsjökull showing the location of the terminus in 2020, as well as the ~4 km long overdeepened bedrock trough through which the glacier is currently retreating. The black dotted line represents current sea level (0 m a.s.l.).

Over recent years Fjallsárlón has started to exert a significant influence on the overall dynamics and retreat patterns of Fjallsjökull, and thus further research is warranted so that its likely future response can be better understood (Schomacker, 2010; Dell et al., 2019).

3.1.1.2 *Climatological Setting*

The Öräfi region experiences a relatively mild maritime climate, with a low mean annual temperature range (~8-15°C) and ~150 precipitation days a year (Bradwell et al., 2013; Hannesdóttir et al., 2015). Mean annual temperatures for the period 1949-2020 at Fagurhólsmyri weather station (63°53'N, 16°39'W, 46 m a.s.l.), the nearest long-term weather station to Fjallsjökull (~20 km to the southwest), were between 3.4 and 6.3°C, and have been generally increasing in this time (Figure 38a) (Chandler et al., 2020). Mean summer temperatures for the same period, meanwhile, range between ~7.2 and ~11.0°C, but daily summer maxima of >20°C are not uncommon (Bradwell et al., 2013; Chandler et al., 2020). The eastern side of Öräfajökull also experiences relatively high annual precipitation totals, often averaging ~3500 mm a⁻¹ but which can locally exceed >7000 mm a⁻¹ on the summit plateau (Bradwell et al., 2013), meaning this region collects one of the highest precipitation totals in Iceland (Figure 38b) (Belart et al., 2020). These meteorological conditions can thus sustain a larger glacier at lower elevations on the eastern side of Öräfajökull than on the western side, but this also means that these eastern glaciers are highly sensitive to any slight variation in summer temperature and winter precipitation, which may cause them to undergo rapid mass loss in future (de Woul and Hock, 2005; Magnússon et al., 2012; Belart et al., 2020).

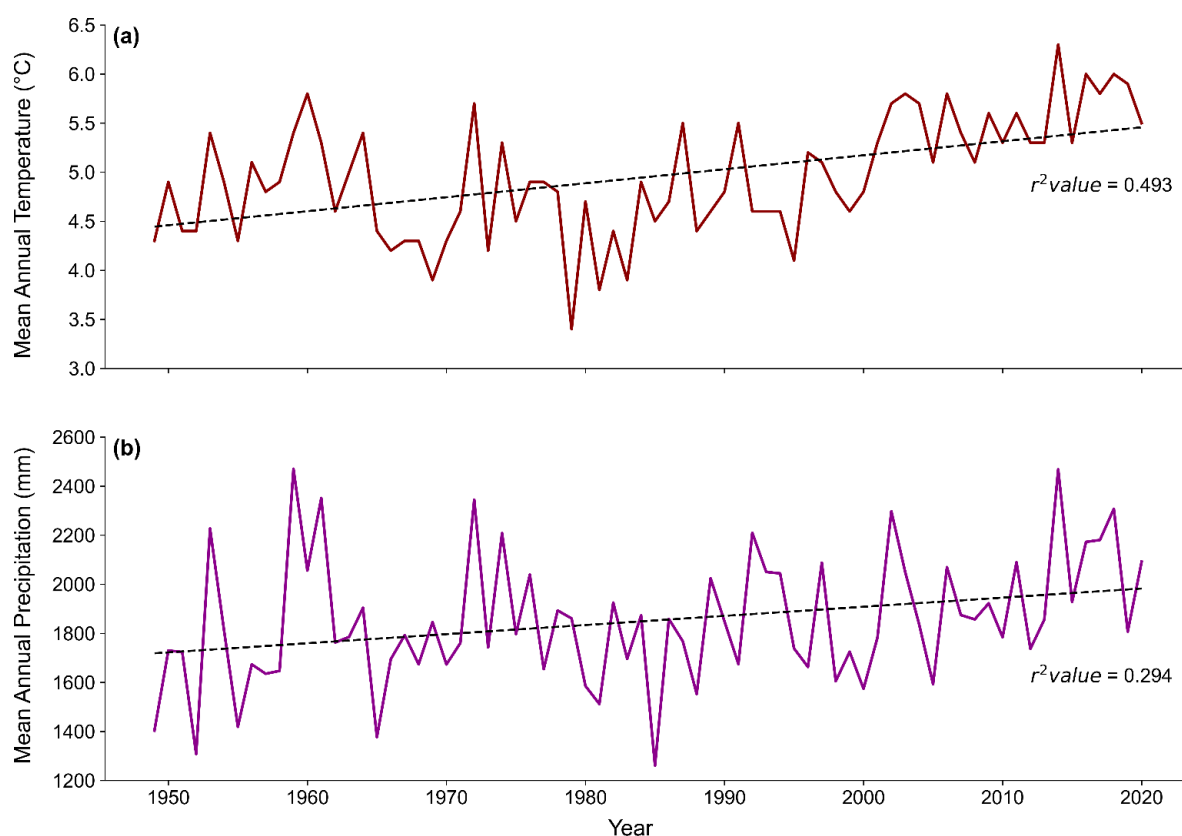


FIGURE 38 (a) Mean annual temperatures and (b) mean annual precipitation recorded at Fagurhólmsmýri weather station for the period 1949–2020. Missing data (from 2008 onwards) were calculated using a transfer function based on the data recorded by the weather station at Höfn (64°16'N, 15°12'W), which has the second longest meteorological record in Iceland.

3.1.2 Previous Work

As mentioned previously, regular monitoring of the annual frontal variations of Fjallsjökull have been undertaken since ~1934 by the IGS (Hannesdóttir et al., 2015; Einarsson, 2017). In the scientific literature, however, Fjallsjökull has received very little attention, especially in comparison to its neighbour, Breiðamerkurjökull. Indeed, until recently the only studies to date which focused on Fjallsjökull did so as part of a wider study, either with another glacier (often Breiðamerkurjökull) being the main focus (e.g. Evans and Twigg, 2002), or where all the outlets of a particular region were focused on equally (e.g. Hannesdóttir et al., 2015; Guðmundsson et al., 2019). It is only recently that this has started to change, with several articles published that focus solely on Fjallsjökull. For example, the most recent of these is the study of Chandler et al. (2020) who investigated the spatial and temporal evolution of the glacial landsystem of Fjallsjökull using a combination of geomorphological mapping and repeat UAV surveys. Meanwhile, Dell et al. (2019) utilised satellite imagery to present a detailed analysis of the changing dynamics and structural regime of Fjallsjökull between 1973 and 2017, in response to variations in local climate.

The authors observed a marked increase in surface velocity from ~ 0.3 to 0.82 m d^{-1} , which coincided with the development of localised fast flow 'corridors' during this period, which conveyed (relatively) faster flow towards the glacier terminus. Furthermore, such increases in velocity were accompanied by an increase in the rate of surface thinning near the terminus, whilst during the same period they also observed a marked increase in both the rate of terminus retreat, and in the growth rate of the proglacial lake, indicating a shift in the dynamic behaviour of the glacier. Indeed, although they attribute the overall change in dynamics to rising air temperatures, they argue that in recent years the subglacial topography and continued expansion of Fjallsárlón have become important controls on the ice-flow velocity and overall retreat patterns of the glacier, particularly over the last ~ 20 years. This, they suggest, highlights the significance of both glacier specific and non-glacier specific factors on the dynamics of the glacier, both at present, and in the future (Dell et al., 2019; Chandler et al., 2020).

Despite these recent contributions, however, there is still a clear lack of studies in the literature that focus on Fjallsjökull, particularly in relation to its proglacial lake, and how this may be influencing the dynamics of the glacier at varying spatial and temporal scales. As a result, this clear research gap will be addressed in this research by utilising ultra-high resolution repeat UAV imagery to provide insights into the changing dynamics of Fjallsjökull at high spatial and temporal resolutions over both the 2019 and 2021 summer melt seasons.

Chapter 4 METHODS

This chapter is structured as follows: Firstly, details of the UAV fieldwork undertaken in both 2019 and 2021 are described in subsequent sections, before the post-processing and SfM methods utilised are outlined in detail. Next, the uncertainty analysis relating to this processing is detailed, with these once again given in separate sections for the 2019 and 2021 surveys. Finally, the methods used to obtain the specific glacier-related products are then described.

4.1 Repeat UAV Surveys

4.1.1 2019 Field Season

4.1.1.1 *UAV and Camera System*

The UAV system utilised for fieldwork during the summer of 2019 was a 3DR Solo quadcopter, a lightweight (5 kg) and durable UAV from 3D Robotics (Figure 39). On full charge, one 5200-mAh Li-Po Solo battery provides a flight time of ~18-20 minutes in calm conditions with camera attached, or 12-15 minutes in windier, more challenging conditions.



FIGURE 39 The 3DR Solo quadcopter used to undertake the UAV surveys in July and September 2019.

The UAV was equipped with a MAPIR Survey 3 camera, comprising a 12-megapixel Sony Exmor R IMX117 sensor and a HFOV 19 mm lens to allow the capture of 24-bit JPG photos at a resolution of 4000x3000 pixels. The camera was also equipped with an external u-blox NEO-M8 GPS/GNSS module that automatically recorded the time, date and geographical position of each image with a positional accuracy of ~10 m. For all flights, the camera was set with an automatic timer to

capture images every 2 seconds, which provided the best image quality based on UAV elevation and speed. In addition, camera settings for all flights were pre-set with the autofocus on, an ISO of 200, and with an automatic shutter speed determined by the camera due to the likelihood of differential surface and lighting conditions over the glacier (e.g. Immerzeel et al., 2014; Wigmore and Mark, 2017). All other settings were kept as standard.

4.1.1.2 Mission Planning and Survey Design

During the summer of 2019, four UAV surveys were conducted over Fjallsjökull over one week in early July (3rd-10th), while three more surveys were conducted over one week in mid-September (18th-25th). Surveys were flown on the 5th, 6th, 7th and 9th July, and the 19th, 20th and 21st of September during daylight hours (9:00 to 15:30). Although it was originally planned that these surveys would cover the entire lower terminus area of Fjallsjökull, due to the flying time afforded by each fully charged battery (~10 minutes), this quickly became unfeasible. Instead, an area of roughly ~0.5 km² was surveyed, with full coverage of this area obtained by undertaking seven individual UAV surveys (with one battery per survey). Although it would have been desirable to fly these seven surveys each day, this often was not the case. As it was, only two full days of surveys were obtained in July (6th and 7th) and one in September (21st). For the other days (5th and 9th July, and 19th September), only four surveys were flown, covering just over half the total area due to time constraints. Finally, due to inclement weather during one day in September (20th), only three surveys were flown. Full details about these surveys including flight times, area covered, and number of photos taken, are given in Table 1.

TABLE 1 Details of each survey undertaken in July and September 2019.

Date	Time	Number of Flights	Number of Survey Lines	Total Area Covered (km ²)	Number of Photos
5 th July	14:11 – 15:23	4	8	0.289	568
6 th July	10:43 – 13:45	7	14	0.511	1006
7 th July	11:14 – 13:10	7	14	0.511	997
9 th July	10:06 – 10:59	4	8	0.289	550
19 th September	12:14 – 12:21	4	8	0.289	554
20 th September	14:33 – 15:07	3	6	0.219	404
21 st September	8:57 – 10:20	7	14	0.511	1012

All survey routes were pre-planned and designed using the free open source software package 'Mission Planner' (<http://ardupilot.org/planner/>), with each survey route defined by a suite of waypoints and parallel lines placed approximately orthogonal to ice flow direction (Figure 40). Mission Planner was utilised in this research to ensure certain parameters, such as survey elevation and speed, were kept consistent throughout. The exact parameters used are presented in Table 2 and briefly discussed here.

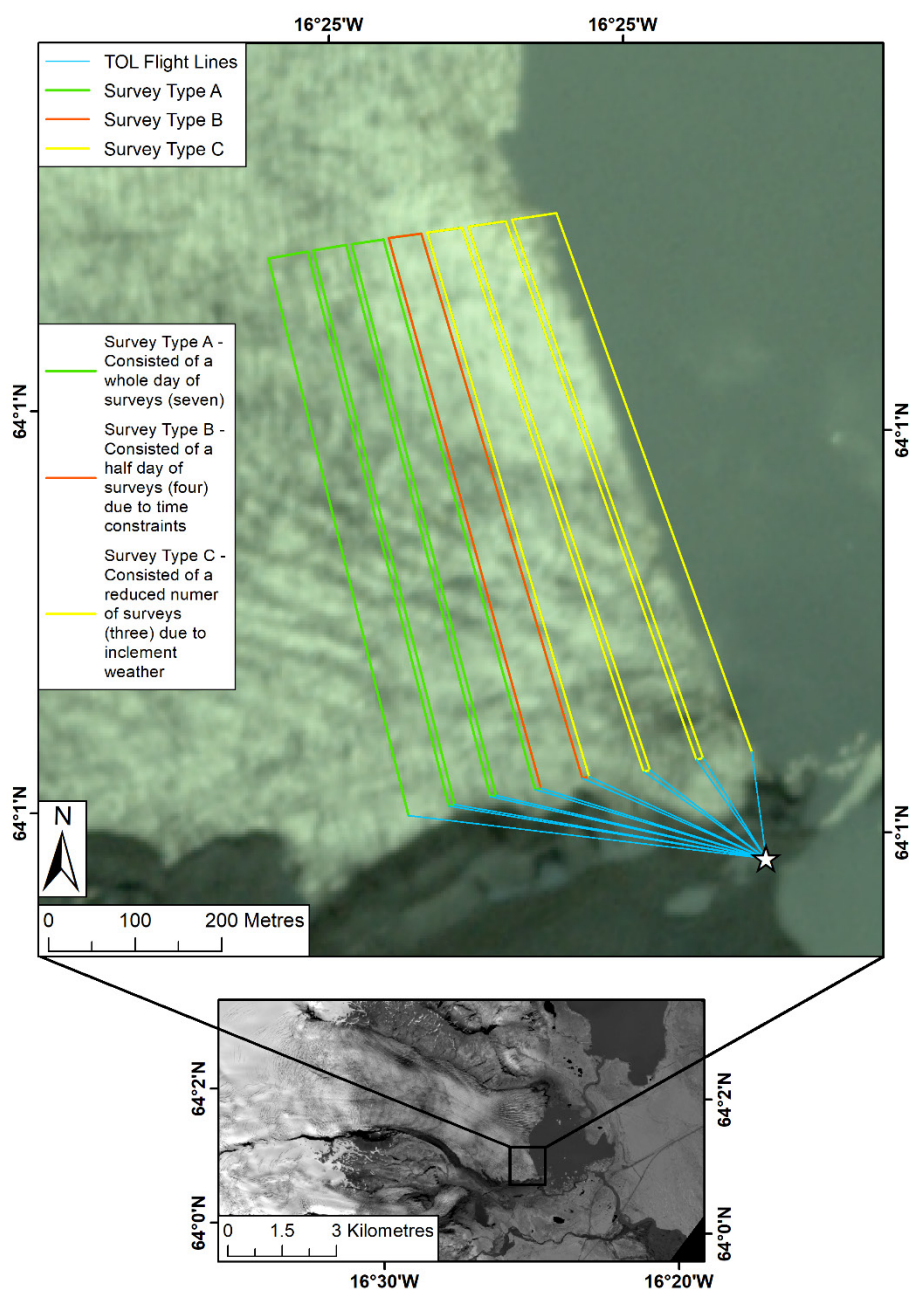


FIGURE 40 Areal coverage of the UAV surveys undertaken in July and September 2019. Top: Figure illustrating the three different surveys flown over the study area in July and September 2019. Take-off and landing (TOL) point is given by the white star. Background is a 4-band PlanetScope acquisition from 7th July 2019. Bottom: Area covered by the UAV surveys in relation to the whole of Fjallsjökull. Background is a Sentinel 2 B8 acquisition from 6th July 2019.

The survey elevation was set at a height of 100 m above lake level because the UAV took off and landed at lake level. However, in reality, the actual survey elevation when flying over the ice surface was closer to ~80 m because the surface of Fjallsjökull was ~15-20 m above the level of the lake. This resulted in (GSD) of ~0.03 m, allowing the ice surface to be imaged at a high spatial resolution (Gindraux et al., 2017; Bash et al., 2018). To ensure good overlap between images, the UAV was flown at a constant speed of 5 m/s, and with an equal spacing between parallel survey lines of 54.64 m, resulting in an image overlap and sidelap of 92% and 70% respectively. This ensured every part of the study area was imaged, even during strong winds that may have caused the UAV to undergo substantial pitch and roll (Jouvet et al., 2019).

TABLE 2 Flight settings used when undertaking the UAV surveys in both July and September 2019.

Survey Parameters	2019
Take-off and Landing (TOL) Altitude (m.a.s.l.)	13.71
UAV flying height above lake level (m)	100
UAV flying height above surface (m)	80-85
Image Overlap	92%
Image Side lap	70%
Ground Sampling Distance (GSD) (m)	0.03

The Mission Planner software was also used as a ground station for two-way telemetry with the UAV system. Before each flight, the relevant survey route to be flown was uploaded to the UAV. Take off for each survey was then done manually using the flight controller to ensure there were no issues with the UAV system. Once checked, the UAV was switched to autopilot (using Mission Planner) to allow it to autonomously undertake and complete the pre-planned survey. During each survey, flight data, such as speed and elevation, as well as the survey route being undertaken, were also monitored in Mission Planner. Once the defined survey had been completed, the UAV returned to launch and manual control was returned to the pilot to ensure the UAV landed safely.

4.1.1.3 Georeferencing

Although the camera was equipped with an external GPS, the positional accuracy of the module was too coarse for the needs of this study. As a result, to increase the accuracy of the final models, and to ensure they were correctly georeferenced to real-world coordinates (Gindraux et

al., 2017), a set of GCPs were deployed around the study area and their positions recorded with a GS09 dGPS from Leica Geosystems. The GCPs utilised in this research were high contrast, thick plastic markers, 1x1 m in size with a clearly defined centroid to aid in locating the target center during processing (Figure 41).



FIGURE 41 Example of one of the 1x1 m GCPs placed in the vicinity of Fjallsjökull to georeference the glacier models to real-world coordinates.

The number of GCPs deployed in July and September 2019 differed slightly. In July 2019, seven GCPs were originally deployed around the study site at the start of fieldwork on the 5th, although this was then increased to nine markers two days later. In comparison, eleven markers were deployed around the study site at the start of fieldwork in September 2019, and these remained in place until the end of the trip (Figure 42). It is always preferable to place GCPs as evenly as possible across the area of interest to ensure a more robust and high-quality model output (James and Robson, 2012; Javernick et al., 2014). However, this is not always possible when working in glacial environments due to the highly crevassed and hazardous nature of the ice surface, which may limit the ability to place GCPs evenly across the scene of interest.

This was the case for both trips in the summer of 2019 due to the lower surface of Fjallsjökull being heavily crevassed and, therefore, inaccessible. Consequently, all GCPs were placed on stable ground near the edge of the glacier in as even and well-distributed manner as possible to ensure multiple GCPs were visible in each photo. Although placing the GCPs in this way can cause georeferencing errors to increase across the model reconstruction with increasing distance from the GCP locations (e.g. James and Robson, 2012; Micheletti et al., 2015), in this case it is unlikely that this significantly impacted upon the overall accuracy of, nor greatly increased the errors within, the models presented in this research (Section 4.2.2).

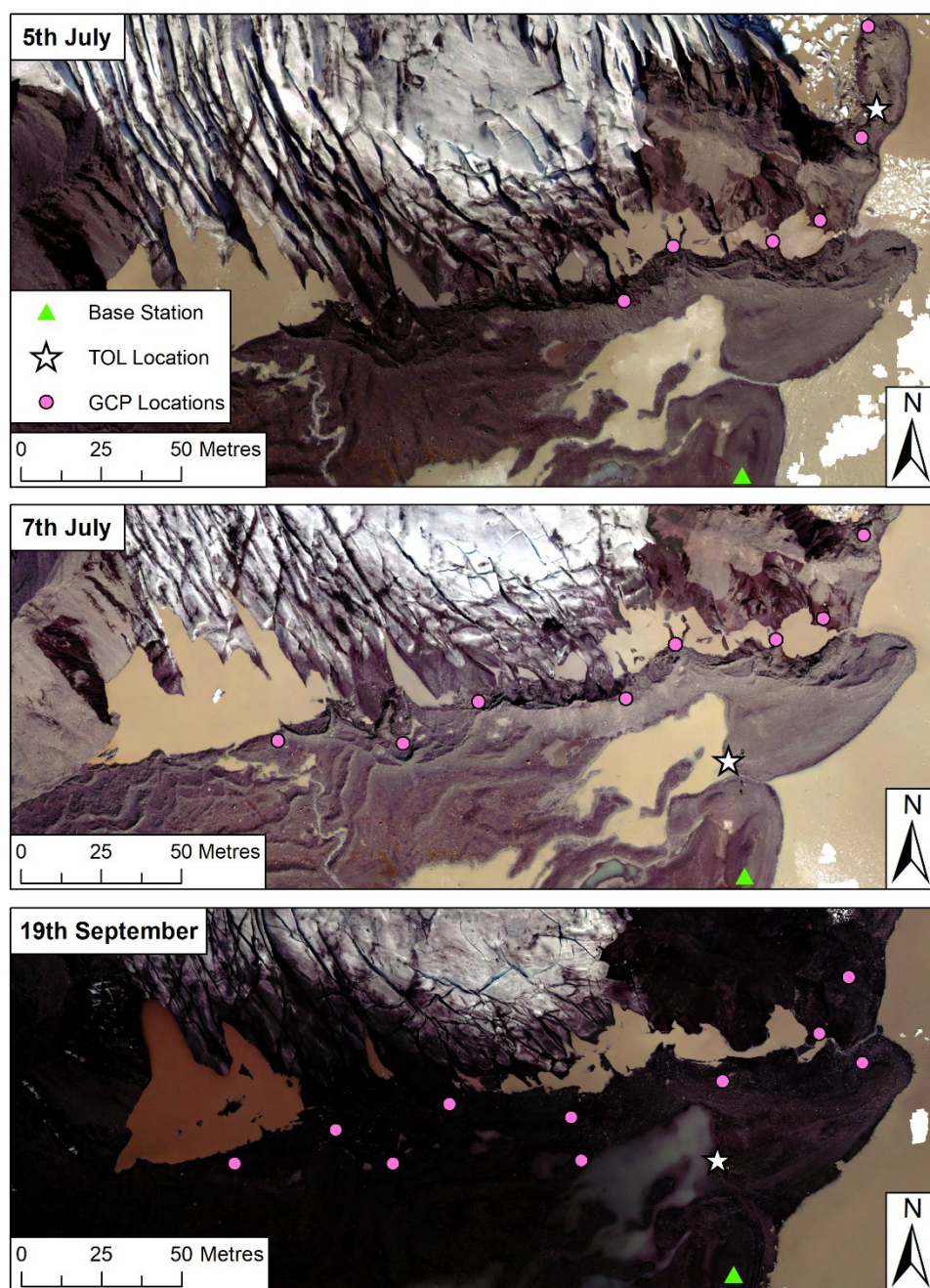


FIGURE 42 GCP locations (pink circles), UAV launch site (TOL, white star) and Leica base station location (green triangle) for the 5th July (top), 7th July (middle) and 19th September (bottom) 2019. All GCPs were resurveyed, and three more added on the 7th July due to the loss of the northern most GCP between the 6th and 7th July. Background in each panel is the orthomosaic for the respective date.

4.1.2 2021 Field Season

4.1.2.1 UAV and Camera System

The UAV system utilised for the fieldwork in July 2021 was an Inspire 2, a lightweight (~3.7 kg), robust and highly durable UAV system from Da-Jiang Innovations (DJI) (Figure 43).



FIGURE 43 The DJI Inspire 2 used to undertake the UAV surveys in July 2021. Note the GNSS antennae fixed to the top of the UAV body to allow for direct georeferencing capabilities.

The UAV is powered by two 4280 mAh Li-Po 6S TB50 batteries which can provide up to 27 minutes of flight time in calm conditions with a Zenmuse X4S camera attached (DJI 2021a), or around 20 minutes in adverse flying conditions. For this fieldwork, the Zenmuse X4S camera was utilised, comprising a 20 megapixel 1" Exmor R CMOS sensor and a custom-engineered 8.8 mm/F2.8-11 compact lens, allowing for the capture of 24-bit JPEG photos at varying pixel resolutions (DJI 2021b). For all flights, the camera was set to automatically capture images at 3-second intervals to provide the best image quality. In addition, it was set to automatically adjust the image ISO with a user-defined shutter speed of 1/1000th to allow the camera to better capture high-quality images over the glacier during variable lighting conditions (e.g. Fugazza et al., 2018; Jouvet et al., 2019; Chudley et al., 2021). All other settings were kept as standard. Finally, differential carrier-phase GNSS (i.e. direct georeferencing) functionality was provided by an Emlid Reach M+ module, which was fixed to the underside of the UAV body and connected to the hot-shoe adaptor of the on-board camera, allowing the time and coordinates of each image to be logged with a post-positional accuracy of ~1 cm (Jouvet et al., 2019; Emlid, 2021a). This direct georeferencing method is discussed in further detail in Section 4.1.2.3.

4.1.2.2 Mission Planning and Survey Design

During the summer of 2021, nine UAV surveys were conducted over Fjallsjökull over two weeks between the 2nd and 16th July. Surveys were flown on the 4th, 6th, 7th, 8th, 9th, 10th, 11th, 12th and 15th, between the hours of 11:30 am and ~14:30 pm. As was the case in 2019, these surveys were again unable to cover the entire terminus of Fjallsjökull. However, due to the greater flying time offered by the Inspire batteries, these surveys were able to cover a much larger area than was obtained in 2019. As a result, a total area of ~0.9 km² was surveyed along a 1.5 km length of the calving front extending to a maximum of 550 m back from the terminus. Full coverage of this area was obtained by undertaking three individual UAV surveys, apart from the 4th July where inclement weather meant only two surveys could be completed. Full details about these surveys, including flight times, area covered, and number of photos taken, are presented in Table 3.

TABLE 3 Details of each survey undertaken in July 2021.

Date	Time	Number of Flights	Number of Survey Lines	Total Area Covered (km ²)	Number of Photos
4 th July	13:10 – 13:45	2	8	0.572	490
6 th July	12:21 – 13:12	3	12	0.858	684
7 th July	13:35 – 14:32	3	12	0.858	684
8 th July	12:05 – 12:55	3	12	0.858	687
9 th July	12:01 – 12:51	3	12	0.858	684
10 th July	12:08 – 12:57	3	12	0.858	686
11 th July	12:43 – 13:49	3	12	0.858	684
12 th July	11:52 – 12:40	3	12	0.858	684
15 th July	11:59 – 12:50	3	12	0.858	684

All surveys undertaken in 2021 were pre-planned and designed using the commercially available app 'DJI Ground Station (GS) Pro' (<https://www.dji.com/uk/ground-station-pro>), with each survey defined by a suite of waypoints and parallel lines which were again placed approximately orthogonal to ice flow direction (Figure 44). GS Pro was utilised in this fieldwork to ensure that certain parameters, such as survey elevation and speed were kept consistent throughout. The exact parameters used are presented in Table 4 and briefly discussed here.

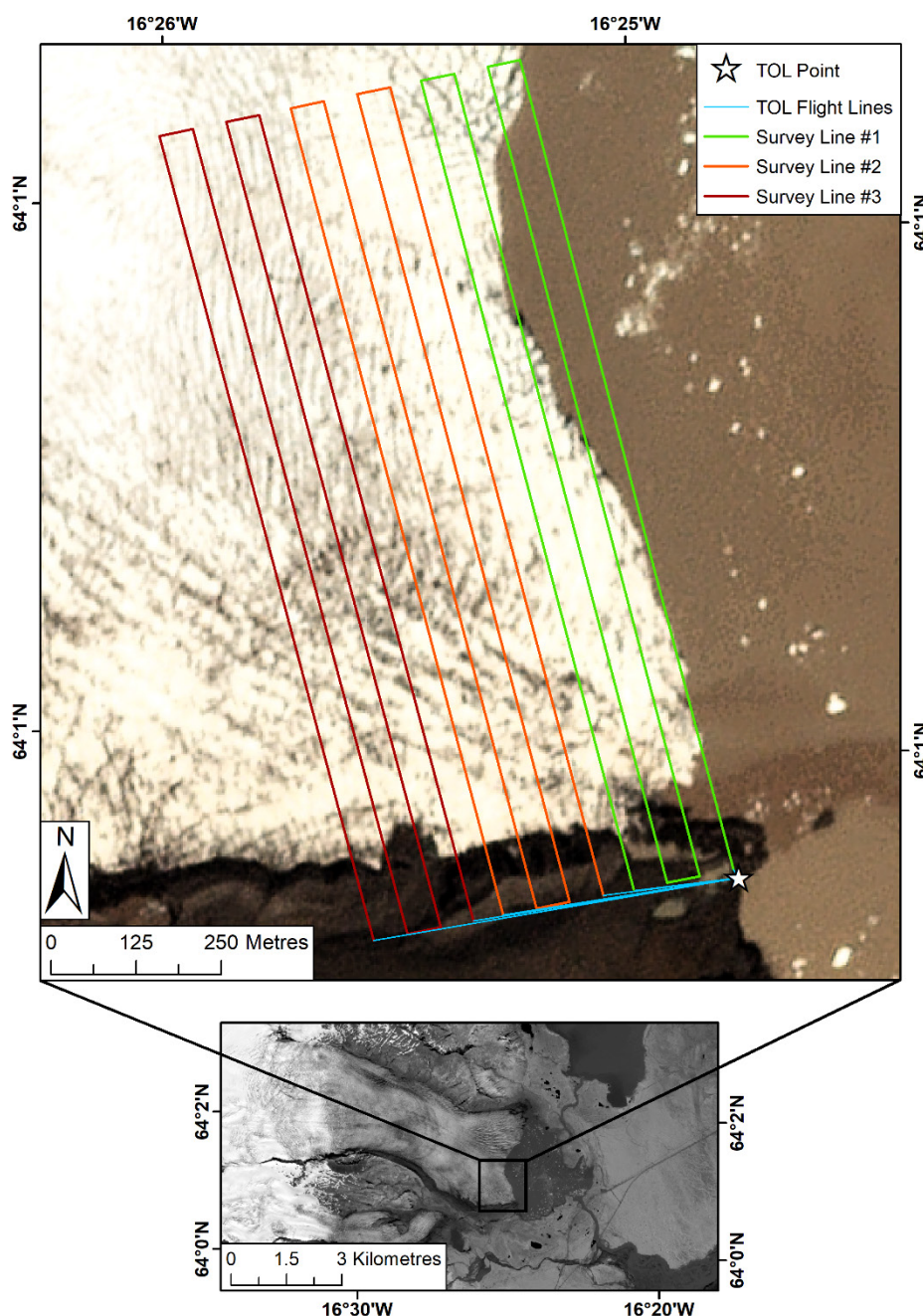


FIGURE 44 Areal coverage of the UAV surveys undertaken in July 2021. Top: Figure illustrating the three surveys flown daily over the study area in July 2021, except for the 4th July when only 2 surveys were completed (lines #1 and #2). Take-off and landing (TOL) point is given by the white star. Background is a 4-band PlanetScope acquisition from 3rd July 2021. Bottom: Area covered by these UAV surveys in relation to whole of Fjallsjökull. Background is a Sentinel-2 B8 acquisition from 7th July 2021.

The survey elevation was set to a height of 110 m (above take-off level next to the lake) to allow greater areal coverage of the glacier to be obtained. However, and similarly to the 2019 surveys, the actual survey elevation when flying over the glacier was between 90-95 m because the surface of Fjallsjökull in this region was some ~15-20 m above the level of the lake. Consequently,

this resulted in a GSD of ~ 0.02 m, allowing the ice surface to be imaged at a much finer spatial resolution than was obtained in 2019. Finally, to ensure optimal spatial coverage (and thus good image overlap), the UAV was flown at a constant speed of 7.5 m/s with an equal spacing between parallel lines of 58 m, equating to an image overlap and sidelap of 80% and 70% respectively.

TABLE 4 Flight settings used when undertaking the UAV surveys in July 2021.

Survey Parameters	2021
Take-off and Landing (TOL) Altitude (m.a.s.l.)	13.85
UAV flying height above lake level (m)	110
UAV flying height above surface (m)	90-95
Image Overlap	80%
Image Side lap	70%
Ground Sampling Distance (GSD) (m)	0.02

All surveys were flown using the GS Pro app. Before each survey, the external antennae and camera were attached to the Inspire, before being connected to the Emlid Reach M+ unit on the underside of the UAV. Next, the relevant survey route to be flown was selected within the GS Pro app. Each survey was then flown automatically from take-off to landing directly within the app, with the UAV autonomously following the pre-defined survey route. Manual input was only then required when necessary, such as during the onset of rain. During each survey, flight data and the survey route being undertaken were directly monitored within GS Pro in case manual intervention was required.

4.1.2.3 *Georeferencing*

To ensure the UAV-derived imagery, and indeed the final 3D models, could be georeferenced to a high level of accuracy using the on-board differential carrier-phase GNSS, it was crucial that a base station was set up within the study area. This was used to provide a stationary reference point, which could then be utilised to provide differential corrections during post processing. In this research, two different base stations were set up in the field (one for redundancy purposes), the first an Emlid Reach RS2, the second a Leica GS10, with the former used for post-processing of the UAV data. Each base was set up on an area of stable ground, ~ 200 m from the glacier with a clear sky view and with over 20 m between the two in order to avoid any potential interference. The height of each base station above ground level was then recorded using a tape measure upon initial setup for each day. Both base stations were set to collect RINEX (Receiver Independent

Exchange Format) data on their relative positions which could then be post-processed using a larger base station network (e.g. AUSPOS, CORS) to obtain a Precise Point Positioning (PPP) solution. Finally, and to allow for optimum post-processing, both base stations were left to log for at least four hours while in the field, with at least one hour of logging before and after the first and last survey were undertaken, respectively.

Whilst the Emlid Reach GNSS module is capable of Real-Time Kinematic (RTK) correction (i.e. by providing accurate positioning of the UAV in real time), it was decided that in this research it would be more suitable to use Post-Processed Kinematic (PPK) mode, i.e. where high accuracies are obtained by post-processing the rover and base log files after each flight had been completed (Chudley et al., 2019; Jouvét et al., 2019). This was done for two main reasons: (i) PPK does not require a reliable real-time radio link be maintained with the GNSS base station during surveys, which can introduce additional technical constraints, and (ii) it is often more accurate than the RTK mode as precise satellite ephemeris data are available during post-processing for both the base station and the rover. This is important as only by knowing satellite locations to the utmost possible degree can high positional accuracies be obtained (Karaim et al., 2018; Chudley et al., 2019). This is discussed in more detail in Section 4.1.3.

As mentioned previously, the key advantage of differential carrier-phase GNSS positioning is that it allows for the accurate georeferencing of UAV-derived imagery (and subsequent 3D models) without the need for a network of GCPs (van der Sluijs et al., 2018; Chudley et al., 2019). However, despite the use of direct georeferencing in this fieldwork, a small network of ten GCPs were still deployed across the study site for redundancy (Figure 45).

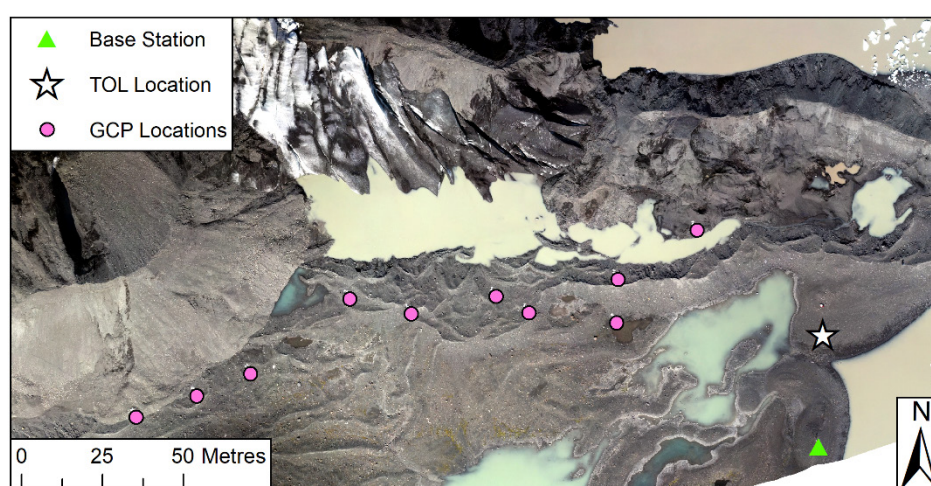


FIGURE 45 GCP locations (pink circles), UAV launch site (TOL, white star) and Leica base station location (green triangle) for the 2021 surveys. Background is the orthomosaic from the 7th July 2021.

The GCPs used here were the same thick, high contrast 1x1 m markers used in 2019, deployed across stable ground near the lateral margin of the glacier ensuring a good spread in the X, Y and Z planes. The positions of each marker were then recorded in the field using a Leica GS15 dGPS with an accuracy of <1 cm. Although it was intended that all UAV-derived imagery would be accurately processed using the direct georeferencing method, a technical issue with the hot-shoe adaptor on the 15th July meant that no positional or timestamp data were recorded for any of the acquired images. As a result, the images from this day were instead georeferenced using the known GCP locations deployed in the field.

4.1.3 Post-Processing of UAV Data

The UAV imagery acquired in 2019 did not require any post-processing, and so each image 'set' (i.e. all the images acquired from one survey day) were directly loaded into Agisoft Metashape for 3D model generation. As a result, this section will focus solely on the post-processing undertaken on the imagery acquired in 2021.

4.1.3.1 GNSS Processing (*Base and Rover*)

The creation of high accuracy PPK positional data for 3D model generation strongly depends on the position of the user base station being precisely known. To do this, the raw base station data for each survey day were uploaded in RINEX format to the web server AUSPOS (<https://gnss.ga.gov.au/auspos>), which then corrected the position of each base station to a high degree of accuracy using the 15 nearest International GNSS Service stations (Dow et al., 2009). The positions of these stations are known to within 1 mm horizontal and 2 mm vertical accuracy, allowing for the precise positional processing of a user base station. This method will result in horizontal and vertical positional accuracies of up to 0.01-0.02 m, assuming the user base station was set up to record for over four hours (Gillins et al., 2019, OPUS, 2020). The reports generated by these servers were then used to improve the positional quality of the original RINEX file through the download of a new RINEX file with updated headings. This updated positional data was subsequently used within the post-processing routine of the Emlid Reach M+ to improve the accuracy of the resultant image locations.

To accurately process this rover data, it was first downloaded in RINEX format before being imported into RTKPOST_QT for processing, which is a modified version of the RTKLIB software provided by Emlid (<https://docs.emlid.com/reach/tutorials/post-processing-workflow/gps-post-processing>). This was then used to update the positional information of each photo tag for each survey using the processed base station data from the same day. In this process, both forward

and backwards Kalman Filtering is utilised, which is designed to estimate unknown variables over time before using these to improve positional accuracy (Kim and Bang, 2018). This refines the flight path of each UAV survey, and provides each survey with a positional solution depending on its post-processed accuracy. Q1, or a fixed solution, is obtained when at least 95% of the survey is defined by cm-level positional accuracy (Emlid, 2021b). Q2, or a float solution, represents a survey defined by sub-metre accuracy, while Q5, or a single solution, represents metre-level accuracy or greater (Emlid, 2021b).

Of the 23 surveys undertaken in July 2021 (not including the 15th), 21 obtained a Q1 positional solution (98% or higher), however, the remaining two, like survey three on the 6th July, were strongly defined by a Q2 solution, which lowered their overall positional accuracy (Figure 46).

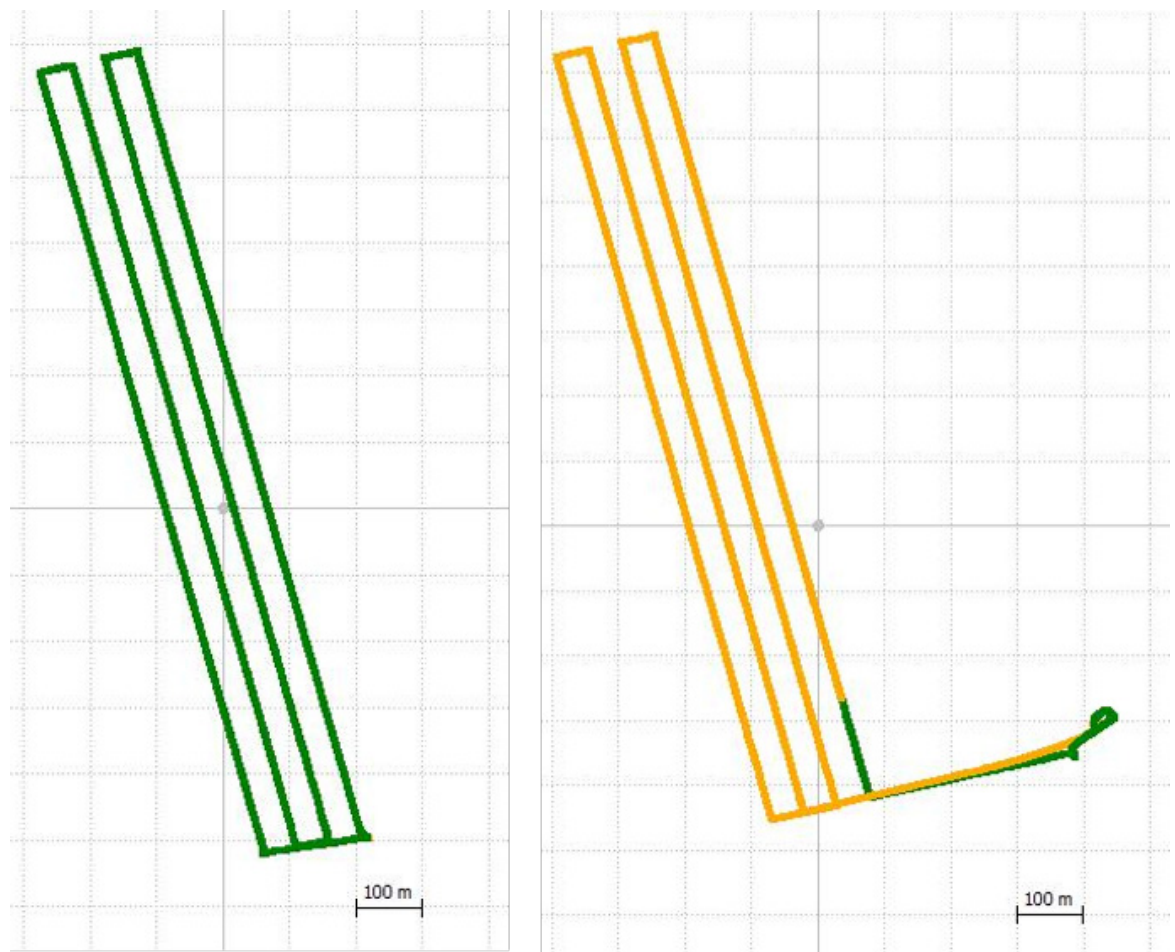


FIGURE 46 Examples of a Q1 (left) and a Q2 (right) positional solution, obtained on the 6th July 2021 for surveys one and three, respectively. These images were directly captured from RTKPLOT_QT.

The reason these surveys were predominately defined by a Q2 solution is likely due to the number and position of satellites in the sky at that time. A low number of visible satellites, as well as poor satellite constellation geometry, means the rover is unable to obtain sufficient corrections

from the base in order to accurately define the position of the UAV at the time of image acquisition (Hall et al., 2010; Karaim et al., 2018; Emlid, 2021b). It is also important to note that although this outputted positional information was accompanied by an events file that specified the location of each image, on numerous occasions these event files were not correctly recorded, meaning several photos did not have corresponding event information. This is likely linked to the hot-shoe error that occurred on the final day of surveying.

4.1.3.2 *Image - Position Matching*

The next step in the post-processing of the rover data was to update the metadata of each image using the position event files created in RTKLIB. Before this could be done, however, the images had to be converted from UTC time (which they were captured in) to GPS time due to the 18-second discrepancy between the two timing conventions. This was achieved using a simple metadata adjustment script within Python, which updated the images before writing them to a new folder in order to maintain copies of the raw data.

The updated images from each individual survey were then imported into the software Toposetter (<https://www.topodrone.org/news/event/software-toposetter-2-0/>) for processing. In this step, manual selection is used to match one image to an appropriate event file (i.e. so their metadata closely match), with the software then matching subsequent images based on their nearest corresponding time. To allow maximum tolerance between image and position timestamp, and because the image timestamps are accurate to the nearest whole second, a tolerance of 1000 m/s was utilised to account for any possible rounding errors. Furthermore, as the images were captured approximately every 3 seconds along a flight line, by utilising this tolerance setting the likelihood that the event positions were assigned to an incorrect image is greatly reduced.

As mentioned previously, some event position files were not correctly recorded when processing the raw RINEX data in RTKLIB, and as such, an additional step must be taken to account for this missing data. When the image and position files are matched in Toposetter, the updated images with new metadata are saved in a subfolder within the directory of the original image folder. As a result, no photos that were not matched in the previous step were copied across to this new folder. However, because each flight collects ~228 photos, undertaking a manual comparison would be time consuming and would likely lead to images being missed. To address this a simple Python script was run instead, which by comparing the contents of both folders allowed all photos present in the original, but not in the updated, folder to be copied across to a new, separate subfolder. Doing so aids in the assignment of relevant accuracy data for each flight when undertaking SfM processing.

Once the above steps were complete, each image 'set' could then be imported into Agisoft Metashape for SfM processing. Firstly, all the matched images with updated metadata were imported and given a positional accuracy of 0.05 m, based on the output quality of the post-processing undertaken. Those images without updated metadata were then imported with their original positions. These were assigned an accuracy of 20 m to reflect their reduced positional quality, which forces Metashape during image alignment to modify the locations of these cameras to better fit with the higher quality image positions. This step is important as it allows the combination of both high- and poor-quality location information, without reducing the quality of the final 3D models.

4.2 3D Model Generation

4.2.1 SfM Photogrammetry

All SfM processing was undertaken using the commercially available software package Agisoft Metashape (Agisoft LLC, 2021). An overview of each step of the workflow is shown in Figure 47, while a more thorough outline of each step, including parameters used, is detailed below. Firstly, an initial alignment procedure was undertaken based off the positional information of the imported imagery. In this step, Metashape finds the camera position and orientation for each photo and builds a sparse point cloud made up of several hundred thousand points. All images were aligned using the 'highest' accuracy setting to allow the software to more accurately estimate camera positions, while all other parameters were kept as default.

For the 2019 surveys, the resultant point clouds were created in an arbitrary coordinate system, so to align the models to real-world coordinates they first had to be georeferenced using the deployed GCPs. In this step, the centre of each GCP was manually marked within each photo and their coordinates (including accuracy and elevation) imported into Metashape to optimise spatial accuracy and 3D model geometry (Rossini et al., 2018). While the majority of the identified GCPs were used to georeference the final model ('control' points), a small subset were not selected for this process, and were instead used as 'check' points. These points were used to independently validate the accuracy of the camera alignment and optimisation procedures, as well as the overall accuracy of the final models (Bash et al., 2018). The number of GCPs used as both 'control' points and 'check' points for each survey date, are shown in Table 5.

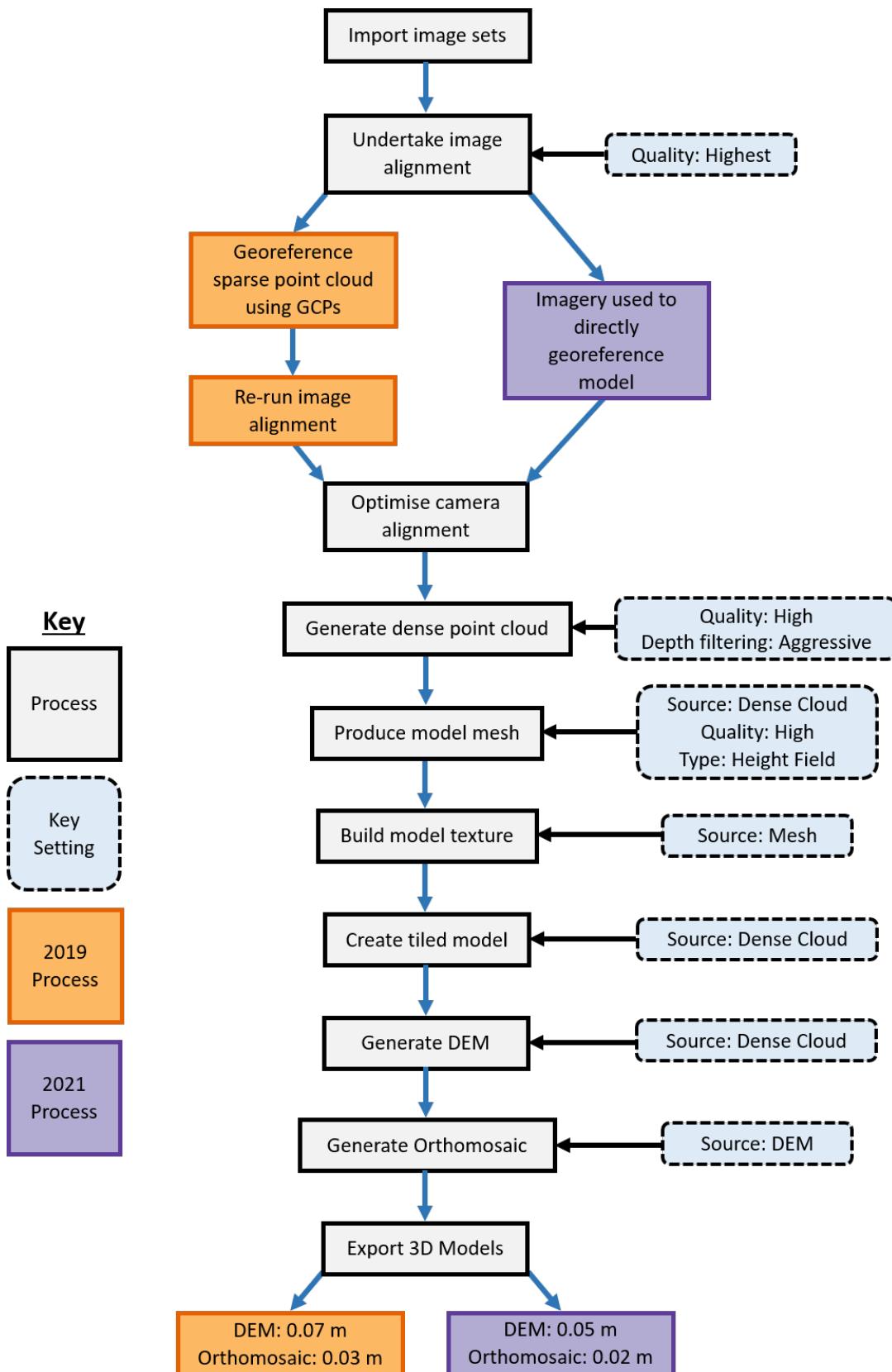


FIGURE 47 The SfM workflow that was utilised to process the UAV-derived imagery from 2019 and 2021 into high-resolution DEMs and orthomosaics of the ice surface. Key settings used and those steps specific to the processing of the 2019 and 2021 imagery are also shown.

TABLE 5 Details of GCPs used for the processing of the UAV imagery from July and September 2019. This includes the overall number, the number of GCPs used as 'control' points (to georeference the model) and the number used as 'check' points (to assess final model accuracy).

Date	Photos Used	Total GCP Number	'Control' Points	'Check' Points
5 th July	559	6	4	2
6 th July	979	6	4	2
7 th July	981	9	6	3
9 th July	539	9	6	3
19 th September	554	11	7	4
20 th September	404	11	7	4
21 st September	1005	11	7	4

This step was not required for the 2021 data as the resultant point clouds were already directly georeferenced using the post-processed image positional data. The only exception to this was for those surveys undertaken on the 15th July, where a technical issue with the hot-shoe adaptor meant no positional information was recorded. Instead, the sparse point cloud was georeferenced using the GCP locations (like in 2019), with seven of the GCPs used as 'control' points, and the remaining three as 'check' points.

Following georeferencing, the camera positions were then optimised using the now-known reference coordinates to remove non-linear deformations and georeferencing errors from the final models (Agisoft LLC, 2021). The next step involved using the camera information from the georeferenced sparse point cloud to generate a dense point cloud, made up of several hundred-million points. These dense point clouds were constructed using the high quality and aggressive depth filtering parameters. The high-quality setting was utilised to balance reconstruction accuracy with computational time, while aggressive depth filtering removed noise on any relatively smooth surfaces, such as snow and ice (Bash et al., 2018). Following this, a polygonal surface mesh was reconstructed, using the high quality and height field surface type parameters. Using a high-quality setting allows more detailed and accurate geometry to be obtained, while the height field surface type is best used for the modelling of planar surfaces. The mesh was also reconstructed using the dense point cloud as the data source to generate a higher quality output (Agisoft LLC, 2021). The next step was to build texture for the final model. This is an important

step as proper texture mapping selection can help obtain optimal texture packing, and consequently, better visual quality of the final model (Agisoft LLC, 2021).

A tiled model could then be generated, which allows for responsive visualisation of large 3D model areas in high resolution, using the dense point cloud as the data source. In this step, the default parameters suggested by Metashape were used. The pixel size of the tiled model was estimated automatically, and reflected the effective resolution of the input imagery (0.03 m in 2019, 0.02 m in 2021). From this, DEMs of the ice surface could be produced, which were based off the dense point cloud data for each survey day to ensure the most accurate model generation (Agisoft LLC, 2021), with the default settings within Metashape again utilised. The resolution of each DEM was estimated from the effective ground resolution of the source data, with the generated DEMs from 2019 and 2021 having a resolution of ~0.07 and ~0.05 m respectively. The final step involved the generation of high-resolution orthomosaics for each survey day. These were created using the previously produced DEM as the data source to ensure efficient data processing, with Metashape automatically estimating orthomosaic resolution using the GSD of the source data. Both the DEMs and orthomosaics were then exported from Metashape at resolutions of 0.07 and 0.03 m (2019), and 0.05 and 0.02 m (2021), for further analysis.

4.2.2 Uncertainty Analysis

The results of the accuracy assessment show that the calculated uncertainties obtained in this research are low (and, therefore, well within the realms of acceptability), with overall mean uncertainties of 0.088 m, 0.291 m and 0.241 m reported for the July and September 2019, and July 2021 surveys, respectively. The assessment methods utilised in both 2019 and 2021, as well as the individual uncertainty values obtained from these surveys will be outlined in more detail below.

4.2.2.1 2019 Field Season

For the 2019 surveys, several different methods were employed with which to test the accuracy of the SfM processing workflow and the overall accuracy of the final, exported DEMs and orthomosaics. The first of these involves what is known as the Reprojection Error, which is the distance, measured in pixels, between the point on the image where a constructed 3D point can be projected and the original projection of that 3D point detected on the photo, which are then used as a basis for the 3D reconstruction procedure (Agisoft LLC, 2021). This marker Reprojection Error is then calculated over all photos where the marker is visible, and is generated automatically by the Metashape software.

The second method relates to the ability of the SfM algorithms to accurately reconstruct the position of each GCP within the model, based off the imported coordinates. This GCP error is automatically generated within Metashape following the image alignment and camera optimisation procedures, and is calculated by measuring, in metres, the distance between the input coordinates of each marker (defined by the user), and the estimated position of the same marker in the reconstructed model (Agisoft LLC, 2021).

The final method involved testing the horizontal and vertical accuracy of the final products (DEMs and orthomosaics) using the check points that were set aside from the original GCPs. To assess horizontal accuracy, the generated orthomosaic and check point locations for each day were imported into ArcMap before manually measuring the distance between the original and reconstructed position of each marker in both the X and Y horizontal plane using the 'measure' tool. This was carried out at a scale of 1:5 to ensure the best identification of the centre of the reconstructed targets (Bash et al., 2018). Vertical accuracy was also assessed in ArcMap, but by using the DEMs instead of the orthomosaics. Generated DEMs for each day, along with the check point locations from the same day were imported into ArcMap, before subtracting the actual elevation of each check point from the reconstructed elevation of the same points. The RMSE of the horizontal and vertical offsets were then calculated separately, before calculating the combined RMSE of both for each survey completed. The final error values for the three methods are shown in Table 6 and 7.

Overall, the lowest reprojection, GCP and final model errors are found for those surveys undertaken in July, whereas greater errors are consistently found for those surveys undertaken in September. The reprojection errors between the surveys are similar, with errors in July and September varying by 0.2 pixels' maximum, but these errors are still consistently lower in the former than the latter. In comparison, the GCP and final model errors are far lower for those surveys undertaken in July than those undertaken in September, by an order of magnitude (cm-dm scale).

Total GCP RMSE, calculated in Metashape for the 5th, 6th, 7th and 9th of July was 0.047 m, 0.038 m, 0.098 m, and 0.049 m, respectively. Final model errors for the same period are slightly higher, but similar to those values reported in Metashape, with 0.122 m (5th), 0.216 m (6th), 0.086 m (7th) and 0.050 m (9th) recorded.

In comparison, total GCP RMSE for 19th, 20th and 21st September was 0.380 m, 0.385 m and 0.378 m, respectively. However, unlike those surveys in July, the final model errors for the September surveys are lower than the GCP RMSE errors, with values of 0.225 m, 0.184 m and 0.189 m recorded for the 19th, 20th and 21st September respectively. Interestingly, closer inspection of the

individual horizontal and vertical errors reveals that in September it is the horizontal errors that are consistently in the dm-scale. The vertical errors, meanwhile, are consistently in the order of a few centimetres, and as a result actually show good agreement with the vertical errors obtained from the July surveys.

TABLE 6 Reported and calculated errors for the GCP placement and final models for the July surveys. Reprojection and GCP errors are calculated within Metashape, final model errors are calculated within ArcGIS.

	5 th July	6 th July	7 th July	9 th July
Reprojection Error (pixels)	0.922	0.773	0.713	0.744
Reported GCP RMSE (m)				
XY (Horizontal)	0.056	0.045	0.111	0.063
Z (Vertical)	0.025	0.037	0.052	0.019
Total	0.047	0.038	0.098	0.049
Final Model Errors (m)				
XY (Horizontal)	0.153	0.159	0.111	0.048
Z (Vertical)	0.092	0.272	0.074	0.081
Total	0.122	0.216	0.086	0.050

TABLE 7 Reported and calculated errors for the GCP placement and final models for the September surveys. Reprojection and GCP errors are calculated within Metashape, final model errors are calculated within ArcGIS.

	19 th September	20 th September	21 st September
Reprojection Error (pixels)	0.945	0.972	0.921
Reported GCP RMSE (m)			
XY (Horizontal)	0.470	0.488	0.486
Z (Vertical)	0.031	0.070	0.030
Total	0.380	0.385	0.378
Final Model Errors (m)			
XY (Horizontal)	0.378	0.348	0.354
Z (Vertical)	0.073	0.080	0.043
Total	0.225	0.184	0.189

Such discrepancies in horizontal model error between the July and September surveys may be due to two different factors. Firstly, the accuracy of the 3D models obtained through SfM photogrammetry is highly dependent on the number and distribution of GCPs used in the procedure, whereby using a larger number of well-distributed GCPs provides a more accurate solution that is less sensitive to error at any one point (James and Robson 2014; Sanz-Ablanedo et al., 2018). Using fewer GCPs, or placing them closer together, can lead to underestimations of error and thus can negatively influence the quality of the final models (Micheletti et al., 2015).

For example, it was shown by Sanz-Ablanedo et al. (2018) that when using a small number of clustered-together GCPs (five) as the control, the horizontal errors reported in Metashape were often extremely low. This is because the deformation that occurs in the model during the Bundle Adjustment procedure satisfies the small number of geometric restrictions imposed by the GCPs, resulting in low errors. However, while this may seem encouraging, following analysis of the check points it becomes evident that this actually results in significant errors at these points, leading to inaccuracies in the final model (James and Robson, 2014; Sanz-Ablanedo et al., 2018). Increasing the number of GCPs, however, will reduce the scatter of the RMSE values for each point, causing the overall horizontal error to increase slightly. This slight increase, however, does not reflect an issue with the georeferencing system, rather it indicates that the robustness of the system has improved as more GCPs are being used, meaning the ability of the Bundle Adjustment procedure to adapt to all the GCPs has decreased (Sanz-Ablanedo et al., 2018). Simply put, the more points there are available for georeferencing, the smoother the average and thus the more robust the error within the system (Sanz-Ablanedo et al., 2018).

This underestimation of error may be present in the results reported here, particularly in the horizontal errors resulting from the July surveys. On the 5th and 6th, only four GCPs were used as control points, with two used as check points, resulting in GCP errors of <0.06 m, but check point errors of ~0.16 m. In contrast on the 7th and 9th, six GCPs were used as control points, with three used as check points, yet while the GCP error increased slightly (~0.11 m), the check point error decreased to between ~0.06 and 0.11 m. Such a pattern suggests that the GCP errors reported on the 5th and 6th may have been underestimations due to the low number of GCPs used to georeference the models on those days. Meanwhile, the values reported on the 7th and 9th are likely to be more accurate because more GCPs are being used as control points, reducing the scatter of RMSE values and thus smoothing the average (Sanz-Ablanedo et al., 2018), which is supported by the lower check point errors also reported on these days compared to the 5th and 6th. Interestingly, in September seven GCPs were used as control points with the remaining four used as check points, yet the GCP error is around three times greater than the same errors obtained in July. The check point errors meanwhile are two and a half times greater than the

values obtained on the 5th and 6th July, and nearly four times greater than those obtained on the 7th and 9th. Although these differences could again simply be due to the greater number of GCPs used in September than in July, leading to a more robust final error, a second factor may be more important in this instance.

Instead, such discrepancies may be due to the different illumination conditions that were present at the time the surveys were undertaken, which may have influenced the scene reconstruction process during image alignment. Image texture and resolution strongly controls the number of keypoint matches identified during the 'Feature Detection' step of the SfM workflow (Westoby et al., 2012). The higher the image resolution and the more textures present within, will lead to a greater number of successful matches, and therefore, more accurate scene reconstruction (Westoby et al., 2012; Smith et al., 2016). Image texture, in turn, is strongly controlled by variations in lighting around the scene of interest (Bemis et al., 2014). Changes in lighting and strong shadows across the scene will negatively influence image texture, interfering with keypoint matching and thus accurate scene reconstruction by introducing greater errors (Smith et al., 2016). As such, illumination conditions when capturing images should ideally be diffuse (bright, but overcast) to ensure scene texture is reconstructed accurately, but not too bright (to avoid shadowing), nor too dark (to ensure no loss of image texture) (James and Robson, 2012; Bemis et al., 2014).

For the July surveys, illumination conditions were consistently favourable to ensure no loss of texture within the captured images (Figure 42), leading to a higher number of keypoint matches, more accurate scene reconstruction, and lower GCP and final model errors as a result (James and Robson, 2012; Westoby et al., 2012). This is because scene geometry can only be accurately determined when the locations of the GCPs within the scene are also accurately reconstructed during the alignment procedure (James and Robson, 2012).

In comparison, illumination conditions in September were much darker (Figure 42) which likely had a significant impact on image texture over parts of the survey area. This is particularly likely for those images taken over the moraine ridge at the lateral margin of Fjallsjökull, upon which the GCP network was placed. This is because the moraine material itself was also particularly dark during this time, much darker than the same material was during the July surveys. These illumination conditions may have also affected the camera shutter speed, potentially resulting in a further reduction in image quality (through blurring of images) and thus image texture (Westoby et al., 2012). It is possible that both these factors, combined with the dark, overcast skies, had a significant impact on the ability of the SfM algorithms to generate a high number of successful keypoint matches within this area due to the lack of image texture. This would have influenced

the accuracy of the scene reconstruction, leading to higher georeferencing errors (James and Robson, 2012) and potentially explaining why dm-scale horizontal errors are observed for the September surveys.

4.2.2.2 2021 Field Season

In comparison to 2019, two slightly different approaches were used for the 2021 surveys to assess both the accuracy of the SfM processing, as well as the overall accuracy of the final 3D models. The first method assessed the ability of the SfM algorithms to accurately reconstruct the camera positions based off the imported imagery, with the error automatically calculated following image alignment and optimisation. This error is calculated by measuring the offset between the imported image coordinates, and the estimated camera positions of the same images following alignment (Agisoft LLC, 2021).

However, because several of the imported images were given accuracies of 20 m (due to missing event files) (Section 4.1.3.2); the resulting processing errors were far greater than the actual error of the method. This was most likely due to the large vertical errors, which were a result of a 30-40 m offset between the unprocessed elevations given in the image metadata, and the actual post-processed elevations. Therefore, by including these images in the alignment procedure it most likely resulted in a far greater processing error because the image matching algorithms had to move the 'wrong' camera positions in line with the 'correct' post-processed positions. To address this, the image reference data for each survey were exported from Metashape post-image alignment and the processing error recalculated using only those images that were originally imported with an accuracy of 0.05 m. As these inaccurate images only made up a small number of the total images used to process each survey, by removing them from the assessment it provides a far more robust and representative solution of the processing error for each survey day.

The second method originally involved assessing the accuracy of the final 3D models using the GCPs deployed across the field site. However, following SfM processing there was a constant offset between the locations of the GCPs recorded using the Leica dGPS, and the reproduced locations of the same GCPs in the orthomosaics which were georeferenced using the Reach base and rover (similar offsets were also found by Jouvét et al. (2019)). This offset was not known, but to estimate it would have introduced large errors and thus it could not be accurately assessed. However, because the locations of the reproduced GCPs were consistent between each survey day, it meant these could be averaged to obtain a new overall estimate of the central position of each GCP (i.e. 10 new GCP locations). These newly estimated center points were then used to approximate the overall accuracy of each model by calculating the XYZ RMSE offset between the new center points, and the reproduced GCP center in each model, thus providing a robust

solution. It is also worth noting that due to technical issues (predominately with batteries), the Leica base stopped logging or switched off entirely on several of the survey days, meaning it could not be used to georeference the Inspire imagery.

These two methods were used to assess the accuracy of all surveys undertaken between the 4th and 12th July 2021. However, the surveys undertaken on the 15th July needed to be assessed slightly differently due to an issue with the camera hot-shoe adaptor (Section 4.1.2.3). Although the images were captured as normal, no event files were recorded with which to update the metadata, meaning the imagery could not post-processed in the same way. Instead, the model was georeferenced using the reproduced GCP locations from the 12th July (as this was the closest date to the 15th, taking into account any warping in the model). As a result, the accuracy of the SfM processing undertaken on the 15th July was assessed using the GCP marker error automatically calculated in Metashape following image alignment (like in 2019). The overall accuracy of the 3D models from the 15th July was then assessed using the three check points set aside from the original 10 GCPs (in a similar way to 2019). These were used to assess the reproduced GCP positions from the 15th to the 12th July, as well as the positions from the 15th to the overall average reproduced GCP positions. These were then combined to give an overall RMSE for this day. The final overall errors for all surveys undertaken in 2021 are shown in Table 8.

TABLE 8 Camera position and final model errors calculated for the July 2021 surveys. The camera errors were calculated within Metashape before being exported for further refinement, while final model errors were calculated using the reproduced GCP locations. *For the surveys undertaken on the 15th July, the processing error was instead calculated using the GCP locations from the 12th July (see text for more details).

	4 th July	6 th July	7 th July	8 th July	9 th July	10 th July	11 th July	12 th July	15 th July*
Reported Camera RMSE (m)									
XY (Horizontal)	0.232	0.458	0.525	0.489	0.526	0.530	0.518	0.496	0.541
Z (Vertical)	0.026	0.081	0.035	0.041	0.034	0.042	0.036	0.037	0.040
Total	0.129	0.270	0.280	0.265	0.280	0.286	0.277	0.267	0.291
Final Model Errors (m)									
XY (Horizontal)	0.597	0.318	0.296	0.215	0.119	0.163	0.111	0.204	0.234
Z (Vertical)	0.503	0.082	0.119	0.262	0.165	0.186	0.260	0.062	0.103
Total	0.550	0.200	0.207	0.238	0.142	0.175	0.185	0.133	0.168

Overall, for all surveys, both the SfM processing errors, and the final model errors, show very good agreement with each other. The average processing error for all surveys is 0.260 m, with eight of the nine days all having a total error of between 0.265 and 0.291 m. The only exception to this is the 4th July, which has an error of 0.129 m. Closer inspection of all individual horizontal and vertical errors show that it is consistently the horizontal errors that are greater than the vertical, by an order of magnitude (dm-cm scale).

In comparison, the final model errors are generally lower than the processing errors, by the order of several centimetres. Indeed, the average final model error for all surveys is 0.222 m, with eight of the nine days having a total error of between 0.142 and 0.238 m. Again, the only exception to this is the 4th July, but interestingly the final model error is much higher than for the other days, at 0.550 m, owing to XYZ errors of >0.5 m. Closer inspection of the individual horizontal and vertical errors again shows the same general pattern, however, four of the surveys have higher vertical errors than horizontal (e.g. 8th, 9th, 10th, 11th July). It is also worth noting that these errors (both processing and final model) show good agreement with those errors obtained from the September 2019 surveys, while they are not significantly greater than those obtained in July 2019. Finally, the cm-dm scale horizontal and vertical uncertainties obtained in this analysis further illustrate how PPK-enabled direct georeferencing can be used to produce highly accurate 3D models, without the need for a network of ground-based GCPs (e.g. Benassi et al. 2017; Chudley et al., 2019; Yang et al., 2020), highlighting its suitability for glacial research in remote locations.

4.2.2.3 *Comparison to Previous Studies*

The horizontal and vertical errors obtained in both the 2019 and 2021 surveys importantly show good agreement with those previous studies in glaciology that have utilised the UAV-SfM approach. For example, Kraaijenbrink et al. (2016) obtained horizontal errors of ~0.2 m during their surveys of Lirung Glacier in Nepal; Rossini et al. (2018) were able to acquire errors of ~0.1 m during their study of Morteratsch Glacier in the Swiss Alps, while Xue et al. (2021) obtained horizontal errors of ~0.5 m over two glaciers in the Tibetan Plateau. Meanwhile, Rossini et al. (2018) obtained vertical errors of between 0.038 m and 0.145 m over Morteratsch Glacier, Bash et al. (2018) obtained errors of between 0.015 m and 0.047 m in their study of Fountain Glacier, Arctic Canada, while in a separate study over the same glacier Whitehead et al. (2013) were able to obtain vertical errors of ~0.04 m.

Furthermore, although the direct georeferencing technique is not yet widely utilised in glaciology, the errors resulting from the 2021 surveys also importantly show good agreement with those few studies to date that have utilised this method in their research. For example, Chudley et al. (2019) obtained horizontal and vertical errors of 0.12 m and 0.14 m respectively over Store Glacier,

Greenland, Jouvét et al. (2019) acquired horizontal errors of between 0.25 m and 0.4 m through their surveys over Eqip Sermia, a large tidewater glacier in west Greenland, while Yang et al. (2020) obtained horizontal errors of ~0.13 m over Parlung No. 4 Glacier, Tibetan Plateau.

Overall then, the results of the uncertainty analysis indicate that the errors found for both the 2019 and 2021 surveys are no greater than the change expected over each period of interest and are thus well within the realm of acceptability. This ultimately means the DEMs and orthomosaics generated from these surveys can be reliably used to undertake further analysis of the glaciological processes occurring at Fjallsjökull during this time.

4.3 Glacier Velocity (Feature Tracking)

Feature tracking is a widely-used technique which involves tracking distinct surface features by cross-correlation of image patterns between two repeat pairs of images to determine the surface velocity (Luckman et al., 2007; Tiwari et al., 2014; Robson et al., 2018), and has been utilised in numerous studies to obtain good results for both satellite (e.g. Haug et al., 2010; Herman et al., 2011) and UAV (e.g. Ryan et al., 2015; Kraaijenbrink et al., 2016) imagery. Here, features were tracked using cross-correlation on orientation images (CCF-O), using the free software *CIAS* (<https://www.mn.uio.no/geo/english/research/projects/icemass/cias/>), developed by the University of Oslo (Kääb and Vollmer, 2000; Kääb, 2002) which allows glacier surface displacements to be calculated with sub-pixel accuracy. CCF-O was chosen in this research over other methods (such as NCC) because it uses the gradients between neighbouring pixel values to calculate displacements, rather than the raw digital values (Robson et al., 2018). This reduces the impact of shadows and changing illumination conditions on the final displacements, both of which are common in glacierised regions (Fitch et al., 2002; Heid and Kääb, 2012).

To quicken processing, each orthomosaic was resampled to a resolution of 0.25 m, before georeferencing each orthomosaic pair in ArcGIS before importing into *CIAS*. The processing parameters varied depending on the temporal separation between orthomosaics, with these given in Table 9. Resulting displacements were filtered by direction and magnitude (Robson et al., 2018). All displacements with a signal-to-noise ratio lower than 0.5 were removed, before manually identifying all displacements whose direction or magnitude varied by more than 20% to the mean values. The displacement fields were then interpolated using ordinary kriging to produce velocity rasters for each time period.

To determine the uncertainty of the velocity calculations, displacements were measured over areas of stable ground that contained variable surface topography (e.g. Chudley et al., 2019; Jouvét et al., 2019). This analysis was undertaken over three distinct zones close to the glacier

margin that were covered by both the 2019 and 2021 surveys (Figure 48), before calculating the combined stochastic standard deviation. Stable ground locations were chosen as theoretically no change should have occurred in these locations, and as such, they provide a good estimation for the accuracy of the feature tracking calculations.

TABLE 9 Parameters used in CIAS for each time period investigated, as well as a brief description of each parameter for reference.

Time Period Between Orthomosaics				
Parameter	24 Hour (1 day)	48 Hour (2 day)	72 Hour (3 days)	Description
Reference Block (pixels)	15	15	15	Size of the block in which the feature to be tracked is located
Search Window (pixels)	20	30	40	How far CIAS should look for the displaced feature
Reference Grid (m)	1	1	1	How many measurements are made - controls final raster resolution

4.4 Surface Elevation Change

To calculate the change in ice surface elevation between two time periods DEM differentiation was utilised, where the earlier DEM was subtracted from the later DEM to give the pattern of negative surface anomalies. For the 2019 surveys, the two periods investigated were the 5th-9th July and the 19th-21st September 2019. For the 2021 surveys, the period investigated was the 6th-15th July because the DEM obtained on the 4th covered a different (i.e. smaller) area compared to those DEMs from the subsequent eight days. To determine the uncertainty of the DEM differencing analysis, changes in elevation were measured over stable ground locations before calculating the combined stochastic standard deviation, following the same method used in Section 4.3. to assess the uncertainty of the velocity calculations (e.g. Chudley et al., 2019).

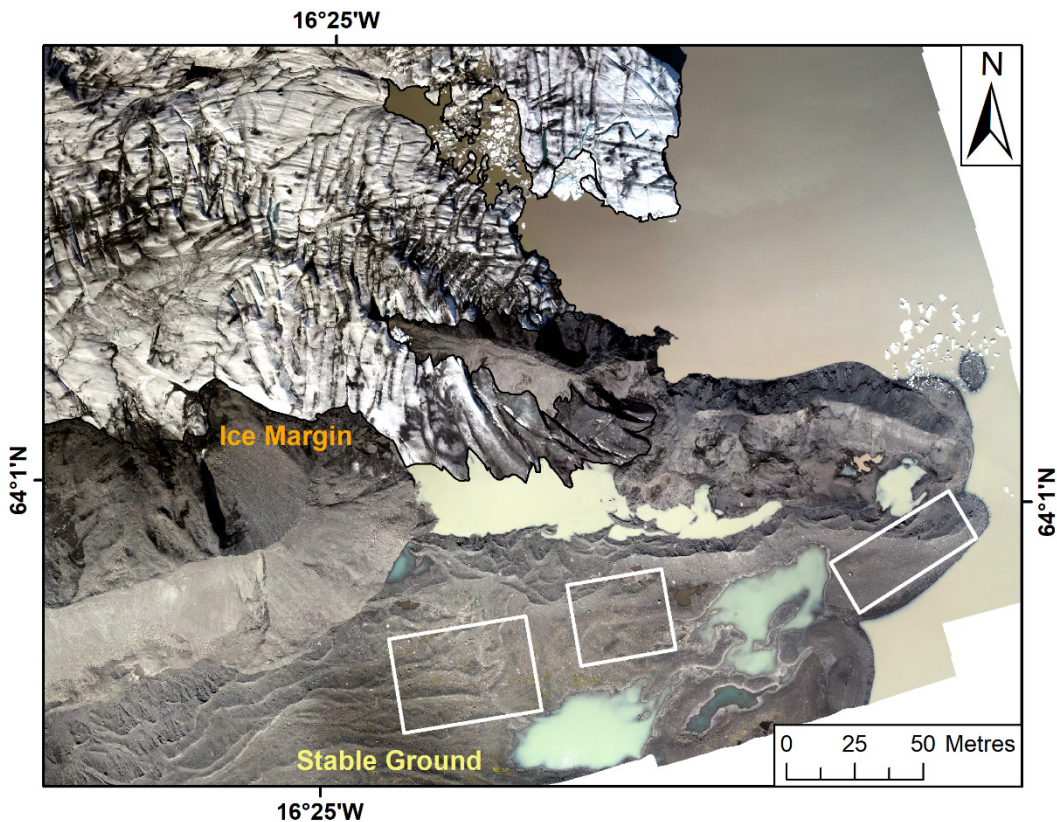


FIGURE 48 Location of the stable ground areas (white boxes) that were used to determine the uncertainty of the feature tracking and DEM differencing calculations (see Section 4.4).

4.5 Frontal Position Change and Calving Events

To assess changes in calving front geometry and evolution, the position of the terminus in each orthomosaic was manually digitising in ArcGIS at a scale of 1:30. This data was further supplemented by direct observations made in the field. To obtain an estimate of the rate of calving front retreat for each period of interest, the rectilinear box method was implemented (Moon and Joughin, 2008; Howat and Eddy, 2011), which quantifies the change in area between different terminus positions using a fixed-width rectilinear box drawn over the glacier trunk. This is then converted to a 1-D figure by dividing the change in area by the change in the width of the terminus (Howat and Eddy, 2011; Lea et al., 2014). This method was implemented in this research due to its robustness and ability to account for asymmetric changes at the calving front, allowing rates of frontal retreat to be more accurately quantified (Lea et al., 2014; Larsen et al., 2016; Dell et al., 2019). Digitisation uncertainty was quantified by repeatedly digitising the terminus of each output 20 times at a scale of 1:30 before calculating the standard error for each time period (after Baurley et al., 2020).

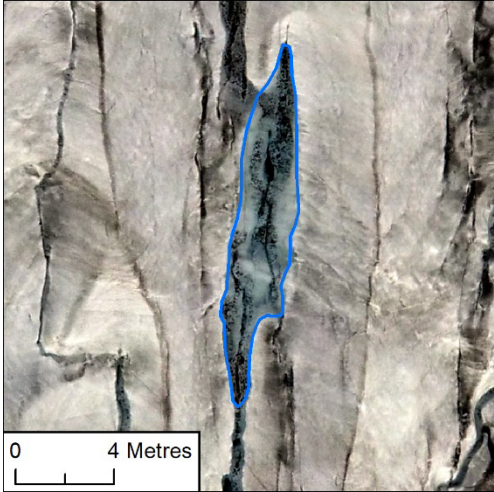
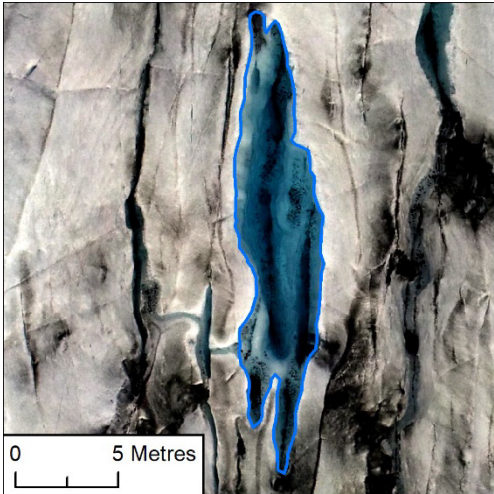
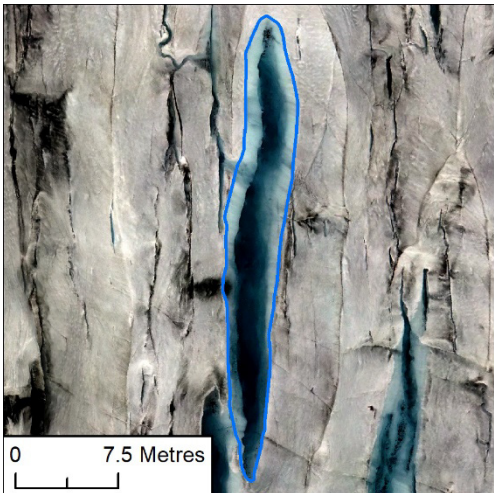
To estimate the area and volume of ice (above the waterline only) that calved between two repeat flights, DEM differentiation was again utilised. The area of each individual calving event

was manually digitised in ArcGIS, using the corresponding differenced DEM to define the horizontal extent of each event. An estimate of calving volume was then calculated for each individual event, using an above-waterline ice thickness of 20 m for both 2019 and 2021. This is the average above-waterline ice thickness for both years, and as such, the resulting calving volumes are likely to be lower-bound estimates. That said, this analysis does still provide a robust estimate of the total volume of ice lost to calving during both time periods.

4.6 Supraglacial Hydrological Mapping

Surface hydrological features, specifically lakes and water-filled crevasses (WfC), were manually digitised on each orthomosaic in ArcGIS for each time period at a scale of 1:30 using the criteria outlined in Table 10, which is a modified version of that used by Chudley et al. (2021). Here, lakes are split into “non-ponded” and “ponded” lakes to visually illustrate to the reader the difference between these features and the WfC. However, for the purpose of the analyses presented later in this research, both these lake types will be counted as one feature (supraglacial lakes) from hereon in. The delineation of these features was aided by using the raw imagery taken by the UAV for the relevant time period because it was easier to distinguish between clean ice and water on the raw images than it was on the orthomosaics (e.g. Ryan et al., 2015). Once digitised, further analysis could then be undertaken, such as investigating the size, number, and distribution of these features and how this varied over different temporal intervals.

TABLE 10 Criteria used to differentiate between the different surface hydrological features observed in this research. An example of each feature is also given for the benefit of the reader.

Feature	Criteria	Example
<div>“non-ponded” Lakes</div>	<div>Variable shape and morphology</div> <div>Pooled in surface depressions</div>	
<div>“Ponded” Lakes</div>	<div>Variable shape and morphology</div> <div>Pooled across crevasses (water not contained within crevasse walls)</div>	
<div>Water-filled Crevasses</div>	<div>Elongate features (L>W)</div> <div>Aligned transverse to flow</div> <div>Pooled in crevasses (water contained within crevasse walls)</div>	

Chapter 5 RESULTS

As mentioned in Section 4.1, the UAV surveys undertaken in both 2019 and 2021 only covered a portion of the total calving front of Fjallsjökull, and hence the results presented in this section only encompass these areas. As reference, therefore, Figure 49 shows the area of one of the UAV-derived orthomosaics from both 2019 and 2021, relative to the overall area of Fjallsjökull to help orientate the reader throughout this section.

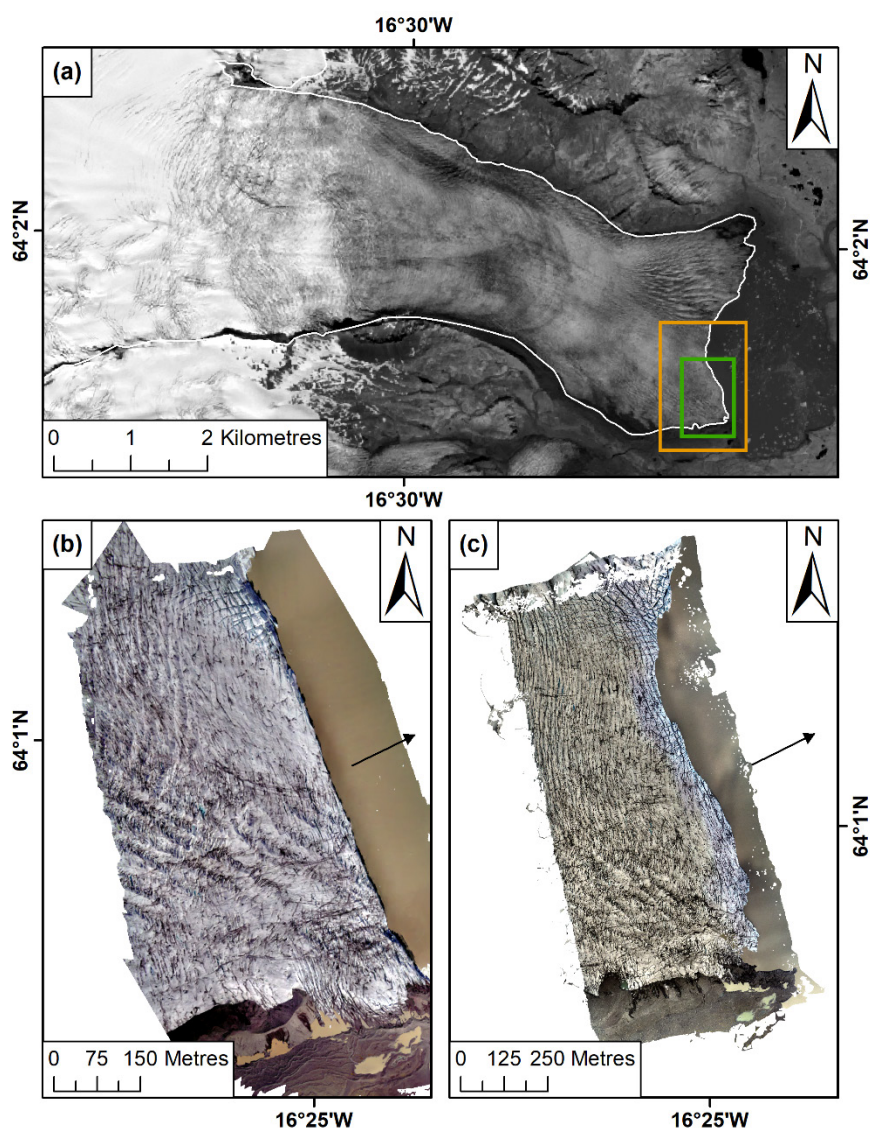


FIGURE 49 (a) Overview of Fjallsjökull, with the green and orange boxes indicating the areal coverage of the UAV surveys undertaken in 2019 and 2021 respectively. White outline is the 2021 glacier area. Background is a Sentinel 2 B8 image from 7th July 2021. (b) Example of one of the UAV-derived orthomosaics from 6th July 2019 and (c) 6th July 2021, which cover the same respective extents as shown in (a). Black arrow signifies ice flow direction.

5.1 Glacier Velocity (Feature Tracking)

5.1.1 2019 Field Season

Overall, a clear pattern of surface velocity can be observed over the study area, where for all time periods in both July and September velocities clearly increase with increasing distance from the grounded southern margin (Figure 50).

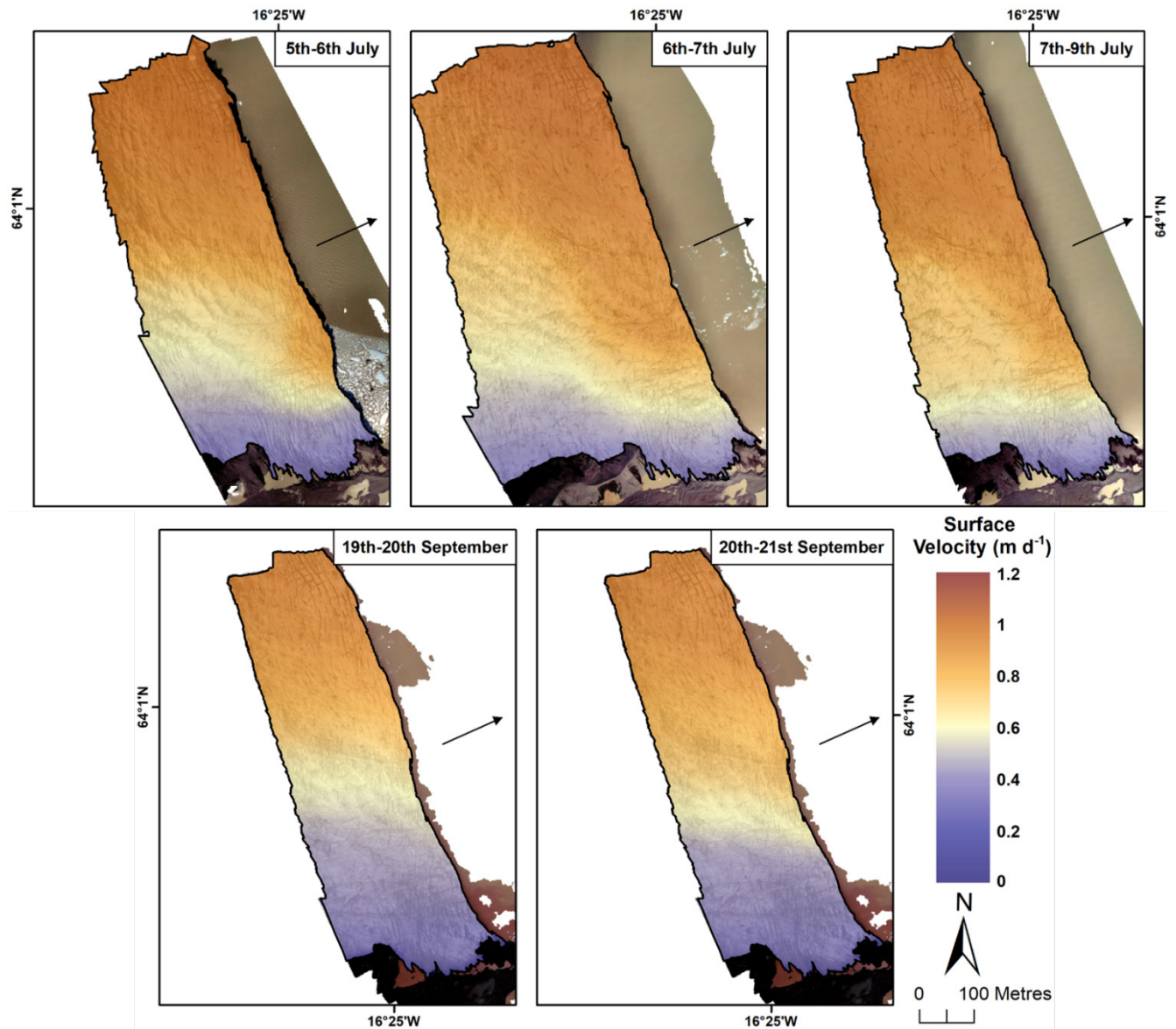


FIGURE 50 Horizontal velocity fields for select time periods in July and September 2019, calculated using feature tracking on UAV-derived orthomosaics. Off-ice, stable-ground areas are shown for reference. Black arrows indicate ice flow direction. Background in each panel is the orthomosaic for the latter time period, apart from in the first and last panels, when it is the former.

Between the 5th and 6th July, velocities increase from $\sim 0.30 \pm 0.25 \text{ m d}^{-1}$ near the grounded margin up to $\sim 0.80 \pm 0.25 \text{ m d}^{-1}$ on average in the upper portion of the study area. Velocities near the calving front in this region peak at $\sim 1.00 \pm 0.25 \text{ m d}^{-1}$, meaning this area of the glacier is flowing over three times faster than those areas at the margin. However, over the same period smaller-scale velocity variations can also be clearly observed to be occurring. For example, a region of locally high velocities can be observed at the calving front in the lower portion of the study area, extending $\sim 70 \text{ m}$ back from the margin and surrounded by areas of relatively slower-moving ice. Between the 6th and 7th July this localised region has greatly increased in size, extending $\sim 200 \text{ m}$ back from the calving margin while also fully coalescing with the large region of high velocities in the upper portion of the study area. As a result, over half of this portion of the glacier is flowing at velocities $> 0.80 \pm 0.20 \text{ m d}^{-1}$. Furthermore, a large portion of the slower-moving areas of ice observed between the 5th and 6th in the lower part of the study area have also sped-up, with velocities increasing from ~ 0.45 to $\sim 0.6 \pm 0.20 \text{ m d}^{-1}$ in this period. Between the 7th and 9th July, the extent of the localised region of high-velocities in the lower portion of the study area has decreased, however, the area of ice immediately behind and south of this region still display elevated velocities (up to $\sim 0.70 \pm 0.22 \text{ m d}^{-1}$), despite overall peak velocities over the entire region decreasing to between 0.85 and $0.90 \pm 0.22 \text{ m d}^{-1}$.

Although the velocity results from September display the same overall pattern than those found in July, they are comparatively lower overall. Between the 19th and 20th September, velocities increase from $\sim 0.20 \pm 0.17 \text{ m d}^{-1}$ at the margin to $\sim 0.90 \pm 0.17 \text{ m d}^{-1}$ near the calving front in the upper portion of the study area. Velocities over much of the rest of the glacier range between 0.30 and $0.60 \pm 0.17 \text{ m d}^{-1}$, particularly in the lower portion of the study area, both near to and away from the calving front. Over the following 24-hour period (20th-21st), however, although the general pattern is still clearly noticeable, the region of fastest velocities in the upper portion of the study area has extended southward and increased in size, resulting in just over half of the glacier flowing at $> 0.60 \pm 0.18 \text{ m d}^{-1}$. Velocities over the rest of this portion of the glacier during this time range from 0.20 and $\sim 0.50 \pm 0.18 \text{ m d}^{-1}$, similar to those velocities observed in July.

5.1.2 2021 Field Season

As was the case for both July and September 2019, the results from July 2021 display a similar overall pattern, with velocity increasing with increasing distance from the southern-grounded margin. However, the key contrast between the two sets of results is that overall this area of Fjallsjökull was flowing faster in July 2021 than it was during either time period in 2019 (Figure 51).

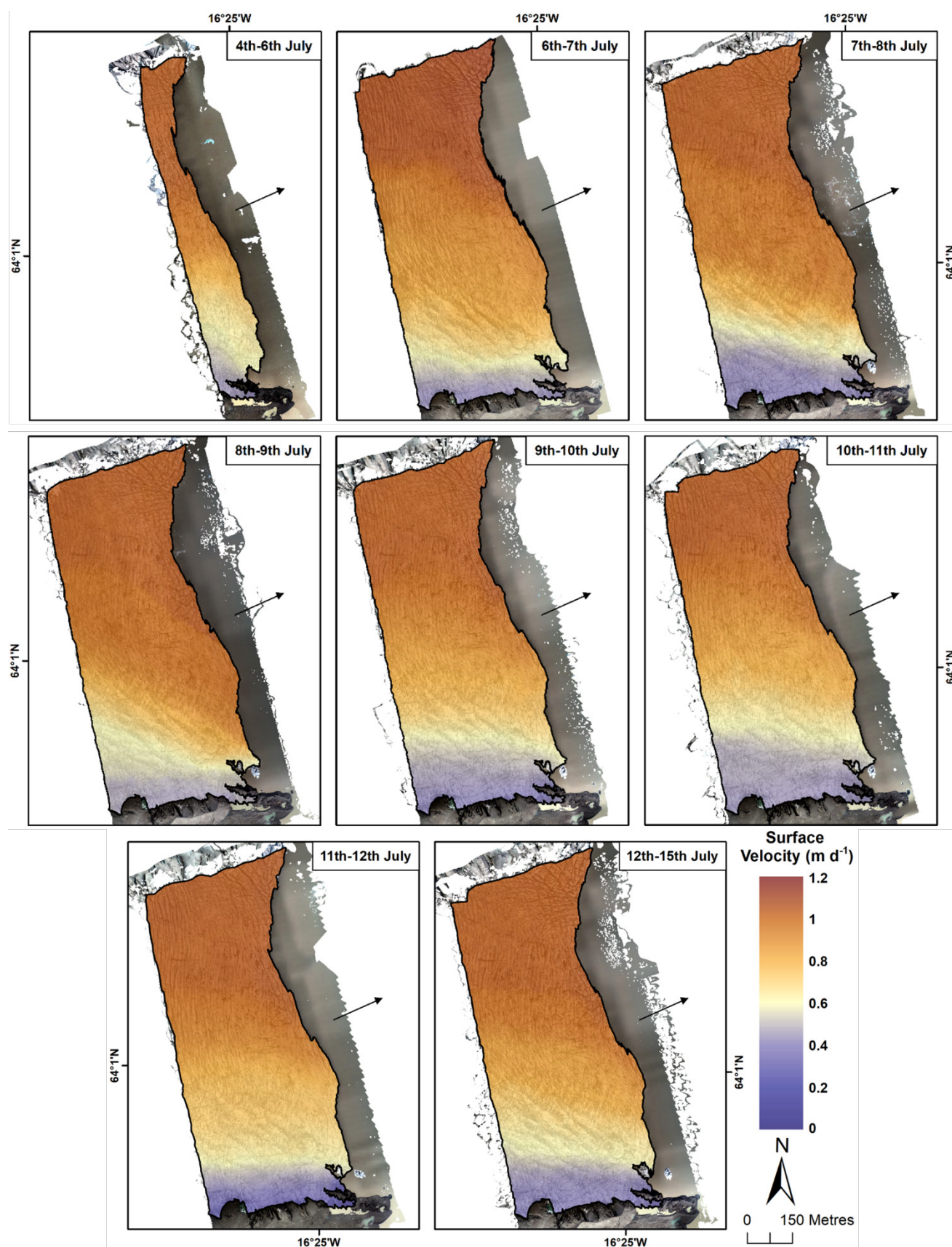


FIGURE 51 Horizontal velocity fields for all time periods in July 2021, calculated using feature tracking on UAV-derived orthomosaics. Off-ice, stable-ground areas are shown for reference. Black arrows indicate ice flow direction. Background in each panel is the orthomosaic for the latter time period, apart from in the first panel when it is the former.

Between the 6th and 7th July (the first day where full coverage of the study area was obtained), velocities near the grounded southern margin range from ~ 0.40 to $0.45 \pm 0.16 \text{ m d}^{-1}$. This region of slower velocities, however, is relatively limited in extent, with velocities rising rapidly to $\sim 0.82 \pm 0.16 \text{ m d}^{-1}$ within $\sim 200 \text{ m}$ of the grounded margin, before further increasing to $\sim 0.90 \pm 0.16 \text{ m d}^{-1}$ around the middle of the study area. Finally, the highest velocities are again found in the upper portion of the study area, with values peaking at $\sim 1.20 \pm 0.16 \text{ m d}^{-1}$, which is around three times higher than those velocities observed near the margin. As a result, well over 75% of the study region is flowing at speeds $> 0.80 \pm 0.16 \text{ m d}^{-1}$, which is in clear contrast to the data obtained from 2019 ($< \sim 0.65 \text{ m d}^{-1}$ on average). Furthermore, such an overall pattern of velocity distribution, and indeed velocity magnitude, is consistent for all time periods in July 2021. However, smaller-scale velocity variations can still also be observed within this overall pattern for each period of interest.

For example, between the 4th and 6th July, the lower portion of the study area is flowing at no greater than $\sim 0.65 \pm 0.23 \text{ m d}^{-1}$, yet, over the following 24-hour period, and as mentioned above, velocities in this region increase to $\sim 0.82 \pm 0.16 \text{ m d}^{-1}$, primarily due to the southward expansion of this region of fast ice flow. Furthermore, between the 7th and 8th July, despite a slight increase in the extent of the slowest-moving ice near the grounded margin ($\sim 0.40 \pm 0.11 \text{ m d}^{-1}$), the large area of faster-moving ice directly north of this is now flowing at $\sim 0.90 \pm 0.11 \text{ m d}^{-1}$. This area of faster-moving ice further increases its velocity over the following 24-hour period (to $\sim 0.95 \pm 0.09 \text{ m d}^{-1}$), while the area of slowest-moving ice also sees a slight increase in its velocity (to $\sim 0.47 \pm 0.09 \text{ m d}^{-1}$), but a small decrease in its overall area. However, between the 9th and 10th July the velocities in this lower region have begun to decrease, with values of ~ 0.75 and $\sim 0.45 \pm 0.12 \text{ m d}^{-1}$ recorded for the fast and slow areas of ice, respectively. This decrease continues over the following 24-hour period, so that by the 11th velocities in the lower region have returned to a similar distribution and magnitude as was observed \sim five days earlier, between the 4th and 6th July. This pattern remains relatively stable between the 11th and 12th July, with the only notable variation being the velocity of the slowest-moving area of ice decreasing slightly from ~ 0.40 to $\sim 0.35 \pm 0.13 \text{ m d}^{-1}$. However, between the 12th and 15th July, the region of fast ice flow has again expanded southward into the lower portion of the study area (although not to the same extent as between the 6th and 7th), resulting in a slight increase in velocity from ~ 0.73 to $\sim 0.85 \pm 0.26 \text{ m d}^{-1}$, despite the slower-moving areas of ice immediately south of this region remaining relatively unchanged.

5.2 Surface Elevation Change

5.2.1 2019 Field Season

Spatially variable changes in ice surface elevation can be seen to have occurred between both the 5th and 9th July, and the 19th and 21st September (Figure 52), and although the overall pattern of change is similar for both time periods, the magnitude of change does vary slightly.

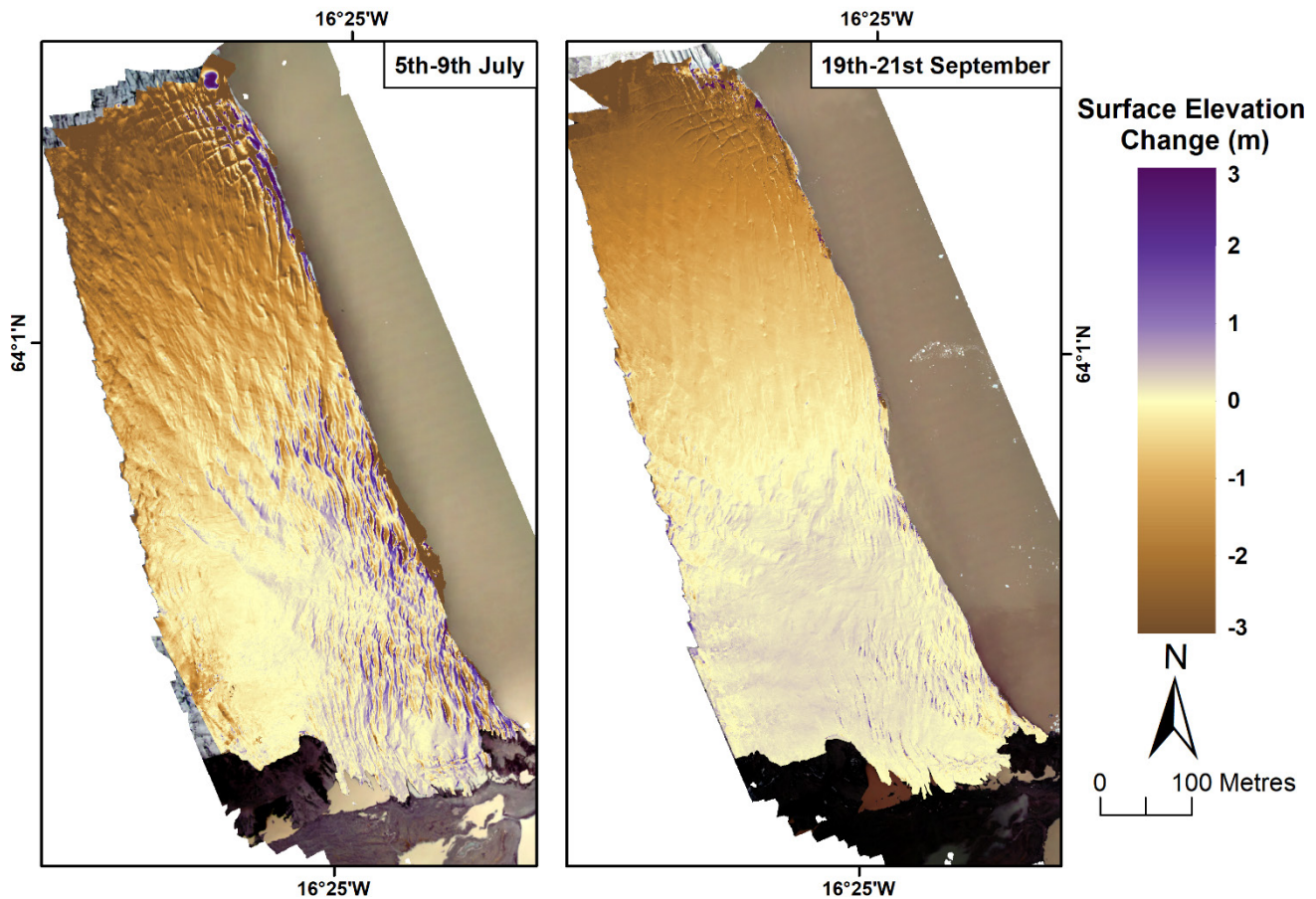


FIGURE 52 Change in ice surface elevation between the 5th-9th July, and the 19th-21st September 2019, calculated using DEM differencing. Note the deep brown areas along the terminus, which represent the largest calving events that occurred over both respective periods. Background is the orthomosaic from the 9th July and 19th September 2019, respectively.

In the lower portion of the study area, near the southern grounded margin and away from the calving front, the surface elevation changes very little, with $+1.00/-1.00 \pm 0.18$ m and $+0.50/-0.50 \pm 0.14$ m of change observed in July and September respectively. Yet in the densely crevassed zone found in this area, and in the crevassed region north of this, more pronounced changes in elevation are found with proximity to the calving front, with between ~ 1.00 and 2.00 ± 0.18 m of both positive and negative surface change observed between the 5th and 9th July. In comparison,

the changes in this region are much less pronounced between the 19th and 21st September. Finally, and in a similar fashion to the velocity results, these changes in surface elevation become more negative with increasing distance from the grounded southern margin. Indeed, the most negative changes have occurred in the upper portion of the study area, with between 2.00 and 2.50 \pm 0.18 m, and between 1.50 and 2.00 \pm 0.14 m of negative surface change observed here in July and September respectively.

5.2.2 2021 Field Season

Spatially variable changes in ice surface elevation have also occurred between the 6th and 15th July 2021, however, the overall pattern and magnitude of this change strongly contrasts to the change observed during both time periods in 2019 (Figure 53). In the lower portion of the study area, near to the grounded margin and away from the calving front, the change in surface elevation is slightly negative, with between -0.50 and \sim -1.50 \pm 0.15 m of change observed. Within 200 m of the southern-grounded margin, however, these surface changes rapidly become more negative, with between 2.00 and 4.50 \pm 0.15 m of negative change observed. Such a pattern of rapid change is very similar to the velocity results described earlier. Furthermore, the changes in surface elevation also generally become more negative with increasing distance from the southern-grounded margin, which again agrees closely with the surface velocity results. Indeed, the most negative changes have occurred in the upper portion of the study area, near to the calving front, where upwards of \sim 5.50 \pm 0.15 m of negative change is observed. However, in those regions of densely crevassed ice (both near to, and away from, the calving front); this change is far more variable, with between \sim 3.50 and \sim 5.50 \pm 0.15 m of both positive and negative surface change observed in this time. Such a complex pattern is likely a result of the movement of these crevasses (and connected ridges) down-glacier between the two time periods of interest (Wigmore and Mark, 2017).

It is worth noting that in the DEMs from both 2019 and 2021, the deep brown areas found along the calving front likely represent large calving events (i.e. mass loss). In contrast, the deep brown and purple areas found to the far north and north-west of the study area (particularly in 2021) likely represent noise in the original DEMs, rather than actual change, due to the warping that can occur around the edges of a scene reconstructed from SfM when the GCPs, or the captured images, do not completely cover the area of interest (James and Robson, 2012; Javernick et al., 2014).

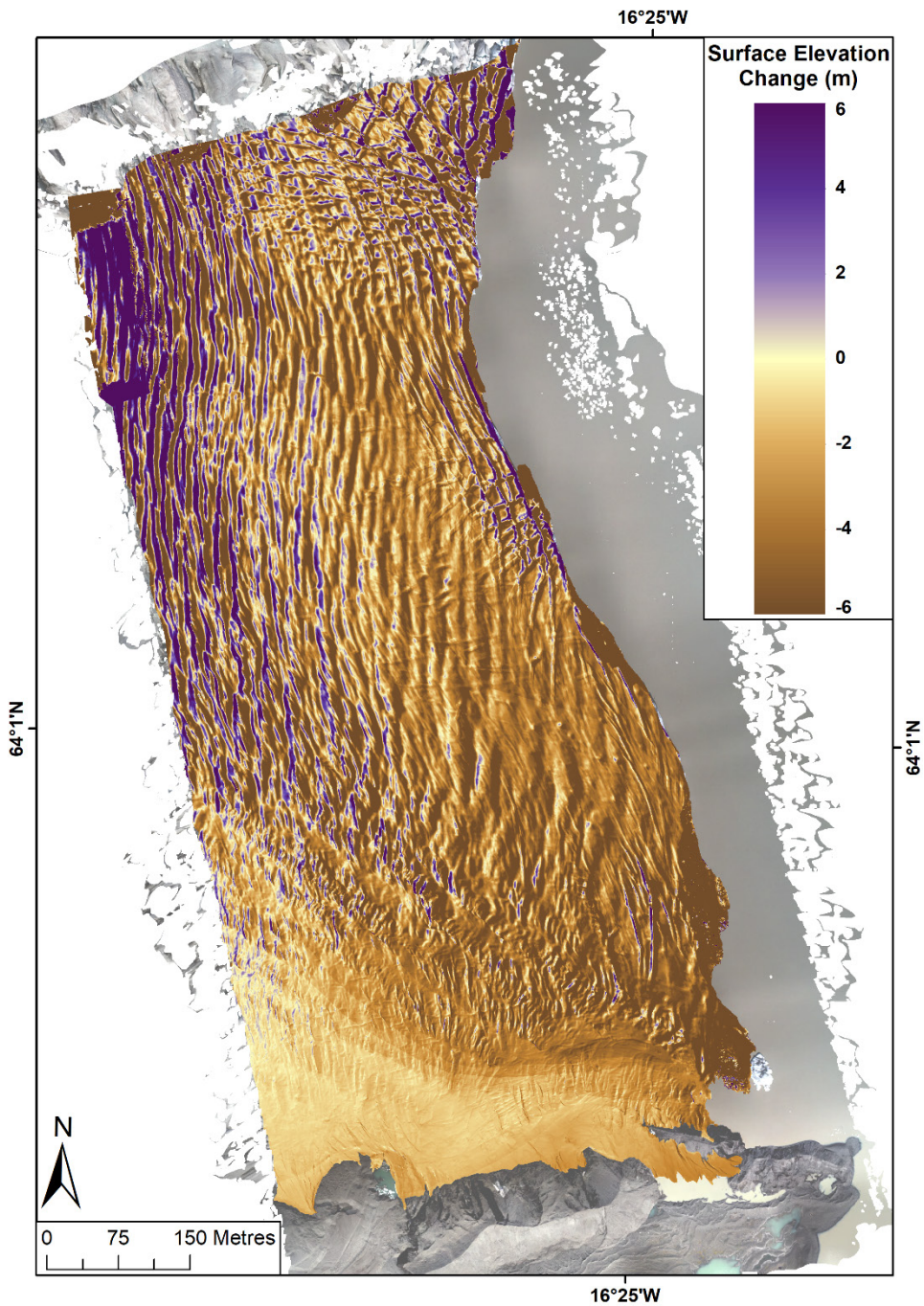


FIGURE 53 Change in ice surface elevation between the 6th-15th July 2021, calculated using DEM differencing. Note the deep brown areas along the terminus, which represent the largest calving events that occurred over this period. Background is the orthomosaic from the 15th July 2021.

5.3 Frontal Position Change and Calving Events

5.3.1 2019 Field Season

In general, the calving front of Fjallsjökull remained relatively stable across all time periods in both July and September 2019, with only a few particularly significant changes in calving front

geometry (i.e. calving events) occurring during this time. Indeed, while these calving events can be seen to have occurred across the entire length of the calving front, the majority of these were relatively small in size, with only one particularly large event observed (in July) (Figure 54). Yet despite remaining relatively stable, an overall pattern of frontal retreat can still be observed across both time periods, with 2.77 m and 0.25 m of retreat calculated respectively (Table 11 and Figure 55). Furthermore, within this overall pattern several interesting daily variations in frontal geometry and calving activity can also be observed, with these described in more detail below.

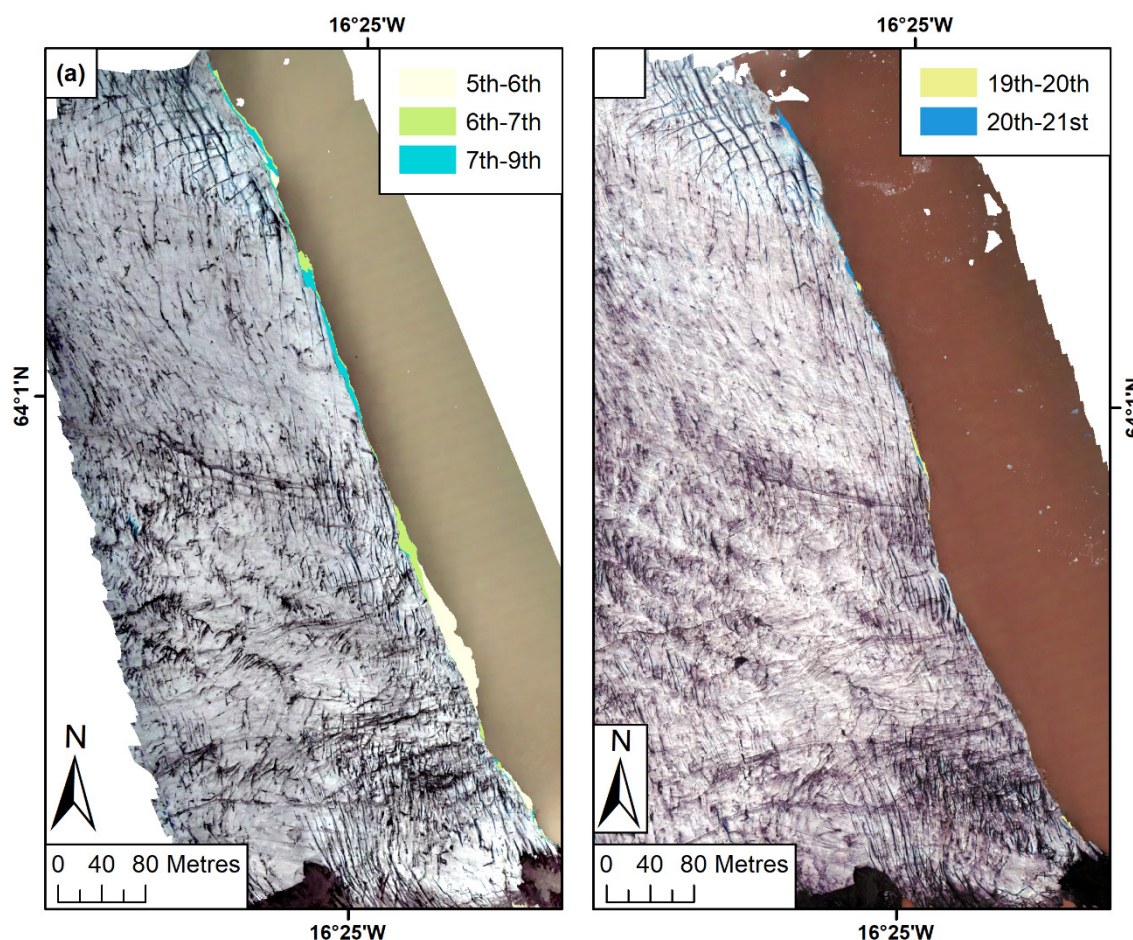


FIGURE 54 Location and areal extent of the calving events that occurred across the study area over (a) 5th- 9th July, and (b) 19th-21st September 2019. Note the relatively active nature of the calving front in (a), compared to the less active (and thus more stable) nature of the calving front in (b). Background is the orthomosaic from the 9th July and 21st September 2019, respectively.

Between the 5th and 6th July, a relatively large calving event occurred in the lower third of the study area, causing $\sim 1,579 \text{ m}^2$ ($\sim 31,581 \text{ m}^3$) of ice to be lost (Figure 56) and the terminus in this region to recede by up to 19.64 m. Alongside this large event, two other much smaller calving events also occurred in this time ($< 200 \text{ m}^2$), resulting in a total ice loss of at least $\sim 1,856 \text{ m}^2$ ($\sim 37,139 \text{ m}^3$) during this 24 hour period (Figure 57).

TABLE 11 Calculated terminus retreat for each time period in July and September 2019. Also shown is the maximum observed length change for each time period. All values indicate frontal retreat unless preceded by a '+', in which case they signify terminus advance.

Period of Interest	Calculated Retreat Rate (m)	Maximum Observed Length Change (m)
5 th -6 th July	0.17	19.64
6 th -7 th July	1.50	12.91
7 th -9 th July	1.10	7.32
5 th -9 th July (whole period)	2.77 (total retreat)	19.93
19 th -20 th September	+0.30	3.29
20 th -21 st September	0.55	2.46
19 th -21 st September (whole period)	0.25 (total retreat)	4.92

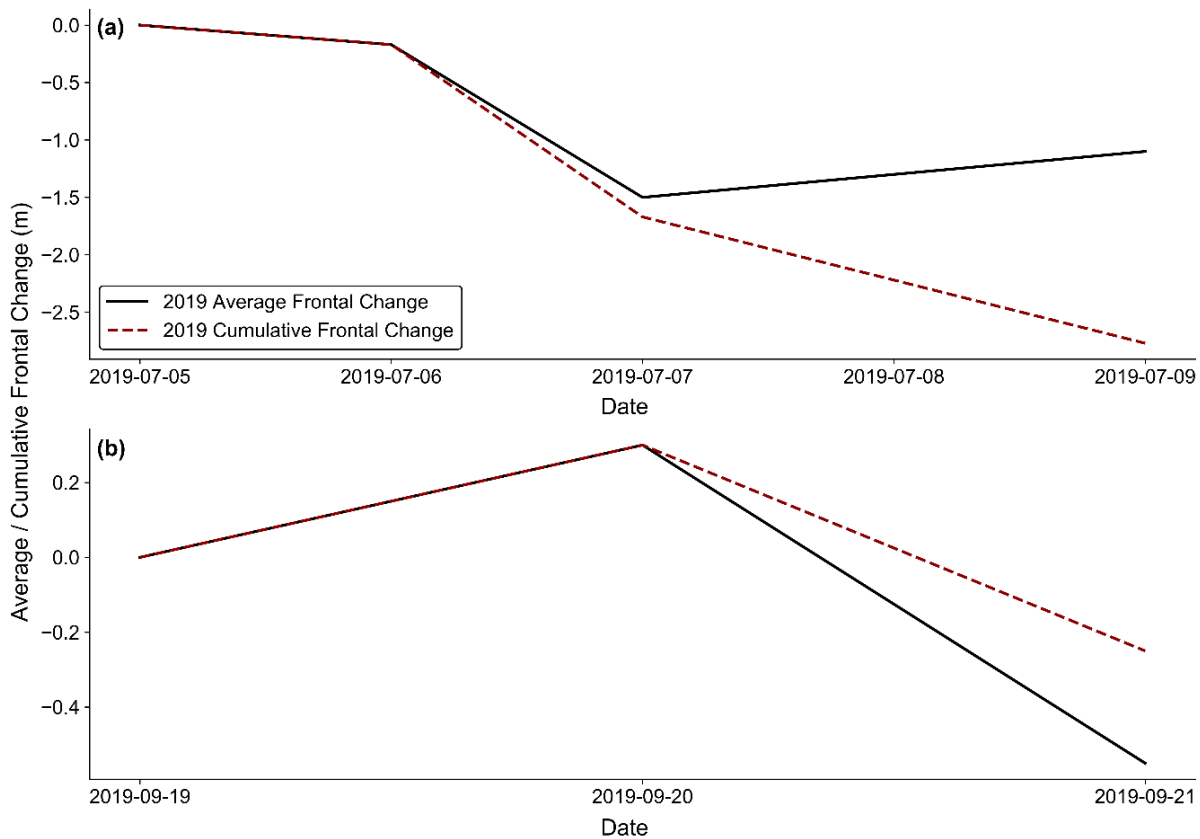


FIGURE 55 (a) Average and cumulative frontal change for July 2019, calculated using the rectilinear box method. (b) Same as (a) but for September 2019.

As a result, this was both the single largest individual calving event, and the single largest loss of ice to calving overall, that occurred over the study area in both July and September 2019. Yet despite the occurrence of these events, much of the rest of the terminus remained relatively stable during this time. Indeed, the calving front on the 6th was in a slightly more advanced position than it was on the 5th, particularly in the areas north of where the large calving event occurred (Figure 56). This may explain why the calculated retreat for this period was only 0.17 m, as the rectilinear box method averages retreat over the entire length of the terminus, providing a much more robust estimation of frontal change.

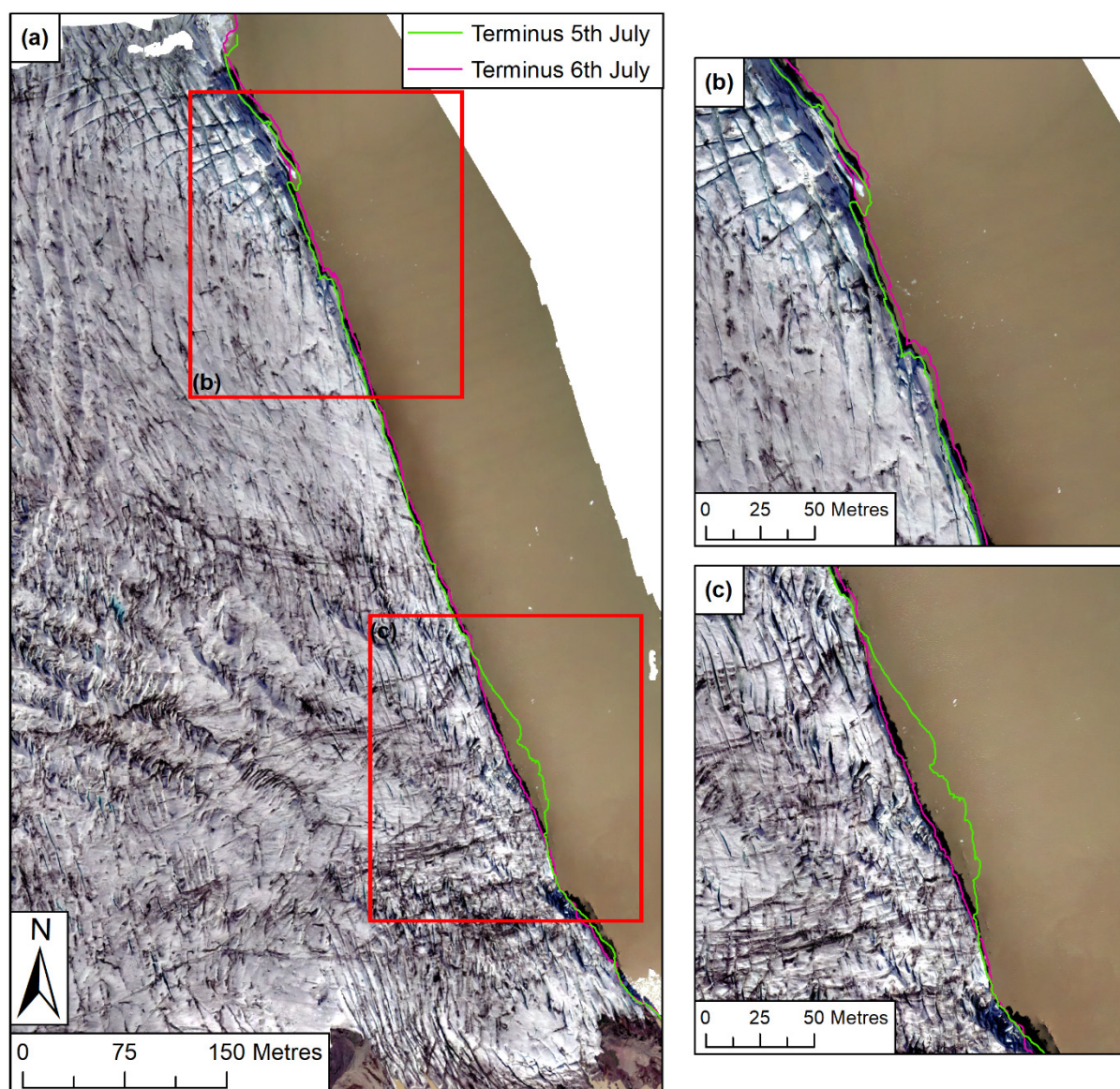


FIGURE 56 (a) Change in calving front position between the 5th and 6th July. Red boxes indicate areas of the ice surface which are of interest, with these presented in panels (b) and (c). Note the large calving event shown in (c). Background is the orthomosaic from the 6th July 2019.

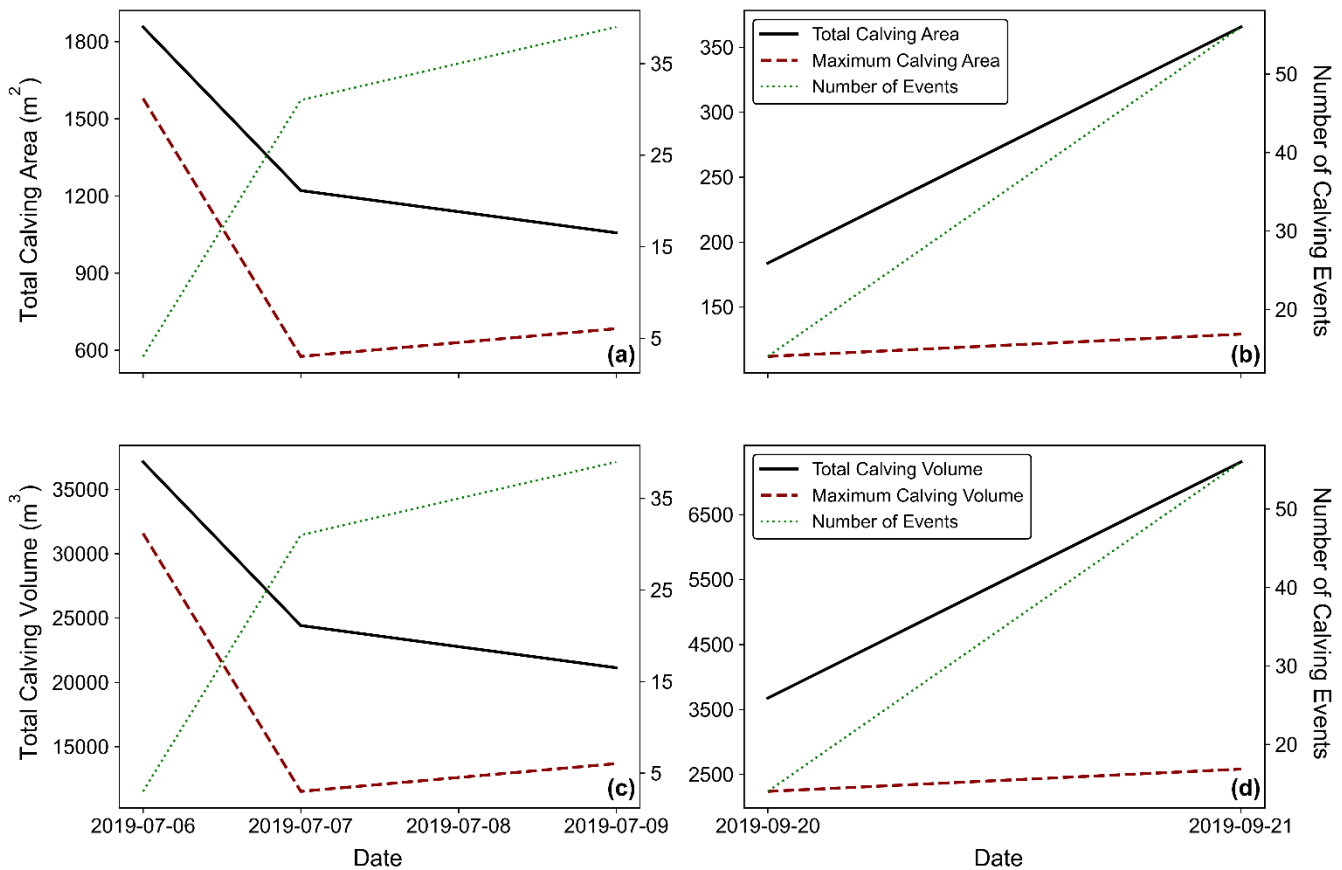


FIGURE 57 Total calving area (black line), maximum calving area lost in a single event (red line), and the total number of calving events (green line) per day for each time period of interest in July (a) and September (b) 2019. (c) & (d) Same as (a) & (b) but for calving volume, rather than area.

In comparison, between the 6th and 7th, although no 'large' calving events occurred (all <600 m² in area), overall a far greater number of these events occurred in this period than were observed between the 5th and 6th (n=31 compared to n=3). Furthermore, while over half of these calving events were very small (i.e. <5 m², n=17), the remaining events were sufficient enough in their size to cause the terminus to recede, particularly in the region north of where the large calving event had occurred 24 hours previously (Figure 58). As a result, the terminus position on the 7th was very rarely in a more advanced position than it was on the 6th, which may explain why a retreat rate of 1.50 m was calculated for this period.

A large number of calving events were also observed to have occurred between the 7th and 9th (n=39), although a significant portion of these were once again <5 m² in area (n=32). However, several comparatively large calving events also occurred in this period, with these predominately focused in the upper portion of the study area (Figure 58), with the largest event having an area (volume) of 683.88 m² (13,677 m³). These events, therefore, are likely responsible for the ~1.10 m of terminus retreat that was calculated for this period.

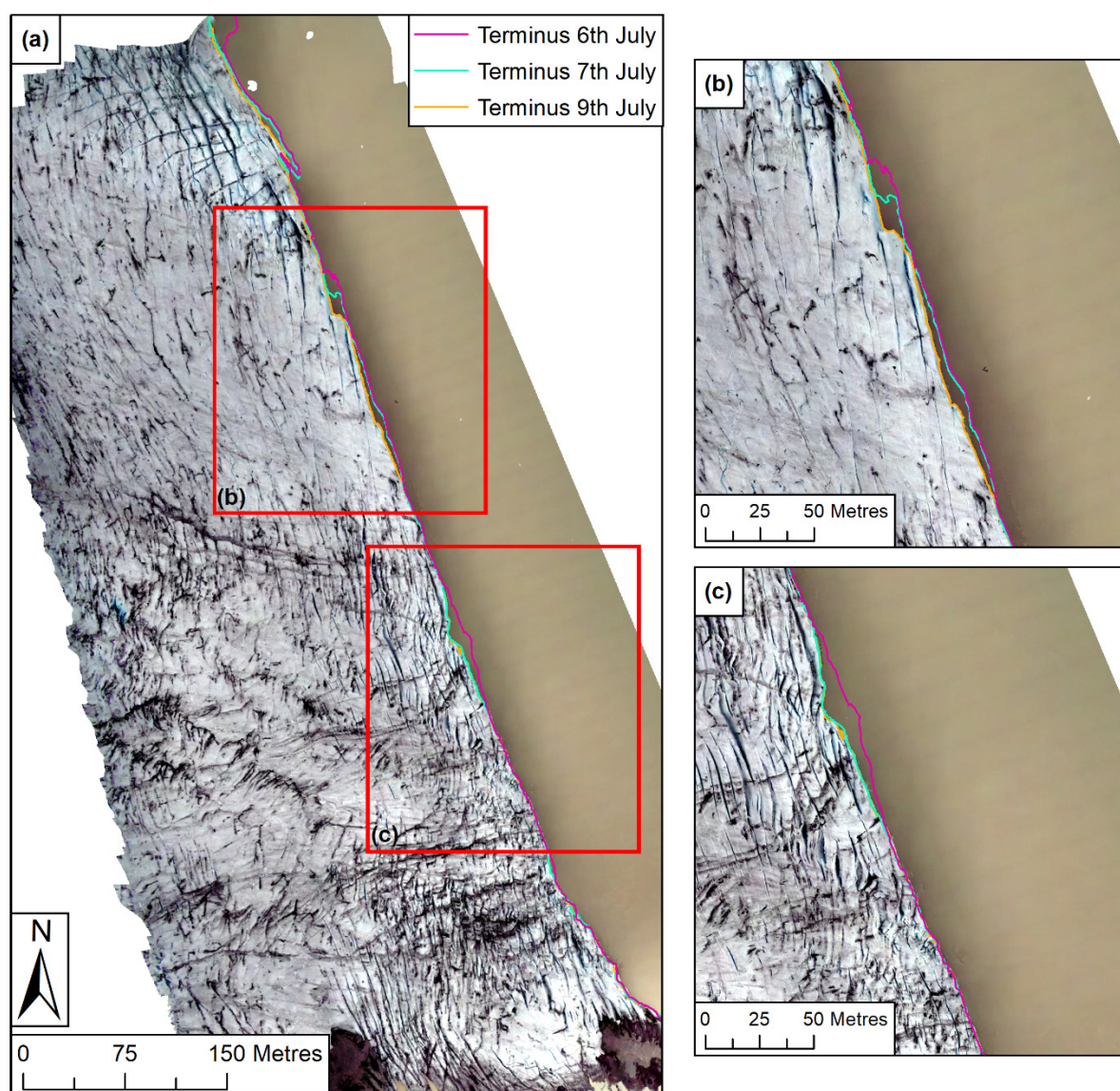


FIGURE 58 (a) Change in calving front position between the 6th and 9th July. Red boxes indicate areas of the ice surface which are of interest, with these presented in panels (b) and (c). Note several smaller calving events occurring across the terminus in this period. Background is the orthomosaic from the 9th July 2019.

In contrast to the fairly large frontal variations that occurred in July, by September these changes had become far less pronounced (Figure 59). Overall, the terminus was much more stable during this period, with no individual calving event greater than $\sim 130 \text{ m}^2$, and no significant changes in terminus geometry observed. For example, between the 19th and 20th, of the 14 observed calving events, 10 of these were $< 5 \text{ m}^2$ in size, while the largest single event in this same period was only $\sim 111.98 \text{ m}^2$. As a result, total calving losses for this period were only $\sim 183.74 \text{ m}^2$ ($3,674 \text{ m}^3$) (Figure 57), which is an order of magnitude less than the calving losses observed between the 5th and 6th July. It is perhaps unsurprising, therefore, that a slight terminus advance of $+0.30 \text{ m}$ was calculated for this period (Figure 55).

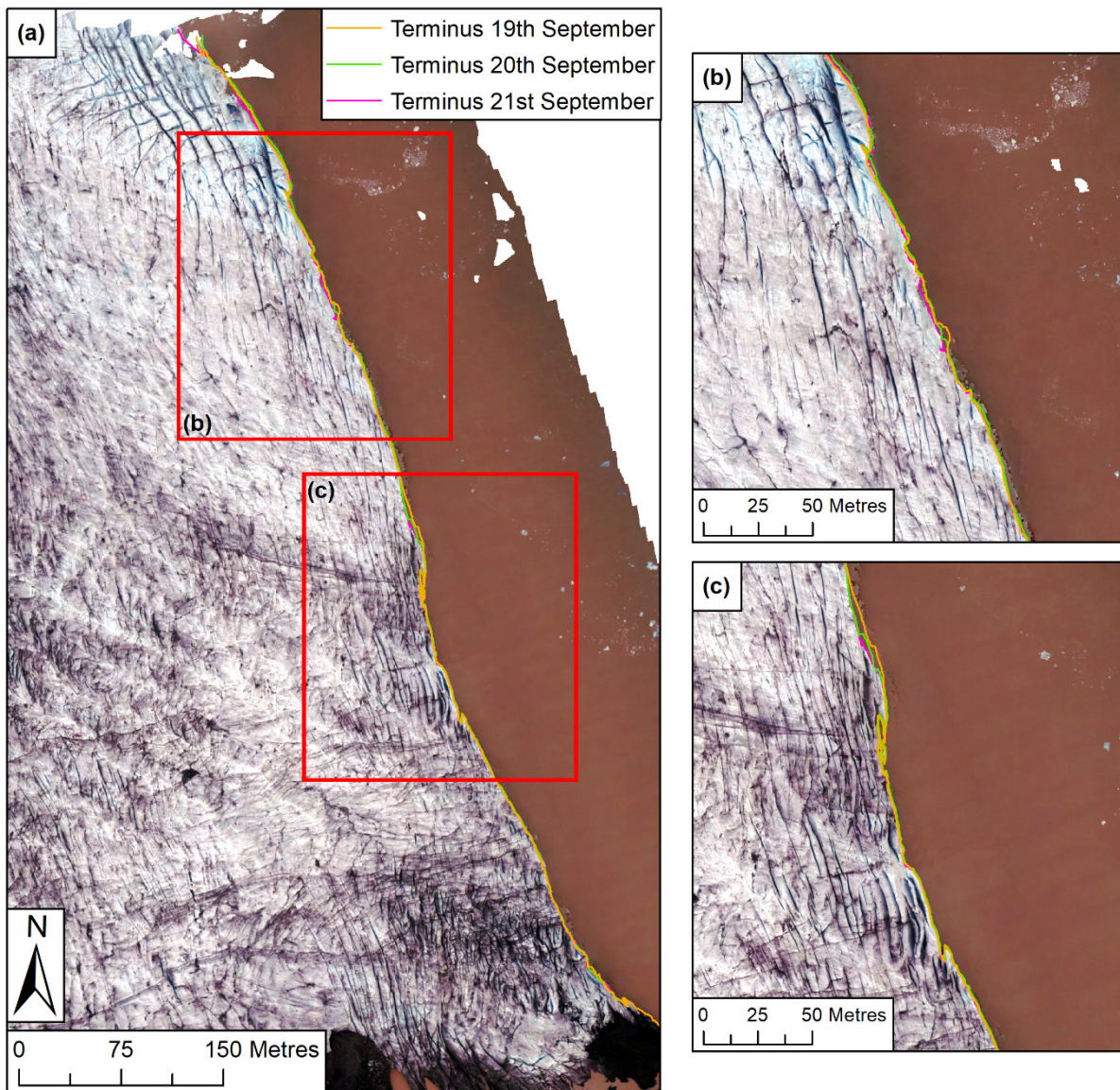


FIGURE 59 (a) Change in calving front position between the 19th and 21st September. Red boxes indicate areas of the ice surface which are of interest, with these presented in panels (b) and (c). Note the relatively stable nature of the calving front in this period. Background is the orthomosaic from the 21st September 2019.

The terminus also remained relatively stable between the 20th and 21st, with 43 of the 56 observed calving events once again $<5 \text{ m}^2$ in size. This may explain why the position of the terminus did not vary significantly between the two dates, particularly in the lower part of the study area. However, several slightly larger calving events ($\sim 50\text{--}130 \text{ m}^2$) can also be seen to have occurred in the upper part of the study area during this same period (Figure 59). As a result, total calving losses for this period were $\sim 365.61 \text{ m}^2$ ($7,312 \text{ m}^3$), which is around twice the calving losses observed over the previous 24 hours. Such factors may explain, therefore, why a slight terminus retreat of 0.55 m was observed in this period.

5.3.2 2021 Field Season

Overall, the calving front of Fjallsjökull was considerably less stable across all time periods in July 2021 than it was across both time periods in 2019, with a significant number of changes in calving front geometry (i.e. large calving events) occurring during this time. Indeed, field observations confirm that the calving front was far more active during this period, with calving events occurring in both greater number, and greater frequency than they did in 2019. Furthermore, although the majority of these calving events seem to be concentrated in the lower half of the study region, overall they can be seen to have occurred across almost the entire length of the calving front (that was covered by the UAV surveys) (Figure 60). As a result, an overall retreat rate of ~ 10.70 m was calculated for the study period (Table 12 and Figure 61), which is nearly four times greater than the ~ 2.77 m of retreat calculated across the four days in July 2019. Furthermore, within this overall pattern, there are several interesting daily variations in frontal geometry and calving activity that can be observed, and these will be described in more detail below.

The two largest calving events that were observed in July 2021 both occurred within the first three days of the study period commencing (4th-7th July). The first of these events occurred between the 4th and 6th, in the lower portion of the study area, and resulted in $\sim 2,948$ m² ($\sim 58,972$ m³) of ice being lost (Figure 62 and 63), and the terminus in this region to recede by ~ 30.44 m. The second event occurred between the 6th and 7th, in the same region as the first, but covering a much greater extent, resulting in $\sim 4,629$ m² ($\sim 92,596$ m³) of ice being lost (Figure 62 and 63), and causing the terminus to recede by ~ 53.02 m. Indeed, these two events correspond to $\sim 70.4\%$ and $\sim 80.2\%$ of the total area (and volume) loss from calving that was observed for the 4th-6th, and the 6th-7th, respectively. As a result, it is perhaps unsurprising that the calculated retreat rate for these two periods was 2.53 m and 4.02 m respectively, which were the two highest retreat values calculated for the entire study period.

In comparison, between the 7th and 8th, although only five calving events were observed during this time, four of these events were >100 m² in area, with the largest event (~ 900 m²) once again situated in the lower half of the study region (Figure 64). Therefore, whilst the terminus did remain relatively stable during this time, it is likely that these events were still sufficient in size to cause the terminus to recede further, which may explain why a retreat rate of 1.14 m was calculated for this period.

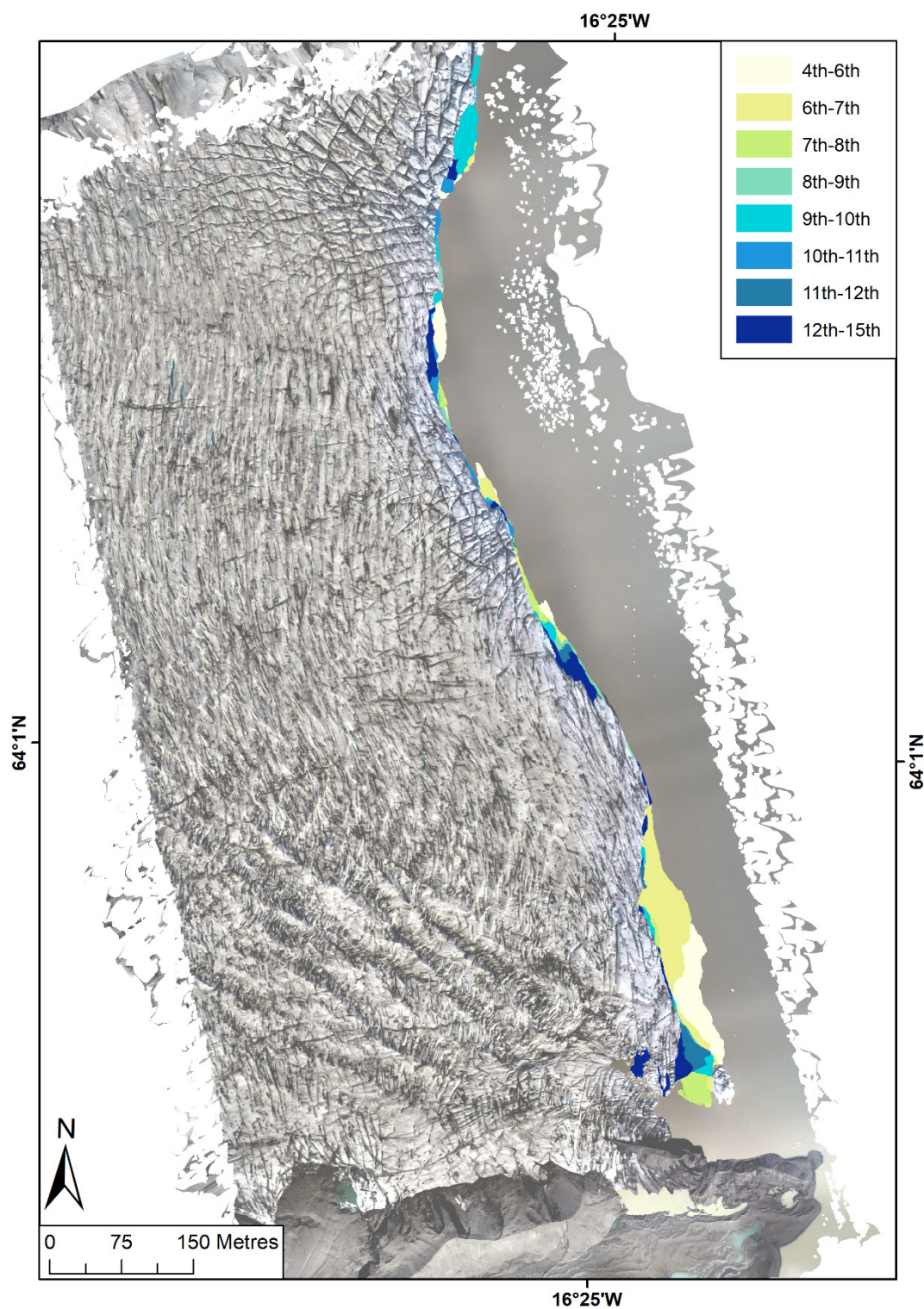


FIGURE 60 Location and areal extent of the calving events that occurred across the study area between the 4th and 15th July 2021. Note the very active (and, therefore, unstable) nature of the calving front, with a number of particularly large calving events occurring. Background is the orthomosaic from the 15th July 2021.

TABLE 12 Calculated terminus retreat for each time period in July 2021. Also shown is the maximum observed length change for each time period. All values indicate frontal retreat unless preceded by a '+', in which case they signify terminus advance.

Period of Interest	Calculated Retreat Rate (m)	Maximum Observed Length Change (m)
4 th -6 th	2.53	30.44
6 th -7 th	4.02	53.02
7 th -8 th	1.14	9.44
8 th -9 th	+0.13	7.62
9 th -10 th	1.25	23.71
10 th -11 th	0.25	8.57
11 th -12 th	0.07	26.69
12 th -15 th	1.29	21.17
4 th -15 th (whole period)	10.70 (total retreat)	52.67



FIGURE 61 Average and cumulative frontal change for July 2021, calculated using the rectilinear box method.

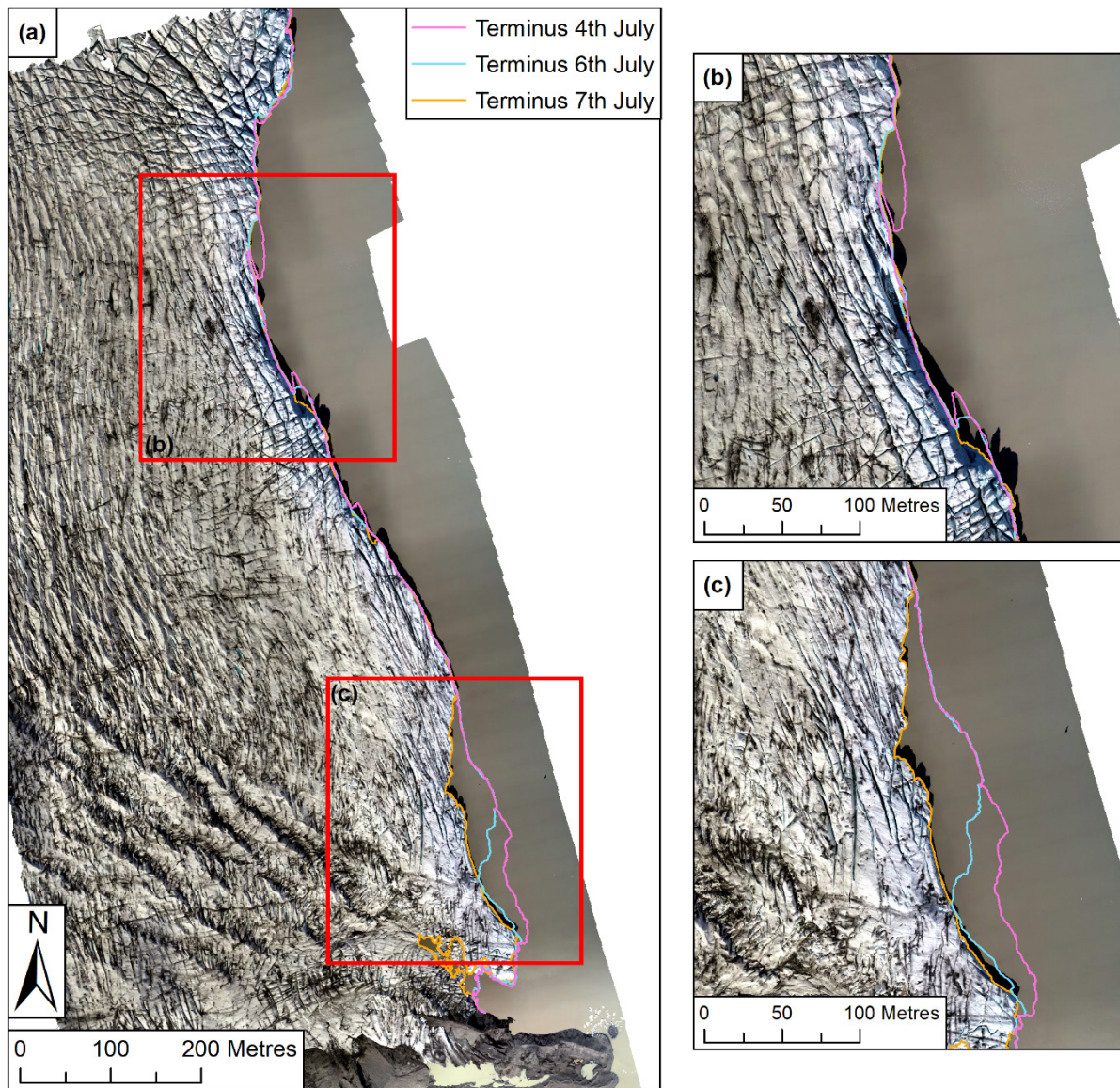


FIGURE 62 (a) Change in calving front position between the 4th and 7th July. Red boxes indicate areas of the ice surface which are of interest, with these presented in panels (b) and (c). Note the two large calving events shown in (c). Background is the orthomosaic from the 7th July 2021.

Over the following 24-hour period, however, despite twice as many calving events occurring than were observed over the previous 24 hours, all but one of these events was $<100 \text{ m}^2$ in size, with the largest event only totalling $\sim 306.69 \text{ m}^2$ ($\sim 6,133 \text{ m}^3$). This means that the total ice loss from calving during this period was only $\sim 634.55 \text{ m}^2$ ($\sim 12,691 \text{ m}^3$), which was the lowest daily total for any time period during July 2021 (Figure 63). As a result, the terminus likely remained particularly stable during this time (Figure 64), which may be why a slight terminus advance of $+0.13 \text{ m}$ was calculated for this period.

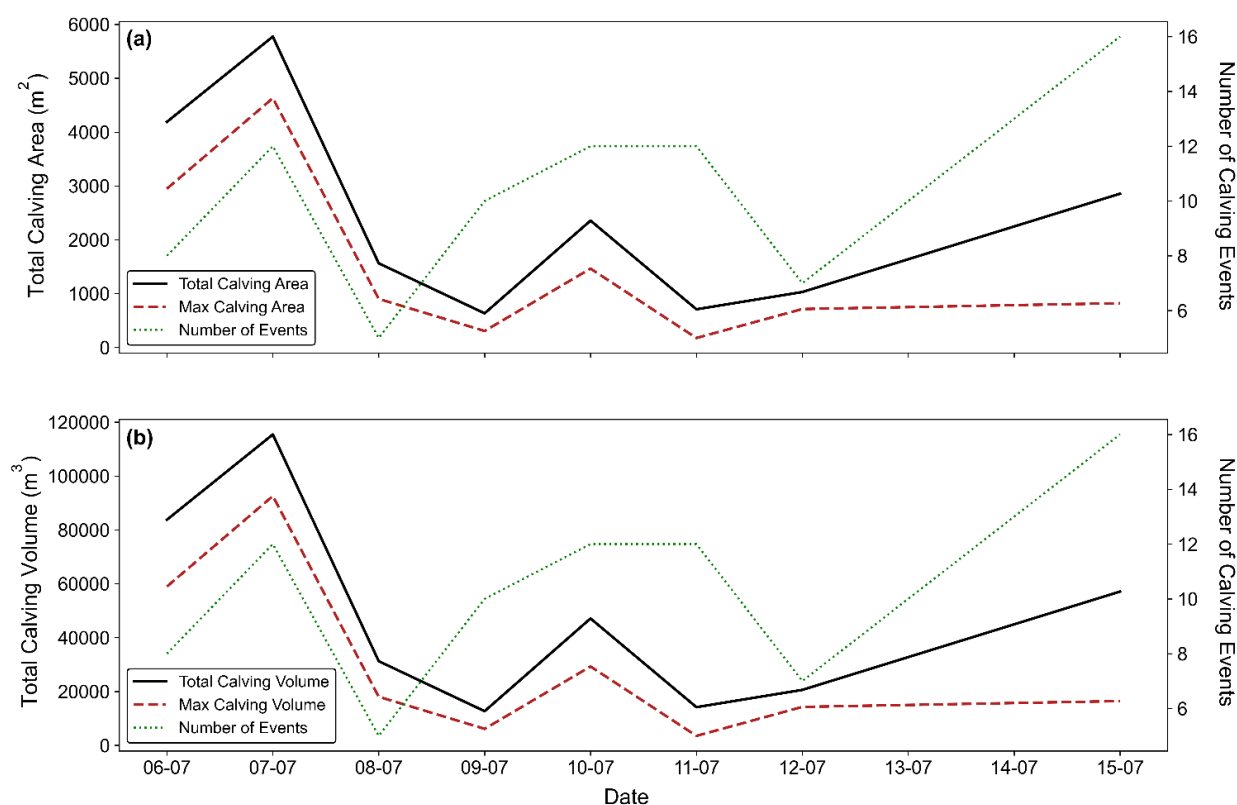


FIGURE 63 (a) Total calving area (black line), maximum calving area lost in a single event (red line), and the total number of calving events (green line) per day for each time period of interest in July 2021. (b) Same as (a) but for calving volume, rather than area.

In contrast to the preceding 24 hours, between the 9th and 10th the terminus had once again become relatively unstable, with a number of calving events observed ($n=12$). Of these, the largest event had an area (volume) of $1,464 \text{ m}^2$ ($29,298 \text{ m}^3$), and occurred in the upper portion of the study region (Figure 65). Several smaller events also occurred in this time ($130\text{--}250 \text{ m}^2$), with these situated in both the upper, and lower portion of the study region, coinciding with the same area where the largest calving events had occurred previously, between the 4th and 7th. As a result, the total losses from calving for this period were $2,355 \text{ m}^2$ ($47,118 \text{ m}^3$), which is around four times greater than the losses observed between the 8th and 9th. Consequently, this may explain why $\sim 1.25 \text{ m}$ of retreat was calculated for this period.

Between the 10th and 11th, however, despite 12 calving events again being observed, total calving losses for this period were only 709.33 m^2 ($14,186 \text{ m}^3$) (Figure 63), with the largest event having an area (volume) of $\sim 176.23 \text{ m}^2$ ($3,524 \text{ m}^3$). These events were predominately focused in the upper portion of the study region, meaning much of the terminus was relatively stable during this time (Figure 65), perhaps explaining why the retreat rate calculated for this period was only 0.25 m .

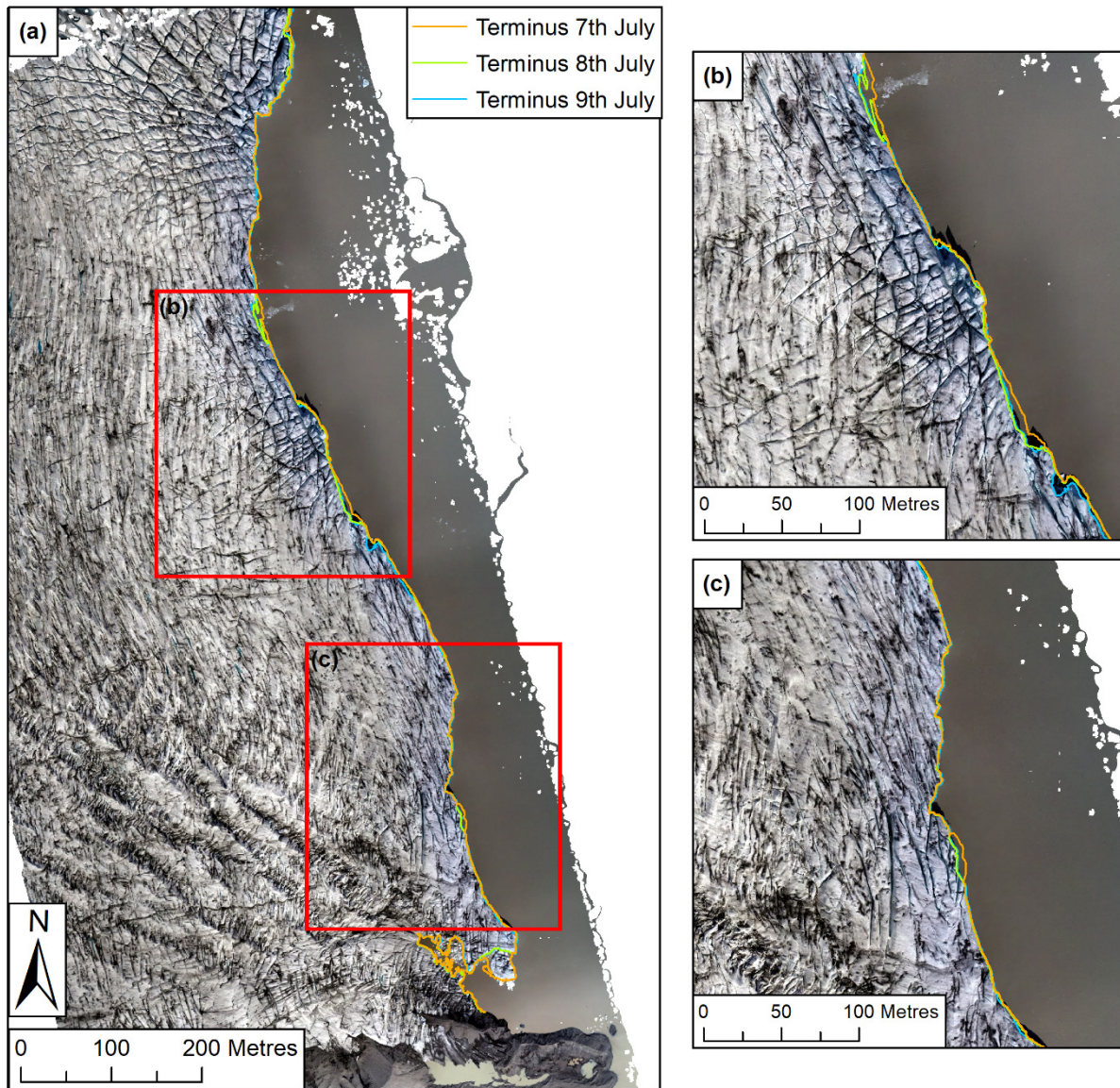


FIGURE 64 (a) Change in calving front position between the 7th and 9th July. Red boxes indicate areas of the ice surface which are of interest, with these presented in panels (b) and (c). Note several smaller calving events occurring across the terminus in this period. Background is the orthomosaic from the 9th July 2021.

A particularly interesting variation in calving activity and terminus retreat can be seen to have occurred between the 11th and 12th. Despite a relatively small number of calving events being observed during this period ($n=7$), the total losses from calving were actually greater than the observed losses from the previous 24 hours ($\sim 1,030 \text{ m}^2$, $20,605 \text{ m}^3$) (Figure 63). Furthermore, the largest calving event to occur during this time ($\sim 710 \text{ m}^2$) caused the terminus in this region to recede by up to $\sim 26.69 \text{ m}$, which was the third greatest change in length that was observed across the entire July study period (Table 12). Yet despite this, the calculated value of retreat for this period was only $\sim 0.07 \text{ m}$, which is around three times smaller than the value calculated for the 10th-11th. This is likely because across the majority of the study region, no other large variations in

frontal position were observed, and as a result, the terminus remained particularly stable during this time (Figure 66).

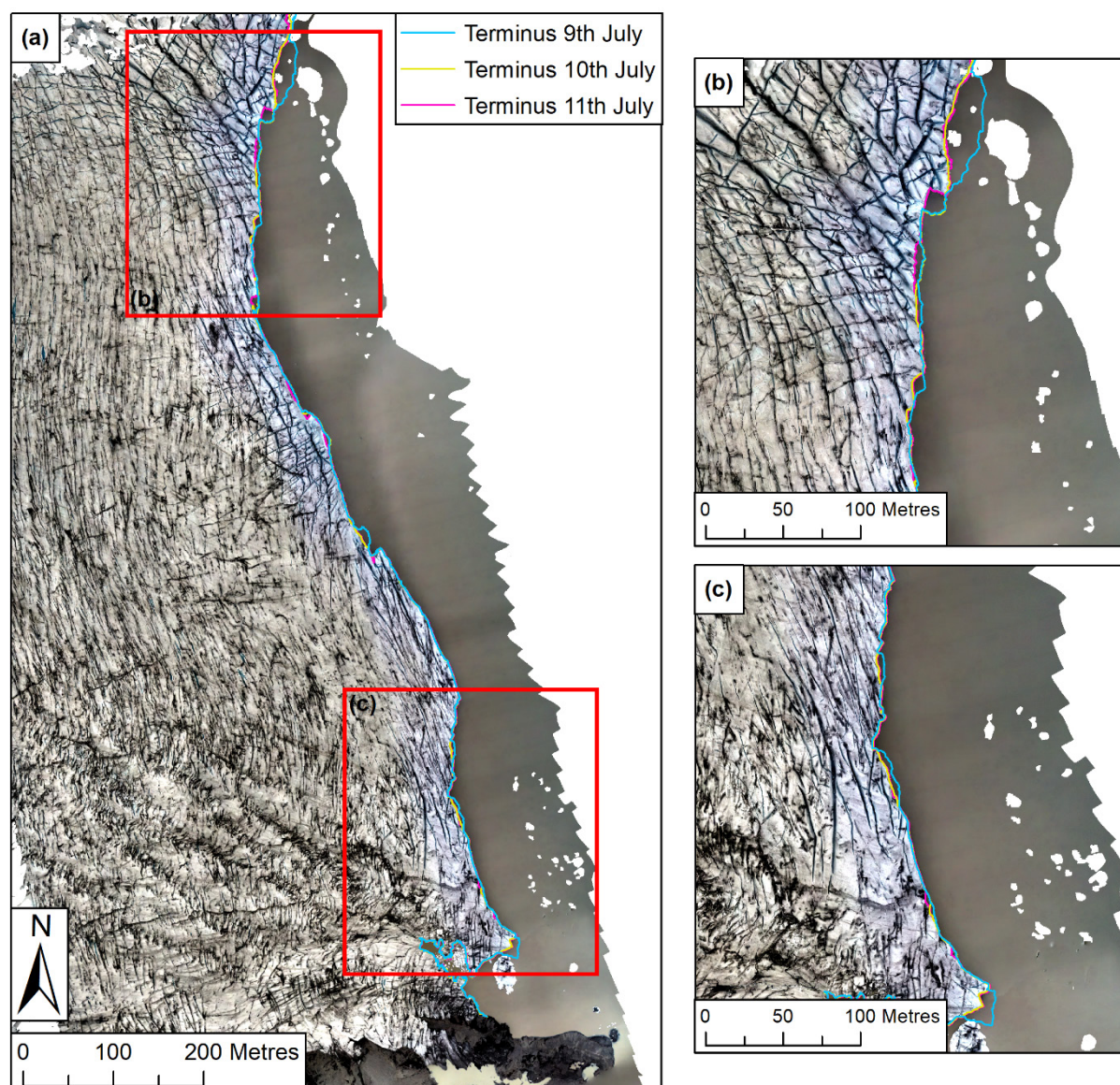


FIGURE 65 (a) Change in calving front position between the 9th and 11th July. Red boxes indicate areas of the ice surface which are of interest, with these presented in panels (b) and (c). Note several smaller, as well as one or two larger calving events occurring across the terminus in this period. Background is the orthomosaic from the 11th July 2021.

In comparison, over twice as many calving events occurred between the 12th and 15th (n=16), with the terminus during this period being far less stable as a result (Figure 66). Of these, the largest event occurred towards the middle of the study region, and resulted in $\sim 822.23 \text{ m}^2$ ($16,444 \text{ m}^3$) of ice being lost (Figure 63). Several slightly smaller events ($\sim 330\text{--}530 \text{ m}^2$) also occurred during this time, with these situated across the whole of the study area.

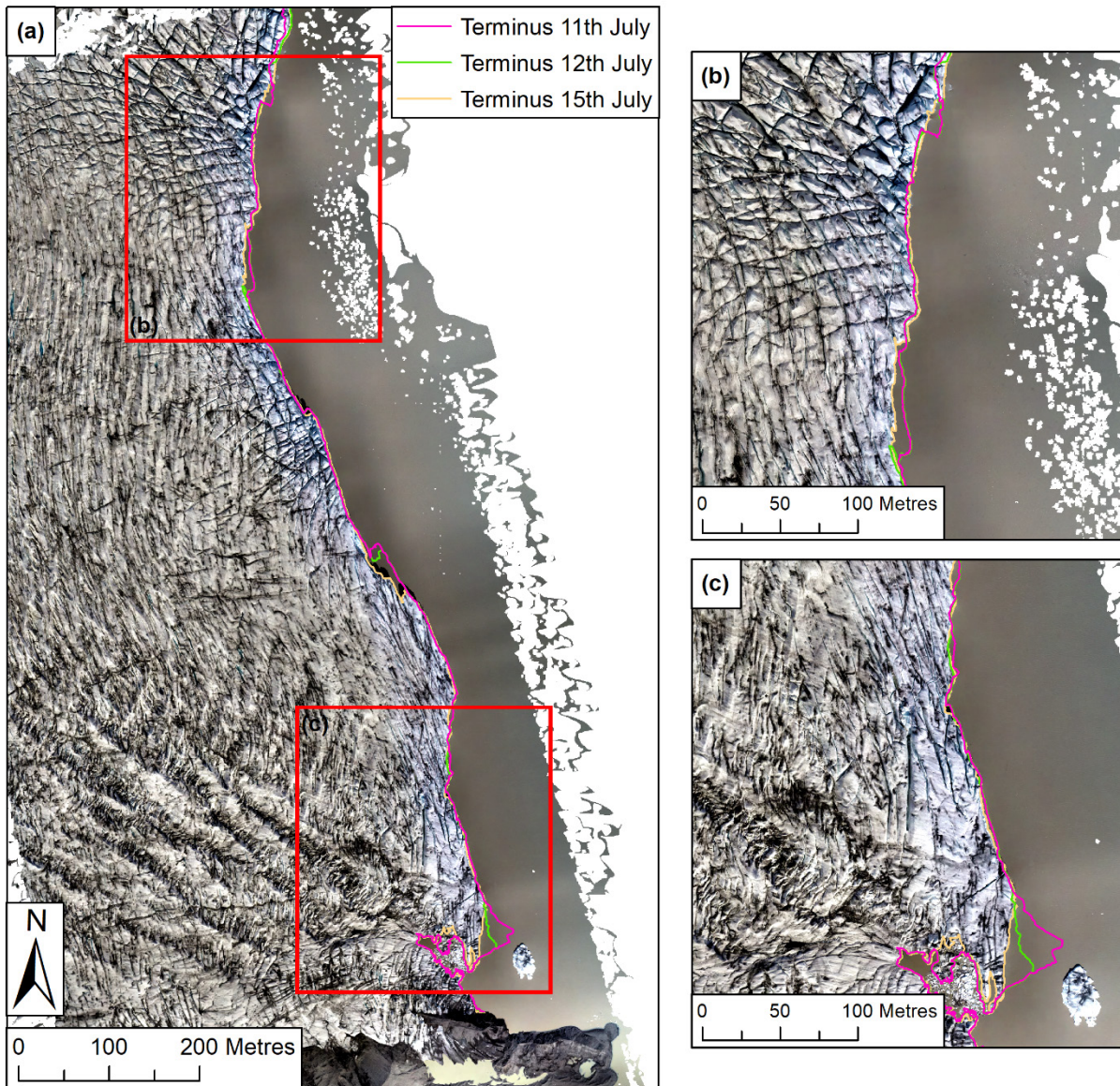


FIGURE 66 (a) Change in calving front position between the 11th and 15th July. Red boxes indicate areas of the ice surface which are of interest, with these presented in panels (b) and (c). Note several smaller, as well as one or two larger calving events occurring across the terminus in this period. Background is the orthomosaic from the 15th July 2021.

As a result, total calving losses for this period were $\sim 2,855 \text{ m}^2$ ($\sim 57,112 \text{ m}^3$), which was the third largest total loss of calving area (and volume) to be observed across the whole study period. This likely explains why $\sim 1.29 \text{ m}$ of retreat was calculated for this period, although it is important to note that this period spans three days, which is a longer time period than was covered by the other periods of interest (majority cover 24 hours). Finally, it is also important to note that the calculated standard error for this analysis was $<1\%$ for all time periods in both July and September 2019, and July 2021, indicating that the calculated uncertainty is not greater than the frontal change observed during this time.

5.4 Supraglacial Hydrological Mapping

To aid the reader in this subsection, Figure 67 illustrates the extent of the respective regions shown in Figures 69, 70, 72 and 73.

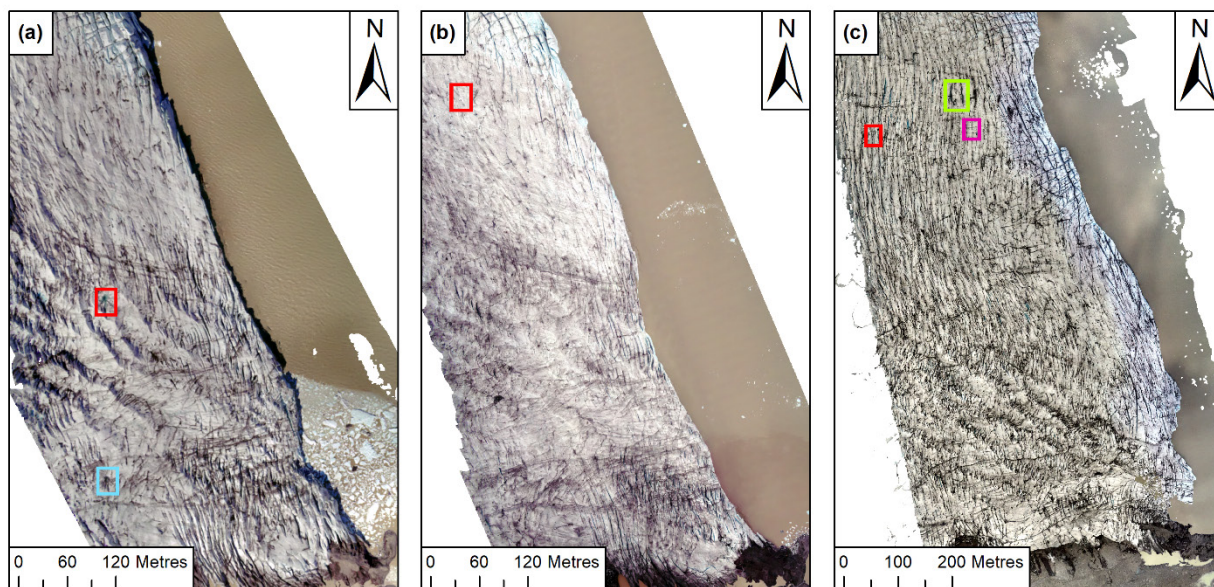


FIGURE 67 Overview figure illustrating the spatial extent of the four different example regions presented in this section, relative to the overall ice surface. (a) Orthomosaic from the 5th July 2019, showing the location of Figure 69a-b (red box) and 69c-d (blue box). (b) Orthomosaic from the 19th September 2019, showing the location of Figure 70. (c) Orthomosaic from 6th July 2021, showing the location of Figures 72a-c (purple box), 72d-f (green box) and 73 (red box).

5.4.1 2019 Field Season

5.4.1.1 Supraglacial Lakes

A large number of supraglacial lakes were manually mapped on all orthomosaics from July and September, with these lakes tending to be distributed over the entire length of the study area in areas of relatively crevasse-free ice and >75 m away from the calving front. Many of these lakes vary in size considerably, and likely either formed via the infilling of crevasses or moulins, or simply through the ponding of water into depressions on the ice surface. An overall decrease in the total number and area of these lakes was observed in both July and September (Figure 68), however, closer inspection of the data from both time periods highlights several interesting daily fluctuations.

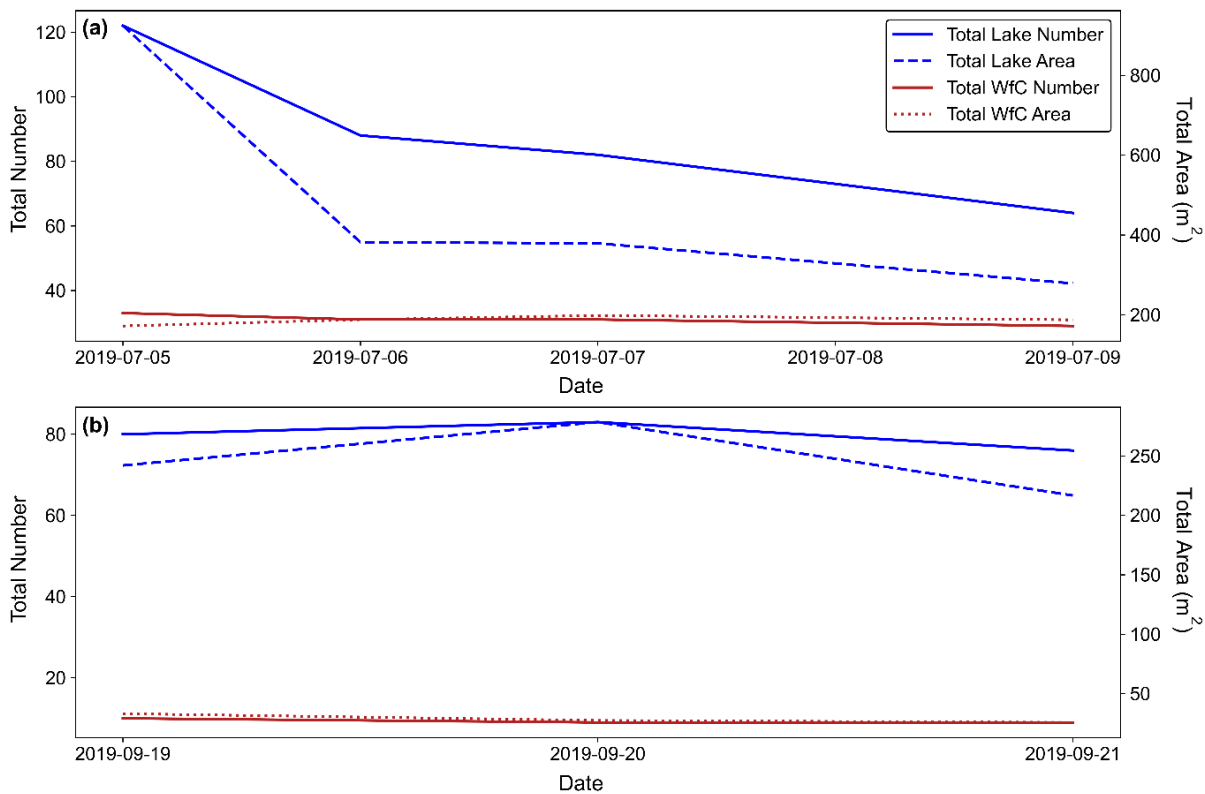


FIGURE 68 Daily variations in the total number and area of supraglacial lakes and water-filled crevasses (WfC) on the ice surface in both July (a) and September (b) 2019. Note that the legend shown in panel (a) is also applicable for the data series shown in panel (b).

Around 122 lakes were mapped over the study area on the 5th July, equating to a total lake area of 924.20 m². Yet by the 9th the number of lakes on the surface had decreased by 46% ($n=65$), while total lake area had dropped to 284.36 m², a decrease of 70% (Figure 68a). Such a decrease in total lake area was largely due to the observed drainage of several large lakes over this period (Figure 69). Further analysis of these changes revealed that many lakes drained in a ~22-hour period between the 5th and 6th July (from 122 to 88 lakes, or a 28% decrease). Indeed, the greatest change in lake area also occurred in this period, decreasing by 59% to 381.92 m². This was the greatest single change in lake number and area observed during July 2019.

In September by contrast a slight increase (~4%) in lake number was observed between the 19th ($n=80$) and 20th ($n=83$), which was coupled with an increase in total lake area of 15%, from 241.97 m² to 278.44 m² (Figure 68). This was also accompanied by a ~100% increase in the area of the largest observed lake on the ice surface over this period, from 18.04 m² to 36.12 m². This change represents the development of a new, large lake forming on the ice surface in this period, rather than an already established lake simply growing in size.

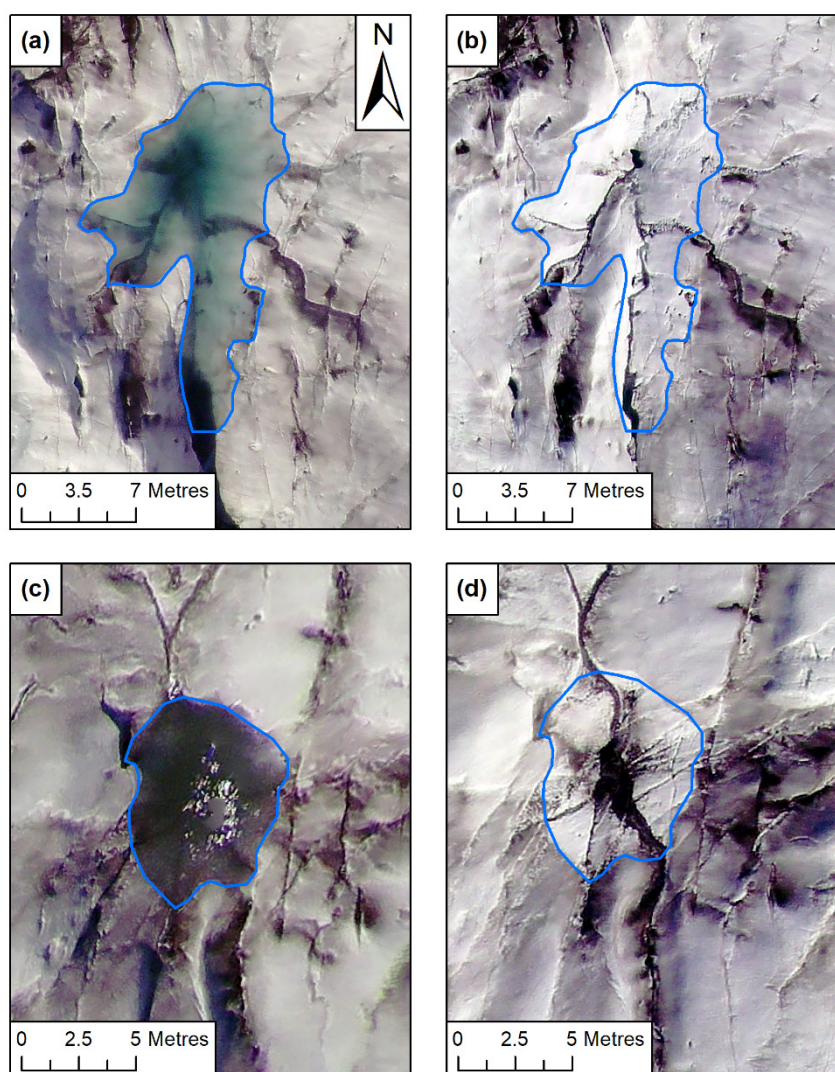


FIGURE 69 The drainage of supraglacial lakes on the ice surface between the 5th and 6th July 2019. (a) Example of one of the large lakes on the surface of Fjallsjökull on the 5th July. (b) Same area as shown in (a) but from the 6th, with the lake now having almost drained entirely. (c) & (d) Same as (a) and (b) respectively but for a different lake on the ice surface which also drained during this period. Approximate previous lake extent in (b) and (d) given by the blue outline. Note the different scale bars between the upper and lower panels. Location of both lakes relative to the overall ice surface is shown in Figure 67a. Background is the orthomosaics for the respective days.

Interestingly, this new lake formed in the depression held by a lake that drained relatively recently, and when formed it covered the same extent as this old lake, indicating that lakes may have been forming and draining on the ice surface relatively rapidly during this time (Figure 70). In comparison, between the 20th and 21st, overall lake number decreased by 8% (from 83 lakes to 76), with a corresponding reduction in overall lake area from 278.44 m² to 216.67 m², or a 22% decrease. The area of the largest lake (which had only formed <24 hours prior) also decreased in this period, from 36.12 m² to 26.11 m², equating to a 28% decrease.

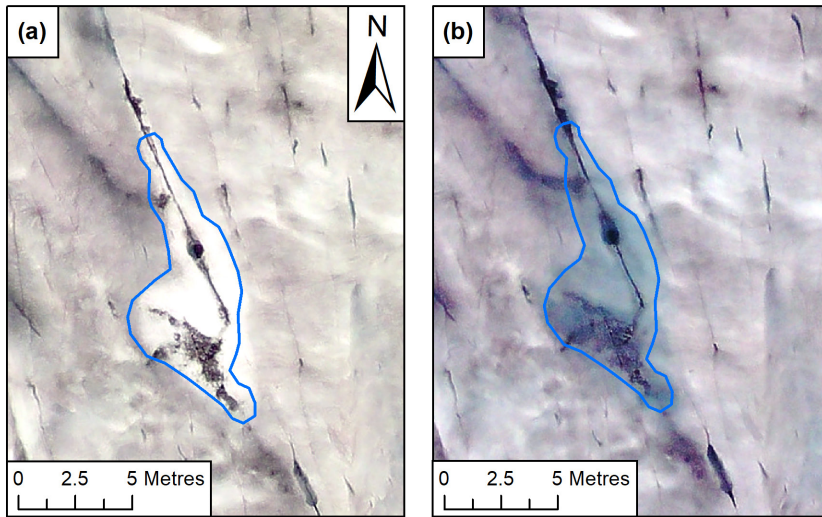


FIGURE 70 Example of the refilling of supraglacial lakes that occurred between the 19th and 20th September 2019. (a) One of the recently drained lakes on the surface of Fjallsjökull on the 19th September, with the extent of the old lake shown by the blue outline and white area. (b) Same area as (a) but from the 20th September, showing a newly formed lake on the ice surface that encompassed almost the exact same extent as the lake that drained previously. Lake location relative to the overall ice surface is shown in Figure 67b. Background is the orthomosaics for the respective day.

5.4.1.2 *Water-filled Crevasses*

In comparison to the observed changes in total lake number and area, the total number and area of water-filled crevasses (WfC) was considerably more stable over both time periods, although again there were some interesting daily fluctuations (Figure 68). On the 5th July, there were 33 such features, with the majority of these found in several distinct clusters across the study region. By the 9th this number had decreased by 12% ($n=29$), however, total WfC area actually increased by ~9% over the same time period, from 172.10 m² to 187.54 m² (Figure 68a). This was likely due to the formation of a ~20.79 m² WfC on the ice surface from the 6th onwards. Additionally, by the 7th, a large (>50 m in length) WfC had formed at the calving front towards the middle of the study area, but rather than be filled with meltwater, it was instead filled with lake water, and was the only feature of this kind to be observed in July 2019.

In comparison, on the 19th September there were 10 WfC on the ice surface, equating to a total area of 33.08 m². By the 21st, this number had decreased by ~10% ($n=9$), while the total area had decreased by 22%, to 25.29 m² (Figure 68b). Closer inspection of the day-to-day variations reveals that the majority of this change occurred between the 19th and 20th, with a 10% and 17% decrease in the number and area of WfC observed during this time. In addition, and as was similarly the

case for July, several WfC that were filled with lake water, rather than meltwater, were observed at the calving front during all time periods in September.

5.4.2 2021 Field Season

5.4.2.1 *Supraglacial Lakes*

A large number of supraglacial lakes were also manually mapped on all orthomosaics in July 2021, with these again distributed over the entire length of the study area in regions of relatively crevasse-free ice. However, in comparison to July 2019, no lakes were found <100 m from the calving front, with only a few very small lakes (<2.50 m²) found within 150 m (majority found >150 m away). Furthermore, while an overall decrease in the total number and area of these lakes is observed, generally they were much more stable in this period, with the magnitude of change being far less than what was observed in July 2019. That said, there were still several interesting daily fluctuations present within this overall pattern, particularly in regard to the areal changes.

Overall, 124 lakes were mapped over the study area on the 6th, covering a total area of 1406.59 m². Yet by the 15th total lake number and area had only decreased by 13% (n=109) and 8% (1294.50 m²), respectively (Figure 71). While this decrease is likely due to the shrinkage and complete disappearance of those smaller lakes from the ice surface in this time, further analysis of the areal changes revealed that some lakes might have undergone a cycle of partial drainage and then regrowth over the same period. For example, between the 6th and 7th, and 7th and 8th, total lake area decreased by ~13% and 7% respectively, yet between the 12th and 15th, total area increased by ~11%. Such a change was likely due to the partial drainage of two large lakes in the upper part of the study region between the 6th and 8th July, and then the regrowth of these same lakes to their previous extents (or greater) by the 15th (Figure 72a-c).

5.4.2.2 *Water-filled Crevasses*

A much greater number of WfC were mapped across the study area in 2021, which strongly contrasts with the comparatively low number mapped in July and September 2019. Such a contrast is not solely a result of increased areal coverage (in 2021), but also because the study area during this time was far more crevassed than it was in 2019, with such regions more likely to favour WfC development. Similar to the observed changes in total lake number and area, the total number and area of WfC also decreased over the study period. However, and in contrast to the observed lake changes, the total number and area of WfC were far less stable in this period, with several large day-to-day fluctuations observed.

On the 6th July, there were 121 WfC mapped across the study region, with these covering a total area of 1138.82 m². By the 15th July, total WfC number had decreased by 14% (n=104), resulting in an aerial coverage of 1073.46 m² (or a 6% decrease) (Figure 71). While this decrease is again likely due to the shrinkage and complete disappearance of those smaller WfC from the ice surface in this time, further analysis of the day-to-day changes indicates that several WfC also display a pattern of partial (or complete) drainage and regrowth, over timescales of 24 hours to several days.

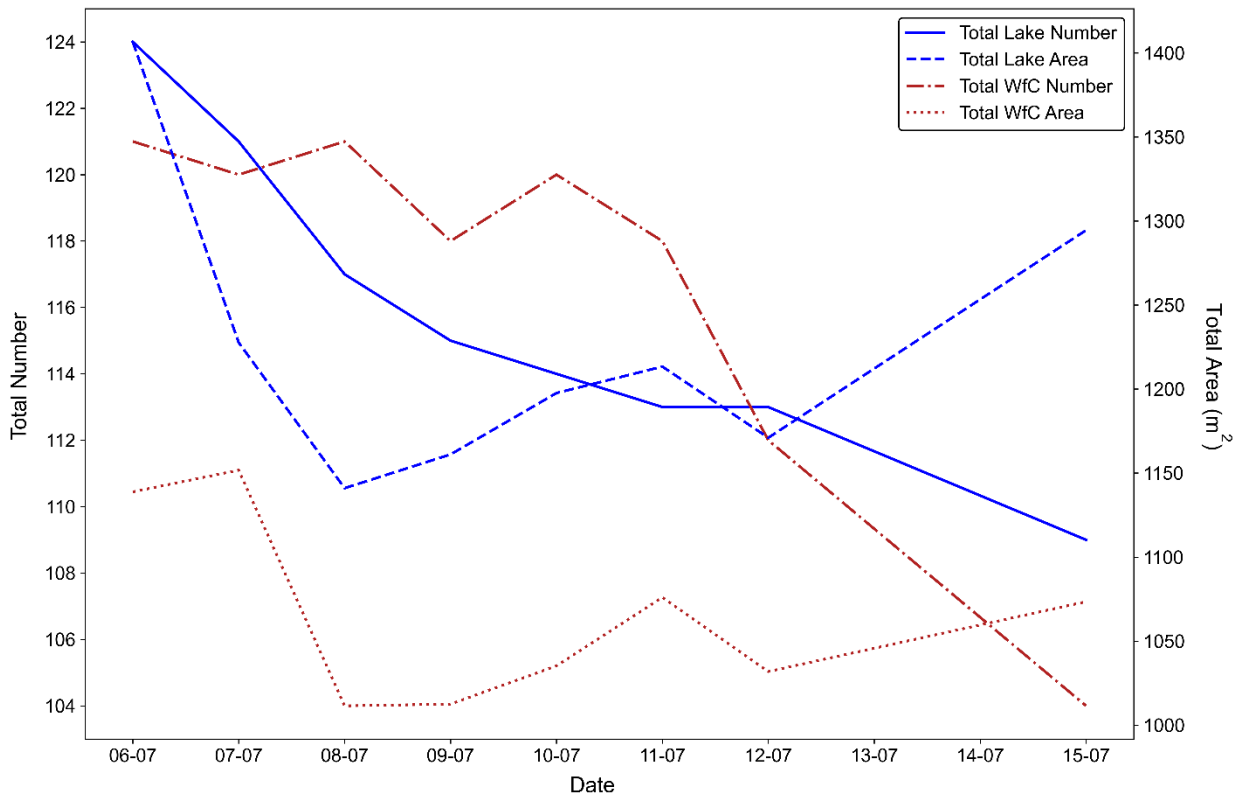


FIGURE 71 Daily variations in the total number and area of supraglacial lakes and WfC on the ice surface in July 2021.

For example, between the 6th and 8th July, total WfC area decreased by 12%, yet between the 12th and 15th, total area increased by ~4%. Although a comparatively small increase, such a change is almost wholly due to the partial drainage of two large WfC in the upper part of the study region between the 6th and 8th July, and then the regrowth of these same WfC to their previous extents (or greater) by the 15th (Figure 72d-f). This is very similar to the pattern of lake shrinkage and growth described in the previous sub-section, and indeed, it occurred in the same region of the glacier.

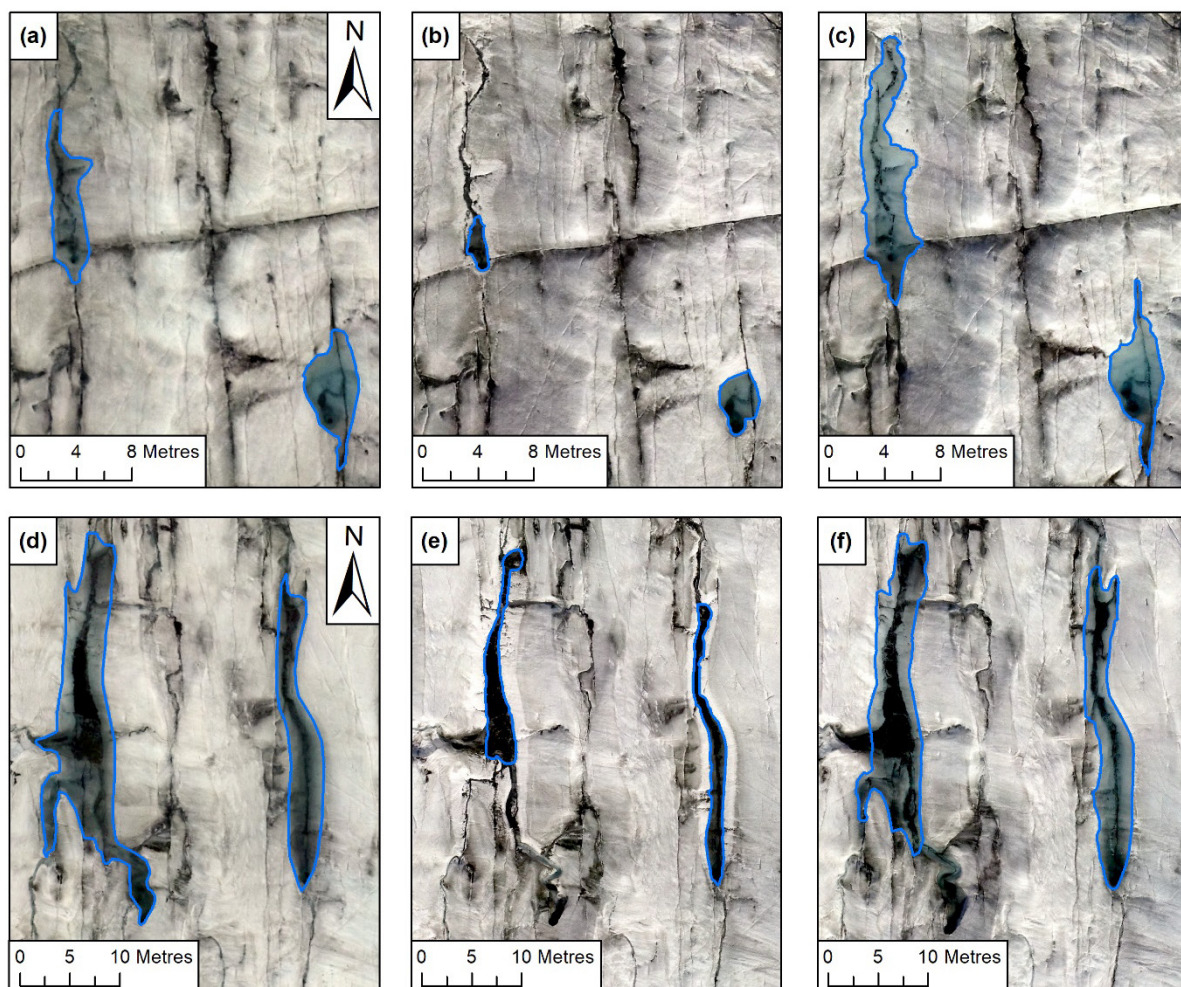


FIGURE 72 Variations in lake and WfC area on the ice surface in July 2021. (a) Example of two large lakes on the upper surface of Fjallsjökull on the 6th July. (b) Same area as shown in (a), but from the 8th, showing how both lakes have considerably decreased in size. (c) Same area as shown in (a) & (b), but from the 15th, showing how both lakes have now increased in size to cover a greater extent than they did on the 6th. (d)-(f) Same as a (a)-(c), but for two large WfC. Location of both sets of features relative to the overall ice surface is shown in Figure 67c. Background is the orthomosaic for the respective day.

Furthermore, near-daily fluctuations in total WfC area and number also occurred between the 7th and 12th July, in the western part of the study area (Figure 73). Here, a new WfC formed on the ice surface sometime between the 7th and 8th, covering an area of $\sim 7.67 \text{ m}^2$. This WfC then completely drained by the 9th, before forming again in the same depression (but to a slightly smaller extent) sometime over the following 24-hour period. By the 11th, however, it had substantially grown in size (from 5.37 m^2 to 19.23 m^2 , or a 258% increase), before completely draining again by the 12th, after which point it did not form again. This growth and drainage between the 10th and 12th is almost wholly responsible for the 4% increase (and subsequent 4% decrease) in total WfC area during this time.

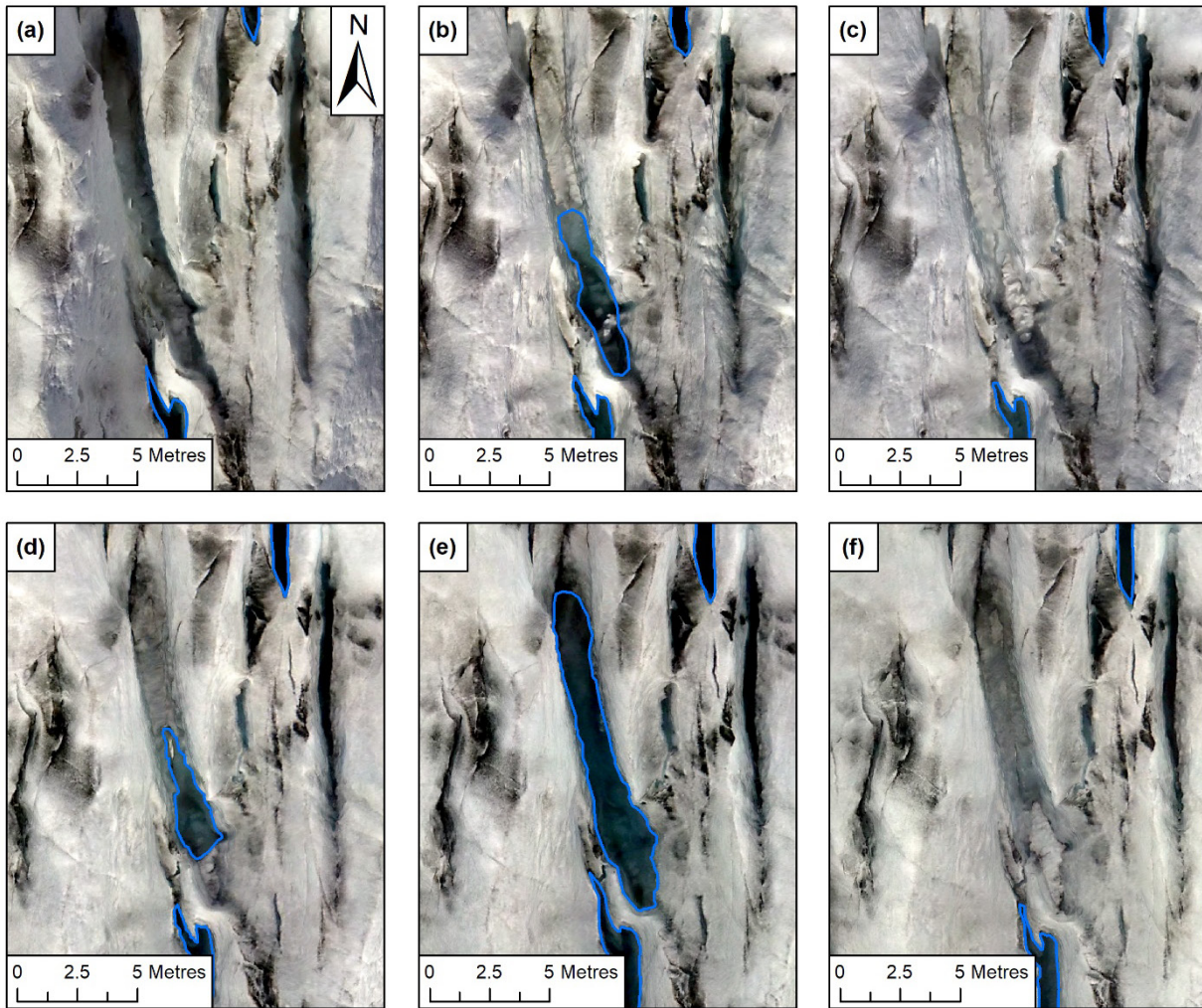


FIGURE 73 (a)-(f) An example of the near-daily variations in WfC number and area that occurred in the western part of the study area between the 7th and 12th July 2021. A full description of these variations is given in the text. WfC location relative to the overall ice surface is shown in Figure 67c. Background is the orthomosaic for the respective day.

Finally, several WfC, which were filled with lake water, rather than meltwater, were also observed near the calving front over the study period, with these remaining fairly stable throughout this time. However, it is worth noting that at some point between the 12th and 15th, one large WfC near the calving front (~90 m in length), evolved from being filled with meltwater to being filled with lake water. This was the only time, in both July and September 2019, and July 2021, where this evolution from a crevasse that was filled with meltwater, to one filled with lake water, was observed.

Chapter 6 INTERPRETATIONS and DISCUSSION

6.1 Variations in the Dynamics of Fjallsjökull

6.1.1 Large-scale Velocity Variations and Links to Basal Topography

Generally speaking, calving glaciers flow faster than their land-terminating counterparts due to higher rates of basal sliding (Benn et al., 2007b; Carrivick and Tweed, 2013). This is because the presence of a water body at the terminus of these glaciers (either freshwater or tidewater) causes an increase in basal water pressure at these locations (Meier and Post, 1987; Carrivick and Tweed, 2013). Such high basal water pressures tend to arise due to lake- or ocean-water propagating up-ice, and because high basal water pressures are required to be able to evacuate basal water from the glacier against the outward pressure of the water body (Sugiyama et al., 2011; Liu et al., 2020). This means that the glacier is effectively supported by the proglacial waterbody in the near-terminus region, and as a result, the ice overburden pressure is equal to the basal water pressure (Meier and Post, 1987; Tsutaki et al., 2013). Therefore, the effective pressure (Section 2.1.) is at or close to zero, meaning basal drag is almost non-existent and thus velocities are (and can remain) elevated (Sugiyama et al., 2011; Carrivick et al., 2020).

This also explains why velocities tend to increase close to the termini of grounded calving glaciers (e.g. O’Neel et al., 2005; Benn et al., 2007b; Tsutaki et al., 2019), a pattern which is clearly visible in the velocity data (Figure 50 and 51). It is also important to note that the high hydraulic head within calving glaciers (due to the propagation of water up-glacier) means that any slight change in water input to the basal system (e.g. through meltwater drainage or depth increase of the water body), or indeed glacier thickness, will cause significant additional increases in velocity to occur because ice overburden is consistently close to the basal water pressures in these regions (Meier and Post, 1987; Benn et al., 2007b; Sugiyama et al., 2011; Tsutaki et al., 2013).

The velocity data (Figure 50 and 51) clearly indicate a region of fast ice flow ($\sim 0.9\text{--}1.0\text{ m d}^{-1}$ in 2019 and $\sim 1.2\text{ m d}^{-1}$ in 2021), situated in the upper portion of the study area, which is a result of the above relationship between reduced effective pressure and increased basal sliding.

However, such high velocities, and indeed the overall spatial variability in velocity that is observed in both 2019 and 2021 is also strongly controlled by the particular basal topography underlying the study area (Figure 34) (Magnússon et al., 2012; Dell et al., 2019). Information about the bedrock topography of Fjallsjökull is provided by Magnússon et al. (2012), who acquired point

measurements from across the ablation area (as well as its proglacial lake) through Radio-Echo Sounding surveys conducted between 1998 and 2006. Although these measurements have an error of ± 20 m in the Z plane (Magnússon et al., 2012), this uncertainty is significantly less than the elevation range observed within the overall dataset. Where data was sparse, e.g. in steep or heavily crevassed regions, they calculated pseudo profiles by estimating the relationship between the surface slope and the ice thickness, before interpolating these data to produce a contour map of Fjallsjökull at 20 m intervals (Magnússon et al., 2012). Importantly, these data reveal that Fjallsjökull, and its proglacial lake Fjallsárlón, sit within a $\sim 3 \times 4$ km subglacial trough, formed during the LIA advance, and which lies up to 206 m below sea level. Within this trough, two deeply incised bedrock channels can also be observed, one under the northern, and the other under the southern portion of the present-day terminus.

The southern bedrock channel, which is ~ 2 km by ~ 2 km and runs from ~ 0 m a.s.l. at the grounded southern margin to ~ -120 m deep at its maximum, is of particular interest here as it directly corresponds to the area covered by the UAV surveys in both 2019 and 2021 (Figure 74). Indeed, the region of elevated velocities consistently observed in the upper portion of the study area directly corresponds to the deepest parts of the subglacial channel (~ 100 - 120 m below sea level). This is because glaciers flow faster when entering deeper water due to the inverse relationship that exists between the effective pressure and basal drag (Warren and Kirkbride, 2003; Benn et al., 2007b; Liu et al., 2020). Deeper water means greater up-ice propagation of lake water, which results in higher basal water pressures, increased bed separation and thus higher overall velocities (Tsutaki et al., 2011; Carrivick and Tweed, 2013; Sutherland et al., 2020). This relationship between water depth and ice velocity likely explains why elevated velocities are consistently found in the upper portion of the study area for all time periods in both years, and why velocities generally decrease as water depth decreases with increasing proximity to the grounded margin, indicating that the basal topography is exerting a first order control on the velocity of Fjallsjökull (Benn et al., 2007b; Storrar et al., 2017; Dell et al., 2019).

Such high velocities in the upper portion of the study area also likely explain why up to $\sim 2.50 \pm 0.18$ m, and $\sim 5.50 \pm 0.15$ m of negative surface elevation change were observed in this region in 2019 and 2021, respectively (Figure 52 and 53). Elevated glacier velocities, driven by the deep bedrock channel, cause the ice surface to undergo longitudinal extension and thus thinning due to compressive vertical strain (Tsutaki et al., 2013; Shapero et al., 2016). This thinning reduces the thickness of the glacier, causing a reduction in the overburden pressure, which as mentioned above is already sensitive to any change in water depth, or indeed ice thickness (Vieli et al., 2001; Benn et al., 2007b; Sugiyama et al., 2011).

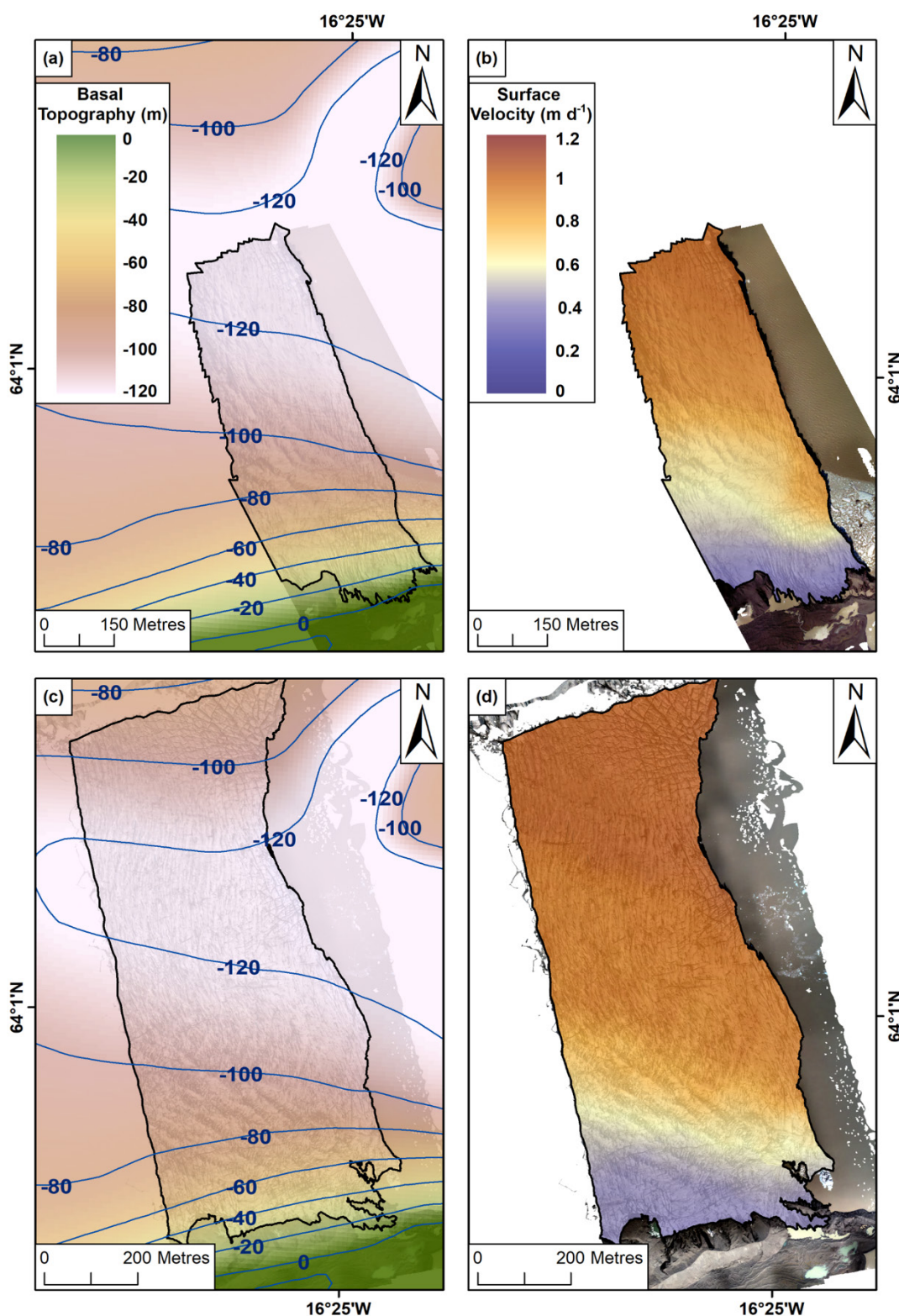


FIGURE 74 Bedrock topography and surface velocity for select periods in July 2019 and 2021. (a) Bedrock topography under the southern portion of Fjallsjökull, indicating the presence of the 120 m deep subglacial channel under the study region. Blue lines represent basal contours at 20 m intervals. (b) Surface velocity for the 5th-6th July 2019, highlighting how the areas of fastest velocity are generally found where the bedrock topography is at its deepest. Background in both panels is the orthomosaic from the 5th July 2019. (c) & (d) Same as (a) & (b), respectively, but for the 7th-8th July 2021. Background in both panels is the orthomosaic from the 8th July 2021.

This leads to a further reduction in the effective pressure, causing an additional increase in velocity and thus further longitudinal extension, thinning and the implementation of a positive feedback mechanism termed 'dynamic thinning' (Section 2.4.3.2.) (Tsutaki et al., 2013; Sakakibara and Sugiyama, 2018; Carrivick et al., 2020; Liu et al., 2020). Furthermore, the influence of the basal topography is highest where the glacier is thinnest (i.e. where the ratio between water depth and ice thickness is highest), which may also explain why the most negative changes in elevation are found where the channel is at its deepest (Benn et al., 2007b; Storrar et al., 2017).

Evidence for the occurrence of longitudinal extension is provided by the presence of large areas of transverse crevasses, particularly in the upper portion of the study region, as well as near the calving front. Such crevasses can only form where the rates of longitudinal stretching (extension) are particularly high, and thus must be related to areas of fast ice flow (Vieli et al., 2000; Mottram and Benn, 2009; Chudley et al., 2021). Furthermore, because the depth to which a crevasse can penetrate also increases with the amount of longitudinal extension, this mechanism can lead to an increase in calving at the terminus by increasing the likelihood of crevasses penetrating to the waterline and thus inducing failure (Nick et al., 2007a; Shapero et al., 2016).

This mechanism can also induce calving by increasing the effect of buoyant forces acting on the normally grounded terminus (van der Veen, 2002; Trüssel et al., 2013; Dell et al., 2019). Any thinning of the ice, either by surface melting, retreat of the glacier into deeper water, or longitudinal extension, subjects the ice to buoyant (upward) forces (Warren et al., 2001; Boyce et al., 2007; Liu et al., 2020). To remain grounded the surface and basal gradients of a locally buoyant ice front must maintain a constant ratio, however, if this is not possible then the buoyant part of the terminus must rotate upwards to restore equilibrium, producing large bending forces near the junction with grounded terminal ice (Benn et al., 2007b; Boyce et al., 2007). This then leads to rapid fracture propagation and calving, with pre-existing crevasses controlling the precise location of failure (van der Veen, 1996; Benn et al., 2007b).

Any increase in calving via either of these two mechanisms can lead to an amplification of the dynamic thinning mechanism, which can exacerbate the retreat of calving glaciers in response to an initial forcing (Vieli et al., 2001; Benn et al., 2007b; Tsutaki et al., 2019). This is because calving leads to sudden mass loss at the terminus, and so to replace these losses the glacier must drawdown ice from higher elevations (Howat et al., 2008b; Carrivick et al., 2020). This increases the surface slope (and consequently the driving stress), leading to increased velocities (and, therefore, increased longitudinal extension), thinning, calving and further retreat (Benn et al., 2007b; Shapero et al., 2016; Carrivick et al., 2020; Sutherland et al., 2020). Although a portion of the thinning observed across both time periods in 2019, as well as in July 2021, would have likely

occurred in response to surface ablation (e.g. Purdie et al., 2008; Trüssel et al., 2013), the magnitude of negative change observed suggests that it has primarily been forced by ice dynamics. For example, while the results from 2019 only cover five and three days, respectively, the fact that $\sim 1.5\text{--}2\text{ m}$ of surface thinning is observed over both time periods, and that in both cases this area of lowering coincides with the area of heightened velocities, suggests that this feedback mechanism could be occurring in this region of Fjallsjökull. This is supported by the fact that away from this region of high velocities only small changes in surface elevation are observed ($\pm 0.5\text{ m}$), which indicates that surface melt is the likely driver of surface change in these regions, rather than ice dynamics.

Although no major calving events were observed in this upper region of Fjallsjökull in either July or September 2019, evidence for buoyancy-driven calving may be provided in both cases by the presence of WfC in this region of the calving front (Figure 75 and 76).

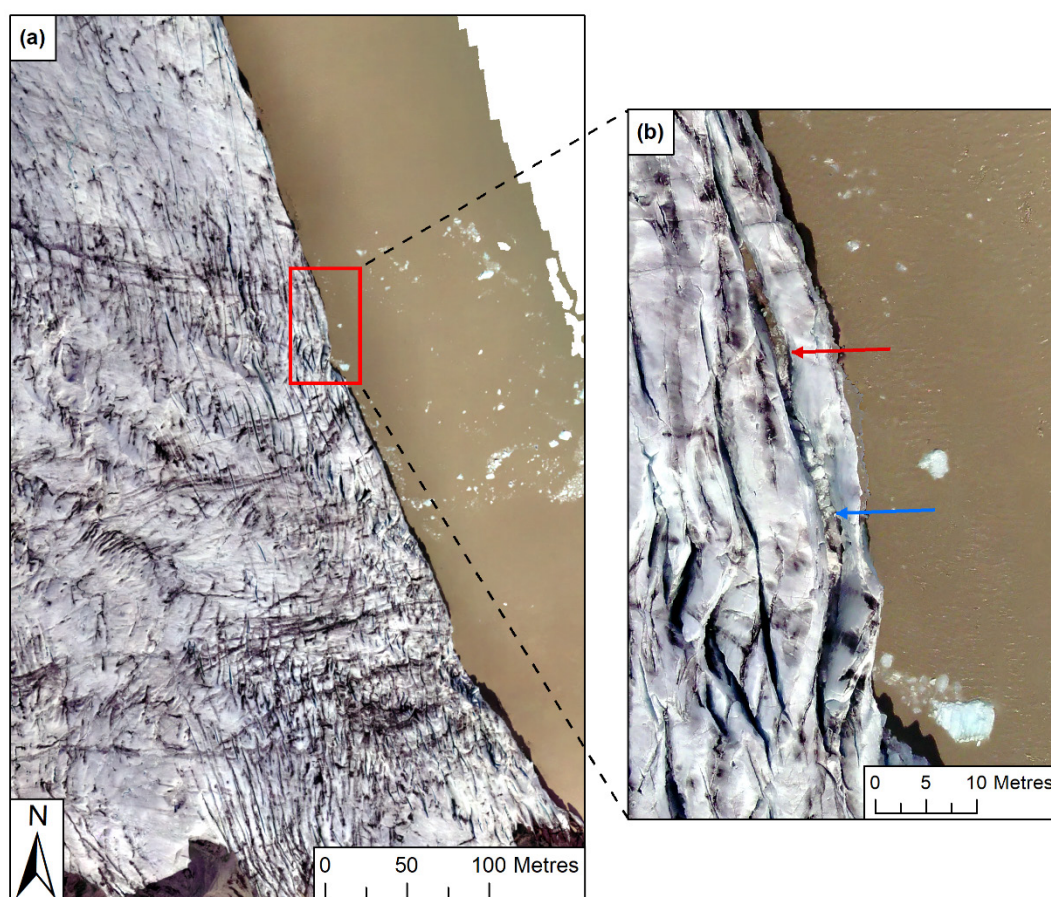


FIGURE 75 Location and size of the basal crevasse that was observed near the terminus of Fjallsjökull on the 7th July 2019, relative to the study region overall. The crevasse is $\sim 65\text{ m}$ long and 2 m wide. Note how the water visible within the crevasse is the same brownish colour as the lake water (red arrow), whilst also note the presence of brash ice within the crevasse, which is floating on the lake-water within (blue arrow). Background in both panels is the orthomosaic from the 7th July 2019.

These crevasses are clearly filled with lake water rather than meltwater, suggesting they were opened and filled from below, with one such crevasse observed in this region in July, and four observed over the same region in September. As basal crevasses can only form in response to the large bending forces acting on a locally-buoyant terminus (van der Veen, 1998a,b, 2002; Boyce et al., 2007), their presence here, although limited, indicates that this portion of the terminus may be subject to buoyant forces (and thus buoyancy-driven calving) as this portion of the glacier retreats through the deepest part of the southern bedrock channel (Magnússon et al., 2012; Dell et al., 2019).

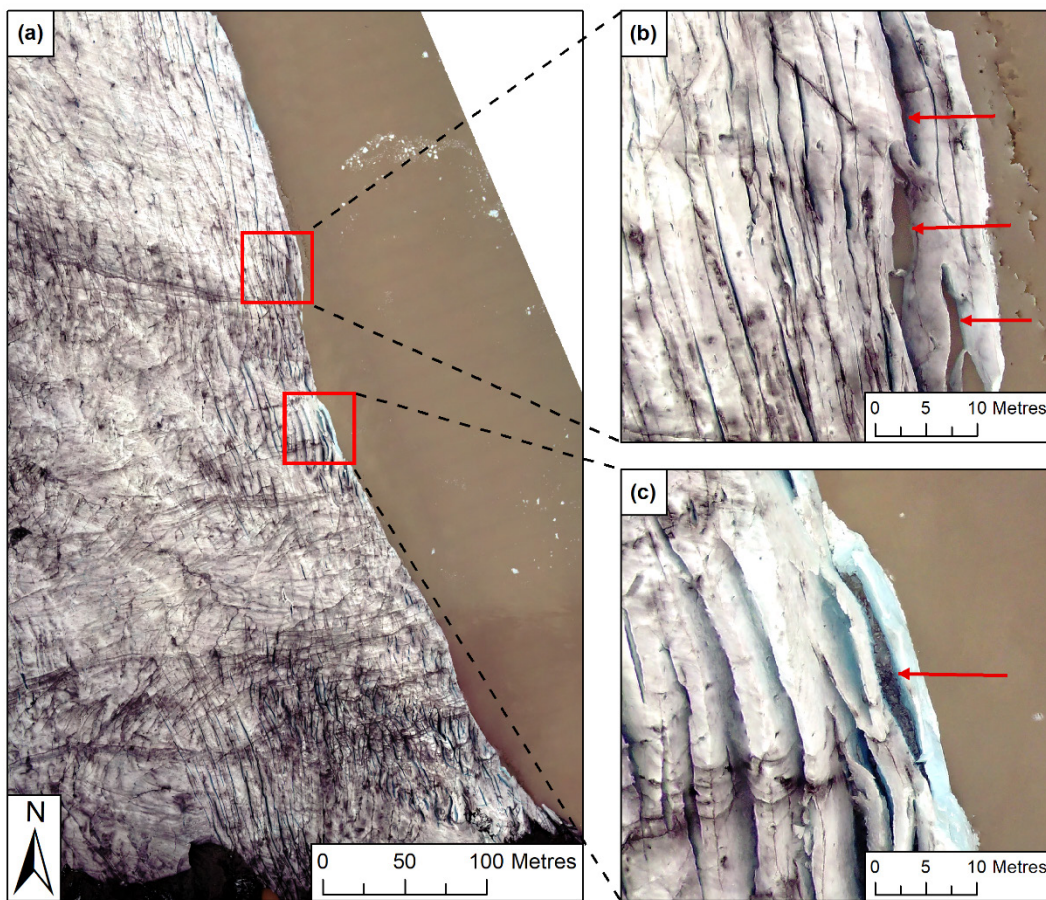


FIGURE 76 Location and size of the four basal crevasses that were observed near the terminus of Fjallsjökull in September 2019, relative to the study region overall. The crevasses range between 10-25 m in length and 1-2 m in width. Note how the water visible within each crevasse is the same brownish colour as the lake water (red arrows). Background in each panel is the orthomosaic from 19th September 2019.

The suggestion that this mechanism of dynamic thinning is occurring at Fjallsjökull is further strengthened by the field data from July 2021, which not only covered a longer time period (~10 days), but also a larger area than was possible in 2019. Indeed, up to ~5.50 m of surface thinning was observed in the upper portion of the study region during this period, with this again corresponding to the area of highest velocities.

However, and perhaps more importantly, this overall pattern of surface thinning was not limited solely to the upper region. Rather, this region had increased in size, meaning a much larger portion of the overall study area was now characterised by these strongly negative surface changes. For example, in the lower portion of the study region, between 3.5 and 4.5 m of negative change were observed in this period, yet two years' prior, this same region was characterised by only ~1-1.5 m of negative change. It is important to reiterate that although a portion of this thinning would have likely occurred in response to surface ablation, the magnitude of negative change observed suggests that it has primarily been forced by ice dynamics. This not only confirms that the dynamic thinning mechanism is occurring at Fjallsjökull, but also suggests that it may now be impacting upon a much larger area of the glacier than it was in 2019. Several previous studies of lake-terminating glaciers have also observed an increase in the areal extent of the dynamic thinning mechanism over time (e.g. Trüssel et al., 2013; King et al., 2018; Liu et al., 2020), reiterating its importance as a key forcing mechanism for the dynamics of Fjallsjökull.

Furthermore, several WfCs that were filled with lake water, rather than meltwater, were also observed in the upper part of the study region in July 2021 ($n=4$, Figure 77). However, in direct contrast to 2019, these features were located in a region where a significant number of calving events (of variable size) were observed. Importantly, these features themselves were actively eroded over the course of the study period (i.e. they were lost to calving), with no such features observed in this region by the 15th July as a result. The presence, and subsequent loss of these features, therefore, provides additional, robust evidence for the occurrence of buoyancy-driven calving in this region of Fjallsjökull, as suggested previously by Dell et al. (2019).

It is important to note that this is unlikely to be the only region of the calving front that is locally buoyant, with evidence from July 2021 suggesting that the lower portion of the study region may also be floating, at least in part. This evidence is provided by a large WfC, ~80 m in length and situated ~40 m from the calving front, which at some point between the 12th and 15th evolved from being partially filled with meltwater to being wholly filled with lake water (Figure 78).

This feature was first observed on the 4th July, but remained completely stable over the following seven days, up until at least the 11th. After this point, it is likely that full fracture propagation occurred, either through the downward pressure of the water within the crevasse, the upward propagation of a basal crevasse, or through some combination of the two. Regardless, once full-thickness propagation had occurred this resulted in the complete drainage of meltwater from the crevasse, followed by the subsequent re-filling (or inundation) of the crevasse by lake water. This is important because it strongly indicates that this region of Fjallsjökull must be locally buoyant, as if this were not the case then it is unlikely this 'switch' could have occurred. It is also important to

note that this is, to the best of our knowledge, the first time a WfC has been observed to evolve in this way, both at Fjallsjökull and for lake-terminating glaciers more generally.

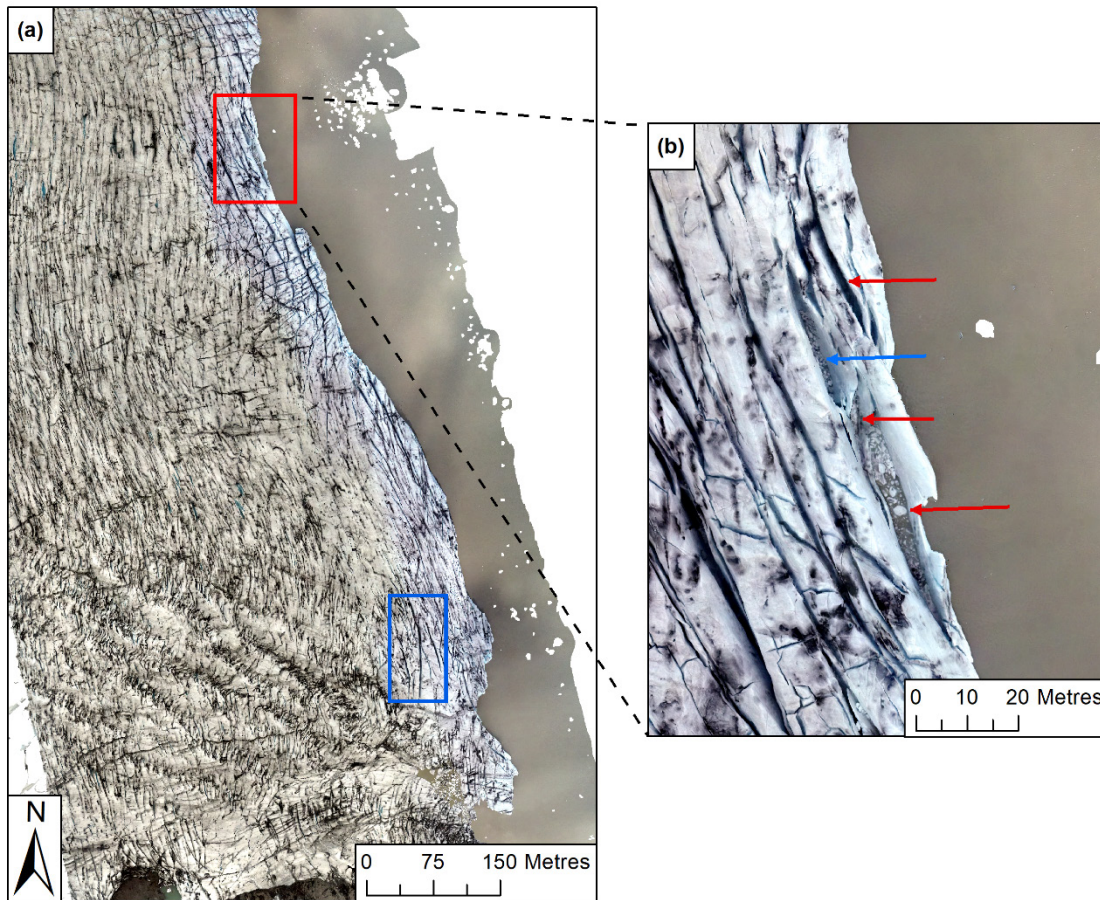


FIGURE 77 Location and size of the four basal crevasses that were observed near the terminus of Fjallsjökull in July 2021, relative to the study region overall. The crevasses range between 10-45 m in length and 2-5 m in width. Note how the water visible within each crevasse is the same brownish colour as the lake water (red arrows), whilst also note the presence of brash ice within one of the crevasses (blue arrow). The blue box in the lower half of the study region gives the extent shown in Figure 78. Background in both panels is the orthomosaic from 6th July 2021.

Therefore, the overall spatial variations in velocity that were observed in both 2019 and 2021 are strongly linked to the location and depth of the bedrock channel under this portion of Fjallsjökull (Dell et al., 2019). Velocities are greatest where the trough is at its deepest because glaciers flow faster when entering deeper water due to the inverse relationship that exists between the effective pressure and basal drag (Benn et al., 2007b; Carrivick and Tweed, 2013; Storrar et al., 2017). This has led to the implementation of a positive feedback mechanism between longitudinal extension, calving activity, frontal retreat and increased velocities to occur, termed dynamic thinning (Trüssel et al., 2013; Tsutaki et al., 2013, 2019). Indeed, the fact that in both 2019 and 2021 the most negative rates of surface thinning were observed in the upper portion of the study area, and that this region directly corresponded to the deepest part of the southern bedrock

channel, strongly indicates that this mechanism is occurring at Fjallsjökull. Finally, it is also likely that this mechanism has led to the terminus in this region to be subject to increased buoyant forces (and thus buoyancy-driven calving), due to the presence of basal crevasses. These features were observed in the upper portion of the study area in both 2019 and 2021, and because they can only form in response to forces that act upon a locally buoyant terminus (e.g. van der Veen, 1998a; Boyce et al., 2007), it means the terminus in this region must be subject to buoyancy-driven calving, particularly where the bedrock channel is deepest.

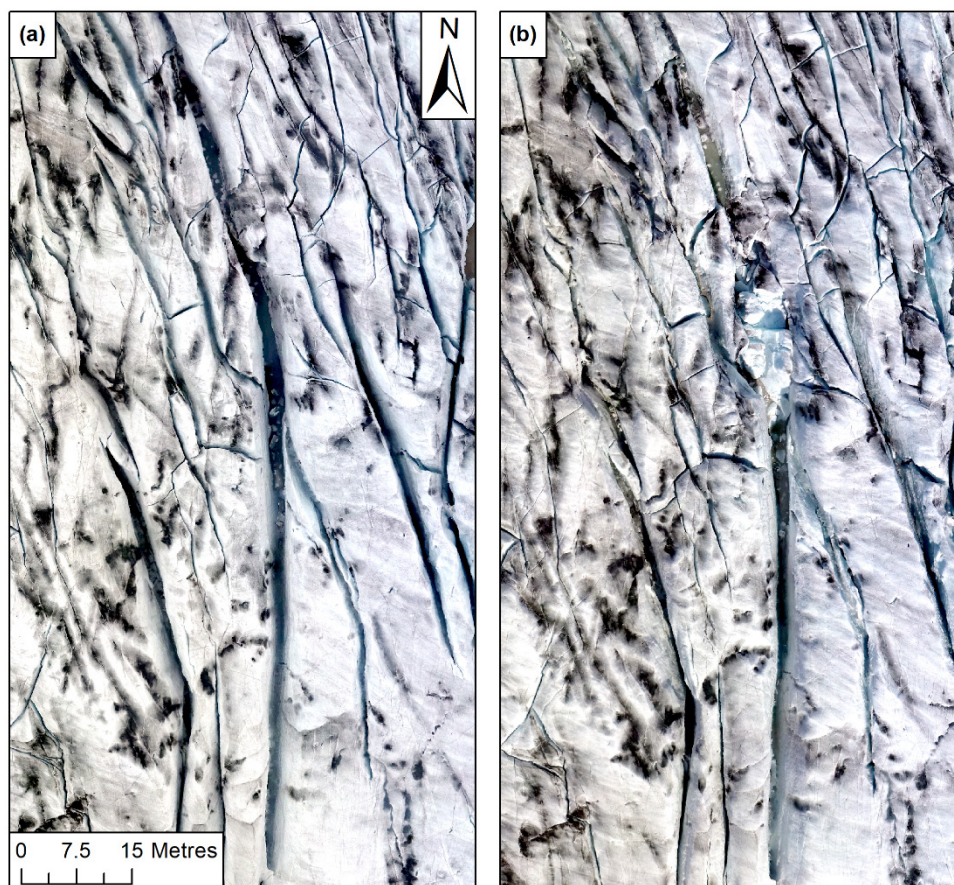


FIGURE 78 Evolution of the large WfC in the lower portion of the study region that went from being partially filled with meltwater to being wholly filled with lake water between the (a) 12th and (b) 15th July 2021. The crevasse is some 80 m in length and ~2.5 m wide. Note how on the 12th the water within the crevasse is a bluey/brown colour, whereas by the 15th the water is the same murky brown as the lake, suggesting that full fracture propagation occurred at some point between the 12th and 15th. Background is the orthomosaic from the (a) 12th and (b) 15th July 2021, respectively.

These findings are supported by the results of Dell et al. (2019) in their multi-faceted investigation of the evolving dynamics of Fjallsjökull between 1973 and 2017. The authors found that although changes in terminus position and lake area were likely controlled by rising air temperatures since 1973, they also attributed its changing dynamic regime to the presence of the deep basal trough

under the glacier, and that its influence had increased over the study period as the glacier had begun to retreat into this trough (Dell et al., 2019). The authors suggest, like is done here, that the trough, and in particular the two deeply incised bedrock channels, have caused an increase in flow acceleration and thinning to occur in these localities, which has led to the initiation of a positive feedback mechanism between retreat, acceleration, surface thinning and calving. The authors also found that the areas of fastest ice flow directly corresponded to the location of these channels, which, they suggest, highlights the key role the subglacial topography has in governing the overall velocity patterns of the glacier (Dell et al., 2019).

However, although the findings of both studies agree that the basal topography of Fjallsjökull has greatly influenced its velocity over recent years, the actual velocities obtained in both studies differ quite substantially. Whereas Dell et al. (2019) recorded max velocities of $\sim 0.82 \text{ m d}^{-1}$ over the southern bedrock channel; peak values observed in this research from July 2021 are around one and a half times greater, at $\sim 1.2 \pm 0.16 \text{ m d}^{-1}$. Such discrepancies may be due to the temporal separation between studies, where Dell et al. (2019) observed their peak values in 2016/2017, whereas the data here is from 2019 and 2021, and as such, a velocity increase would be expected over this period as the glacier retreats further into its trough. Similarly, as their results are annual velocities, not daily, then it is likely that any seasonal periods of higher velocities may have been averaged out over their longer time period. However, the most plausible reason for the contrast in velocities is the differences in the spatial resolution of the imagery. Dell et al. (2019) utilised 10 m resolution Sentinel 2 imagery, whereas the resolution of the UAV orthomosaics used for the velocity analyses (0.25 m) is ~ 40 times finer. As a result, fine-scale velocity gradients occurring at the terminus of Fjallsjökull can more easily be picked out and tracked in the UAV imagery, whereas the coarser resolution of the Sentinel imagery means such gradients will likely have been smoothed-over and missed (Nagler et al., 2015; Joughin et al., 2018). The ability of UAV imagery to pick out such fine-scale velocity gradients is one of the primary reasons why they have become so popular in glaciological research over recent years, and highlights their importance for investigating the short-term dynamics of fast-flowing calving glaciers, particularly in their near-terminus regions (e.g. Ryan et al., 2015; Chudley et al., 2019; Jouvét et al., 2019).

6.1.2 Localised Velocity Variations and Links to Subaqueous Melt

However, not all the velocity variations observed during both 2019 and 2021 can necessarily be attributed solely to the influence of the bedrock topography. Dell et al. (2019) suggested that calving at Fjallsjökull likely occurs via a combination of buoyant forces acting on the terminus, force imbalances at terminal ice cliffs and subaqueous melting, although they could not provide direct evidence for any of these processes occurring. However, field observations from both July

and September 2019, as well as July 2021 provide direct evidence that subaqueous melting is occurring at the terminus of Fjallsjökull, due to the presence of extensive thermal erosion notches at the waterline (Figure 79 and 80). In addition, this means that calving may also occur by force imbalances at the terminus, due to the strong link between the two mechanisms (Benn et al., 2007b; Mallalieu et al., 2020).

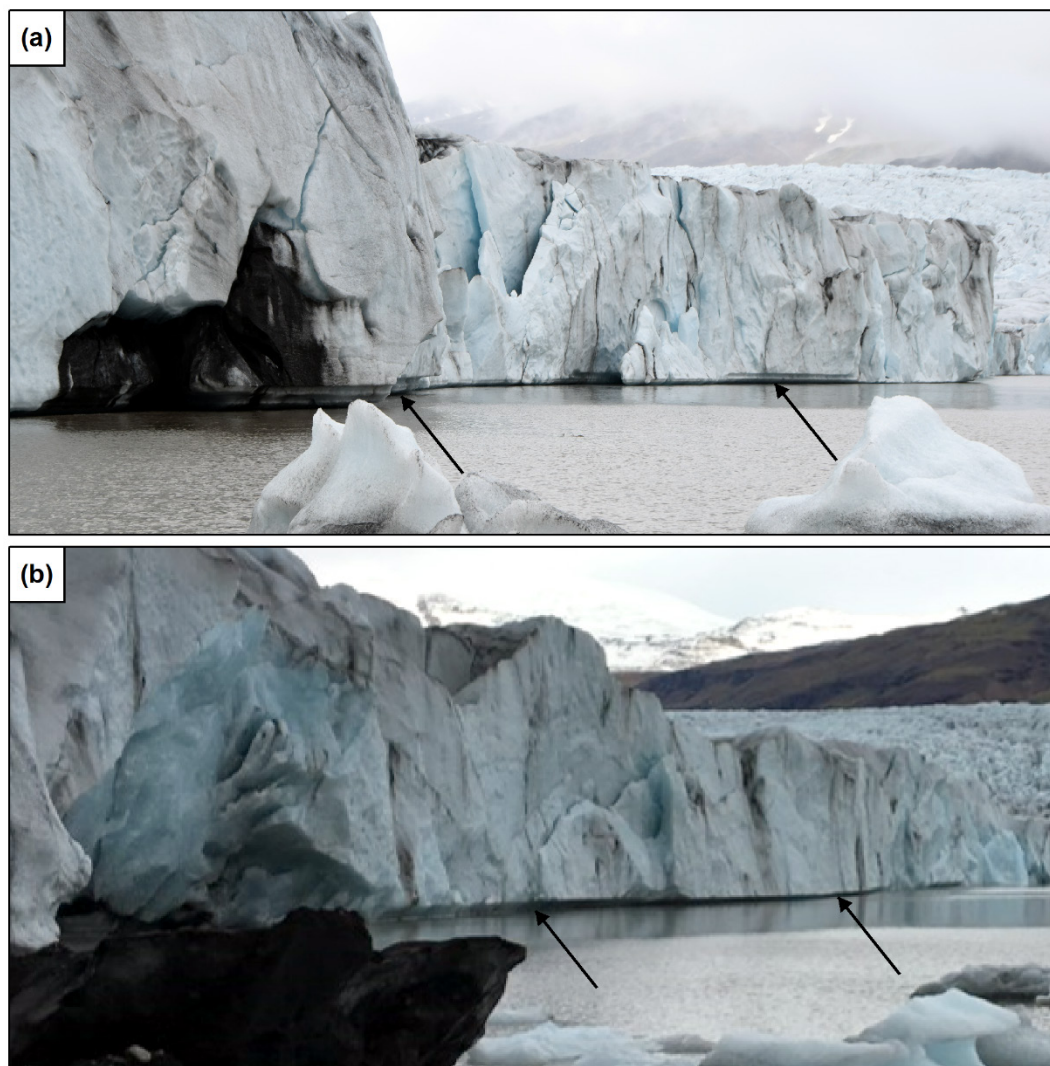


FIGURE 79 Photographs of the southern margin of Fjallsjökull acquired on the (a) 4th July and (b) 19th September 2019, highlighting the presence of extensive thermal erosion notches at the waterline (black arrows) in this region. The fact that in both photographs the notches sit above the waterline suggests that the level of the lake fell since they were formed, which would increase the force imbalance at these locations. Also note the steep and highly crevassed nature of the calving front. For reference the calving front here is ~20 m high.

Thermal erosion notches form via melt at the waterline, with the size (depth and height) of the notch dependent on how much the level of the water body fluctuates (Röhl, 2006; Benn et al., 2007b; Mallalieu et al., 2020). The largest notches develop when water levels are relatively

constant as this allows the heat energy from the surface water to be concentrated in a narrower band of ice (Benn et al., 2007b; Schild et al., 2018).

Very few measurements of notch melting at lake-margins have been made, however, rates of 0.8 m d^{-1} were reported by Haresign and Warren (2005) at Glacier Leon, while rates of between 0.2 and 0.3 m d^{-1} have been recorded at Miage (Diolaiuti et al., 2006) and Tasman (Röhl, 2006) glaciers. More recently, it has been suggested that such rates of notch erosion may be occurring at the termini of Glaciar Perito Moreno, Patagonia (Minowa et al., 2017) and Russel Glacier, Greenland (Mallalieu et al., 2020), although neither study were able to provide direct measurements. Similarly, while direct measurements were also unable to be made here, it is not inconceivable that such rates could be found to be occurring at the margin of Fjallsjökull. Indeed, the fact the observed notches seemed fairly extensive, particularly in depth, would suggest the level of Fjallsárlón remained relatively consistent over an extended period of time (in both 2019 and 2021), permitting significant amounts of thermal melt to occur.

Thermal notches are integral to the calving process because they can undercut the terminus at the waterline, which increases the force imbalance in these localities and thus promotes calving failure (Benn et al., 2007b; Minowa et al., 2017; Mallalieu et al., 2020). As mentioned previously (Section 5.3.) a relatively large calving event ($1,579 \text{ m}^2$) occurred in the lower portion of the study area at some point between the 5th and 6th July 2019 (Figure 56). Yet although the bedrock channel is between 60-90 m deep in this region, the fact that the velocity increase that occurred in response to this event was only limited (initially) to the area immediately surrounding the calving front suggests other processes may have caused this event to occur. Importantly, thermal erosion notches were observed at the waterline of Fjallsjökull on the 4th July, near to and within the area in which the eventual calving event occurred, suggesting they may have been the primary driver behind the event.

Thermal erosion notches were also likely responsible for the two large calving events ($2,948$ and $4,629 \text{ m}^2$) that occurred in this same region of Fjallsjökull between the 4th and 7th July 2021 (Figure 62). Indeed, extensive thermal notches were observed at the waterline on the 4th, in the same region where the first calving event later occurred at some point between the 4th and 6th (Figure 80a), which strongly suggests these notches may have been the primary driver. Yet even after this event, there were still several notches visible at the waterline on the 6th (Figure 80b), which were located in the same region where the second (larger) calving event occurred between the 6th and 7th.

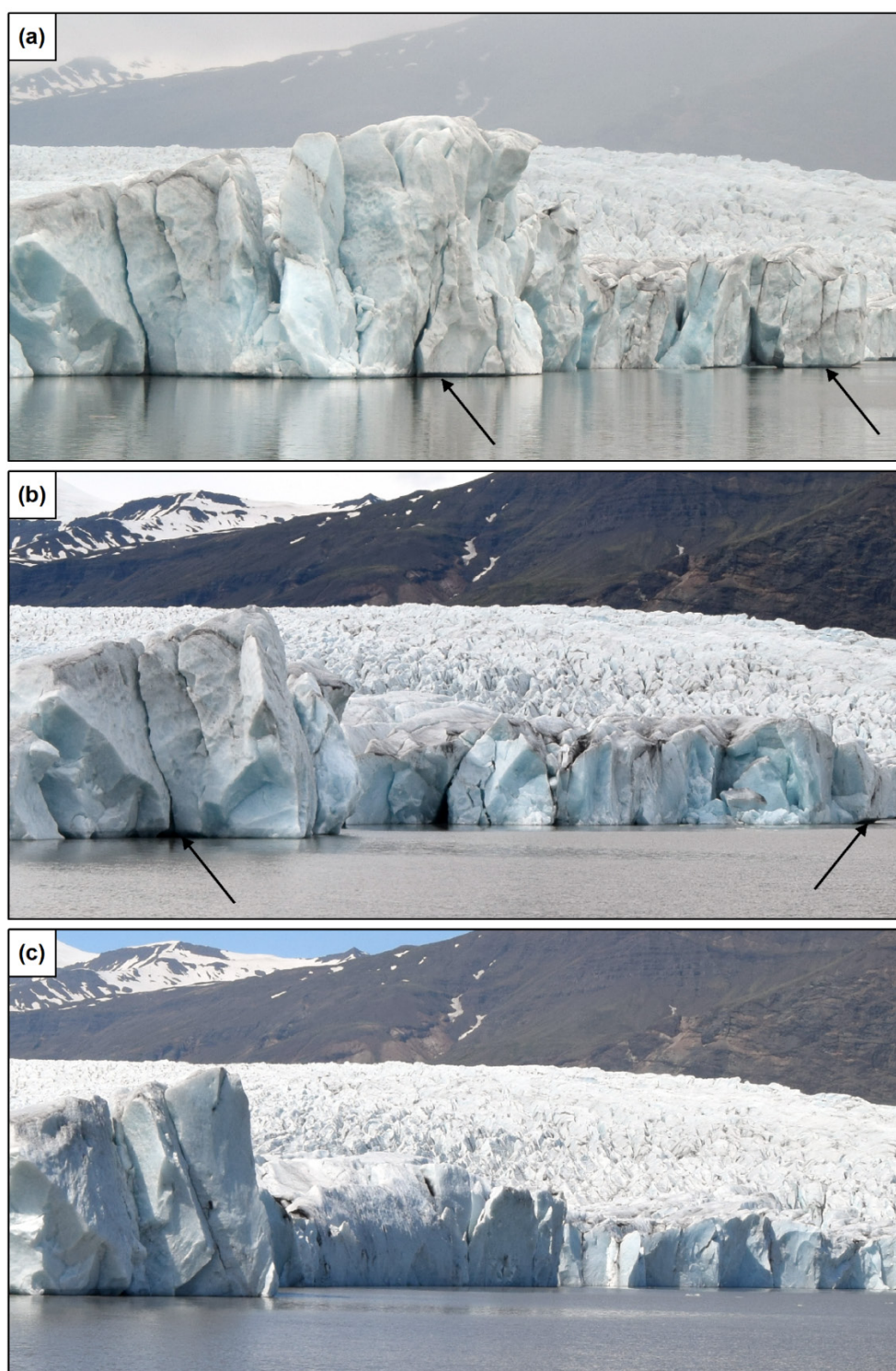


FIGURE 80 Photographs of the southern margin of Fjallsjökull acquired on the (a) 4th (b) 6th and (c) 7th July 2021. (a) Highlights the presence of extensive thermal notches at the waterline (black arrows), and was obtained before either of the large calving events occurred (see text). (b) Was acquired after the first of the two large calving events occurred, and although thermal notches are again present (black arrows), these are much less extensive than those observed on the 4th. (c) This image was obtained after the two large calving events had occurred, and illustrates how no thermal notches are now present in this region as a result of these events. For reference the calving front here is ~20 m high.

In this instance, a combination of thermal notches, as well as the local stress imbalance resulting from the sudden loss of a large volume of ice, were most likely responsible for the occurrence of this second event. It was only by the 7th (i.e. after these two large events occurred), that there were no longer any thermal notches visible at the waterline in this region of Fjallsjökull (Figure 80c), which suggests that these notches were only present in the region where calving occurred.

Furthermore, the longer duration of the July 2021 study period (~11 days) has also allowed the formation and growth of new thermal notches to be directly observed, with this occurring in the days that followed the second large calving event. For example, while no notches were present in this region on the 7th, less than 24 hours later, by the 8th, relatively small notches could already be observed at the waterline (Figure 81a), with these continuing to grow and develop over the following two (Figure 81b) and four (Figure 81c) days. As a result, by the 12th these notches were as extensive (both in size and in area covered) as those first observed on the 4th, before the large calving events had occurred. These observations are important, not only because they confirm that notch erosion is actively occurring, but also because they indicate that the *rate* of notch erosion must be significant to allow these features to form and grow at the waterline in such a relatively short period of time.

As mentioned previously, no direct measurements of notch erosion could be made in this research, however, the fact these notches formed and evolved so rapidly means it is not inconceivable that rates of 0.5-1.0 m d⁻¹ could have been occurring in this region of Fjallsjökull during this time. Such rates could only have occurred, however, if the water level of Fjallsárlón remained relatively consistent, as this would have allowed the heat energy from the lake surface to be more efficiently concentrated in a narrower band of ice (e.g. Röhl, 2006; Benn et al., 2007b). Unfortunately, no physical measurements of lake level could be obtained in this research either, but direct observations made in the field (documented via photographs), suggest that the level of the lake fluctuated very little during this time, which would have allowed such rates of notch erosion to occur. To our knowledge, this is the first research that has directly observed the formation and growth of new thermal notches at the waterline of a lake-terminating glacier. As a result, these observations are significant as they further emphasise the importance of thermal notches as drivers of localised calving failure at Fjallsjökull.

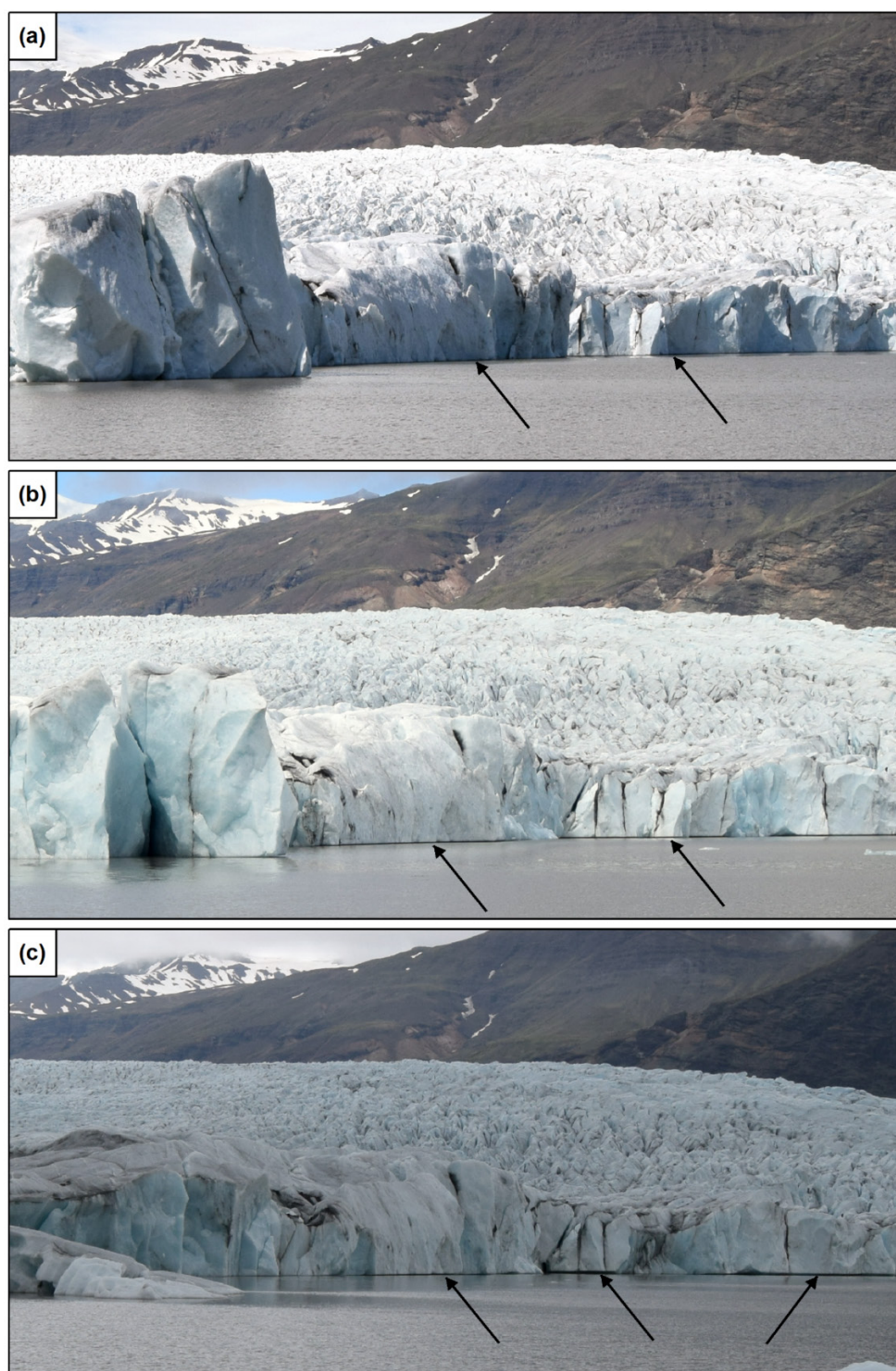


FIGURE 81 Photographs of the southern margin of Fjallsjökull acquired on the (a) 8th (b) 10th and (c) 12th July 2021, illustrating the formation and growth of thermal notches at the waterline (black arrows) which occurred in the days after the 7th (when no such features were observed). Note how by the 12th these new thermal notches are as extensive as those which were observed on the 4th (Figure 80), indicating that the rate of notch erosion must have been fairly significant during this time. For reference the calving front here is ~20 m high.

It was illustrated by Benn et al. (2017) through discrete element modelling that thermal notch undercutting is associated with two types of calving failure: (i) low-magnitude events that occur where loss of support by undercutting exacerbates existing faults in the ice cliff, causing localised shallow subaerial failures, and (ii) high-magnitude events which are associated with the propagation of suitably orientated surface fractures and outward bending of the ice cliff over the undercut, leading to collapse of the entire column. Through analysis of the calving front before each event occurred, and based on the size of each event overall, the type of calving failure observed in both July 2019 and 2021 was most similar to mode (ii) (Figure 82).

Before each event, a number of large, suitably orientated crevasses were observed at the ice surface in the same region where these calving events later occurred, and thus it is proposed that the undercutting of the terminus via notch development increased the force imbalances acting on the terminal face, leading to a corresponding increase in the stresses acting on the ice surface, which promoted fracture propagation until full failure occurred (Benn et al., 2007b, 2017; Chudley et al., 2021).

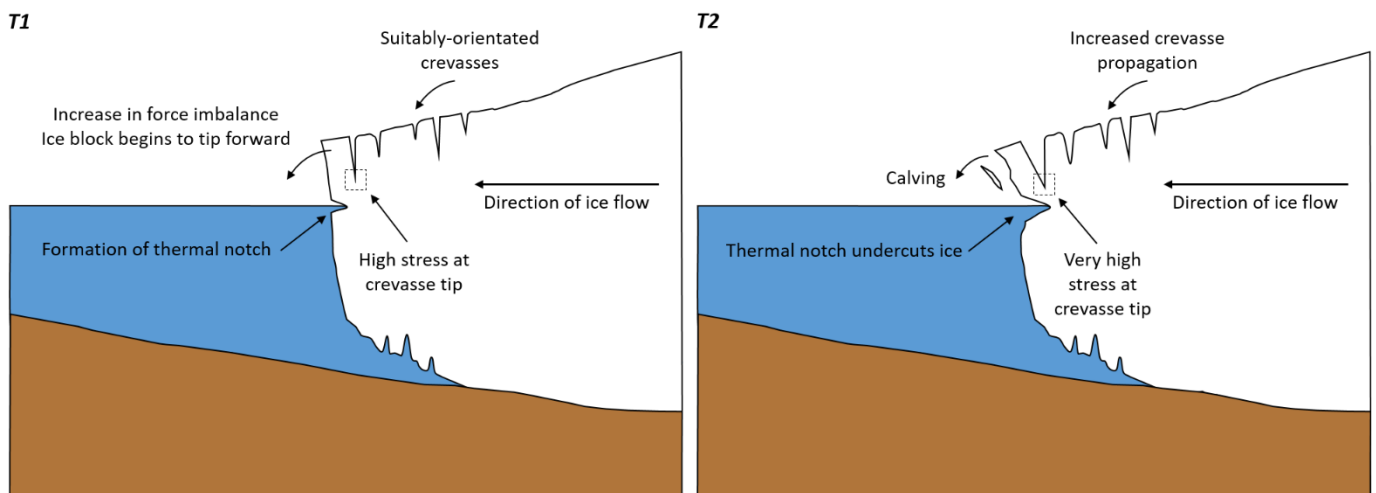


FIGURE 82 Schematic illustrating the mechanism by which calving failure at Fjallsjökull can result from thermal notch erosion at the waterline, based on the observations made in this research. This is an updated version of the schematic presented in Section 2.4.2 (Figure 12), which itself is a figure modified from Bendle (2020).

Importantly, these calving events are also likely responsible for the localised increases in velocity that were observed in this region in both July 2019 and 2021, particularly in the days that followed each individual event. It has been demonstrated that the balance of glacier stresses which control the flow of calving glaciers are highly sensitive to any change in the position of, or indeed the thickness of the calving front (Thomas, 2004; Nick et al., 2009). As outlined above, thinning reduces the effective pressure at the bed, leading to a reduction in basal drag (and thus resistive stress) leading to faster ice flow (Carrivick and Tweed, 2013; Tsutaki et al. 2013).

However, any sudden changes in the position of the calving front, whether glacier-wide, or localised (like observed here), will also cause a reduction in the resistive stresses due to the sudden loss of a significant volume of ice (Joughin et al., 2008a). In response, the glacier speeds up and draws-down ice from higher elevations to provide the additional longitudinal and lateral stress gradients (resistive stresses) that are necessary to restore the stress balance (Howat et al., 2005; Joughin et al., 2008a). As a result, brief periods of calving activity and retreat, lasting days or less, can result in an acceleration of ice flow that is sustained over much longer periods of time as the glacier evolves following the perturbation at the front (Joughin et al., 2008c; Howat et al., 2010). Such a response is clearly visible in the velocity results presented in this research; with the following sequence of events likely having occurred in early July 2021 (a similar sequence of events also occurred in this region in July 2019, but over a slightly shorter timescale):

- (i) The first calving event occurred between the 4th and 6th July, leading to locally high velocities ($\sim 0.7 \text{ m d}^{-1}$) in the region immediately behind the new position of the calving front, but with little change in velocity observed elsewhere.
- (ii) The second large calving event occurred over the following 24 hours, causing this region of locally high velocities to not only increase in size, but to also increase in magnitude (to $\sim 0.8 \text{ m d}^{-1}$). Consequently, it now extended some $\sim 300 \text{ m}$ back from the calving front (encompassing much of the lower study region as a result), as well as northwards, joining with the large region of high velocities in the upper portion of the study area. Such a change likely reflects the speed-up and drawdown of ice from further up-glacier in an attempt to restore the stress balance, following the sudden loss of a large volume of ice.
- (iii) Over the following 48-hour period (7th-9th), although there was very little change in the overall size of this region, a further increase in velocity was observed during this time (to $\sim 0.95 \text{ m d}^{-1}$), indicating how ice acceleration following calving failure can be sustained for several days after the event has taken place.
- (iv) It was only by the 11th that velocities in this region returned to their pre-speed-up level, around six days after the event started. Such short-term increases in velocity, occurring over relatively large areas of the glacier in response to what were two large, but fundamentally, localised, calving events, highlights the importance of subaqueous melt as a key control on both calving losses and localised ice dynamics (e.g. Röhl 2006; Minowa et al., 2017; Mallalieu et al., 2020).

At Fjallsjökull, therefore, although the basal topography exerts a first order control on the *overall* dynamics of the glacier, it is highly likely that processes of subaqueous melt, (and related force imbalances) are equally important for forcing *localised* changes in glacier dynamics (for example in regions of the glacier where the bedrock channel is shallower) and as such these processes are

'superimposed' on the first order mechanism, providing a means with which to explain almost every aspect of the dynamic behaviour of the glacier.

6.1.3 Supraglacial Lake Drainage and Short-Term Velocity Variations

Recent research on land-terminating glaciers in Arctic Canada and the Greenland Ice Sheet has highlighted how short-term increases in velocity can result from the sudden and rapid drainage of supraglacial lakes to the base of these glaciers (e.g. Das et al., 2008; Hoffman et al., 2011; Clason et al., 2012; Arnold et al., 2014). The sudden increase in meltwater to the bed following drainage is often sufficient to overwhelm the capacity of the subglacial drainage system, increasing basal water pressures and thus facilitating rapid sliding over short (daily) timescales (Das et al., 2008; Clason et al., 2012). However, only a very small number of studies to date have observed, let alone assessed the impact of supraglacial lake drainage on short-term calving glacier fluctuations (e.g. Danielson and Sharp, 2013; Everett et al., 2016; How et al., 2017).

Supraglacial lakes can form by one of two mechanisms on the surface of calving glaciers: (i) 'Perched' lakes form in topographic depressions following surface melt and are isolated from the influence of subglacial hydrology (Danielson and Sharp, 2013; How et al., 2017). As a result, they tend to drain via the process of hydrofracture, which rapidly connects the lake to the bed (e.g. van der Veen 2007). (ii) The second type are termed 'Subglacially-connected' lakes, and effectively form 'from below' due to the high hydraulic head within calving glaciers, which essentially squeezes subglacial water to the ice surface (Sugiyama et al., 2011; How et al., 2017). As a result, this water often contains subglacial sediment and is much more turbid, sharing characteristics with the proglacial water body, making them easily distinguishable (Andersen et al., 2011; Everett et al., 2016). In the case of this study, all the observed lakes in both July and September 2019, as well as July 2021, were clear blue in colour and showed no signs of turbidity, and as such it can be ascertained that these lakes were formed by mechanism one.

As outlined in Section 5.4.1.1. ~122 supraglacial lakes were observed over the study area on the 5th July, yet ~22 hours later nearly a third of these had drained (28%), leading to a ~59% decrease in total lake area and thus representing the greatest observed change in lake number and area over this period. From the data available, two possible mechanisms can likely explain why such a large number of lakes drained between the 5th and 6th July. The first mechanism involves the drainage of lakes as they become connected to the subglacial system, which occurs through the ability of surface water to take advantage of existing planes of structural weakness, such as surface fractures (Hanson and Hooke, 2000; Benn et al., 2007a; Nick et al., 2010). This increases the downward pressure acting on the fracture (due to the weight of water) permitting downward

propagation through the ice until a connection with the subglacial system is established (Das et al., 2008; Arnold et al., 2014). Once established, any additional meltwater generated over the coming days can be quickly routed into these now hydrologically connected moulins and crevasses, removing it from the surface and thus keeping the connection open (Das et al., 2008; Clason et al., 2012).

Evidence for this mechanism occurring may be provided by air temperature data obtained by the Icelandic Met Office from their nearby weather station at Kvísker (63°58'N, 16°26'W, ~30 m a.s.l.), located ~5 km from Fjallsjökull to the south. Average air temperatures on the 5th July were ~11.5°C, yet on the 6th July the average temperature was ~13.9°C, and as result more melt (and thus supraglacial lake formation) would be expected on the 6th July, yet this was not observed (Figure 83a). It may be that the additional meltwater produced on these warmer days was automatically routed into the topographic depressions held by the former lakes, but because a surface-to-bed connection already existed in these depressions, the water was routed to the bed and thus no new lakes formed, providing support for the above theory. However, it seems odd that so many lakes would drain via this mechanism in such a relatively short space of time, especially when the only controlling factor is the rate at which the water can propagate downwards to the bed, which crevasse theory suggests would vary for each lake (e.g. van der Veen, 2007).

Conversely, the second mechanism involves a geometric change occurring at the calving front, such as uplift or calving failure. This may allow several fractures to suddenly open at once, connecting large areas of the surface to the bed simultaneously and thus allowing rapid and widespread lake drainage to occur. However, because the basal water pressure near the termini of calving glaciers is equal to ice overburden, bed separation is likely already occurring, and as such, it is difficult to fully assess the role any additional surface uplift would have on lake drainage.

On the other hand, a large calving event, such as the one that occurred in the lower portion of the study area between the 5th and 6th July, may have been able to produce sufficient extensional forces at the surface to open several fractures at once, permitting widespread lake drainage to occur (Figure 83b) (e.g. Benn et al., 2007b). Closer inspection of the distribution of the lakes that drained during this period shows that of the 122 lakes on the surface on the 5th July, 34% were lost in the lower portion of the study area while 24% were lost in the upper portion. The differences are greater for the overall change in lake area, with a decrease of 79% and 47% found for the lower and upper portions respectively. Therefore, it seems plausible that the widespread drainage of lakes between the 5th and 6th July ensued primarily in response to the calving event

that occurred in the lower portion of the study area during this time (i.e. when overall calving volume was also at its highest). However, further research is required in order to confirm the control that glacier calving may have on widespread supraglacial lake drainage.

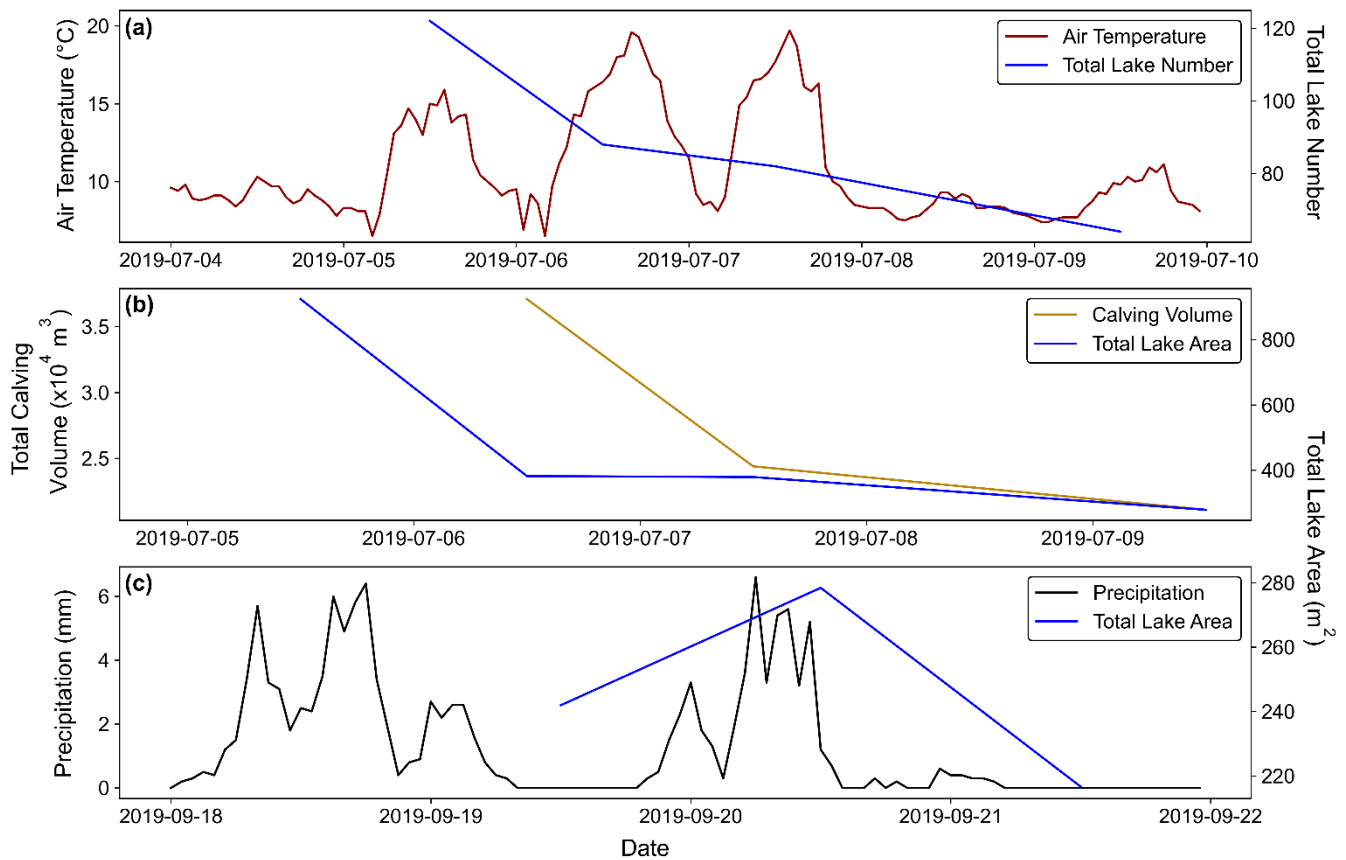


FIGURE 83 (a) Hourly air temperature data from the meteorological station at Kvísker plotted alongside the overall change in lake number between the 5th and 9th July 2019. Note how although air temperatures remain relatively high over the study period, lake number shows a continuous decrease, particularly between the 5th and 6th. (b) Same as (a) but with total estimated calving volume for the research period (with logarithmic scale). Note how the rapid decrease in lake area between the 5th and 6th corresponds to when the estimated volume losses from calving were at their highest. (c) Hourly precipitation data from the meteorological station at Kvísker plotted alongside the overall change in lake area between the 19th and 21st September 2019. Note how the increase in lake area between the 19th and 20th directly corresponds to the large rainfall event that occurred in the 19-hour period between when the two sets of UAV surveys were taken.

In comparison to the clear decrease in surface lakes that was observed in July 2019, between the 19th and 20th September overall lake number and area actually increased by 4% and 15%, respectively. This increase is perhaps not wholly unexpected following analysis of meteorological data from the nearby weather station at Kvísker, which suggests that at least ~48 mm of rain fell over the glacier in a 19-hour period between when the UAV surveys were undertaken (Figure

83c). Many of the lakes observed during this period seemed to be relatively small, shallow features, which would likely disappear from the ice surface after a short period of time, rather than the generally larger, deeper lakes observed in July. The input of a large amount of water to the ice surface in a relatively short period of time (~19 hours), therefore, may have had the effect of both refilling or 'topping up' the shallow lakes already present (by increasing the area), and by creating new, shallow lakes in depressions on the ice surface. The observed overall increase in lake number and area, and the fact that one of the new lakes that formed in this period was also the largest lake observed on the ice surface in this time may support this viewpoint (Section 5.4.1.1).

However, over the following 24-hour period total lake number and area decreased fairly substantially (8% and 22%, respectively) in a similar pattern to that observed in July, but in contrast no large calving event occurred between the 20th and 21st September which can offer an explanation for relatively rapid lake drainage over a short time period. Instead it is possible that because these surveys were undertaken toward the end of the melt season, it meant that a large number of the crevasses and moulins present on the ice surface, particularly those in depressions where lakes would preferentially form, were already hydrologically connected to the basal environment (Das et al., 2008; Hoffman et al., 2011). However, the reason the large amount of rainfall that fell between the 19th and 20th September was not immediately routed from the surface to the bed through these connections may be due to the hydraulic head that exists near the terminus of calving glaciers which can cause water to back-up the basal hydrological system (Sugiyama et al., 2011; Carrivick and Tweed, 2013).

As a result, whenever there was any significant addition of water to the ice surface over a short period of time (e.g. high melt days or heavy rain), it is unlikely this water could be readily incorporated into the basal environment (Carrivick and Tweed, 2013; How et al., 2017; Chudley et al., 2021), which would lead to the formation of short-lived, shallow lakes as observed here. It is only once the water input to the surface was reduced that these newly formed lakes could begin to drain. Indeed, only 2.7 mm of rain fell between the 20th and 21st September (Figure 83c), and so in the absence of any significant additional increase in water input to the ice surface in this period, it seems plausible that these shallow, pooled lakes could now begin to drain to the bed via the hydrologically-connected moulins and crevasses, leading to the fairly rapid reduction in lake number and area observed in this time. This may also explain why the lakes that formed between the 19th and 20th did so in the depressions held by recently-drained lakes, suggesting that a continual cycle of lake formation and drainage may be occurring on the ice surface in response to high melt or heavy rainfall events.

A further important observation from the September field data is that there is a small, yet clear increase in the areal extent of the region of fastest ice velocities in the 24 hours following the period of heavy rainfall (Figure 50). Although a small calving event (111.98 m^2) did occur here in the 24-hour period before the region sped up, this event was much smaller in comparison to the large calving event that occurred in July 2019 and thus is unlikely to be the sole factor forcing this observed areal increase in velocity. Instead, it is possible that this was a supraglacial lake-drainage-induced localised speed-up event, forced initially by the period of heavy rainfall (e.g. Vincent and Moreau, 2016; How et al., 2017). This would have the same impact on ice velocity that the drainage of a large supraglacial lake would (e.g. Das et al., 2008) because the effective pressure of a calving glacier is highly sensitive to transient changes in water input to the basal system (Sugiyama et al., 2011; Tsutaki et al., 2011). Therefore, a large increase in the amount of water falling on the ice surface over a short period of time, and which is then subsequently routed to the bed, would further raise basal water pressures, leading to an additional reduction in the effective pressure, basal drag and facilitating the localised, short-term increase in velocity observed here (Benn et al., 2007b; Sugiyama et al., 2011; Tsutaki et al., 2013). Although this study period only covered three days, it is likely that this increase would have only lasted a day or two at most before velocities subsided to pre-speed-up levels, akin to the patterns observed in previous studies (e.g. Hoffman et al., 2011; Danielson and Sharp, 2013).

It is also possible that the heavy rainfall event that occurred between the 19th and 20th September might have sufficiently raised the water level of Fjallsárlón so that it could also have attributed to the velocity increase mentioned above. Calving glaciers are highly sensitive to any change in water depth relative to the thickness of the glacier, so any change in either or both of these variables can cause significant increases in velocity to occur (Sugiyama et al., 2011; Tsutaki et al., 2013). At Fjallsjökull, the retreat of the glacier into deeper water (as it retreats into the bedrock channel) is responsible for the overall velocity variations observed in this research. However, short-term increases in the water level of the lake could also arise from heavy rainfall events, which itself can force short-term variations in velocity or calving behaviour (e.g. Kirkbride and Warren, 1997; Boyce et al., 2007; Dykes et al., 2011). Indeed, since the 19th September the water level of Fjallsárlón had noticeably increased over the study period, following direct observations via photographs made at the field site on the 23rd (Figure 84). However, because the lake level was not quantitatively measured, it is difficult to ascertain exactly how significant it may have been in forcing the observed short-term increase in velocity.

In comparison to the mass drainage of supraglacial lakes that was observed between 5th and 6th July 2019 (which occurred in response to a large calving event), in July 2021 no such mass drainage of lakes was observed, despite a (considerably) larger calving event occurring in the

same region between the 6th and 7th (a large calving event also occurred between the 4th and 6th, however, because full coverage of the study region could not be obtained on the 4th, it means no assessment of lake change could be made for this time period). Indeed, while lake number does decrease over the course of the study period (by ~13%), the day-to-day variations are much smaller (<3% decrease), with lake number only decreasing by 2% between the 6th and 7th. This contrasts considerably with the 28% decrease in lake number observed between the 5th and 6th July 2019.

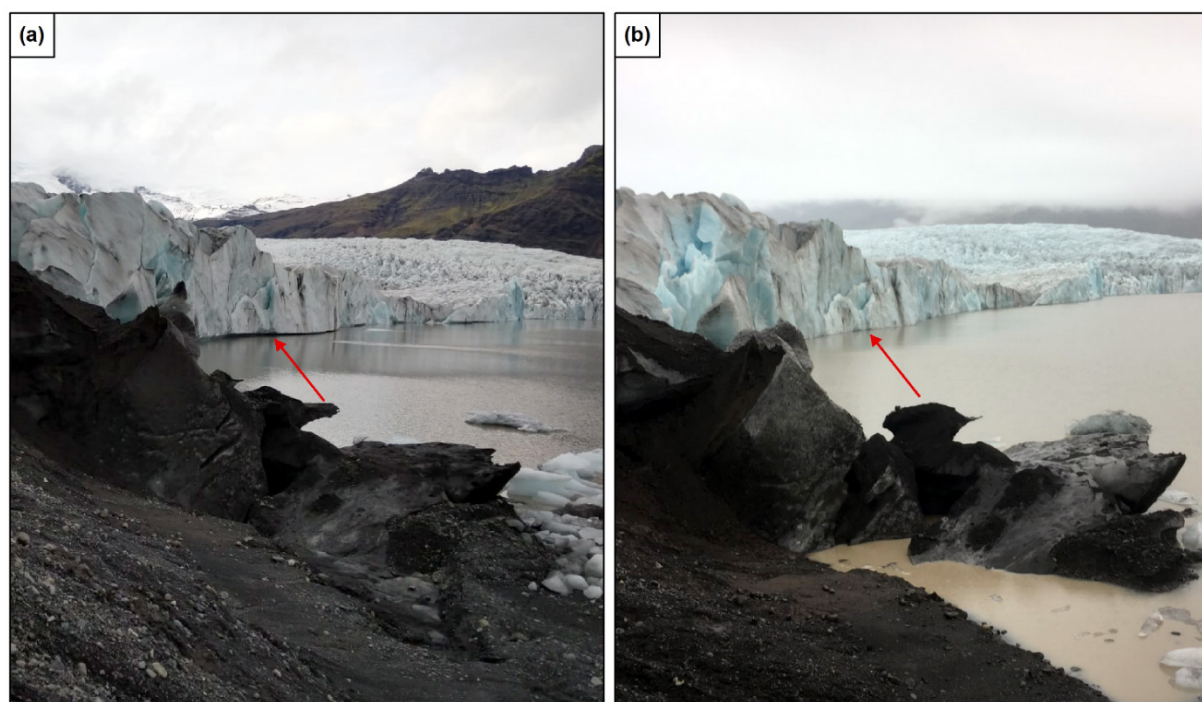


FIGURE 84 (a) The southern margin of Fjallsjökull on the 19th September, showing the presence of thermal erosion notches, which sit above the level of the lake at the time the photo was taken (red arrow). (b) Same as (a) but from the 23rd September. Evidence for a rise in lake level is given by the inundation of lake water onto the moraine material in the foreground of the image, as well as by the disappearance of the thermal erosion notches, which have been covered by the rising lake water (red arrow).

A possible explanation for this difference may be because the majority of lakes observed in 2021 were already hydrologically connected to the basal environment (i.e. this hydrologic connection occurred earlier in the melt season than it did in July 2019) (Das et al., 2008; How et al., 2017). However, the reason these lakes had not drained previously may have been due to the high hydraulic head that exists in the near-terminus region of calving glaciers, which forces meltwater to be backed up the subglacial system and up towards the surface (Benn et al., 2007b; Sugiyama et al., 2011). As a result, these lakes would only have been able to drain slowly over the course of the study period, with the rate of drainage wholly dependent on conditions at the bed. This would

have also made these lakes far less sensitive to any geometric change occurring at the calving front, perhaps further explaining why lake number only decreased by ~2% between the 6th and 7th, even though a large calving event occurred during this period. Additional support for this may be provided by meteorological data from the weather station at Kvísker, which shows that air temperatures during this period were, on average, ~1°C higher than they were in July 2019 (Figure 85a). Warmer temperatures would result in increased surface melt production, with this additional meltwater routed automatically into these lakes, keeping them relatively stable, or even causing them to increase in size. For example, it is likely that a period of particularly high air temperatures between the 8th and 9th July (max 17-20°C) were responsible for the ~6% increase in lake area that was observed between the 9th and 11th (Figure 85b).

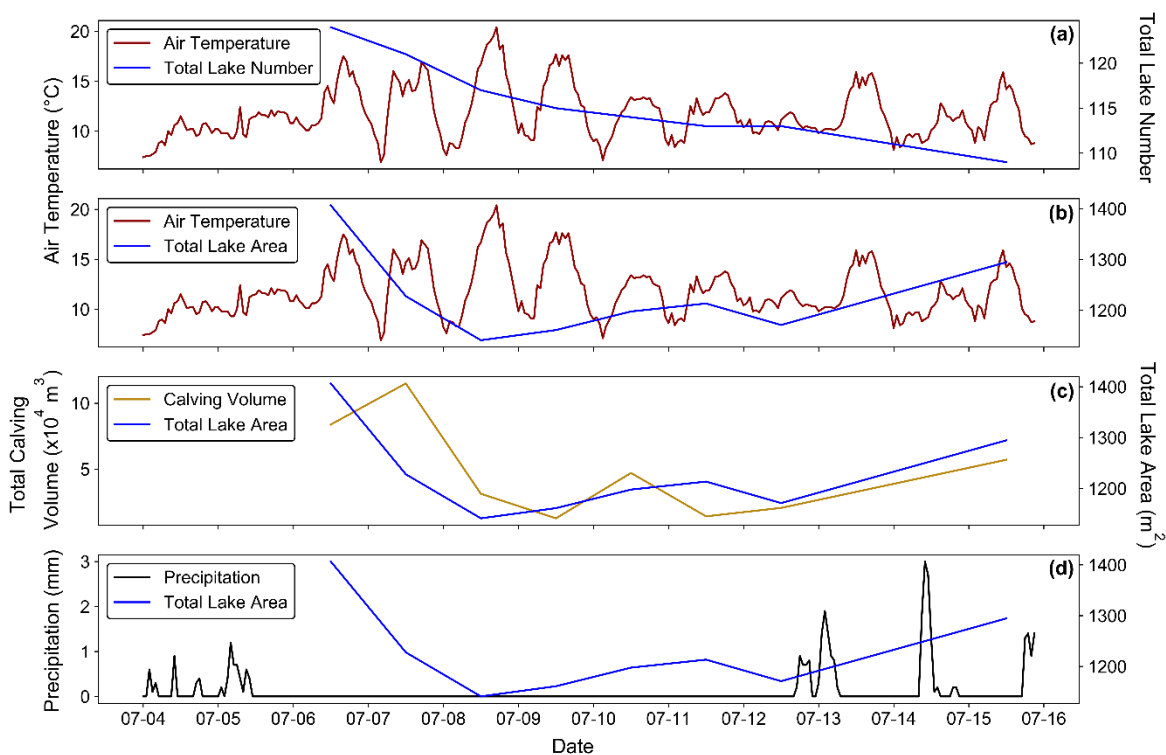


FIGURE 85 (a) Hourly air temperature data from the meteorological station at Kvísker plotted alongside the overall change in lake number between the 6th and 15th July 2021. Note how lake number displays a relatively stable and continuous decrease during this period. (b) Same as (a) but with total lake area. Note the increase in lake area that occurred between the 9th and 11th following a period of high air temperatures between the 8th and 9th. (c) Same as (b) but with total estimated calving volume for the research period (with logarithmic scale). Note how the rapid decrease in lake area between the 6th and 7th corresponds to when the estimated volume losses from calving were at their highest. (d) Same as (b) but with hourly precipitation data from the meteorological station at Kvísker. Note how the clear increase in lake area between the 12th and 15th closely corresponds to the rainfall events that occurred during this period.

Yet, while lake number seemed relatively insensitive to these geometric changes, lake *area* seemed significantly more sensitive, particularly between the 6th and 8th July. Indeed, lake area decreased by ~13% between the 6th and 7th, coinciding with the occurrence of the large calving event (and thus total calving volume), while it decreased by a further 7% over the following 24 hours (Figure 85c). Based on the data available, it is not clear why lake area decreased so rapidly in this time, yet lake number changed very little. It may be possible that this calving event (4,629 m²) was large enough to produce sufficient extensional forces over the majority of the study region, which may have permitted some of these lakes to drain more rapidly over a very short period of time. It was only over the following 24 hours when the effect of this event had subsided that lake area could again begin to stabilise, as was observed on the 8th. It is also possible that the ~45% increase in total calving volume that was observed between the 11th and 12th may have also been sufficient to cause the 3% decrease in lake area that occurred over the same period, which may add further support for the importance of such calving events on daily variations in lake area.

However, it seems unlikely that this change in extensional forces would have only caused the complete drainage of three lakes to occur, especially when it was focused over a large portion of the study region. Similarly, if calving activity were indeed the forcing mechanism, then it would be expected that daily variations in lake area would closely mirror those variations in calving volume, yet this is not the case, and thus it is unclear whether such variations were forced by this mechanism. Furthermore, while the increased air temperatures during this time may explain why there was little observed change in lake *number* over the study period (and also why lake *area* increased slightly between the 9th and 11th), it does not provide any additional explanation as to why lake area decreased by ~20% between the 6th and 8th. Additional work is required, therefore, to better understand the factors controlling supraglacial lake drainage on lake-terminating glaciers such as Fjallsjökull.

In contrast to the above uncertainties (and indeed to the short-term growth of lakes that occurred in response to warmer temperatures), the observed *increase* in lake area that occurred between the 12th and 15th can most likely be attributed to the significant amount of precipitation that fell during this period. Indeed, data from the meteorological station at Kvísker suggests ~19.7 mm of rain fell between the 12th and 14th July (Figure 85d), and although this was considerably less than the ~48 mm that fell over the study period in September 2019, it may have still had the effect of refilling, or 'topping up' many of the lakes on the ice surface during this time. This resulted in an overall increase in lake area of ~11% (Figure 71), and thus reiterates the importance of rainfall events for the evolution and longevity of lakes on the surface of the glacier. However, in contrast to September 2019, it is not clear whether this rainfall event was sufficient to cause any localised increase in velocity during this time. Indeed, while a small increase in velocity was observed in the

lower portion of the study area between the 12th and 15th, this increase is located close to where several relatively large calving events ($>500 \text{ m}^2$) were also observed to have occurred in the same period. As such, and based off data presented previously (e.g. Section 6.1.2), although it is not inconceivable that the rainfall event may have contributed to this increase, it is more likely that these calving events were more important in forcing this particular localised increase in velocity.

In light of the above discussion, it is important to highlight that this is the first research to date which has observed such a large number of supraglacial lakes on the lower surface of a lake-terminating glacier across two different summer melt seasons. It is also the first research into a calving glacier where the systematic drainage of a large number of lakes over the same short period of time (~ 22 hours) has been observed, and where the cyclical refilling (and drainage) of lakes on the surface in response to heavy rain events has also been observed. Some previous studies have been able to link supraglacial lake drainage and large rainfall events to short-term increases in velocity on calving glaciers (e.g. Danielson and Sharp, 2013; How et al., 2017). Indeed, this process may have occurred at Fjallsjökull across all time periods in both 2019 and 2021, but seems particularly likely from the data acquired in September 2019 because the velocity increase directly followed a period of heavy rainfall (i.e. within 24 hours). In all periods, however, because the exact timing of lake drainage is not known, it is difficult at present to directly attribute any short-term, localised velocity increase solely to lake drainage. Instead, other factors such as calving events, regardless of their size, are likely to be equally, if not more important in forcing the short-term speed-up events observed at Fjallsjökull.

This is supported by the results of previous studies which have investigated the effect of lake drainage, and increased meltwater routing to the bed more generally, on the short-term velocity fluctuations of calving glaciers (e.g. Andersen et al., 2011; Sole et al., 2011; Danielson and Sharp, 2013; Cavanagh et al., 2017). Although these studies have clearly shown that the rapid routing of meltwater to the bed of calving glaciers can cause short-term increases in velocity, particularly over the summer melt season, these variations were small when compared to calving front changes which exerted a significantly greater control on overall ice motion (Andersen et al., 2011; Hoffman et al., 2011; Sole et al., 2011; Cavanagh et al., 2017). This has led several authors to suggest that many fast-flowing calving glaciers may be fairly insensitive to transient changes in meltwater production, or indeed the formation and drainage of supraglacial lakes (e.g. Joughin et al., 2008a; Sole et al., 2011; Danielson and Sharp, 2013; Nienow et al., 2017). Instead, it is more likely that changes in the position and geometry of the calving front are more important in forcing the behaviour and sensitivity of the majority of calving glaciers over longer timescales (Nick et al., 2009; Howat et al., 2010; Shapero et al., 2016; Nienow et al., 2017). As such, although it is currently difficult to assess the role that supraglacial lake drainage and rainfall events may have

on forcing short-term localised changes in the dynamics of Fjallsjökull, it seems plausible that they could be important, particularly at the local scale, and consequently their influence, at present, cannot be ruled out until further research is undertaken.

6.1.4 July 2019 and July 2021: A Comparison

A key component of glacier monitoring is investigating how glaciers are changing over time, i.e. across one melt season, annually, and over (and between) multiple years. This allows glaciologists to examine whether the dynamic behaviour of these glaciers is evolving, and thus can provide insights into their likely future response (at least in the short term). Indeed, in this research it was possible to obtain UAV data from two different time periods across the *same* summer melt season, but also from the same time period across two *different* summer melt seasons: July 2019 and July 2021. This not only provides the opportunity to compare and contrast the data acquired between these two years, but also to assess whether this data suggests a change in the dynamic behaviour of the glacier is underway. As such, a summary of the key data acquired in both years is given in Table 13.

TABLE 13 Summary of the key glaciological data acquired in both July 2019 and July 2021. *Note that in July 2021 the change in surface elevation was calculated over nine days (6th-15th) and not 11, due to the surveys on the 4th not obtaining full coverage of the whole study region.

	July 2019	July 2021
Time Period Covered	5 th -9 th (four days)	4 th -15 th (11 days)
Areal Coverage (km ²)	0.511	0.858
Peak Velocity (m d ⁻¹)	~1.00	~1.20
Average Velocity (m d ⁻¹)	0.54	0.72
Max Surface Elevation Change (m)	~-2.50	~-5.50*
Overall Frontal Change (m)	-2.77	-10.70
Largest Calving Event (m ²)	1,579	4,629
Largest Calving Event (m ³)	31,581	92,596

From the table, the key point to highlight is that the highest velocities (both peak and average), most negative changes in surface elevation, greatest overall change in frontal position, and the

largest calving events (both in area and volume) were all observed in July 2021. As a result, the above data seems to indicate that the glacier is flowing faster, thinning more (and over a much larger area), undergoing greater change in its frontal position and calving with greater magnitude than it was in 2019, despite preceding weather conditions being similar between both years. It is important to note, however, that this difference is not just a result of the different area covered, or the time period investigated. For example, the largest calving events that were observed in both years always occurred in the same area of the study region. Furthermore, even if the 2019 value of frontal change is multiplied (by 2.75) to match the 2021 time period, the resulting value is still some 3 m short of the 10.70 m of frontal change calculated in 2021. Similarly, if the 2019 max surface elevation change value is doubled to match the 2021 time period (and assuming the observed rate of elevation change remained relatively constant), then a value of ~5.00 is obtained, which is still slightly less than the value obtained in 2021.

This is important as it implies that the differences between years may have instead been forced by (and perhaps signify a further change in) the dynamic behaviour of the glacier. Indeed, it is possible that the continued retreat of the upper portion of the study region through the deepest parts of the bedrock channel is the primary driver behind this change. This retreat has caused a further increase in velocities, resulting in more calving (due to increased likelihood of crevasse propagation), and, therefore, further retreat. It is also responsible for the increase in extent of the region affected by the dynamic thinning mechanism, as any additional increase in velocity will lead to a subsequent increase in surface thinning. This pattern will likely continue until this region of Fjallsjökull begins to retreat out of the deepest part of the southern bedrock channel, at which point it may then be able to stabilise.

6.1.5 Dynamics of Fjallsjökull: A Summary of Forcing Mechanisms

As the foregoing discussion has illustrated, and based off the UAV data acquired in this research, several complex processes are influencing the dynamics of Fjallsjökull, with a schematic illustrating each of these shown in Figure 86 and summarised here. It is important to note that all of these processes influence the dynamics of Fjallsjökull over spatial and temporal scales that are clearly distinct from one another, which, therefore, makes it possible to categorise the relative importance of each process for the dynamics of the glacier.

6.1.5.1 First Order Processes

The retreat of Fjallsjökull down its reverse-bed slope into deeper water is having a first order control on its overall dynamics. As it retreats into progressively deeper and deeper water the

glacier speeds up due to the inverse relationship that exists between the effective pressure and basal drag (e.g. Warren and Kirkbride, 2003; Carrivick and Tweed, 2013). Retreat into deeper water also allows lake water to propagate further up-ice, causing an additional increase in basal water pressures, bed separation and velocities to occur (Harper et al., 2010; Tsutaki et al., 2011). This leads to a corresponding increase in the overall driving stress of the glacier, permitting crevasse propagation at the ice surface due to increased longitudinal stretching, which in turn allows calving to occur (Benn et al., 2007b; Mottram and Benn, 2009; Minowa et al., 2017). At Fjallsjökull, calving primarily occurs via this mechanism, or through buoyant forces acting on parts of the locally buoyant terminus as it retreats into the deepest part of the bedrock channel.

Calving then leads to increased mass loss and frontal retreat, which steepens the ice surface and allows the drawdown of mass from up-glacier, leading to a further increase in the driving stress and, therefore, glacier velocities (Storrar et al., 2017; Dell et al., 2019). This then results in an additional increase in calving, mass loss, retreat and ice velocities to occur. This is further exacerbated by the thinning of the glacier surface which has occurred in response to the increase in driving stress and velocities, leading to the implementation of a positive feedback mechanism termed 'dynamic thinning' (e.g. Tsutaki et al., 2013; Carrivick et al., 2020). This suite of processes, forced primarily by the retreat of Fjallsjökull into deeper water, has meant its behaviour has become decoupled from climate (at least partially), and as such this pattern of mass loss and retreat is expected to continue in future until it begins to retreat out of the deepest parts of its bedrock channel (Dell et al., 2019; Baurley et al., 2020). The importance of the bedrock channel in forcing the overall behaviour of the glacier is highlighted by the UAV results, which clearly show that the areas of highest velocities and most negative elevation changes directly coincide with the deepest parts of the bedrock channel. Furthermore, the data from July 2021 also seems to suggest that this dynamic behaviour may have evolved, with higher overall velocities, as well as an increase in the extent of the region characterised by the most negative surface changes, observed during this time in comparison to 2019, reiterating the importance of the bedrock topography in forcing the overall dynamics of Fjallsjökull.

6.1.5.2 *Second Order Processes*

Although the overall dynamics of Fjallsjökull are being driven by its particular bedrock topography, more localised variations in its dynamics are being forced by additional processes, such as thermal notch erosion. Extensive notches cut into the terminal face of Fjallsjökull were observed at the waterline across all time periods in both 2019 and 2021, and likely formed at a time when water levels were relatively constant so to allow the heat energy from the surface water to be concentrated in a narrower band of ice (e.g. Röhl, 2006; Schild et al., 2018). Indeed, although no

direct measurements of notch erosion could be made in this research, observations made in the field in July 2021 suggests that such features may be forming and evolving at the waterline in a relatively short space of time (i.e. within <24 hours). These notches are important because they undercut the terminus face of Fjallsjökull, leading to an increase in the force imbalance at these locations which can promote calving failure when suitably orientated crevasses are present in the region before calving occurs (Benn et al., 2017; Mallalieu et al., 2020).

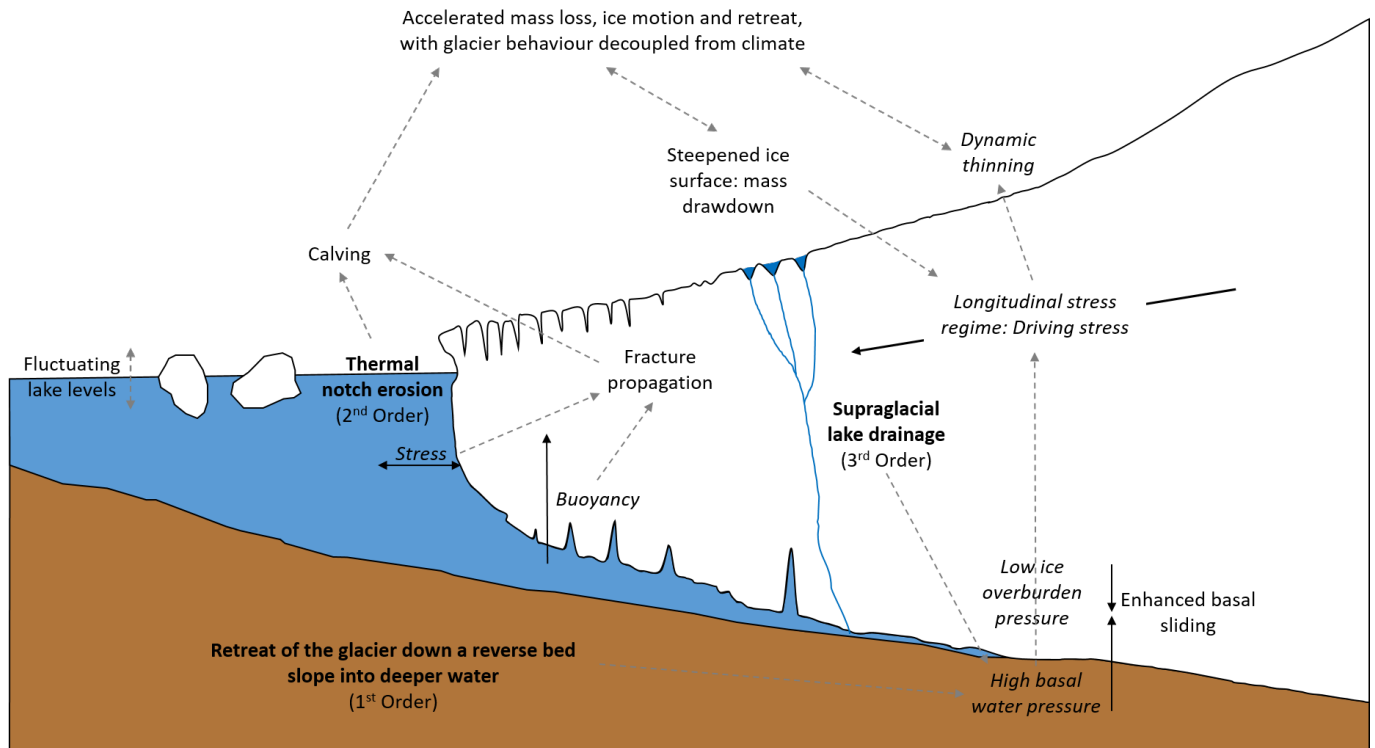


FIGURE 86 Summary schematic of the processes occurring at the margin of Fjallsjökull and the impacts these processes are having on the overall dynamics of the glacier, based on the UAV data presented in this research. The three specific forcing mechanisms are highlighted in bold and labelled as appropriate. Forces are shown in italicised text with thick black arrows while processes are shown in black text with dashed grey lines to denote interactions. This is an updated version of the schematic presented in Section 2.4.4 (Figure 17), which itself is a figure modified from Carrick and Tweed (2013).

Following the sudden loss of a large volume of ice, the glacier speeds up, initially in the area immediately surrounding where the event occurred, and then subsequently over a much wider area which is then sustained for several days following the event. Such a response reflects the speed-up and drawdown of ice from further up-glacier in an attempt to provide the additional resistive stresses that are necessary to restore the stress balance (e.g. Joughin et al., 2008a; Howat et al., 2010). A relatively large calving event, and the speed-up that followed, were observed in July 2019, although no such event occurred later that year in September. In comparison, two much larger calving events were also observed in July 2021, with the subsequent

speed-up sustained for around six days after the occurrence of the first event, after which velocities in this region returned to their pre-event magnitude. As a result, such short-term increases in velocity occurring over relatively large areas of the glacier in response to what were large, yet localised, calving events, highlights the importance of thermal notch erosion as a key control on both the calving losses from and, the localised dynamics of, Fjallsjökull. Therefore, these can be termed 'second order' processes, which are 'superimposed' on the first order mechanism, providing a means with which to explain almost every aspect of the dynamic behaviour of Fjallsjökull.

6.1.5.3 *Third Order Processes*

Short-term (<24 hour), localised variations in the dynamics of Fjallsjökull may also occur through the rapid routing of large quantities of water to the bed, sourced from either supraglacial lake drainage or heavy rainfall events. In both cases, the sudden input of a large amount of water to the basal system is sufficient to cause an additional increase in the basal water pressure at these localities, temporarily increasing the velocity of the glacier for several hours (e.g. Das et al., 2008; How et al., 2017). Widespread supraglacial lake drainage was observed between the 5th and 6th July 2019, although it is difficult to discern the impact this had on the short-term dynamics of Fjallsjökull because the drainage occurred in response to a large calving event, which as discussed previously likely had a greater impact in forcing glacier dynamics in this region. Conversely, in September 2019, an increase in velocities was observed over a small area of Fjallsjökull in the 24-hour period following a large rainfall event, and thus it is possible that this increase occurred primarily in response to this event. In comparison, although a large rainfall event also occurred between the 12th and 15th July 2021, it is not clear whether this event was sufficient to cause the localised increase in velocity that was observed during this time. Indeed, several relatively large calving events were also observed in this region during the same period, and thus it is likely these events were more important in forcing this particular localised increase in velocity. As a result, although the influence of such events on the dynamics of Fjallsjökull are less important in comparison to the first and second order processes described above, they clearly have a key role to play in forcing local-scale dynamic variations, and thus can be classed as 'third order' processes, with further research needed so that their full impact can be assessed.

6.2 Wider Relevance and Implications

6.2.1 Wider Climatological Perspective

As discussed previously (Section 2.4), one of the most important characteristics of calving glaciers is that their dynamic behaviour can be at least partially decoupled from climate (Benn et al., 2007b; Chernos et al., 2016; Watson et al., 2020). This is not to say that changes in mass balance, or that periods of high surface ablation cannot also influence their dynamics (e.g. Boyce et al., 2007; Trüssel et al., 2013), but rather it means that other factors which are independent of climate, such as water depth, can often exert a greater influence on the dynamics and retreat patterns of these glaciers (e.g. Meier and Post, 1987; Carrivick and Tweed, 2013; Baurley et al., 2020). These additional factors are important because they can cause calving glaciers to undergo considerably greater rates of retreat than would otherwise be observed if surface ablation were the sole mass loss mechanism, indicating that these glaciers can often display a highly non-linear response to an initial climatic forcing (Benn et al., 2007a; Sakakibara et al., 2013; Carrivick et al., 2020). Indeed, such a non-linear response can be seen to have occurred at Fjallsjökull over recent decades (Figure 87).

Interestingly, the retreat at both the land- and lake-terminating margins demonstrates a similar pattern from 1945 until about 1990. This is perhaps unsurprising as for much of the early to mid-20th century the proglacial lake Fjallsárlón was relatively small, and thus its ability to impact upon the overall velocity or retreat patterns of the glacier was limited (i.e. there was little calving), with this retreat instead being forced by rising air temperatures in the region during this time.

However, from 1990 onwards it becomes clear that the two different regions have been retreating at different rates. Indeed, nearly three times as much retreat has occurred at the lake-terminating margin than at the land-terminating margin since 1990 (1554 m compared to 576 m), equating to a retreat rate of -52 m a^{-1} and -19 m a^{-1} respectively, despite both regions undergoing the same climatic forcing ($+0.4^\circ\text{C}$) during this time. This clearly indicates that the retreat of the lake-terminating margin during this time has likely been primarily forced by glacier specific factors (i.e. the growth of Fjallsárlón, influence of bedrock topography and calving processes), rather than by solely rising air temperatures in the region.

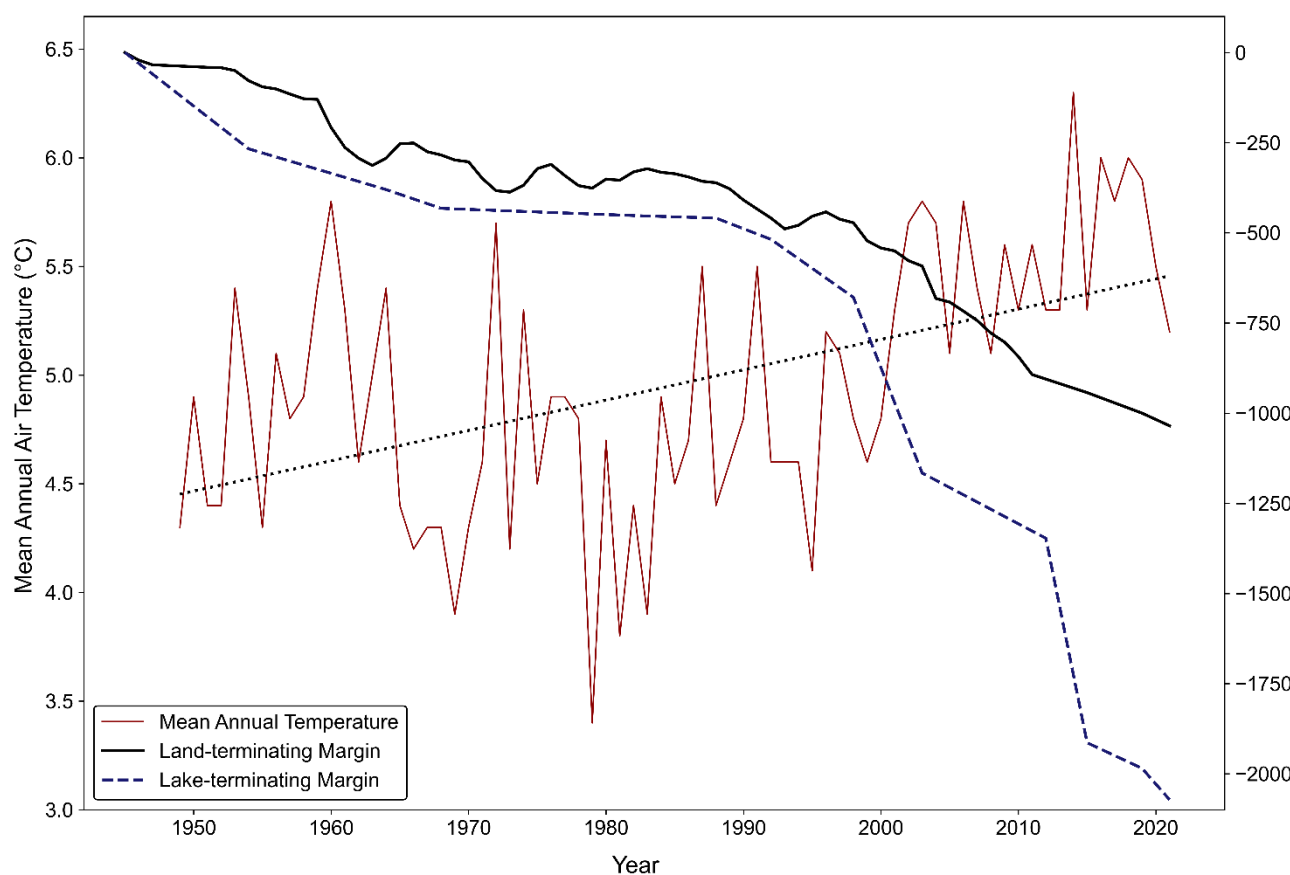


FIGURE 87 Mean annual air temperatures from the weather station at Fagurhólmýri, plotted alongside the cumulative retreat of Fjallsjökull at its land- and lake-terminating margins for the period 1945–2021. The r^2 for the temperature series is 0.49. Further detail on how the air temperature data was obtained can be found in Section 3.1.1.2. The retreat data for the land-terminating margin was taken from measurements acquired by the IGS and WGMS (first shown in Section 3.1.1.1, Figure 36), while the data for the lake-terminating margin was calculated using the rectilinear box method, which was applied to selected orthorectified aerial photographs and satellite images from 1945 onwards.

Over the last few decades, as Fjallsjökull has continued to retreat in response to rising air temperatures, it has receded into the $\sim 3 \times 4$ km, ~ 206 m deep bedrock trough it calved during its LIA advance (Magnússon et al., 2012; Dell et al., 2019). As a result, the area, and importantly, the depth, of Fjallsárlón has also increased in response, causing the glacier to flow faster as it enters deeper water due to the inverse relationship that exists between effective pressure and basal drag (Warren and Kirkbride, 2003; Benn et al., 2007b; Carrivick and Tweed, 2013). This in turn would have resulted in an increase in surface thinning (due to increased longitudinal stretching), leading to a corresponding increase in calving activity and, therefore, the rate of retreat (Nick et al., 2007a; Storrar et al., 2017; King et al., 2018). Further retreat of the glacier into the deepest parts of the bedrock trough would have caused the lake depth to increase further, resulting in an additional increase in ice velocity and leading to further thinning, calving, retreat and so on

(Tsutaki et al., 2013; Dell et al., 2019; Baurley et al., 2020). As such, the observed pattern of increased mass loss can be directly attributed to the retreat of Fjallsjökull back into, and through its deep bedrock trough.

This is important for several reasons: Firstly, the processes outlined above are the exact same as the 'first order' processes that have been observed to be occurring in this thesis, which were captured using ultra high-resolution UAV imagery. Indeed, in this research the fastest velocities, highest rates of surface thinning, and greatest changes in frontal position were all found where the bedrock topography is at its deepest (i.e. under the southern bedrock channel), with these evolving through time (i.e. increasing in magnitude) as the glacier has continued its retreat through the deepest parts of the bedrock channel. Such similarities further reiterate how UAV imagery is a powerful tool for investigating and monitoring the dynamics of calving glaciers.

Secondly, the dynamic processes occurring at Fjallsjökull may be analogous for those processes that may yet occur, or have already occurred, at other lake-terminating glaciers, in both Iceland and elsewhere. For example, the processes observed here show a very similar response to what has already been observed at Breiðamerkurjökull (e.g. Baurley et al., 2020), while they may also reflect the future response of other lake-terminating glaciers in south Iceland (discussed in more detail in Section 6.2.2).

Thirdly, and most importantly, it highlights how the growth of Fjallsárlón, and the calving processes that have been initiated as a result, have (at least partially) decoupled Fjallsjökull from the effects of the changing climate. As such, the dynamic response that is now underway is occurring beyond what would be expected through climate alone, i.e. the glacier is losing more mass and retreating more rapidly than would otherwise be observed if it were being forced solely by climate, with such a response predicted to continue until the glacier retreats out of the bedrock trough and into shallower water (Dell et al., 2019). It is worth noting that the role of climate has been, and still is, important for the glacier, both at present and in the future. For example, rates of surface thinning, even over the deepest parts of the trough, will still be influenced to an extent by rising air temperatures, while the retreat of those regions not in contact with the lake will still be forced by surface melt. In addition, once the glacier does retreat out of the trough and into shallower water, its dynamic behaviour and future pattern of retreat will once again be primarily controlled by rising air temperatures in the region (i.e. its behaviour will become coupled to the changing climate).

In general, however, the changes that the glacier has undergone over recent years are both too significant, and too rapid to have been forced solely by the observed changes in climate. This reiterates the importance of glacier calving, not only for its ability to decouple the behaviour of a

glacier from climate, but also for controlling how these glaciers will respond in future, highlighting how further research and continued monitoring of these glaciers is required in order to better predict and understand their future response (Boyce et al., 2007; Sakakibara et al., 2013; Dell et al., 2019; Carrivick et al., 2020).

6.2.2 Basal Topography and its Influence on Ice Dynamics

As mentioned previously, a similar pattern of heightened dynamic glacier response following retreat into overdeepened basal troughs has also been observed in Iceland for the neighbouring glacier to Fjallsjökull, Breiðamerkurjökull, by several authors (e.g. Voytenko et al., 2015; Storrar et al., 2017). Most recently, Baurley et al. (2020) attributed the recent rapid increase in flow velocities and retreat rate of the glacier to the increase in size and depth of its proglacial lake Jökulsárlón as the glacier retreated into the 200-300 m deep bedrock trough it formed during the LIA. The authors found near-terminus velocities increased from $\sim 1.00 \pm 0.36 \text{ m d}^{-1}$ in 1991 to $3.50 \pm 0.25 \text{ m d}^{-1}$ in 2015, with velocities remaining elevated from 2008 onwards, while up to 130 m of thinning was also recorded in this terminus region between 2012 and 2017. Furthermore, nearly 3.5 km of retreat was observed between 1982 and 2018, with $\sim 2.6 \text{ km}$ of this occurring since ~ 2006 , coinciding with a 270% increase in the area of Jökulsárlón (Baurley et al., 2020). The authors suggest that while initial retreat was instigated by rising air temperatures following the LIA, once Jökulsárlón increased to a sufficient size where it was able to start influencing frontal retreat and ice flow, then this became the dominant mechanism in causing the rapid retreat, thinning and flow velocities observed since the turn of the 21st century, with such a response likely to continue until the glacier recedes out of the deepest part of the bedrock trough and into shallower water (Baurley et al., 2020).

This feedback mechanism may not just be limited to Fjallsjökull and Breiðamerkurjökull, however, as there is a strong possibility that the other southern outlets of Vatnajökull will undergo a similar pattern of retreat and mass loss in future (Schomacker, 2010; Guðmundsson et al., 2019). Indeed, many of these outlets also carved deep bedrock troughs in the underlying sediments during their LIA advance, and consequently have reverse-sloping beds that sit some 100-300 m below the current elevation of their termini (Magnússon et al., 2012; Hannesdóttir et al., 2015). Particularly deep troughs exist under the outlets Svínafellsjökull ($\sim 320 \text{ m}$) and Skaftafellsjökull (230 m) to the west of Fjallsjökull, and under Heinabergsjökull (200-300 m) to the east (Hannesdóttir et al., 2015; Guðmundsson et al., 2019). Furthermore, these outlets, like Fjallsjökull and Breiðamerkurjökull, have been retreating rapidly since the end of the LIA in response to warming air temperatures and, therefore, have also seen the development and growth of proglacial lakes at their termini during this time (Guðmundsson et al., 2017). However, particularly rapid lake growth has been

observed to have occurred since the turn of the century, with total lake area (excluding Fjallsjökull and Breiðamerkurjökull) increasing by ~593% between ~2000 and 2018, from 2.83 km² to ~19.62 km² (Guðmundsson et al., 2019). Although at present these lakes are currently situated in the outermost part of these bedrock troughs, this means they are likely to further grow as these glaciers continue to retreat rapidly in response to warming air temperatures (Hannesdóttir et al., 2015; Guðmundsson et al., 2019). This will cause these glaciers to recede down their reverse-sloping beds into deeper water, increasing velocities, calving, and likely initiating a dynamic response similar to that observed here for Fjallsjökull and by Baurley et al. (2020) for Breiðamerkurjökull, leading to a pattern of rapid retreat and mass loss that is (at least partially) decoupled from climate (Carrivick and Tweed, 2013; Guðmundsson et al., 2019).

Similar patterns of flow acceleration and rapid retreat linked to recession down reverse-sloping beds into deeper water have also been observed at, and modelled for, lake-terminating glaciers in other glaciated regions. For example, at Mendenhall Glacier, Alaska, Motyka et al. (2003) found that as the glacier thinned and retreated into deeper water, the buoyant forces acting on the terminus increased, allowing the terminus to reach floatation and begin to destabilise. Once this was underway, the terminus began to calve at an increased rate into its proglacial lake, causing the glacier to retreat further into deeper water and initiating a positive feedback mechanism (Motyka et al., 2003). Meanwhile Sakakibara et al. (2013) attributed the observed recession and acceleration at Glacier Upsala, Patagonia, to a change in the longitudinal stress exerted by the bed in response to the glacier retreating over a bedrock rise and down a reversed slope into deeper water. Prior to this retreat, the glacier was undergoing a period of relative stability, with 670 m of retreat observed from 2000 to 2008, however, after detachment from the bedrock rise in 2008, the glacier began to rapidly retreat (2890 m between 2008 and 2011), at a retreat rate (880 m a⁻¹) which was ten times larger than that observed between 2000 and 2008 (Sakakibara et al., 2013). The authors argue that this close agreement between the onset of retreat and acceleration is consistent with the hypothesis that the speed-up was triggered by the back stress reduction following the retreat from the bedrock rise into deeper water, further highlighting the importance of the water depth in controlling lake-terminating glacier dynamics (Sakakibara et al., 2013; Sakakibara and Sugiyama, 2014).

Liu et al. (2020) in their multi-decadal study of the dynamics of Longbasaba Glacier, Chinese Himalaya between 1989 and 2018 attributed the observed onset of fast velocities and rapid frontal retreat to the detachment of the glacier from its terminal moraine and recession down a reverse-bed slope into the ~100 m deep basal trough. Overall, the authors observed an increase in max velocities from ~15 to 35 m a⁻¹ and total retreat of 1.5 km since 1988 (Liu et al., 2020). The authors suggest that such high rates of frontal retreat must be balanced by drawdown of ice from

further up-glacier, leading to dynamic thinning over a large area of the glacier, which they observed to be occurring in the latter years of their study (Liu et al., 2020). Such a dynamic response, they suggest, will likely continue until the glacier terminus retreats to a steeper bed where the water is shallower leading to a reduction in calving activity and overall mass loss (Liu et al., 2020). Similar dynamic responses of lake-terminating Himalayan glaciers to changes in water depth have also been observed by King et al. (2018) for the Central Himalaya and Tsutaki et al. (2019) for the Bhutanese Himalaya.

Finally, Sutherland et al. (2020) used the BISICLES ice flow model to analyse the effects of Lake Pukaki on the dynamic response of the Pukaki Glacier, New Zealand, during its recession following the Last Glacial Maximum, finding that the terminus in contact with the lake receded four times further and eight times faster than a land-terminating glacier under the same warming. Such a rate of recession was short-lived, however, accounting for ~10% of the entire simulation (about 300 years) for the time where the terminus began retreating down a reverse-bed slope into >200 m deep water (Sutherland et al., 2020). The authors suggest that this retreat led to increased ice flow rates at the grounding line and in the driving stress, allowing calving to occur. This led to a further increase in flow, causing the terminal zone to compress, steepening the ice surface slope, and increasing the longitudinal stress, forcing the glacier to progressively thin and further accelerate until the bedrock slope became shallower, at which point the ice velocity and retreat rate could begin to stabilise (Sutherland et al., 2020).

Although there are notable differences between the processes influencing lake-terminating glaciers in these regions (both in the past and present) and those occurring at lake-terminating glaciers in Iceland, there are many clear similarities in their overall dynamics. In particular, the feedback mechanism that can be introduced once a glacier starts retreating down a reverse-bed slope into deeper water is extremely important, particularly because it can lead to very high rates of mass loss and frontal retreat above what may be predicted solely based on current observations (Carrivick and Tweed, 2013; Baurley et al., 2020). There is a need, therefore, to investigate these processes further and to monitor these glaciers more closely so that their likely future response can be more accurately predicted under a changing climate (Carrivick et al., 2020; Shugar et al., 2020).

6.2.3 UAV Imagery as a Tool for Monitoring Lake-Terminating Glacier Dynamics

The results presented in this research have further highlighted how the relative merits of UAV imagery compared to satellite remote sensing make them both highly suitable and important

tools for investigating and monitoring the changing dynamics of lake-terminating glaciers. The most important advantage of UAVs is that the system can be deployed 'on demand', which allows the researcher to undertake surveys of the area of interest at repeat intervals defined by the needs of the study (Immerzeel et al., 2014; Jouvét et al., 2019). Surveys can be undertaken at weekly, daily or even sub-daily intervals, with the only limiting factors being battery life and the weather conditions at the time of surveying (Ryan et al., 2015; Jouvét et al., 2019). Indeed, in this research UAV surveys were undertaken almost every day (where weather permitted), which allowed variations in ice velocity and wider dynamics to be investigated at a temporal resolution that would be nearly impossible to obtain using satellite remote sensing alone. For example, the localised speed-up events that occurred in early July 2019 and 2021, which followed large calving events, would have potentially been missed if the same analysis were undertaken using satellite imagery. This is because the longer temporal baseline between image acquisitions would have caused such a velocity increase to have been averaged out over the longer time period, causing its impact to be missed (Joughin et al., 2018; Bhushan et al., 2020).

In addition, the other key advantage of UAV surveys is that they are able to acquire imagery at sub-dm scale resolution, which although dependent on the camera model and survey parameters used, is significantly finer than what can currently be captured by the majority of satellite sensors (i.e. metres) (Whitehead et al., 2013; Ely et al., 2017; Chudley et al., 2019). This means that features on the ice surface can be picked out with extreme clarity when using UAV imagery, allowing the development and evolution of such features to be more accurately quantified through time (Tonkin et al., 2014; Ely et al., 2017; Benoit et al., 2019). For example, in this research, a number of supraglacial lakes and WfC were observed to be evolving and disappearing on the ice surface across all time periods in both 2019 and 2021, and such changes were only observed due to the ultra-high resolution (0.02-0.03 m) of the orthomosaics produced from the UAV surveys. In comparison, two of the most widely used and freely available optical satellite sensors, Sentinel-2 and Landsat, provide imagery at resolutions of 10 m and 15 m respectively. This means that the majority, if not all of the lakes and WfC observed in this research, and indeed their development through time, would have been missed if either of these two satellites sensors had been used instead of UAV imagery. Although higher resolution satellite sensors are becoming more commonplace, such as the 3 m resolution imagery offered by Planet, even this would have been unsuitable to pick out the majority of the supraglacial lakes and WfC observed here, having a resolution ~120 times coarser than what was captured by both UAVs (Figure 88). Furthermore, even if higher-resolution satellite sensors did become more widely available, the temporal baseline would still be far too coarse to be able to capture the daily variations in lake drainage observed in this research, meaning any subsequent short-term velocity changes resulting from

this drainage would also be missed (Whitehead et al., 2013; Chudley et al., 2019; Yang et al., 2020).

The overall velocity and related velocity patterns observed in this research would have also been impacted if it had been derived using satellite, rather than UAV, imagery. This is because areas of fast-flowing ice (such as those observed in the upper portion of the study area) are able to be picked out and tracked in the ultra-high resolution UAV imagery, but in coarser satellite imagery these areas would be smoothed over, masking the overall signal (Heid and Kääb, 2012a; Dehecq et al., 2015), as has already been illustrated when comparing the results of Dell et al. (2019) to the results presented here.

Furthermore, over the slower-moving areas of the glacier near the margin, the use of satellite imagery would likely also result in higher errors because the larger pixel size would suppress the number of trackable features between the two images (e.g. Heid and Kääb, 2012a; Bhushan et al., 2020), whereas the two UAV systems utilised here have allowed these slow-moving areas to be accurately picked out with relatively low errors. As such, the above advantages clearly emphasise the important role UAVs have in investigating the dynamics of lake-terminating glaciers, and in particular the more localised, short-term changes which cannot be captured through the use of satellite remote sensing alone (Wigmore and Mark, 2017; Chudley et al., 2019).

However, despite these clear advantages, the method does suffer from some important limitations relative to what can be provided by satellite remote sensing (Whitehead et al., 2013; Bhardwaj et al., 2016). One of the most important limitations is that the areal coverage of the surveys is fundamentally linked to the UAV model used, and in particular the flight time provided by the UAV battery (Wigmore and Mark, 2017; Jouvet et al., 2019). Although recent technical advances in UAV weight and battery power have increased the survey area of both fixed- and rotary-wing UAV systems, many of these off-the-shelf, newer systems are expensive (e.g. Ely et al., 2017; Chudley et al., 2019; Groos et al., 2019) which limits their usage in many studies. Indeed, it was originally planned that the UAV surveys undertaken in this research would cover the whole terminus region of Fjallsjökull; however, this quickly became unfeasible due to the flight time afforded by the two different sets of UAV batteries.

For example, while the 2019 surveys did cover a relatively large portion of the terminus region (~33%), this still meant that a significant portion of the remaining area was not surveyed in this way. It is possible that this missing data could have added additional support and provided further validity to the overall findings presented from this time. Indeed, the 2021 UAV surveys go some way to address this, covering a much larger area than was obtained in 2019 (0.858 km² compared to 0.511 km²). Importantly, these surveys not only support the findings from 2019, but also provide

additional insight into the different dynamic processes occurring at Fjallsjökull, and the extent over which these occur. That said, despite this increased aerial coverage, there was still a large portion of the glacier not surveyed in 2021 (~50%). It is possible that the data from this region could have also provided further insight into the dynamic behaviour of the glacier, which may have been missed in the area covered by the 2019 and 2021 surveys. Furthermore, the UAV surveys from September 2019 were also considerably impacted by inclement weather (e.g. Ely et al., 2017), with rainfall limiting the number of surveys, and survey days overall, that could be undertaken. It would have been beneficial to have undertaken surveys over the remainder of the September period (22nd-24th) to see whether the variations observed up to that point, such as the cyclical drainage and refilling of supraglacial lakes, continued for the remainder of the study period.

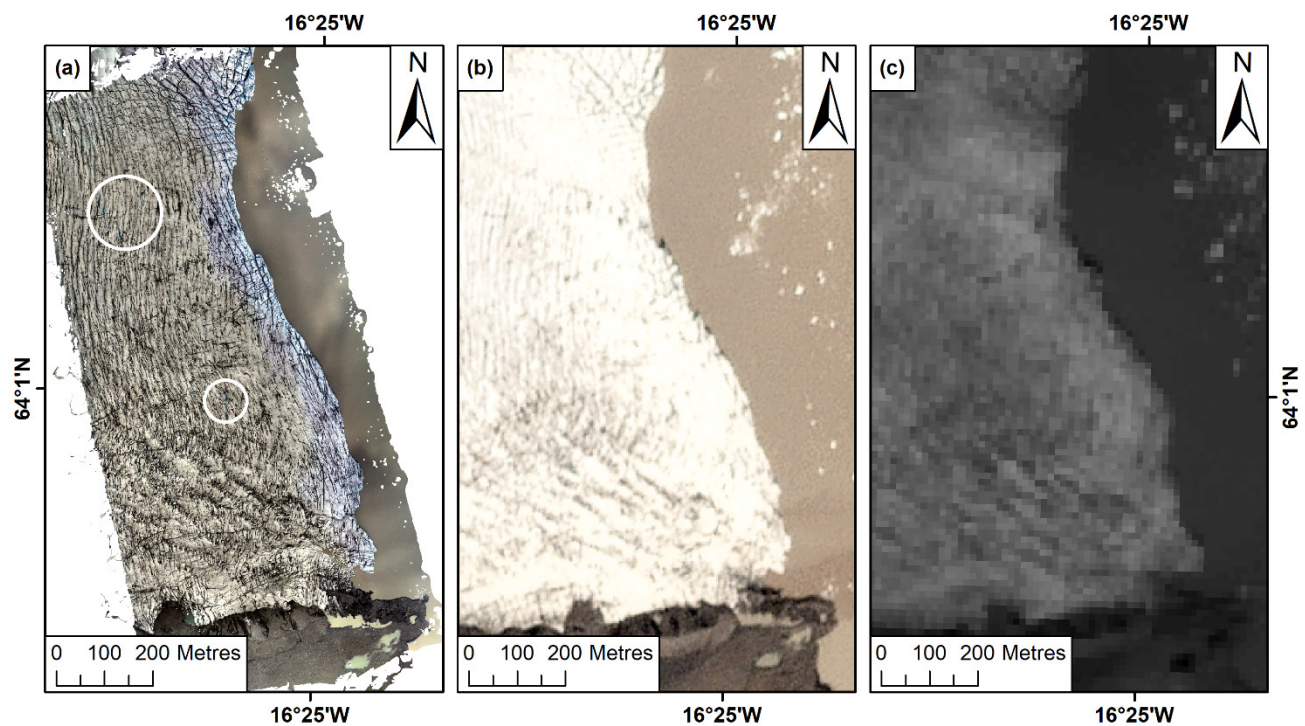


FIGURE 88 Comparison between the spatial resolution of UAV and satellite imagery. (a) Spatial resolution of one of the UAV-derived orthomosaics (0.02 m) from 6th July 2021, compared to (b) a PlanetScope image (3 m) from 3rd July 2021 and (c) a Sentinel-2 B8 acquisition (10 m) from 7th July 2021. White circles in (a) delineate several large supraglacial lakes visible on the orthomosaic even when displayed at this extent, highlighting the need for high-resolution imagery when mapping supraglacial lake evolution.

An additional key limitation is that access to the field site is required when undertaking UAV surveys, which can not only be logistically and financially expensive (Immerzeel et al., 2014; Jouvét et al., 2019), but also means that the data can only be collected during the fieldwork period. This subsequently means that it can be difficult to say with any certainty that the data

collected during this period is representative of any longer-term trends (Bhardwaj et al., 2016; Jouvét et al., 2020). For example, the 2019 data was obtained over one week in early July and one week in mid-September, reflecting two particular periods of the summer ablation season (early and late), while the data from 2021 was obtained over two weeks in July. Indeed, the results from both periods in 2019 are very similar, which suggests that the dynamic processes observed during these two periods may reflect the wider ablation season trend. Furthermore, the data from July 2021 is also very similar to the results obtained in 2019, which not only supports the fact that the processes observed in this time may reflect an overall ablation season trend, but also suggests that these findings may be representative of a longer-term (i.e. multiyear) trend as well. However, it is important to note that the data from 2019 and 2021 both only cover two weeks in total across two separate ablation seasons. This means that although the acquired data is likely representative of a longer-term trend, at present this cannot be stated with complete certainty until additional research is undertaken that covers a longer time period (i.e. several weeks).

A final key limitation of the UAV method is that GCPs are required to be located around the study area in order to scale and georeference the resulting 3D models to real-world coordinates (James and Robson, 2014; Javernick et al., 2014). It has been widely shown that the quantity and distribution of GCPs placed around a scene can have a significant impact on the accuracy of the final 3D models (e.g. Shahbazi et al., 2015; Gindraux et al., 2017; James et al., 2017). However, in glacial environments this is often highly unfeasible and impractical, which has meant that to date most applied glaciological studies have only been able to install their GCPs on the valley sides near the lateral margin of the glacier (e.g. Ryan et al., 2015; Kraaijenbrink et al., 2016), resulting in larger errors than is theoretically possible with the method. That said, although a GCP network was used to georeference the UAV imagery acquired in both July and September 2019, it did not have a significant impact upon the overall accuracy of the produced models from this time (Section 4.2.2). However, the placement of the GCPs along the lateral margin of the glacier did result in some doming within the 3D models, which is known to occur when GCPs are placed in this way (e.g. James and Robson, 2014; Tonkin et al., 2014; Sanz-Ablanedo et al., 2018).

A potential solution to this is through the recent development of lightweight and low-cost differential carrier-phase GNSS technology which can be equipped to UAV systems to provide accurate georeferencing mid-flight (i.e. direct georeferencing) (Benassi et al., 2017; Chudley et al., 2019). This technique has been shown to result in cm-scale positional accuracy without the need for a GCP network, resulting in highly accurate 3D models (van der Sluijs et al., 2018; Tomsett and Leyland, 2019). As a result, this method was used to georeference the UAV imagery acquired in July 2021, and was found to have several advantages over the 2019 imagery, which were georeferenced using GCPs. For example, the 3D models were characterised by considerably less

doming and warping because the control measurements (i.e. the camera positions) were distributed evenly across and surrounding the volume encompassing the survey area (James and Robson, 2014; James et al., 2017), rather than being focussed on the lateral margin of the glacier as is usually the case when using GCPs.

However, despite these advantages, the use of the method did result in several different additional issues. For example, the method is heavily reliant on the number and position of satellites in the sky at the time the images were acquired. A low number of visible satellites, and poor satellite constellation geometry, can often result in the rover being unable to obtain sufficient corrections from the base to accurately define the position of the UAV (Hall et al., 2010; Karaim et al., 2018). This was the case for two of the surveys, which lowered their overall positional accuracy as a result. Furthermore, technical issues with the camera hot-shoe adaptor also meant that on numerous occasions the events file (which specified the location of where each image was taken) was not correctly recorded, meaning several surveys were characterised by higher errors than was technically possible with the method.

In light of the above issues, it would have been beneficial to have used a combination of both on-board GNSS technology and ground based GCPs to georeference the UAV imagery from 2021. Several studies (e.g. Benassi et al., 2017) have shown that the error resulting from 3D models that have been directly georeferenced can be further constrained by the introduction of at least one GCP into processing, resulting in accuracies that are only slightly worse than those obtained using traditional, dense GCP networks. This is particularly important for studies in glacial environments, as although constructing a dense and well-distributed GCP network is difficult over glacial terrain, the introduction of one GCP is far more achievable (Chudley et al., 2019). Indeed, it was intended that the 2021 imagery would be georeferenced using a combination of both techniques, and a GCP network was again placed across the lateral margin of the glacier in order to achieve this.

However, as mentioned previously this was not possible because there was found to be a consistent offset between the positions of the GCPs recorded in the field, and the reproduced positions of the same GCPs in the directly georeferenced models. As this offset was not known, to include these GCPs in processing would have introduced large errors into the final models, which limited their usage. As such, it is suggested that future studies within glaciology utilise a combination of on-board GNSS technology and ground based GCPs for georeferencing purposes, due to the overall increase in accuracy that can result from their joint use. Despite this, however, in general commercial off-the-shelf UAV systems with direct georeferencing capabilities remain highly expensive (>£20,000) which currently makes them an unfeasible option for many studies,

and as a result the use of GCP networks will be a necessity in glacial UAV research for the foreseeable future (Gindraux et al., 2017; Chudley et al. 2019; Groos et al., 2019).

Yet while the overall applicability of UAV imagery is constrained by the above limitations, satellite remote sensing on the other hand, is not, which means its usage can solve nearly all of the issues faced by UAV systems. Indeed, a key advantage of satellite remote sensing is that it facilitates the monitoring of a large number of glaciers over extended periods of time without the effort and costs associated with field research (Gjermundsen et al., 2011; Fitzpatrick et al. 2013; Rieg et al., 2018). This means that velocities over the entire glacier can be calculated, allowing for the creation of a longer time-series of data encompassing single melt seasons to several years or decades (e.g. Heid and Kääb, 2012b; Dehecq et al., 2015; Joughin et al., 2018; Robson et al., 2018; Dell et al., 2019). Although spatial resolution can be an issue over smaller glaciers, the resolution of relatively new sensors (such as Planet) is much finer than that of more traditional sensors, offering a more beneficial compromise between resolution and aerial coverage for glacial research (e.g. Steiner et al., 2018; Millan et al., 2019; Watson et al., 2020; Bhushan et al., 2020, 2021).

Furthermore, while scenes acquired using optical imagery can be hindered by cloud cover, SAR sensors, such as TerraSAR-X (2 m) and the more widely available Sentinel-1 (10 m), are not, and thus have been widely used to investigate the velocity and changing dynamics of numerous glaciers worldwide (e.g. Nagler et al., 2015; Schellenberger et al., 2015; Lal et al., 2018; Baurley et al., 2020). Depending on the acquisition period between images, several different methods can also be employed when using SAR data, such as SAR interferometry and offset tracking, each with their own advantages and disadvantages (e.g. Schneevoigt et al., 2012; Nagler et al., 2015; Fahnestock et al., 2016). Acquiring satellite imagery is also generally free and logistically simple (although this does depend on the sensor), and the provided data are usually georeferenced. As a result, several images can be rapidly processed in a short amount of time, allowing glacier dynamics to be more easily quantified in comparison to data obtained from field studies (Karpilo, 2009; Gjermundsen et al., 2011; Nagler et al., 2015).

It is clear, therefore, that at present it is impractical to solely use UAVs to investigate the large-scale and long-term changes in ice dynamics currently occurring at lake-terminating glaciers in many glaciated regions such as Iceland (Immerzeel et al., 2014; Bhardwaj et al., 2016; Juvet et al., 2020). As a result, the method in its current form is not a direct replacement for glacier monitoring via satellite remote sensing (Bhardwaj et al., 2016; Fugazza et al., 2018; Chudley et al., 2019). Instead, the results of this research highlight that UAV surveys should, for the time being, be utilised in tandem with satellite remote sensing to allow both the glacier-wide changes in

dynamics, but also the more localised, short-term and fine-scale dynamic changes that occur within this glacier-wide pattern to more accurately quantified and understood (Immerzeel et al., 2014; Rossini et al., 2018; Juvet et al. 2019). This will allow for more accurate and informative monitoring of lake-terminating glaciers and their dynamic behaviour to be undertaken, which may then aid in our understanding of how these glaciers may respond in future (Bhardwaj et al., 2016; Wigmore and Mark, 2017; Chudley et al., 2019).

Chapter 7 CONCLUSIONS

7.1 Research Synthesis and Conclusions

This research utilised ultra-high resolution repeat UAV imagery to investigate the changing dynamic behaviour of Fjallsjökull, a large lake-terminating glacier in southeast Iceland, across the 2019 and 2021 ablation season, and is the first research of its kind to do so. The velocity data, calculated at different temporal intervals across both years, clearly shows an increase in velocity with increasing distance from the southern-grounded margin, which closely corresponds to the presence of a 100-120 m deep bedrock channel under the northern part of the study area. Velocities in this region are consistently elevated, reaching peaks of $\sim 0.9\text{--}1.0\text{ m d}^{-1}$ in 2019, and up to 1.2 m d^{-1} in 2021. Furthermore, the surface elevation change data displays a similar pattern, whereby the most negative surface changes are again found with increasing distance from the grounded margin, with up to $\sim 2.50 \pm 0.18\text{ m}$, and $\sim 5.50 \pm 0.15\text{ m}$ of negative change observed in this region in 2019 and 2021, respectively. Importantly, these negative changes coincide closely with the region of fastest ice velocities, and, consequently, the deepest parts of the bedrock channel.

The frequency and magnitude of calving events were also investigated, with it being found that calving exerts a strong control on the position and stability of the terminus across all time periods. Indeed, although there were significant inter-daily variations, overall -2.77 and -0.25 m of frontal change (i.e. retreat) was observed in July and September 2019, while -10.70 m of change was observed in July 2021. In addition, it was also found that the largest calving events were significant enough in their size to force localised, short-term increases in velocity, particularly in the lower part of the study region, despite this region not coinciding with the deepest parts of the bedrock channel. Finally, detailed information on the evolution of supraglacial lakes and WfCs was also obtained, which demonstrated that such features could grow, shrink, or disappear entirely over very short periods of time (e.g. hours to days) in response to different factors, such as periods of heavy rain, or large calving events. This indicates that the drainage of such features may be important in forcing very short (i.e. daily) localised increases in velocity, with such an event believed to have occurred in September 2019.

Based on the data obtained in this research, it is suggested that there is a hierarchy of forcing mechanisms which are influencing the dynamics of Fjallsjökull over different spatial and temporal scales: (i) Large-scale velocity variations and links to basal topography, (ii) Localised velocity

variations and links to subaqueous melt and (iii) Supraglacial lake drainage and short-term velocity variations.

The overall spatial variations in velocity that were observed in both 2019 and 2021 are strongly controlled by the location and depth of the bedrock channel under the upper portion of the study region. As Fjallsjökull has retreated into the deepest parts of the bedrock channel the water depth has increased, causing the glacier to speed up due to the inverse relationship that exists between the effective pressure and basal drag. This has caused the surface of the glacier to undergo longitudinal stretching (i.e. surface thinning), permitting crevasse propagation and, therefore, calving to occur. At Fjallsjökull, calving primarily occurs via this mechanism, or through buoyant forces acting on parts of the locally buoyant terminus as it retreats into the deepest part of the bedrock channel. This calving has resulted in increased mass loss and frontal retreat, leading to a further increase in velocities, longitudinal stretching and the implementation of a positive feedback mechanism termed dynamic thinning. Indeed, the fact the most negative rates of surface thinning are observed in the upper portion of the study area, and that this region directly corresponds to the deepest part of the bedrock channel, strongly indicates that this mechanism is occurring here. This suite of processes, forced primarily by the retreat of Fjallsjökull into deeper water, suggests the underlying bedrock topography is exerting a first order control on the overall dynamics of the glacier.

Additional processes, such as thermal notch erosion, however, are instead likely forcing those more localised variations in the dynamics of the glacier. Extensive notches were observed at the waterline of Fjallsjökull across all time periods in both 2019 and 2021, with direct observations made in July 2021 suggesting such features could be forming and evolving at the waterline in a relatively short space of time (i.e. <24 hours). These notches are important because they can undercut the terminus face of Fjallsjökull, leading to an increase in the force imbalance at these locations, which can then result in calving. Following the sudden loss of a large volume of ice, the glacier speeds up, initially in the area immediately surrounding where the event occurred, and then subsequently over a much wider area which is then sustained over several days. Such a response reflects the speed-up and drawdown of ice from further up-glacier to provide the additional resistive stresses that are necessary to restore the stress balance. Such short-term and localised increases in velocity, occurring in response to a large calving event, were observed in both July 2019 and 2021, highlighting the importance of thermal notch erosion as a key control on both the calving losses from, and the localised dynamics of, Fjallsjökull, and as such these can be termed second order processes.

Short-term (<24 hour), localised variations in the dynamics of Fjallsjökull may also occur through the rapid routing of large quantities of water to the bed, which can be sourced from either supraglacial lake drainage or heavy rainfall events. The sudden input of a large amount of water to the bed is often sufficient to cause an additional increase in basal water pressure, temporarily increasing the velocity of the glacier for several hours. Yet although widespread supraglacial lake drainage was observed between the 5th and 6th July 2019, it is difficult to discern the impact this had on the short-term dynamics of the glacier because the drainage occurred in response to a large calving event, which likely had a greater impact on its localised dynamics. Conversely, in September 2019, an increase in velocity was observed over a localised region of Fjallsjökull in the 24-hour period following a large rainfall event, and thus it is possible that this increase occurred primarily in response to this event. However, although a large rainfall event also occurred between the 12th and 15th July 2021, it is unlikely this event was sufficient to cause the localised increase in velocity that was observed because several relatively large calving events also occurred in this region during this time, which were likely more important in forcing this event. As a result, although the influence of such events on the dynamics of Fjallsjökull are less important in comparison to the first and second order processes, they are important for forcing local-scale dynamic variations, and thus can be classed as third order processes, with further research required so that their full impact can be assessed.

This research has also addressed one of the most important components of glacier monitoring: investigating how glaciers change over time. Indeed, because it was possible to obtain UAV data in both July 2019 and July 2021, it has meant an assessment could be made as whether the dynamic behaviour of the glacier has changed and evolved in this time. This demonstrated that the highest velocities, most negative changes in surface elevation, greatest overall change in frontal position, and the largest calving events were all observed in July 2021. As a result, this indicates that the glacier was flowing faster, thinning more, undergoing greater change in its frontal position and calving with greater magnitude in 2021 than it was in 2019, despite preceding weather conditions being similar between both years. This is important as it suggests that the difference between years may have instead been forced by, and signify a further change in, the dynamic behaviour of Fjallsjökull as the glacier continues to retreat through the deepest parts of the bedrock channel.

Importantly, the above processes, forced primarily by the retreat of Fjallsjökull back into and through the deepest parts of the bedrock channel, strongly suggests that the overall dynamic behaviour of the glacier has become, at least partially, decoupled from the changing climate. Indeed, such a dynamic response is occurring beyond what would be expected through climate alone, with this predicted to continue in future until the glacier retreats out of the deepest parts

of the bedrock channel and into the water. Such a dynamic response is not only highlighted by the UAV data presented in this research (i.e. where the highest velocities and rates of surface thinning are found where the channel is most deep), but also by the overall retreat pattern of the glacier since 1945. This indicates that since ~1990 the lake-terminating margin of Fjallsjökull has retreated three times faster than its land-terminating counterpart, despite both regions undergoing the same climatic forcing during this time. This further reiterates that the retreat of the lake-terminating margin during this time, as well as the resulting change in ice dynamics, has been forced primarily by glacier specific factors (i.e. the deep bedrock topography and the onset of calving), and not solely by the changing climate.

Furthermore, the dynamic processes observed here at Fjallsjökull may be analogous for those processes that have already occurred, or that may occur in future, at other lake-terminating glaciers in Iceland. For example, these processes show a close resemblance to those already observed to be underway at the neighbouring glacier to Fjallsjökull, Breiðamerkurjökull, while they may also reflect the future response of several other lake-terminating glaciers in south Iceland, which are also beginning to retreat into their own deep bedrock troughs. In addition, similar patterns of flow acceleration and rapid retreat, linked to the presence of deep bedrock troughs, have also been observed at several lake-terminating glaciers in other glaciated regions, providing further validity for the findings presented in this research.

Lastly, the ultra-high resolution UAV data acquired and presented in this research further reiterates how the UAV-SfM approach is both a highly suitable and important tool for investigating and monitoring the changing dynamics of lake-terminating glaciers. The ability to deploy the UAV system 'on demand' meant that a large amount of high-quality data could be acquired at very high spatial and temporal resolutions, which has provided important insights into a set of dynamic processes that would have been nearly impossible to capture using traditional satellite remote sensing alone. For example, the overall velocity pattern observed in this research would have been impacted if it had been derived using satellite imagery, especially over the areas of fast-flowing ice, as the coarser resolution of the imagery would have smoothed the overall velocity signal. Similarly, those localised velocity increases that followed large calving events would have also been missed if the same analysis were undertaken using satellite imagery because the longer temporal baseline between image acquisitions would have caused such an increase to be averaged out over the longer time period. Finally, the ultra-high spatial resolution of the UAV imagery also meant that surface features, like lakes, could be accurately delineated and their development monitored, yet such features (and their evolution) would have been completely overlooked had satellite imagery been utilised instead. As a result, this suggests that the UAV-SfM approach can be utilised to investigate the dynamics of other lake-terminating

glaciers, and, when combined with new, higher-resolution satellite imagery, can be used to gain a more complete understanding of these dynamic processes and how they may dictate the response of these glaciers in future.

7.2 Future Work

The aim of this research was to demonstrate how the UAV-SfM approach can be used to accurately investigate the dynamics of a large lake-terminating glacier at high spatial and temporal resolutions. Indeed, the findings of this research have certainly determined that this is the case, with several distinct forcing mechanisms observed which have been shown to exert a key control on the dynamic behaviour of Fjallsjökull at different spatial and temporal scales. However, there are several avenues of research that could be explored in order to further develop these findings, with the aim of gaining a more complete understanding of the changing dynamics of Fjallsjökull and how it may respond in future.

As mentioned in Section 6.2.3, one of the primary limitations of this research was that the UAV surveys did not cover the whole of the lower terminus region of the glacier. Although this was planned for originally, it soon became unfeasible because a UAV system with sufficient flight time to cover this region was neither readily available nor financially viable. However, recent technical advancements in UAV battery life mean that this could be addressed in future by utilising either a fixed-wing UAV or a new quadcopter system, such as the DJI M300. This would mean the complete lower terminus region of the glacier could be surveyed, providing a more comprehensive insight into the overall dynamics and changing behaviour of this region.

To more accurately determine when individual calving events occurred, time-lapse cameras could have been deployed around the edge of the lake before any UAV surveys were undertaken. Indeed, a time-lapse camera was already set up overlooking the calving front of Fjallsjökull prior to those research trips undertaken in both 2019 and 2021, but unfortunately technical issues in both cases meant that no imagery could be obtained. If such technical issues are addressed in future, then the deployment of time-lapse cameras at the field site may be beneficial to not only determine the exact timing of calving events, but also to provide information on the longer-term calving behaviour of the glacier beyond the period encompassed by the UAV surveys.

Furthermore, recent technological advances in UAV surveying, in particular the development and miniaturisation of new payloads, such as compact laser scanners, have the potential to provide new insights into glacial processes that would be challenging to capture using the UAV-SfM approach. For example, a UAV-mounted laser scanner not only has the potential to quantify changes in surface elevation more accurately (e.g. thinning), but may also allow for more accurate

estimation of the size (i.e. area and volume) of those calving events that occur between repeat surveys. In addition, such a system could also be used to predict future calving events due to the ability of the laser scanner to capture and reconstruct crevasse morphology, and in particular the depth to which individual crevasses may penetrate more accurately. It would be beneficial, therefore, to employ such a system at Fjallsjökull, as it would allow the calving behaviour of the glacier to be more accurately quantified, which in turn would mean the overall dynamics of the glacier could also be better understood.

One of the key findings of this research was that thermal notch erosion was directly observed to be occurring at the waterline of Fjallsjökull, with it being suggested that this process is important for inducing calving (and subsequent velocity increases) in those areas of the glacier not in proximity to the deepest parts of the bedrock channel. However, no direct measurements of notch erosion could be made in this research, and indeed attempting this in future would be highly dangerous due to the active nature of the calving front. Instead, future work could focus on measuring variations in lake level as a proxy for the amount of melt occurring. Indeed, it is widely established that notch erosion is most effective when the level of the lake remains stable as this allows the melt to be concentrated in a narrower band of ice. As a result, by measuring variations in lake level it would provide some indication as to the relative effectiveness of thermal notch erosion at Fjallsjökull, and how this can vary over different temporal scales (e.g. sub-daily, daily).

An additional key finding of this research was the role that supraglacial lake drainage may have in forcing short-term (i.e. sub daily) localised increases in velocity. Yet while supraglacial drainage was observed across all time periods, the exact timing of these events could not be determined because only one UAV survey was undertaken each day. As such, future research could focus on undertaking multiple surveys each day (e.g. in the morning, at midday and in the afternoon) to quantify the timing of supraglacial lake drainage more accurately, which in turn may provide further insight into the importance of this process for forcing short-term speed up events at Fjallsjökull.

Finally, the UAV imagery acquired in this research could have been supplemented with velocity data obtained using (relatively) high-resolution Planet imagery, and elevation change data acquired using a high-resolution global DEM dataset such as ArcticDEM. This would allow glacier velocity and changes in surface elevation to be obtained over a much larger spatial and temporal scale, and although unfortunately beyond the scope of this thesis, it is likely that such data would have provided additional insight and support to the key findings presented here. This would allow for more accurate monitoring of the dynamic behaviour of Fjallsjökull to be undertaken, which in turn would provide important additional insight into the likely future response of the glacier.

List of References

- Aðalgeirsdóttir, G., Magnússon, E., Pálsson, F., Thorsteinsson, T., Belart, J., Jóhannesson, T., Hannesdóttir, H., Sigurðsson, O., Gunnarsson, A., Einarsson, B. and Berthier, E., 2020. Glacier changes in Iceland from ~1890 to 2019. *Frontiers in Earth Science*, 8(520). <https://doi.org/10.3389/feart.2020.523646>
- Agisoft LLC., 2021. Agisoft Metashape User Manual: Professional edition, Version 1.7. [online]. Agisoft LLC. Available from: <https://www.agisoft.com/downloads/user-manuals/>. [Accessed: 23rd September 2021].
- Ahmadabadian, A.H., Robson, S., Boehm, J., Shortis, M., Wenzel, K. and Fritsch, D., 2013. A comparison of dense matching algorithms for scaled surface reconstruction using stereo camera rigs. *ISPRS Journal of Photogrammetry and Remote Sensing*, 78, pp.157-167. <https://doi.org/10.1016/j.isprsjprs.2013.01.015>
- Ahn, Y. and Howat, I.M., 2011. Efficient automated glacier surface velocity measurement from repeat images using multi-image/multichip and null exclusion feature tracking. *IEEE Transactions on Geoscience and Remote Sensing*, 49(8), pp.2838-2846. <https://doi.org/10.1109/TGRS.2011.2114891>
- Alley, R.B., Blankenship, D.D., Bentley, C.R. and Rooney, S.T., 1986. Deformation of till beneath ice stream B, West Antarctica. *Nature*, 322(6074), pp.57-59. <https://doi.org/10.1038/322057a0>
- Alley, R.B., Blankenship, D.D., Bentley, C.R. and Rooney, S.T., 1987a. Till beneath ice stream B: 3. Till deformation: evidence and implications. *Journal of Geophysical Research: Solid Earth*, 92(B9), pp.8921-8929. <https://doi.org/10.1029/JB092iB09p08921>
- Alley, R.B., Blankenship, D.D., Rooney, S.T. and Bentley, C.R., 1987b. Till beneath ice stream B: 4. A coupled ice-till flow model. *Journal of Geophysical Research: Solid Earth*, 92(B9), pp.8931-8940. <https://doi.org/10.1029/JB092iB09p08931>
- Alley, R.B., Blankenship, D.D., Rooney, S.T. and Bentley, C.R., 1987c. Continuous till deformation beneath ice sheets. *International Association of Hydrological Sciences, Publication*, 170, pp.81-91.
- Alley, R.B., 1989. Water-pressure coupling of sliding and bed deformation: I. Water system. *Journal of Glaciology*, 35(119), pp.108-118. <https://doi.org/10.3189/002214389793701527>
- Alley, R.B., 1992. Flow-law hypotheses for ice-sheet modeling. *Journal of Glaciology*, 38(129), pp.245-256. <https://doi.org/10.3189/S0022143000003658>
- Alley, R.B., Dupont, T.K., Parizek, B.R. and Anandakrishnan, S., 2005. Access of surface meltwater to beds of sub-freezing glaciers: preliminary insights. *Annals of Glaciology*, 40, pp.8-14. <https://doi.org/10.3189/172756405781813483>
- Altena, B. and Käab, A., 2017a. Weekly glacier flow estimation from dense satellite time series using adapted optical flow technology. *Frontiers in Earth Science*, 5, pp.1-12. <https://doi.org/10.3389/feart.2017.00053>
- Altena, B. and Käab, A., 2017b. Glacier ice loss monitored through the Planet cubesat constellation. In *2017 9th International Workshop on the Analysis of Multitemporal Remote Sensing Images (MultiTemp)* (pp.1-4). IEEE. <https://doi.org/10.1109/Multi-Temp.2017.8035235>
- Andersen, M.L., Nettles, M., Elosegui, P., Larsen, T.B., Hamilton, G.S. and Stearns, L.A., 2011. Quantitative estimates of velocity sensitivity to surface melt variations at a large Greenland outlet glacier. *Journal of Glaciology*, 57(204), pp.609-620. <http://doi.org/10.3189/002214311797409785>

List of References

- Andrews, L.C., Catania, G.A., Hoffman, M.J., Gulley, J.D., Lüthi, M.P., Ryser, C., Hawley, R.L. and Neumann, T.A., 2014. Direct observations of evolving subglacial drainage beneath the Greenland Ice Sheet. *Nature*, 514(7520), pp.80-83. <https://doi.org/10.3189/2012JoG12J018>
- Armstrong, W.H., Anderson, R.S., Allen, J. and Rajaram, H., 2016. Modelling the WorldView-derived seasonal velocity evolution of Kennicott Glacier, Alaska. *Journal of Glaciology*, 62(234), pp.763-777. <https://doi.org/10.1017/jog.2016.66>
- Armstrong, W.H. and Anderson, R.S., 2020. Ice-marginal lake hydrology and the seasonal dynamical evolution of Kennicott Glacier, Alaska. *Journal of Glaciology*, 66(259), pp.699-713. <https://doi.org/10.1017/jog.2020.41>
- Arnold, N.S., Banwell, A.F. and Willis, I.C., 2014. High-resolution modelling of the seasonal evolution of surface water storage on the Greenland Ice Sheet. *The Cryosphere*, 8(4), pp.1149-1160. <https://doi.org/10.5194/tc-8-1149-2014>
- Arya, S., Mount, D.M., Netanyahu, N.S., Silverman, R. and Wu, A.Y., 1998. An optimal algorithm for approximate nearest neighbour searching fixed dimensions. *Journal of the ACM (JACM)*, 45(6), pp.891-923. <https://doi.org/10.1145/293347.293348>
- Bach, E., Radić, V. and Schoof, C., 2018. How sensitive are mountain glaciers to climate change? Insights from a block model. *Journal of Glaciology*, 64(244), pp.247-258. <https://doi.org/10.1017/jog.2018.15>
- Bartholomew, I., Nienow, P., Mair, D., Hubbard, A., King, M.A. and Sole, A., 2010. Seasonal evolution of subglacial drainage and acceleration in a Greenland outlet glacier. *Nature Geoscience*, 3(6), pp.408-411. <https://doi.org/10.1029/2011JF002220>
- Bartholomew, I., Nienow, P., Sole, A., Mair, D., Cowton, T. and King, M.A., 2012. Short-term variability in Greenland Ice Sheet motion forced by time-varying meltwater drainage: Implications for the relationship between subglacial drainage system behavior and ice velocity. *Journal of Geophysical Research: Earth Surface*, 117(F3). <https://doi.org/10.1029/2011JF002220>
- Bash, E.A., Moorman, B.J. and Gunther, A., 2018. Detecting short-term surface melt on an Arctic Glacier using UAV surveys. *Remote Sensing*, 10(10), pp.1-17. <https://doi.org/10.3390/rs10101547>
- Baurley, N.R., Robson, B.A. and Hart, J.K., 2020. Long-term impact of the proglacial lake Jökulsárlón on the flow velocity and stability of Breiðamerkurjökull glacier, Iceland. *Earth Surface Processes and Landforms*, 45(11), pp.2647-2663. <https://doi.org/10.1002/esp.4920>
- Bay, H., Ess, A., Tuytelaars, T. and van Gool, L., 2008. Speeded-up robust features (SURF). *Computer Vision and Image Understanding*, 110(3), pp.346-359. <https://doi.org/10.1016/j.cviu.2007.09.014>
- Behrens, H., Bergmann, H., Moser, H., Ambach, W. and Jochum, O., 1975. On the water channels of the internal drainage system of the Hintereisferner, Ötztal Alps, Austria. *Journal of Glaciology*, 14(72), pp.375-382. <https://doi.org/10.3189/S0022143000021900>
- Belart, J., Magnússon, E., Berthier, E., Gunnlaugsson, Á.Þ., Pálsson, F., Aðalgeirsdóttir, G., Jóhannesson, T., Thorsteinsson, T. and Björnsson, H., 2020. Mass balance of 14 Icelandic glaciers, 1945–2017: spatial variations and links with climate. *Frontiers in Earth Science*, 8(163). <https://doi.org/10.3389/feart.2020.00163>
- Bemis, S.P., Micklethwaite, S., Turner, D., James, M.R., Akciz, S., Thiele, S.T. and Bangash, H.A., 2014. Ground-based and UAV-based photogrammetry: A multi-scale, high-resolution mapping tool for structural geology and paleoseismology. *Journal of Structural Geology*, 69, pp.163-178. <https://doi.org/10.1016/j.jsg.2014.10.007>
- Benassi, F., Dall'Asta, E., Diotri, F., Forlani, G., Morra di Cella, U., Roncella, R. and Santise, M., 2017. Testing accuracy and repeatability of UAV blocks oriented with GNSS-supported aerial triangulation. *Remote Sensing*, 9(2), pp.1-23. <https://doi.org/10.3390/rs9020172>

- Bendle, J., 2020. *Calving of freshwater glaciers*. [online] AntarcticGlaciers.org. Available at: <http://www.antarcticglaciers.org/glacier-processes/glacial-lakes/calving-of-freshwater-glaciers/> [Accessed 23rd March 2021].
- Benn, D.I., 1995. Fabric signature of subglacial till deformation, Breiðamerkurjökull, Iceland. *Sedimentology*, 42(5), pp.735-747. <https://doi.org/10.1111/j.1365-3091.1995.tb00406.x>
- Benn, D.I., Hulton, N.R. and Mottram, R.H., 2007a. 'Calving laws', 'sliding laws' and the stability of tidewater glaciers. *Annals of Glaciology*, 46, pp.123-130. <https://doi.org/10.3189/172756407782871161>
- Benn, D.I., Warren, C.R. and Mottram, R.H., 2007b. Calving processes and the dynamics of calving glaciers. *Earth-Science Reviews*, 82(3-4), pp.143-179. <https://doi.org/10.1016/j.earscirev.2007.02.002>
- Benn, D. and Evans, D.J., 2010. *Glaciers and glaciation (2nd Edition)*. London: Routledge.
- Benn, D.I., Åström, J.A.N., Zwinger, T., Todd, J.O.E., Nick, F.M., Cook, S., Hulton, N.R. and Luckman, A., 2017. Melt-under-cutting and buoyancy-driven calving from tidewater glaciers: new insights from discrete element and continuum model simulations. *Journal of Glaciology*, 63(240), pp.691-702. <https://doi.org/10.1017/jog.2017.41>
- Benn, D.I. and Åström, J.A., 2018. Calving glaciers and ice shelves. *Advances in Physics: X*, 3(1), p.1513819. <https://doi.org/10.1080/23746149.2018.1513819>
- Benoit, L., Gourdon, A., Vallat, R., Irrazaval, I., Gravey, M., Lehmann, B., Prasicek, G., Graff, D., Herman, F. and Mariethoz, G., 2019. A high-resolution image time series of the Gorner Glacier-Swiss Alps-derived from repeated unmanned aerial vehicle surveys. *Earth System Science Data*, 11(2), pp.579-588. <https://doi.org/10.5194/essd-11-579-201>
- Bernstein, R., 1983. Manual of remote sensing. *American Society of Photogrammetry, Falls Chyrch, VA, Ch. Image geometry and rectification (pp.881-884)*.
- Berthier, E., Raup, B. and Scambos, T., 2003. New velocity map and mass-balance estimate of Mertz Glacier, East Antarctica, derived from Landsat sequential imagery. *Journal of Glaciology*, 49(167), pp.503-511. <https://doi.org/10.3189/172756503781830377>
- Berthier, E., Vadon, H., Baratoux, D., Arnaud, Y., Vincent, C., Feigl, K.L., Remy, F. and Legresy, B., 2005. Surface motion of mountain glaciers derived from satellite optical imagery. *Remote Sensing of Environment*, 95(1), pp.14-28. <https://doi.org/10.1016/j.rse.2004.11.005>
- Berthier, E. and Vincent, C., 2012. Relative contribution of surface mass-balance and ice-flux changes to the accelerated thinning of Mer de Glace, French Alps, over 1979-2008. *Journal of Glaciology*, 58(209), pp.501-512. <https://doi.org/10.3189/2012JoG11J083>
- Bhardwaj, A., Joshi, P.K., Sam, L. and Snehmani, 2015. Remote sensing of alpine glaciers in visible and infrared wavelengths: A survey of advances and prospects. *Geocarto International*, 31(5), pp.557-574. <https://doi.org/10.1080/10106049.2015.1059903>
- Bhardwaj, A., Sam, L., Martín-Torres, F.J. and Kumar, R., 2016. UAVs as remote sensing platform in glaciology: Present applications and future prospects. *Remote Sensing of Environment*, 175, pp.196-204. <https://doi.org/10.1016/j.rse.2015.12.029>
- Bhushan, S., Shean, D., Alexandrov, O. and Henderson, S., 2020. Automated tools to derive short-term glacier velocity from high-resolution commercial satellite imagery. *Earth and Space Science Open Archive ESSOAr*.
- Bhushan, S., Shean, D., Alexandrov, O. and Henderson, S., 2021. Automated digital elevation model (DEM) generation from very-high-resolution Planet SkySat triplet stereo and video imagery. *ISPRS Journal of Photogrammetry and Remote Sensing*, 173, pp.151-165. <https://doi.org/10.1016/j.isprsjprs.2020.12.012>

List of References

- Bindschadler, R.R., 1980. The predicted behaviour of Griesgletscher and its possible threat to a nearby dam. *Zeitschrift für Gletscherkunde und Glazialgeologie*, 16, 45–59.
- Bindschadler, R., 1983. The importance of pressurized subglacial water in separation and sliding at the glacier bed. *Journal of Glaciology*, 29(101), pp.3-19. <https://doi.org/10.3189/S0022143000005104>
- Bindschadler, R.A. and Scambos, T.A., 1991. Satellite-image-derived velocity field of an Antarctic ice stream. *Science*, 252, pp.242-246. <https://doi.org/10.1126/science.252.5003.242>
- Björnsson, H. and Pálsson, F., 2008. Icelandic glaciers. *Jökull*, 58(58), pp.365-386.
- Björnsson, H., Pálsson, F., Guðmundsson, S., Magnússon, E., Adalgeirsdóttir, G., Jóhannesson, T., Berthier, E., Sigurdsson, O. and Thorsteinsson, T., 2013. Contribution of Icelandic ice caps to sea level rise: Trends and variability since the Little Ice Age. *Geophysical Research Letters*, 40(8), pp.1546-1550. <https://doi.org/10.1002/grl.50278>
- Blake, E., Clarke, G.K. and Gérin, M.C., 1992. Tools for examining subglacial bed deformation. *Journal of Glaciology*, 38(130), pp.388-396. <https://doi.org/10.3189/S0022143000002264>
- Boufama, B., Mohr, R. and Veillon, F., 1993, May. Euclidean constraints for uncalibrated reconstruction. In *1993 (4th) International Conference on Computer Vision* (pp. 466-470). IEEE. <https://doi.org/10.1109/ICCV.1993.378179>
- Bougamont, M., Christoffersen, P., A L, H., Fitzpatrick, A.A., Doyle, S.H. and Carter, S.P., 2014. Sensitive response of the Greenland Ice Sheet to surface melt drainage over a soft bed. *Nature Communications*, 5(1), pp.1-9. <https://doi.org/10.1038/ncomms6052>
- Boulton, G.S., 1974. Processes and patterns of glacial erosion. In Coates, D.R., (eds). *Glacial Geomorphology* (pp. 41-87). Dordrecht: Springer
- Boulton, G.S., 1979. Processes of glacier erosion on different substrata. *Journal of glaciology*, 23(89), pp.15-38. <https://doi.org/10.3189/S0022143000029713>
- Boulton, G.S. and Jones, A.S., 1979. Stability of temperate ice caps and ice sheets resting on beds of deformable sediment. *Journal of Glaciology*, 24(90), pp.29-43. <https://doi.org/10.3189/S0022143000014623>
- Boulton, G.S. and Hindmarsh, R.C.A., 1987. Sediment deformation beneath glaciers: rheology and geological consequences. *Journal of Geophysical Research: Solid Earth*, 92(B9), pp.9059-9082. <https://doi.org/10.1029/JB092iB09p09059>
- Boulton, G.S., 1996. Theory of glacial erosion, transport and deposition as a consequence of subglacial sediment deformation. *Journal of Glaciology*, 42(140), pp.43-62. <https://doi.org/10.3189/S0022143000030525>
- Boulton, G.S., Dobbie, K.E. and Zatsepin, S., 2001. Sediment deformation beneath glaciers and its coupling to the subglacial hydraulic system. *Quaternary International*, 86(1), pp.3-28. [https://doi.org/10.1016/S1040-6182\(01\)00048-9](https://doi.org/10.1016/S1040-6182(01)00048-9)
- Boyce, E.S., Motyka, R.J. and Truffer, M., 2007. Flotation and retreat of a lake-calving terminus, Mendenhall Glacier, southeast Alaska, USA. *Journal of Glaciology*, 53(181), pp.211-224. <https://doi.org/10.3189/172756507782202928>
- Bradwell, T., Sigurdsson, O. and Everest, J., 2013. Recent, very rapid retreat of a temperate glacier in SE Iceland. *Boreas*, 42(4), pp.959-973. <https://doi.org/10.1111/bor.12014>
- Brasington, J., Vericat, D. and Rychkov, I., 2012. Modeling river bed morphology, roughness, and surface sedimentology using high resolution terrestrial laser scanning. *Water Resources Research*, 48(11). <https://doi.org/10.1029/2012WR012223>

- Budd, W.F., Keage, P.L. and Blundy, N.A., 1979. Empirical studies of ice sliding. *Journal of glaciology*, 23(89), pp.157-170. <https://doi.org/10.3189/S0022143000029804>
- Burgess, E.W., Forster, R.R. and Larsen, C.F., 2013. Flow velocities of Alaskan glaciers. *Nature Communications*, 4(1), pp.1-8. <https://doi.org/10.1038/ncomms3146>
- Carrivick, J.L. and Tweed, F.S., 2013. Proglacial lakes: Character, behaviour and geological importance. *Quaternary Science Reviews*, 78, pp.34-52. <https://doi.org/10.1016/j.quascirev.2013.07.028>
- Carrivick, J.L. and Quincey, D.J., 2014. Progressive increase in number and volume of ice-marginal lakes on the western margin of the Greenland Ice Sheet. *Global and Planetary Change*, 116, pp.156-163. <https://doi.org/10.1016/j.gloplacha.2014.02.009>
- Carrivick, J.L., Tweed, F.S., Sutherland, J.L. and Mallalieu, J., 2020. Toward numerical modelling of interactions between ice-marginal proglacial lakes and glaciers. *Frontiers in Earth Science*, 8, p.500. <https://doi.org/10.3389/feart.2020.577068>
- Cavanagh, J.P., Lampkin, D.J. and Moon, T., 2017. Seasonal variability in regional ice flow due to meltwater injection into the shear margins of Jakobshavn Isbræ. *Journal of Geophysical Research: Earth Surface*, 122(12), pp.2488-2505. <https://doi.org/10.1002/2016JF004187>
- Cazenave, A. and WCRP Global Sea Level Budget Group., 2018. Global sea-level budget 1993-present. *Earth System Science Data*, 10, pp.1551-1590. <https://doi.org/10.3929/ethz-b-000287786>
- Chandler, D.M., Wadham, J.L., Lis, G.P., Cowton, T., Sole, A., Bartholomew, I., Telling, J., Nienow, P., Bagshaw, E.B., Mair, D. and Vinen, S., 2013. Evolution of the subglacial drainage system beneath the Greenland Ice Sheet revealed by tracers. *Nature Geoscience*, 6(3), pp.195-198. <https://doi.org/10.1038/ngeo1737>
- Chandler, B.M., Evans, D.J., Chandler, S.J., Ewertowski, M.W., Lovell, H., Roberts, D.H., Schaefer, M. and Tomczyk, A.M., 2020. The glacial landsystem of Fjallsjökull, Iceland: Spatial and temporal evolution of process-form regimes at an active temperate glacier. *Geomorphology*, 361(107192), pp.1-28. <https://doi.org/10.1016/j.geomorph.2020.107192>
- Chernos, M., Koppes, M. and Moore, R.D., 2016. Ablation from calving and surface melt at lake-terminating Bridge Glacier, British Columbia, 1984–2013. *The Cryosphere*, 10(1), pp.87-102. <https://doi.org/10.5194/tc-10-87-2016>
- Chinn, T.J., 1988. The dry valleys of Victoria Land. In: *Satellite Image Atlas of Glaciers of the World, Antarctica*. USGS Professional Paper, 1386-B.
- Chudley, T., Christoffersen, P., Doyle, S.H., Abellan, A. and Snooke, N., 2019. High accuracy UAV photogrammetry of ice sheet dynamics with no ground control. *The Cryosphere*, 13(3), pp.955-968. <https://doi.org/10.5194/tc-13-955-2019>
- Chudley, T.R., Christoffersen, P., Doyle, S.H., Dowling, T.P.F., Law, R., Schoonman, C.M., Bougamont, M. and Hubbard, B., 2021. Controls on water storage and drainage in crevasses on the Greenland Ice Sheet. *Journal of Geophysical Research: Earth Surface*, 126(9), p.e2021JF006287. <https://doi.org/10.1029/2021JF006287>
- Clarke, G.K., 1987a. A short history of scientific investigations on glaciers. *Journal of Glaciology*, 33(S1), pp.4-24. <https://doi.org/10.3189/S00221430000215785>
- Clarke, G.K., 1987b. Fast glacier flow: Ice streams, surging, and tidewater glaciers. *Journal of Geophysical Research: Solid Earth*, 92(B9), pp.8835-8841. <https://doi.org/10.1029/JB092iB09p08835>
- Clason, C., Mair, D.W., Burgess, D.O. and Nienow, P.W., 2012. Modelling the delivery of supraglacial meltwater to the ice/bed interface: Application to southwest Devon Ice Cap, Nunavut, Canada. *Journal of Glaciology*, 58(208), pp.361-374. <https://doi.org/10.3189/2012JoG11J129>

List of References

- Colomina, I. and Molina, P., 2014. Unmanned aerial systems for photogrammetry and remote sensing: A review. *ISPRS Journal of Photogrammetry and Remote Sensing*, 92, pp.79-97. <https://doi.org/10.1016/j.isprsjprs.2014.02.013>
- Cook, K.L., 2017. An evaluation of the effectiveness of low-cost UAVs and structure from motion for geomorphic change detection. *Geomorphology*, 278, pp.195-208. <https://doi.org/10.1016/j.geomorph.2016.11.009>
- Copland, L., Pope, S., Bishop, M.P., Shroder, J.F., Clendon, P., Bush, A., Kamp, U., Seong, Y.B. and Owen, L.A., 2009. Glacier velocities across the central Karakoram. *Annals of Glaciology*, 50(52), pp.41-49. <https://doi.org/10.3189/172756409789624229>
- Cowton, T., Nienow, P., Sole, A., Wadham, J., Lis, G., Bartholomew, I., Mair, D. and Chandler, D., 2013. Evolution of drainage system morphology at a land-terminating Greenlandic outlet glacier. *Journal of Geophysical Research: Earth Surface*, 118(1), pp.29-41. <https://doi.org/10.1029/2012JF002540>
- Creys, T.T. and Schoof, C.G., 2009. Drainage through subglacial water sheets. *Journal of Geophysical Research: Earth Surface*, 114(F4). <https://doi.org/10.1029/2008JF001215>
- Cuffey, K.M. and Paterson, W.S.B., 2010. *The Physics of Glaciers*. London: Academic Press.
- Dall'Asta, E., Thoeni, K., Santise, M., Forlani, G., Giacomini, A. and Roncella, R., 2015. Network design and quality checks in automatic orientation of close-range photogrammetric blocks. *Sensors*, 15(4), pp.7985-8008. <https://doi.org/10.3390/s150407985>
- Dandois, J.P. and Ellis, E.C., 2013. High spatial resolution three-dimensional mapping of vegetation spectral dynamics using computer vision. *Remote Sensing of Environment*, 136, pp.259-276. <https://doi.org/10.1016/j.rse.2013.04.005>
- Danielson, B. and Sharp, M., 2013. Development and application of a time-lapse photograph analysis method to investigate the link between tidewater glacier flow variations and supraglacial lake drainage events. *Journal of Glaciology*, 59(214), pp.287-302. <https://doi.org/10.3189/2013JoG12J108>
- Das, S.B., Joughin, I., Behn, M.D., Howat, I.M., King, M.A., Lizarralde, D. and Bhatia, M.P., 2008. Fracture propagation to the base of the Greenland Ice Sheet during supraglacial lake drainage. *Science*, 320(5877), pp.778-781. <https://doi.org/10.1126/science.1153360>
- Davies, B., 2020. *Stress and strain*. [online] AntarcticGlaciers.org. Available at: <https://www.antarcticglaciers.org/glacier-processes/glacier-flow-2/glacier-flow-ii-stress-and-strain/>. [Accessed 5th May 2022].
- De Woul, M. and Hock, R., 2005. Static mass-balance sensitivity of Arctic glaciers and ice caps using a degree-day approach. *Annals of Glaciology*, 42, pp.217-224. <https://doi.org/10.3189/172756405781813096>
- Debella-Gilo, M. and Käab, A., 2012. Locally adaptive template sizes for matching repeat images of Earth surface mass movements. *ISPRS Journal of Photogrammetry and Remote Sensing*, 69, pp.10-28. <https://doi.org/10.1016/j.isprsjprs.2012.02.002>
- DeConto, R.M. and Pollard, D., 2016. Contribution of Antarctica to past and future sea-level rise. *Nature*, 531(7596), pp.591-597. <https://doi.org/10.1038/nature17145>
- Dehecq, A., Gourmelen, N. and Trouvé, E., 2015. Deriving large-scale glacier velocities from a complete satellite archive: Application to the Pamir–Karakoram–Himalaya. *Remote Sensing of Environment*, 162, pp.55-66. <https://doi.org/10.1016/j.rse.2015.01.031>
- Dehecq, A., Gourmelen, N., Gardner, A.S., Brun, F., Goldberg, D., Nienow, P.W., Berthier, E., Vincent, C., Wagnon, P. and Trouvé, E., 2019. Twenty-first century glacier slowdown driven by mass loss in

- High Mountain Asia. *Nature Geoscience*, 12(1), pp.22-27. <https://doi.org/10.1038/s41561-018-0271-9>
- Dell, R., Carr, R., Phillips, E. and Russell, A.J., 2019. Response of glacier flow and structure to proglacial lake development and climate at Fjallsjökull, south-east Iceland. *Journal of Glaciology*, 65(250), pp.321-336. <https://doi.org/10.1017/jog.2019.18>
- Dietrich, J.T., 2016. Riverscape mapping with helicopter-based Structure-from-Motion photogrammetry. *Geomorphology*, 252, pp.144-157. <https://doi.org/10.1016/j.geomorph.2015.05.008>
- Diolaiuti, G., Citterio, M., Carnielli, T., D'agata, C., Kirkbride, M. and Smiraglia, C., 2006. Rates, processes and morphology of freshwater calving at Miage Glacier (Italian Alps). *Hydrological Processes: An International Journal*, 20(10), pp.2233-2244. <https://doi.org/10.1002/hyp.6198>
- DJI., 2021a. Inspire 2. [online] <https://www.dji.com/uk/inspire-2>. [Accessed: 16th September 2021].
- DJI., 2021b. Zenmuse X4S Specs. [online]. <https://www.dji.com/uk/zenmuse-x4s/info#specs>. [Accessed: 16th September 2021].
- Doneus, M., Verhoeven, G., Fera, M., Briese, C., Kucera, M. and Neubauer, W., 2011. From deposit to point cloud—a study of low-cost computer vision approaches for the straightforward documentation of archaeological excavations. *Geoinformatics FCE CTU*, 6, pp.81-88. <https://doi.org/10.14311/gi.6.11>
- Dow, J.M., Neilan, R.E. and Rizos, C., 2009. The international GNSS service in a changing landscape of global navigation satellite systems. *Journal of Geodesy*, 83(3), pp.191-198. <https://doi.org/10.1007/s00190-008-0300-3>
- Dykes, R.C., Brook, M.S., Robertson, C.M. and Fuller, I.C., 2011. Twenty-First Century Calving Retreat of Tasman Glacier, Southern Alps, New Zealand. *Arctic, Antarctic, and Alpine Research*, 43(1), pp.1-10. <https://doi.org/10.1657/1938-4246-43.1.1>
- Echelmeyer, K. and Wang, Z., 1987. Direct observation of basal sliding and deformation of basal drift at sub-freezing temperatures. *Journal of Glaciology*, 33(113), pp.83-98. <https://doi.org/10.3189/S0022143000005396>
- Einarsson, B., 2017. Jöklabreytingar 1930–1970, 1970–1995, 1995–2015 og 2015–2016. *Jökull*, 67, pp.65-69.
- Eltner, A., Baumgart, P., Maas, H.G. and Faust, D., 2015. Multi-temporal UAV data for automatic measurement of rill and interrill erosion on loess soil. *Earth Surface Processes and Landforms*, 40(6), pp.741-755. <https://doi.org/10.1002/esp.3673>
- Ely, J.C., Graham, C., Barr, I.D., Rea, B.R., Spagnolo, M. and Evans, J., 2017. Using UAV acquired photography and structure from motion techniques for studying glacier landforms: Application to the glacial flutes at Isfallsglaciären. *Earth Surface Processes and Landforms*, 42(6), pp.877-888. <https://doi.org/10.1002/esp.4044>
- Emlid., 2021a. Emlid Reach. [online]. Available at: <https://emlid.com/reach/>. [Accessed 16th September 2021].
- Emlid., 2021b. Understanding PPK solution and analyzing logs from Reach. [online]. Available at: <https://docs.emlid.com/reach/tutorials/post-processing-workflow/analyzing-logs>. [Accessed: 23rd September 2021].
- Evans, D.J. and Twigg, D.R., 2002. The active temperate glacial landsystem: a model based on Breiðamerkurjökull and Fjallsjökull, Iceland. *Quaternary science reviews*, 21(20-22), pp.2143-2177. [https://doi.org/10.1016/S0277-3791\(02\)00019-7](https://doi.org/10.1016/S0277-3791(02)00019-7)

List of References

- Everett, A., Murray, T., Selmes, N., Rutt, I.C., Luckman, A., James, T.D., Clason, C., O'Leary, M., Karunarathna, H., Moloney, V. and Reeve, D.E., 2016. Annual down-glacier drainage of lakes and water-filled crevasses at Helheim Glacier, southeast Greenland. *Journal of Geophysical Research: Earth Surface*, 121(10), pp.1819-1833. <https://doi.org/10.1002/2016JF003831>
- Fahnestock, M., Scambos, T., Moon, T., Gardner, A., Haran, T. and Klinger, M., 2016. Rapid large-area mapping of ice flow using Landsat 8. *Remote Sensing of Environment*, 185, pp.84-94. <https://doi.org/10.1016/j.rse.2015.11.023>
- Fallourd, R., Harant, O., Trouvé, E., Nicolas, J.M., Gay, M., Walpersdorf, A., Mugnier, J.L., Serafini, J., Rosu, D., Bombrun, L. and Vasile, G., 2011. Monitoring temperate glacier displacement by multi-temporal TerraSAR-X images and continuous GPS measurements. *IEEE Journal of Selected Topics in Applied Earth Observations and Remote Sensing*, 4(2), pp.372-386. <https://doi.org/10.1109/JSTARS.2010.2096200>
- Farinotti, D., Brinkerhoff, D.J., Clarke, G.K., Fürst, J.J., Frey, H., Gantayat, P., Gillet-Chaulet, F., Girard, C., Huss, M., Leclercq, P.W. and Linsbauer, A., 2017. How accurate are estimates of glacier ice thickness? Results from ITMIX, the Ice Thickness Models Intercomparison eXperiment. *The Cryosphere*, 11(2), pp.949-970. <https://doi.org/10.5194/tc-11-949-2017>
- Farinotti, D., Huss, M., Fürst, J.J., Landmann, J., Machguth, H., Maussion, F. and Pandit, A., 2019. A consensus estimate for the ice thickness distribution of all glaciers on Earth. *Nature Geoscience*, 12(3), pp.168-173. <https://doi.org/10.1038/s41561-019-0300-3>
- Favalli, M., Fornaciai, A., Isola, I., Tarquini, S. and Nannipieri, L., 2012. Multiview 3D reconstruction in geosciences. *Computers and Geosciences*, 44, pp.168-176. <https://doi.org/10.1016/j.cageo.2011.09.012>
- Fieber, K.D., Mills, J.P., Miller, P.E., Clarke, L., Ireland, L. and Fox, A.J., 2018. Rigorous 3D change determination in Antarctic Peninsula glaciers from stereo WorldView-2 and archival aerial imagery. *Remote Sensing of Environment*, 205, pp.18-31. <https://doi.org/10.1016/j.rse.2017.10.042>
- Fischler, M.A. and Bolles, R.C., 1981. Random sample consensus: A paradigm for model fitting with applications to image analysis and automated cartography. *Communications of the ACM*, 24(6), pp.381-395. <https://doi.org/10.1145/358669.358692>
- Fisher, R.B., Breckon, T.P., Dawson-Howe, K., Fitzgibbon, A., Robertson, C., Trucco, E. and Williams, C.K., 2013. *Dictionary of Computer Vision and Image Processing*. Chichester: John Wiley & Sons.
- Fitch, A.J., Kadyrov, A., Christmas, W.J. and Kittler, J., 2002. Orientation correlation. *British Machine Vision Conference* (pp. 133-142).
- Fitzpatrick, A.A., Hubbard, A., Joughin, I., Quincey, D.J., van As, D., Mikkelsen, A.P., Doyle, S.H., Hasholt, B. and Jones, G.A., 2013. Ice flow dynamics and surface meltwater flux at a land-terminating sector of the Greenland ice sheet. *Journal of Glaciology*, 59(216), pp.687-696. <https://doi.org/10.3189/2013JoG12J143>
- Flowers, G.E., Marshall, S.J., Björnsson, H. and Clarke, G.K., 2005. Sensitivity of Vatnajökull ice cap hydrology and dynamics to climate warming over the next 2 centuries. *Journal of Geophysical Research: Earth Surface*, 110(F2). <https://doi.org/10.1029/2004JF000200>
- Fonstad, M.A., Dietrich, J.T., Courville, B.C., Jensen, J.L. and Carbonneau, P.E., 2013. Topographic structure from motion: A new development in photogrammetric measurement. *Earth surface Processes and Landforms*, 38(4), pp.421-430. <https://doi.org/10.1002/esp.3366>
- Foresta, L., Gourmelen, N., Pálsson, F., Nienow, P., Björnsson, H. and Shepherd, A., 2016. Surface elevation change and mass balance of Icelandic ice caps derived from swath mode CryoSat-2 altimetry. *Geophysical Research Letters*, 43(23), pp.12-138. <https://doi.org/10.1002/2016GL071485>

- Förstner, W., 1986. A feature based correspondence algorithm for image matching. *International Archives of Photogrammetry and Remote Sensing*, 26, pp.150-166.
- Fountain, A.G., 1994. Borehole water-level variations and implications for the subglacial hydraulics of South Cascade Glacier, Washington State, USA. *Journal of Glaciology*, 40(135), pp.293-304. <https://doi.org/10.3189/S0022143000007383>
- Fountain, A.G. and Walder, J.S., 1998. Water flow through temperate glaciers. *Reviews of Geophysics*, 36(3), pp.299-328. <https://doi.org/10.1029/97RG03579>
- Fowler, A.C., 1987. Sliding with cavity formation. *Journal of Glaciology*, 33(115), pp.255-267. <https://doi.org/10.3189/S0022143000008820>
- Frankl, A., Stal, C., Abraha, A., Nyssen, J., Rieke-Zapp, D., De Wulf, A. and Poesen, J., 2015. Detailed recording of gully morphology in 3D through image-based modelling. *Catena*, 127, pp.92-101. <https://doi.org/10.1016/j.catena.2014.12.016>
- Fried, M.J., Catania, G.A., Bartholomaeus, T.C., Duncan, D., Davis, M., Stearns, L.A., Nash, J., Shroyer, E. and Sutherland, D., 2015. Distributed subglacial discharge drives significant submarine melt at a Greenland tidewater glacier. *Geophysical Research Letters*, 42(21), pp.9328-9336. <https://doi.org/10.1002/2015GL065806>
- Fryer, J., Mitchell, H. and Chandler, J.H., 2007. *Applications of 3D measurement from images*. Caithness: Whittles Publishing.
- Fugazza, D., Scaioni, M., Corti, M., D'Agata, C., Azzoni, R.S., Cernuschi, M., Smiraglia, C. and Adele Diolaiuti, G., 2018. Combination of UAV and terrestrial photogrammetry to assess rapid glacier evolution and map glacier hazards. *Natural Hazards and Earth System Sciences*, 18, pp.1055-1071. <https://doi.org/10.5194/nhess-18-1055-2018>
- Fujita, K., Sakai, A., Nuimura, T., Yamaguchi, S. and Sharma, R.R., 2009. Recent changes in Imja Glacial Lake and its damming moraine in the Nepal Himalaya revealed by in situ surveys and multi-temporal ASTER imagery. *Environmental Research Letters*, 4(4), p.045205. <https://doi.org/10.1088/1748-9326/4/4/045205>
- Funk, M. and Röthlisberger, H., 1989. Forecasting the effects of a planned reservoir which will partially flood the tongue of Unteraargletscher in Switzerland. *Annals of Glaciology*, 13, pp.76-81. <https://doi.org/10.3189/S0260305500007679>
- Furukawa, Y. and Ponce, J., 2009. Accurate, dense, and robust multiview stereopsis. *IEEE Transactions on Pattern Analysis and Machine Intelligence*, 32(8), pp.1362-1376. <https://doi.org/10.1109/TPAMI.2009.161>
- Furukawa, Y., Curless, B., Seitz, M. and Szeliski, R., 2010. Clustering view for multi-view stereo. *IEEE Conference on Computer Vision and Pattern Recognition*, pp.1434-1441.
- Fyfe, G.J., 1990. The effect of water depth on ice-proximal glaciolacustrine sedimentation: Salpausselkä I, southern Finland. *Boreas*, 19(2), pp.147-164. <https://doi.org/10.1111/j.1502-3885.1990.tb00576.x>
- Gardner, A.S. and 15 others., 2013. A reconciled estimate of glacier contributions to sea level rise: 2003 to 2009. *Science*, 340(6134), pp.852-857. <https://doi.org/10.1126/science.1234532>
- Gillins, D.T., Kerr, D. and Weaver, B., 2019. Evaluation of the online positioning user service for processing static GPS surveys: OPUS-Projects, OPUS-S, OPUS-Net, and OPUS-RS. *Journal of Surveying Engineering*, 145(3), pp.05019002. [https://doi.org/10.1061/\(ASCE\)SU.1943-5428.0000280](https://doi.org/10.1061/(ASCE)SU.1943-5428.0000280)

List of References

- Gindraux, S., Boesch, R. and Farinotti, D., 2017. Accuracy assessment of digital surface models from unmanned aerial vehicles' imagery on glaciers. *Remote Sensing*, 9(2), pp.1-15.
<https://doi.org/10.3390/rs9020186>
- Gjermundsen, E.F., Mathieu, R., Kääb, A., Chinn, T., Fitzharris, B. and Hagen, J.O., 2011. Assessment of multispectral glacier mapping methods and derivation of glacier area changes, 1978–2002, in the central Southern Alps, New Zealand, from ASTER satellite data, field survey and existing inventory data. *Journal of Glaciology*, 57(204), pp.667-683. <https://doi.org/10.3189/002214311797409749>
- Glen, J.W., 1955. The creep of polycrystalline ice. *Proceedings of the Royal Society of London. Series A. Mathematical and Physical Sciences*, 228(1175), pp.519-538.
<https://doi.org/10.1098/rspa.1955.0066>
- Gomez, R., Arigony-Neto, J., De Santis, A., Vijay, S., Jaña, R. and Rivera, A., 2019. Ice dynamics of union glacier from SAR offset tracking. *Global and Planetary Change*, 174, pp.1-15.
<https://doi.org/10.1016/j.gloplacha.2018.12.012>
- Gómez-Gutiérrez, Á., Schnabel, S., Berenguer-Sempere, F., Lavado-Contador, F. and Rubio-Delgado, J., 2014. Using 3D photo-reconstruction methods to estimate gully headcut erosion. *Catena*, 120, pp.91-101. <https://doi.org/10.1016/j.catena.2014.04.004>
- Gong, Y., Zwinger, T., Åström, J., Altena, B., Schellenberger, T., Gladstone, R. and Moore, J.C., 2018. Simulating the roles of crevasse routing of surface water and basal friction on the surge evolution of Basin 3, Austfonna ice cap. *The Cryosphere*, 12(5), pp.1563-1577. <https://doi.org/10.5194/tc-12-1563-2018>
- Gray, A.L., Mattar, K.E., Vachon, P.W., Bindshadler, R., Jezek, K.C., Forster, R. and Crawford, J.P., 1998. InSAR results from the RADARSAT Antarctic Mapping Mission data: Estimation of glacier motion using a simple registration procedure. In *IGARSS'98. Sensing and Managing the Environment. 1998 IEEE International Geoscience and Remote Sensing. Symposium Proceedings*, 3, pp.1638-1640. IEEE. <https://doi.org/10.1109/IGARSS.1998.691662>
- Groos, A.R., Bertschinger, T.J., Kummer, C.M., Erlwein, S., Munz, L. and Philipp, A., 2019. The potential of low-cost UAVs and open-source photogrammetry software for high-resolution monitoring of Alpine glaciers: A case study from the Kanderfirn (Swiss Alps). *Geosciences*, 9(8), p.356.
<https://doi.org/10.3390/geosciences9080356>
- Guðmundsson, S., Björnsson, H. and Pálsson, F., 2017. Changes of Breiðamerkurjökull glacier, SE-Iceland, from its late nineteenth century maximum to the present. *Geografiska Annaler: Series A, Physical Geography*, 99(4), pp.338-352. <https://doi.org/10.1080/04353676.2017.1355216>
- Guðmundsson, S., Björnsson, H., Pálsson, F., Magnússon, E., Sæmundsson, Þ. and Jóhannesson, T., 2019. Terminus lakes on the south side of Vatnajökull ice cap, SE-Iceland. *Jökull*, 69, pp.1-34.
- Haeberli, W., Buetler, M., Huggel, C., Friedli, T.L., Schaub, Y. and Schleiss, A.J., 2016. New lakes in deglaciating high-mountain regions—opportunities and risks. *Climatic Change*, 139(2), pp.201-214.
<https://doi.org/10.1007/s10584-016-1771-5>
- Hall, K.W., Gagliardi, P. and Lawton, D.C., 2010. GPS accuracy part 2: RTK float versus RTK fixed. [online]. *CRWES Research Report*, 22, pp.1-8. Available at:
<https://www.crewes.org/Documents/ResearchReports/2010/CRR201029.pdf>
- Hannesdóttir, H., Björnsson, H., Pálsson, F., Aðalgeirsdóttir, G. and Guðmundsson, S., 2015. Changes in the southeast Vatnajökull ice cap, Iceland, between~ 1890 and 2010. *The Cryosphere*, 9(2), pp.565-585. <https://doi.org/10.5194/tc-9-565-2015>
- Hanson, B. and Hooke, R.L., 2000. Glacier calving: a numerical model of forces in the calving-speed/water-depth relation. *Journal of Glaciology*, 46(153), pp.188-196.
<https://doi.org/10.3189/172756500781832792>

- Hanson, B. and Hooke, R.L.B., 2003. Buckling rate and overhang development at a calving face. *Journal of Glaciology*, 49(167), pp.577-586. <https://doi.org/10.3189/172756503781830476>
- Hardin, P.J. and Hardin, T.J., 2010. Small-scale remotely piloted vehicles in environmental research. *Geography Compass*, 4(9), pp.1297-1311. <https://doi.org/10.1111/j.1749-8198.2010.00381.x>
- Haresign, E.C., 2004. Glacio-limnological interactions at lake-calving glaciers. (PhD thesis, University of St Andrews.)
- Haresign, E. and Warren, C.R., 2005. Melt rates at calving termini: a study at Glaciar León, Chilean Patagonia. *Geological Society, London, Special Publications*, 242(1), pp.99-109. <https://doi.org/10.1144/GSL.SP.2005.242.01.09>
- Harper, J.T., Humphrey, N.F., Pfeffer, W.T. and Lazar, B., 2007. Two modes of accelerated glacier sliding related to water. *Geophysical Research Letters*, 34(12). <https://doi.org/10.1029/2007GL030233>
- Harper, J.T., Bradford, J.H., Humphrey, N.F. and Meierbachtol, T.W., 2010. Vertical extension of the subglacial drainage system into basal crevasses. *Nature*, 467(7315), pp.579-582. <https://doi.org/10.1038/nature09398>
- Harrison, W.D., Echelmeyer, K.A., Cosgrove, D.M. and Raymond, C.F., 1992. The determination of glacier speed by time-lapse photography under unfavorable conditions. *Journal of Glaciology*, 38(129), pp.257-265. <https://doi.org/10.3189/S002214300000366X>
- Hart, J.K., Rose, K.C., Waller, R.I., Vaughan-Hirsch, D. and Martinez, K., 2011. Assessing the catastrophic break-up of Briksdalsbreen, Norway, associated with rapid climate change. *Journal of the Geological Society*, 168(3), pp.673-688. <https://doi.org/10.1144/0016-76492010-024>
- Hart, J.K., Rose, K.C., Clayton, A. and Martinez, K., 2015. Englacial and subglacial water flow at Skálafellsjökull, Iceland derived from ground penetrating radar, in situ Glacswab probe and borehole water level measurements. *Earth Surface Processes and Landforms*, 40(15), pp.2071-2083. <https://doi.org/10.1002/esp.3783>
- Hart, J.K., Martinez, K., Basford, P.J., Clayton, A.I., Bragg, G.M., Ward, T. and Young, D.S., 2019a. Surface melt-driven seasonal behaviour (englacial and subglacial) from a soft-bedded temperate glacier recorded by in situ wireless probes. *Earth Surface Processes and Landforms*, 44(9), pp.1769-1782. <https://doi.org/10.1002/esp.4611>
- Hart, J.K., Martinez, K., Basford, P.J., Clayton, A.I., Robson, B.A. and Young, D.S., 2019b. Surface melt driven summer diurnal and winter multi-day stick-slip motion and till sedimentology. *Nature Communications*, 10(1), pp.1-11. <https://doi.org/10.1038/s41467-019-09547-6>
- Haug, T., Kääb, A. and Skvarca, P., 2010. Monitoring ice shelf velocities from repeat MODIS and Landsat data-a method study on the Larsen C ice shelf, Antarctic Peninsula, and 10 other ice shelves around Antarctica. *The Cryosphere*, 4(2), pp.161-178. <https://doi.org/10.5194/tc-4-161-2010>
- Heid, T. and Kääb, A., 2012a. Evaluation of existing image matching methods for deriving glacier surface displacements globally from optical satellite imagery. *Remote Sensing of Environment*, 118, pp.339-355. <https://doi.org/10.1016/j.rse.2011.11.024>
- Heid, T. and Kääb, A., 2012b. Repeat optical satellite images reveal widespread and long term decrease in land-terminating glacier speeds. *The Cryosphere*, 6(2), pp.467-478. <https://doi.org/10.5194/tc-6-467-2012>
- Heng, B.C.P., Chandler, J.H. and Armstrong, A., 2010. Applying close range digital photogrammetry in soil erosion studies. *The Photogrammetric Record*, 25(131), pp.240-265. <https://doi.org/10.1111/j.1477-9730.2010.00584.x>

List of References

- Herman, F., Anderson, B. and Leprince, S., 2011. Mountain glacier velocity variation during a retreat/advance cycle quantified using sub-pixel analysis of ASTER images. *Journal of Glaciology*, 57(202), pp.197-207. <https://doi.org/10.3189/002214311796405942>
- Hodson, A., Anesio, A.M., Ng, F., Watson, R., Quirk, J., Irvine-Fynn, T., Dye, A., Clark, C., McCloy, P., Kohler, J. and Sattler, B., 2007. A glacier respire: Quantifying the distribution and respiration CO₂ flux of cryoconite across an entire Arctic supraglacial ecosystem. *Journal of Geophysical Research: Biogeosciences*, 112(G4). <https://doi.org/10.1029/2007JG000452>
- Hoffman, M.J., Catania, G.A., Neumann, T.A., Andrews, L.C. and Rumrill, J.A., 2011. Links between acceleration, melting, and supraglacial lake drainage of the western Greenland Ice Sheet. *Journal of Geophysical Research: Earth Surface*, 116(F4). <https://doi.org/10.1029/2010JF001934>
- Hoffman, M.J., Andrews, L.C., Price, S.F., Catania, G.A., Neumann, T.A., Lüthi, M.P., Gulley, J., Ryser, C., Hawley, R.L. and Morris, B., 2016. Greenland subglacial drainage evolution regulated by weakly connected regions of the bed. *Nature communications*, 7(1), pp.1-12. <https://doi.org/10.1038/ncomms13903>
- Hooke, R.L., 1981. Flow law for polycrystalline ice in glaciers: comparison of theoretical predictions, laboratory data, and field measurements. *Reviews of Geophysics*, 19(4), pp.664-672. <https://doi.org/10.1029/RG019i004p00664>
- Hooke, R.L., Brzozowski, J. and Bronge, C., 1983. Seasonal variations in surface velocity, Storglaciären, Sweden. *Geografiska Annaler: Series A, Physical Geography*, 65(3-4), pp.263-277. <https://doi.org/10.1080/04353676.1983.11880091>
- Hooke, R.L., 1989. Englacial and subglacial hydrology: a qualitative review. *Arctic and Alpine Research*, 21(3), pp.221-233. <https://doi.org/10.1080/00040851.1989.12002734>
- Hooke, R.L., Calla, P., Holmlund, P., Nilsson, M. and Stroeve, A., 1989a. A 3 year record of seasonal variations in surface velocity, Storglaciären, Sweden. *Journal of Glaciology*, 35(120), pp.235-247. <https://doi.org/10.3189/S0022143000004561>
- Hooke, R.L., Laumann, T. and Kennett, M.I., 1989b. Austdalsbreen, Norway: Expected reaction to a 40 m increase in water level in the lake into which the glacier calves. *Cold Regions Science and Technology*, 17(2), pp.113-126. [https://doi.org/10.1016/S0165-232X\(89\)80002-3](https://doi.org/10.1016/S0165-232X(89)80002-3)
- Hooke, R.L., Laumann, T. and Kohler, J., 1990. Subglacial water pressures and the shape of subglacial conduits. *Journal of Glaciology*, 36(122), pp.67-71. <https://doi.org/10.3189/S0022143000005566>
- How, P., Benn, D.I., Hulton, N.R., Hubbard, B., Luckman, A., Sevestre, H., van Pelt, W.J., Lindbäck, K., Kohler, J. and Boot, W., 2017. Rapidly changing subglacial hydrological pathways at a tidewater glacier revealed through simultaneous observations of water pressure, supraglacial lakes, meltwater plumes and surface velocities. *The Cryosphere*, 11(6), pp.2691-2710. <https://doi.org/10.5194/tc-11-2691-2017>
- Howat, I.M., Joughin, I., Tulaczyk, S. and Gogineni, S., 2005. Rapid retreat and acceleration of Helheim Glacier, east Greenland. *Geophysical Research Letters*, 32(22). <https://doi.org/10.1029/2005GL024737>
- Howat, I.M., Joughin, I. and Scambos, T.A., 2007. Rapid changes in ice discharge from Greenland outlet glaciers. *Science*, 315(5818), pp.1559-1561. <https://doi.org/10.1126/science.1138478>
- Howat, I.M., Tulaczyk, S., Waddington, E. and Björnsson, H., 2008a. Dynamic controls on glacier basal motion inferred from surface ice motion. *Journal of Geophysical Research: Earth Surface*, 113(F3). <https://doi.org/10.1029/2007JF000925>
- Howat, I.M., Joughin, I., Fahnestock, M., Smith, B.E. and Scambos, T.A., 2008b. Synchronous retreat and acceleration of southeast Greenland outlet glaciers 2000–06: Ice dynamics and coupling to

- climate. *Journal of Glaciology*, 54(187), pp.646-660.
<https://doi.org/10.3189/002214308786570908>
- Howat, I.M., Box, J.E., Ahn, Y., Herrington, A. and McFadden, E.M., 2010. Seasonal variability in the dynamics of marine-terminating outlet glaciers in Greenland. *Journal of Glaciology*, 56(198), pp.601-613. <https://doi.org/10.3189/002214310793146232>
- Howat, I.M. and Eddy, A., 2011. Multi-decadal retreat of Greenland's marine-terminating glaciers. *Journal of Glaciology*, 57(203), pp.389-396.
<https://doi.org/10.3189/002214311796905631>
- Huang, L. and Li, Z., 2011. Comparison of SAR and optical data in deriving glacier velocity with feature tracking. *International Journal of Remote Sensing*, 32(10), pp.2681-2698.
<https://doi.org/10.1080/01431161003720395>
- Hubbard, B.P., Sharp, M.J., Willis, I.C., Nielsen, M. and Smart, C.C., 1995. Borehole water-level variations and the structure of the subglacial hydrological system of Haut Glacier d'Arolla, Valais, Switzerland. *Journal of Glaciology*, 41(139), pp.572-583.
<https://doi.org/10.3189/S0022143000034894>
- Hubbard, B. and Nienow, P., 1997. Alpine subglacial hydrology. *Quaternary Science Reviews*, 16(9), pp.939-955. [https://doi.org/10.1016/S0277-3791\(97\)00031-0](https://doi.org/10.1016/S0277-3791(97)00031-0)
- Hubbard, B. and Glasser, N.F., 2005. *Field Techniques in Glaciology and Glacial Geomorphology*. Chichester: John Wiley & Sons.
- Hughes, T., 1998. *Ice Sheets*. Oxford: Oxford University Press.
- Hughes, T., 2002. Calving bays. *Quaternary Science Reviews*, 21(1-3), pp.267-282.
[https://doi.org/10.1016/S0277-3791\(01\)00092-0](https://doi.org/10.1016/S0277-3791(01)00092-0)
- Huss, M. and Hock, R., 2015. A new model for global glacier change and sea-level rise. *Frontiers in Earth Science*, 3, p.54.. <https://doi.org/10.3389/feart.2015.00054>
- Huss, M. and Hock, R., 2018. Global-scale hydrological response to future glacier mass loss. *Nature Climate Change*, 8(2), pp.135-140. <https://doi.org/10.1038/s41558-017-0049-x>
- Hutter, K., 2017. *Theoretical Glaciology: Material science of ice and the mechanics of glaciers and ice sheets* (Vol. 1). Springer.
- Iken, A., 1981. The effect of the subglacial water pressure on the sliding velocity of a glacier in an idealized numerical model. *Journal of Glaciology*, 27(97), pp.407-421.
<https://doi.org/10.3189/S0022143000011448>
- Iken, A., Röthlisberger, H., Flotron, A. and Haeberli, W., 1983. The uplift of Unteraargletscher at the beginning of the melt season—a consequence of water storage at the bed? *Journal of Glaciology*, 29(101), pp.28-47. <https://doi.org/10.3189/S0022143000005128>
- Iken, A. and Bindshadler, R.A., 1986. Combined measurements of subglacial water pressure and surface velocity of Findelengletscher, Switzerland: conclusions about drainage system and sliding mechanism. *Journal of Glaciology*, 32(110), pp.101-119.
<https://doi.org/10.3189/S0022143000006936>
- Iken, A. and Truffer, M., 1997. The relationship between subglacial water pressure and velocity of Findelengletscher, Switzerland, during its advance and retreat. *Journal of Glaciology*, 43(144), pp.328-338. <https://doi.org/10.3189/S00221430000032826>
- IMBIE., 2018. Mass balance of the Antarctic Ice Sheet from 1992 to 2017. *Nature*, 558, pp.219-222.
<https://doi.org/10.1038/s41586-018-0179-y>
- Immerzeel, W.W., Kraaijenbrink, P.D.A., Shea, J.M., Shrestha, A.B., Pellicciotti, F., Bierkens, M.F.P. and De Jong, S.M., 2014. High-resolution monitoring of Himalayan glacier dynamics using unmanned

List of References

- aerial vehicles. *Remote Sensing of Environment*, 150, pp.93-103.
<https://doi.org/10.1016/j.rse.2014.04.025>
- Irvine-Fynn, T.D., Sanz-Ablanedo, E., Rutter, N., Smith, M.W. and Chandler, J.H., 2014. Measuring glacier surface roughness using plot-scale, close-range digital photogrammetry. *Journal of Glaciology*, 60(223), pp.957-969. <https://doi.org/10.3189/2014JoG14J032>
- Iverson, N.R., 1990. Laboratory simulations of glacial abrasion: comparison with theory. *Journal of Glaciology*, 36(124), pp.304-314. <https://doi.org/10.3189/002214390793701264>
- Iverson, N.R., Hanson, B., Hooke, R.L. and Jansson, P., 1995. Flow mechanism of glaciers on soft beds. *Science*, 267(5194), pp.80-81. <https://doi.org/10.1126/science.267.5194.80>
- Iverson, N.R., 1999. Coupling between a glacier and a soft bed: II Model results. *Journal of Glaciology*, 45(149), pp.41-53. <https://doi.org/10.3189/S0022143000003026>
- Iverson, N.R., Baker, R.W., Hooke, R.L., Hanson, B. and Jansson, P., 1999. Coupling between a glacier and a soft bed: I. A relation between effective pressure and local shear stress determined from till elasticity. *Journal of Glaciology*, 45(149), pp.31-40. <https://doi.org/10.3189/S0022143000003014>
- Iverson, N.R., 2010. Shear resistance and continuity of subglacial till: hydrology rules. *Journal of Glaciology*, 56(200), pp.1104-1114. <https://doi.org/10.3189/002214311796406220>
- James, M.R. and Robson, S., 2012. Straightforward reconstruction of 3D surfaces and topography with a camera: Accuracy and geoscience application. *Journal of Geophysical Research: Earth Surface*, 117(F3). <https://doi.org/10.1029/2011JF002289>
- James, M.R. and Robson, S., 2014. Mitigating systematic error in topographic models derived from UAV and ground-based image networks. *Earth Surface Processes and Landforms*, 39(10), pp.1413-1420. <https://doi.org/10.1002/esp.3609>
- James, M.R., Robson, S. and Smith, M.W., 2017. 3-D uncertainty-based topographic change detection with structure-from-motion photogrammetry: precision maps for ground control and directly georeferenced surveys. *Earth Surface Processes and Landforms*, 42(12), pp.1769-1788.
<https://doi.org/10.1002/esp.4125>
- James, T.D., Murray, T., Selmes, N., Scharrer, K. and O'Leary, M., 2014. Buoyant flexure and basal crevassing in dynamic mass loss at Helheim Glacier. *Nature Geoscience*, 7(8), pp.593-596.
<https://doi.org/10.1038/ngeo2204>
- Jansson, P., 1995. Water pressure and basal sliding on Storglaciären, northern Sweden. *Journal of Glaciology*, 41(138), pp.232-240. <https://doi.org/10.3189/S0022143000016130>
- Javernick, L., Brasington, J. and Caruso, B., 2014. Modelling the topography of shallow braided rivers using Structure-from-Motion photogrammetry. *Geomorphology*, 213, pp.166-182.
<https://doi.org/10.1016/j.geomorph.2014.01.006>
- Jiskoot H., 2011. Dynamics of Glaciers. In: Singh V.P., Singh P. and Haritashya, U.K., (eds). *Encyclopaedia of Snow, Ice and Glaciers* (pp.245-257). Encyclopaedia of Earth Sciences Series. Dordrecht: Springer. https://doi.org/10.1007/978-90-481-2642-2_127
- Jóhannesson, T., Pálmason, B., Hjartarson, Á., Jarosch, A.H., Magnússon, E., Belart, J.M. and Gudmundsson, M.T., 2020. Non-surface mass balance of glaciers in Iceland. *Journal of Glaciology*, 66(258), pp.685-697. <https://doi.org/10.1017/jog.2020.37>
- Jones, C., Ryan, J., Holt, T. and Hubbard, A., 2018. Structural glaciology of isunguata sermia, West Greenland. *Journal of Maps*, 14(2), pp.517-527. <https://doi.org/10.1080/17445647.2018.1507952>
- Jones, P.D., Lister, D.H., Osborn, T.J., Harpham, C., Salmon, M. and Morice, C.P., 2012. Hemispheric and large-scale land-surface air temperature variations: An extensive revision and an update to 2010. *Journal of Geophysical Research: Atmospheres*, 117(D5).
<https://doi.org/10.1029/2011JD017139>

- Joughin, I., Howat, I., Alley, R.B., Ekstrom, G., Fahnestock, M., Moon, T., Nettles, M., Truffer, M. and Tsai, V.C., 2008a. Ice-front variation and tidewater behaviour on Helheim and Kangerdlugssuaq Glaciers, Greenland. *Journal of Geophysical Research: Earth Surface*, 113(F1). <https://doi.org/10.1029/2007JF000837>
- Joughin, I., Das, S.B., King, M.A., Smith, B.E., Howat, I.M. and Moon, T., 2008b. Seasonal speedup along the western flank of the Greenland Ice Sheet. *Science*, 320(5877), pp.781-783. <https://doi.org/10.1126/science.1153288>
- Joughin, I., Howat, I.M., Fahnestock, M., Smith, B., Krabill, W., Alley, R.B., Stern, H. and Truffer, M., 2008c. Continued evolution of Jakobshavn Isbrae following its rapid speedup. *Journal of Geophysical Research: Earth Surface*, 113(F4). <https://doi.org/10.1029/2008JF001023>
- Joughin, I., Smith, B.E., Howat, I.M., Floricioiu, D., Alley, R.B., Truffer, M. and Fahnestock, M., 2012. Seasonal to decadal scale variations in the surface velocity of Jakobshavn Isbrae, Greenland: Observation and model-based analysis. *Journal of Geophysical Research: Earth Surface*, 117(F2). <https://doi.org/10.1029/2011JF002110>
- Joughin, I., Smith, B.E. and Medley, B., 2014. Marine ice sheet collapse potentially under way for the Thwaites Glacier Basin, West Antarctica. *Science*, 344(6185), pp.735-738. <https://doi.org/10.1126/science.1249055>
- Joughin, I., Smith, B.E. and Howat, I., 2018. Greenland Ice Mapping Project: Ice Flow Velocity Variation at sub-monthly to decadal time scales. *The Cryosphere*, 12(7), pp.2211-2227. <https://doi.org/10.5194/tc-12-2211-2018>
- Jouvet, G., Weidmann, Y., Seguinot, J., Funk, M., Abe, T., Sakakibara, D., Seddik, H. and Sugiyama, S., 2017. Initiation of a major calving event on the Bowdoin Glacier captured by UAV photogrammetry. *The Cryosphere*, 11(2), pp.911-921. <https://doi.org/10.5194/tc-11-911-2017>
- Jouvet, G., Weidmann, Y., van Dongen, E., Luethi, M., Vieli, A. and Ryan, J., 2019. High-endurance UAV for monitoring calving glaciers: Application to the Inglefield Bredning and Equip Sermia, Greenland. *Frontiers in Earth Science*, 7, pp.1-15. <https://doi.org/10.3389/feart.2019.00206>
- Jouvet, G., Dongen, E.V., Lüthi, M.P. and Vieli, A., 2020. In situ measurements of the ice flow motion at Equip Sermia Glacier using a remotely controlled unmanned aerial vehicle (UAV). *Geoscientific Instrumentation, Methods and Data Systems*, 9(1), pp.1-10. <https://doi.org/10.5194/gi-9-1-2020>
- Kääb, A. and Funk, M., 1999. Modelling mass balance using photogrammetric and geophysical data: a pilot study at Griesgletscher, Swiss Alps. *Journal of Glaciology*, 45(151), pp.575-583. <https://doi.org/10.3189/S00222143000001453>
- Kääb, A. and Vollmer, M., 2000. Surface geometry, thickness changes and flow fields on creeping mountain permafrost: Automatic extraction by digital image analysis. *Permafrost and Periglacial Processes*, 11(4), pp.315-326. [https://doi.org/10.1002/1099-1530\(200012\)11:4%3C315::AID-PPP365%3E3.0.CO;2-J](https://doi.org/10.1002/1099-1530(200012)11:4%3C315::AID-PPP365%3E3.0.CO;2-J)
- Kääb, A., 2002. Monitoring high-mountain terrain deformation from repeated air-and spaceborne optical data: Examples using digital aerial imagery and ASTER data. *ISPRS Journal of Photogrammetry and Remote Sensing*, 57(1-2), pp.39-52. [https://doi.org/10.1016/S0924-2716\(02\)00114-4](https://doi.org/10.1016/S0924-2716(02)00114-4)
- Kääb, A., 2005. Combination of SRTM3 and repeat ASTER data for deriving alpine glacier flow velocities in the Bhutan Himalaya. *Remote Sensing of Environment*, 94(4), pp.463-474. <https://doi.org/10.1016/j.rse.2004.11.003>
- Kääb, A., Girod, L.M.R. and Berthling, I.T., 2014. Surface kinematics of periglacial sorted circles using structure-from-motion technology. *The Cryosphere*, 8, pp.1041-1056. <https://doi.org/10.5194/tc-8-1041-2014>

List of References

- Kääb, A., Winsvold, S.H., Altena, B., Nuth, C., Nagler, T. and Wuite, J., 2016. Glacier remote sensing using Sentinel-2. Part I: Radiometric and geometric performance, and application to ice velocity. *Remote Sensing*, 8(7), p.598. <https://doi.org/10.3390/rs8070598>
- Kamb, B., Raymond, C.F., Harrison, W.D., Engelhardt, H., Echelmeyer, K.A., Humphrey, N., Brugman, M.M. and Pfeffer, T., 1985. Glacier surge mechanism: 1982-1983 surge of Variegated Glacier, Alaska. *Science*, 227(4686), pp.469-479. <https://doi.org/10.1126/science.227.4686.469>
- Kamb, B., 1987. Glacier surge mechanism based on linked cavity configuration of the basal water conduit system. *Journal of Geophysical Research: Solid Earth*, 92(B9), pp.9083-9100. <https://doi.org/10.1029/JB092iB09p09083>
- Kamb, B., 1991. Rheological nonlinearity and flow instability in the deforming bed mechanism of ice stream motion. *Journal of Geophysical Research: Solid Earth*, 96(B10), pp.16585-16595. <https://doi.org/10.1029/91JB00946>
- Karaim, M., Elsheikh, M., Noureldin, A. and Rustamov, R.B., 2018. GNSS error sources, in Rustamov, R.B. and Hashimov, AM., (eds.) *Multifunctional Operation and Application of GPS*. London: IntechOpen, pp.69-85. <https://doi.org/10.5772/intechopen.75493>
- Karpilo, R.D.J., 2009. Glacier monitoring techniques. In: Young, R. and Norby, L., (eds). *Geological monitoring* (pp.141-162). Boulder: The Geological Society of America.
- Kaufmann, V. and Seier, G., 2016. Long-term monitoring of glacier change at Gössnitzkees (Austria) using terrestrial photogrammetry. *International Archives of the Photogrammetry, Remote Sensing & Spatial Information Sciences*, 41-B8, pp.495-502. https://ui.adsabs.harvard.edu/link_gateway/2016ISPAr41B8..495K/doi:10.5194/isprs-archives-XLI-B8-495-2016
- Kennett, M., Laumann, T. and Kjølmoen, B., 1997. Predicted response of the calving glacier Svartisheibreen, Norway, and outbursts from it, to future changes in climate and lake level. *Annals of Glaciology*, 24, pp.16-20. <https://doi.org/10.3189/S0260305500011861>
- Khan, S.A., Aschwanden, A., Bjørk, A.A., Wahr, J., Kjeldsen, K.K. and Kjaer, K.H., 2015. Greenland ice sheet mass balance: A review. *Reports on Progress in Physics*, 78(4), p.046801. <https://doi.org/10.1088/0034-4885/78/4/046801>
- Kim, Y. and Bang, H., 2019. Introduction to Kalman filter and its applications, in Govaers, F., (ed.) *Introduction and Implementations of the Kalman Filter*. London: IntechOpen, pp.7-22. <https://doi.org/10.5772/intechopen.80600>
- King, O., Dehecq, A., Quincey, D. and Carrivick, J., 2018. Contrasting geometric and dynamic evolution of lake and land-terminating glaciers in the central Himalaya. *Global and Planetary Change*, 167, pp.46-60. <https://doi.org/10.1016/j.gloplacha.2018.05.006>
- Kirkbride, M.P. and Warren, C.R., 1997. Calving processes at a grounded ice cliff. *Annals of Glaciology*, 24, pp.116-121. <https://doi.org/10.3189/S0260305500012039>
- Kjær, K.H., Larsen, E., van der Meer, J., Ingólfsson, Ó., Krüger, J., Benediktsson, Í.Ö., Knudsen, C.G. and Schomacker, A., 2006. Subglacial decoupling at the sediment/bedrock interface: a new mechanism for rapid flowing ice. *Quaternary Science Reviews*, 25(21-22), pp.2704-2712. <https://doi.org/10.1016/j.quascirev.2006.06.010>
- König, M., Winther, J.G. and Isaksson, E., 2001. Measuring snow and glacier ice properties from satellite. *Reviews of Geophysics*, 39(1), pp.1-27. <https://doi.org/10.1029/1999RG000076>
- Kraaijenbrink, P., Meijer, S.W., Shea, J.M., Pellicciotti, F., De Jong, S.M. and Immerzeel, W.W., 2016. Seasonal surface velocities of a Himalayan glacier derived by automated correlation of unmanned aerial vehicle imagery. *Annals of Glaciology*, 57(71), pp.103-113. <https://doi.org/10.3189/2016AoG71A072>

- Krimmel, R.M., 2001. Photogrammetric data set, 1957–2000, and bathymetric measurements for Columbia Glacier, Alaska. *Water Resources Investigations Report, No. 14089*.
- Lal, P., Vaka, D.S. and Rao, Y.S., 2018. Mapping Surface Flow Velocities of Siachen and Gangotri Glaciers Using Terrasar-X and SENTINEL-1A Data by Intensity Tracking. *ISPRS Annals of the Photogrammetry, Remote Sensing and Spatial Information Sciences*, 4, pp.325-329.
- Lane, S.N., Richards, K.S. and Chandler, J.H., 1993. Developments in photogrammetry: The geomorphological potential. *Progress in Physical Geography*, 17(3), pp.306-328.
<https://doi.org/10.1177%2F030913339301700302>
- Larsen, D.J., Miller, G.H., Geirsdóttir, Á. and Thordarson, T., 2011. A 3000-year varved record of glacier activity and climate change from the proglacial lake Hvítárvatn, Iceland. *Quaternary Science Reviews*, 30(19-20), pp.2715-2731. <https://doi.org/10.1016/j.quascirev.2011.05.026>
- Larsen, S.H., Khan, S.A., Ahlstrøm, A.P., Hvidberg, C.S., Willis, M.J. and Andersen, S.B., 2016. Increased mass loss and asynchronous behavior of marine-terminating outlet glaciers at Upernavik Isstrøm, NW Greenland. *Journal of Geophysical Research: Earth Surface*, 121(2), pp.241-256.
<https://doi.org/10.1002/2015JF003507>
- Laumann, T. and Wold, B., 1992. Reactions of a calving glacier to large changes in water level. *Annals of Glaciology*, 16, pp.158-162. <https://doi.org/10.3189/1992AoG16-1-158-162>
- Lea, J.M., Mair, D.W. and Rea, B.R., 2014. Evaluation of existing and new methods of tracking glacier terminus change. *Journal of Glaciology*, 60(220), pp.323-332.
<https://doi.org/10.3189/2014JoG13J061>
- Lemos, A., Shepherd, A., McMillan, M., Hogg, A.E., Hatton, E. and Joughin, I., 2018a. Ice velocity of Jakobshavn Isbræ, Petermann Glacier, Nioghalvfjærdsfjorden, and Zachariæ Isstrøm, 2015–2017, from Sentinel 1-a/b SAR imagery. *The Cryosphere*, 12(6), pp.2087-2097.
<https://doi.org/10.5194/tc-12-2087-2018>
- Lemos, A., Shepherd, A., McMillan, M. and Hogg, A.E., 2018b. Seasonal variations in the flow of land-terminating glaciers in Central-West Greenland using sentinel-1 imagery. *Remote Sensing*, 10(12), p.1878. <https://doi.org/10.3390/rs10121878>
- Leprince, S., Barbot, S., Ayoub, F. and Avouac, J.P., 2007. Automatic and precise orthorectification, coregistration, and subpixel correlation of satellite images, application to ground deformation measurements. *IEEE Transactions on Geoscience and Remote Sensing*, 45(6), pp.1529-1558.
<https://doi.org/10.1109/TGRS.2006.888937>
- Leprince, S., Berthier, E., Ayoub, F., Delacourt, C. and Avouac, J.P., 2008. Monitoring earth surface dynamics with optical imagery. *EOS, Transactions American Geophysical Union*, 89(1), pp.1-2.
<https://doi.org/10.1029/2008EO010001>
- Lingle, C.S., Post, A., Herzfeld, U.C., Molnia, B.F., Krimmel, R.M. and Roush, J.J., 1993. Bering Glacier surge and iceberg-calving mechanism at Vitus Lake, Alaska, USA. *Journal of Glaciology*, 39(133), pp.722-727. <https://doi.org/10.3189/S0022143000016683>
- Liu, Q., Mayer, C., Wang, X., Nie, Y., Wu, K., Wei, J. and Liu, S., 2020. Interannual flow dynamics driven by frontal retreat of a lake-terminating glacier in the Chinese Central Himalaya. *Earth and Planetary Science Letters*, 546, p.116450. <https://doi.org/10.1016/j.epsl.2020.116450>
- Lliboutry, L., 1968. General theory of subglacial cavitation and sliding of temperate glaciers. *Journal of Glaciology*, 7(49), pp.21-58. <https://doi.org/10.3189/S0022143000020396>
- Lliboutry, L., 1976. Physical processes in temperate glaciers. *Journal of Glaciology*, 16(74), pp.151-158.
<https://doi.org/10.3189/S002214300003149X>

List of References

- Lliboutry, L., 1979. Local friction laws for glaciers: a critical review and new openings. *Journal of Glaciology*, 23(89), pp.67-95. <https://doi.org/10.3189/S0022143000029750>
- Lliboutry, L., 1983. Modifications to the theory of intraglacial waterways for the case of subglacial ones. *Journal of Glaciology*, 29(102), pp.216-226. <https://doi.org/10.3189/S0022143000008273>
- Longuet-Higgins, H.C., 1981. A computer algorithm for reconstructing a scene from two projections. *Nature*, 293(5828), pp.133-135. <https://doi.org/10.1038/293133a0>
- Lourakis, M.I. and Argyros, A.A., 2009. SBA: A software package for generic sparse bundle adjustment. *ACM Transactions on Mathematical Software (TOMS)*, 36(1), pp.1-30. <https://doi.org/10.1145/1486525.1486527>
- Lowe, D.G., 1999. Object recognition from local scale-invariant features. In *Proceedings of the Seventh IEEE International Conference on Computer Vision*, 2, pp.1150-1157). IEEE. <https://doi.org/10.1109/ICCV.1999.790410>
- Lowe, D.G., 2004. Distinctive image features from scale-invariant keypoints. *International Journal of Computer Vision*, 60(2), pp.91-110. <https://doi.org/10.1023/B:VISI.0000029664.99615.94>
- Lucchitta, B.K. and Ferguson, H.M., 1986. Antarctica: Measuring glacier velocity from satellite images. *Science*, 234(4780), pp.1105-1108. <https://doi.org/10.1126/science.234.4780.1105>
- Lucieer, A., Jong, S.M.D. and Turner, D., 2014. Mapping landslide displacements using Structure from Motion (SfM) and image correlation of multi-temporal UAV photography. *Progress in Physical Geography*, 38(1), pp.97-116. <https://doi.org/10.1177%2F0309133313515293>
- Luckman, A., Quincey, D. and Bevan, S., 2007. The potential of satellite radar interferometry and feature tracking for monitoring flow rates of Himalayan glaciers. *Remote Sensing of Environment*, 111(2-3), pp.172-181. <https://doi.org/10.1016/j.rse.2007.05.019>
- Ma, Y., Tripathy, C.S. and Bassis, J.N., 2017. Bounds on the calving cliff height of marine terminating glaciers. *Geophysical Research Letters*, 44(3), pp.1369-1375. <https://doi.org/10.1002/2016GL071560>
- Magnússon, E., Pálsson, F., Björnsson, H. and Guðmundsson, S., 2012. Removing the ice cap of Öraefajökull central volcano, SE Iceland: mapping and interpretation of bedrock topography, ice volumes, subglacial troughs and implications for hazards assessments. *Jökull*, 62, pp.131-150.
- Malenovsky, Z., Rott, H., Cihlar, J., Schaepman, M.E., García-Santos, G., Fernandes, R. and Berger, M., 2012. Sentinels for science: Potential of Sentinel-1,-2, and-3 missions for scientific observations of ocean, cryosphere, and land. *Remote Sensing of Environment*, 120, pp.91-101. <https://doi.org/10.1016/j.rse.2011.09.026>
- Mallalieu, J., Carrivick, J.L., Quincey, D.J. and Smith, M.W., 2020. Calving seasonality associated with melt-undercutting and lake ice cover. *Geophysical Research Letters*, 47(8). <https://doi.org/10.1029/2019GL086561>
- Marta, S., 2019. Planet Imagery Product Specifications. <https://assets.planet.com/docs/combined-imagery-product-spec-final-august-2019.pdf>
- Marzeion, B., Cogley, J.G., Richter, K. and Parkes, D., 2014. Attribution of global glacier mass loss to anthropogenic and natural causes. *Science*, 345(6199), pp.919-921. <https://doi.org/10.1126/science.1254702>
- Marzeion, B., Kaser, G., Maussion, F. and Champollion, N., 2018. Limited influence of climate change mitigation on short-term glacier mass loss. *Nature Climate Change*, 8(4), pp.305-308. <https://doi.org/10.1038/s41558-018-0093-1>
- McNabb, R.W., Hock, R., O'Neel, S., Rasmussen, L.A., Ahn, Y., Braun, M., Conway, H., Herreid, S., Joughin, I., Pfeffer, W.T. and Smith, B.E., 2012. Using surface velocities to calculate ice thickness

- and bed topography: A case study at Columbia Glacier, Alaska, USA. *Journal of Glaciology*, 58(212), pp.1151-1164. <https://doi.org/10.3189/2012JoG11J249>
- Medrzycka, D., Benn, D.I., Box, J.E., Copland, L. and Balog, J., 2016. Calving behavior at Rink Isbræ, West Greenland, from time-lapse photos. *Arctic, Antarctic, and Alpine Research*, 48(2), pp.263-277. <https://doi.org/10.1657/AAAR0015-059>
- Meier, M.F. and Post, A., 1987. Fast tidewater glaciers. *Journal of Geophysical Research: Solid Earth*, 92(B9), pp.9051-9058. <https://doi.org/10.1029/JB092iB09p09051>
- Meier, M., Lundstrom, S., Stone, D., Kamb, B., Engelhardt, H., Humphrey, N., Dunlap, W.W., Fahnestock, M., Krimmel, R.M. and Walters, R., 1994. Mechanical and hydrologic basis for the rapid motion of a large tidewater glacier: 1. Observations. *Journal of Geophysical Research: Solid Earth*, 99(B8), pp.15219-15229. <https://doi.org/10.1029/94JB00237>
- Meier, M.F., Dyurgerov, M.B., Rick, U.K., O'neel, S., Pfeffer, W.T., Anderson, R.S., Anderson, S.P. and Glazovsky, A.F., 2007. Glaciers dominate eustatic sea-level rise in the 21st century. *Science*, 317(5841), pp.1064-1067. <https://doi.org/10.1126/science.1143906>
- Meierbachtol, T., Harper, J. and Humphrey, N., 2013. Basal drainage system response to increasing surface melt on the Greenland ice sheet. *Science*, 341(6147), pp.777-779. <https://doi.org/10.1126/science.1235905>
- Messerli, A. and Grinsted, A., 2015. Image georectification and feature tracking toolbox: ImGRAFT. *Geoscientific Instrumentation, Methods and Data Systems*, 4(1), pp.23-34. <https://doi.org/10.5194/gi-4-23-2015>
- Micheletti, N., Chandler, J.H. and Lane, S.N., 2015. Investigating the geomorphological potential of freely available and accessible structure-from-motion photogrammetry using a smartphone. *Earth Surface Processes and Landforms*, 40(4), pp.473-486. <https://doi.org/10.1002/esp.3648>
- Millan, R., Mouginot, J., Rabatel, A., Jeong, S., Cusicanqui, D., Derkacheva, A. and Chekki, M., 2019. Mapping surface flow velocity of glaciers at regional scale using a multiple sensors approach. *Remote Sensing*, 11(21), p.2498. <https://doi.org/10.3390/rs11212498>
- Minowa, M., Sugiyama, S., Sakakibara, D. and Skvarca, P., 2017. Seasonal variations in ice-front position controlled by frontal ablation at Glaciar Perito Moreno, the Southern Patagonia Icefield. *Frontiers in Earth Science*, 5, pp.1-15. <https://doi.org/10.3389/feart.2017.00001>
- Moon, T. and Joughin, I., 2008. Changes in ice front position on Greenland's outlet glaciers from 1992 to 2007. *Journal of Geophysical Research: Earth Surface*, 113(F2). <https://doi.org/10.1029/2007JF000927>
- Morel, J.M. and Yu, G., 2009. ASIFT: A new framework for fully affine invariant image comparison. *SIAM Journal on Imaging Sciences*, 2(2), pp.438-469. <https://doi.org/10.1137/080732730>
- Mottram, R.H. and Benn, D.I., 2009. Testing crevasse-depth models: A field study at Breiðamerkurjökull, Iceland. *Journal of Glaciology*, 55(192), pp.746-752. <https://doi.org/10.3189/002214309789470905>
- Motyka, R.J., O'Neel, S., Connor, C.L. and Echelmeyer, K.A., 2003. Twentieth century thinning of Mendenhall Glacier, Alaska, and its relationship to climate, lake calving, and glacier run-off. *Global and Planetary Change*, 35(1-2), pp.93-112. [https://doi.org/10.1016/S0921-8181\(02\)00138-8](https://doi.org/10.1016/S0921-8181(02)00138-8)
- Mouginot, J., Rignot, E., Scheuchl, B. and Millan, R., 2017. Comprehensive annual ice sheet velocity mapping using Landsat-8, Sentinel-1, and RADARSAT-2 data. *Remote Sensing*, 9(4), p.364. <https://doi.org/10.3390/rs9040364>
- Murray, T., Selmes, N., James, T.D., Edwards, S., Martin, I., O'Farrell, T., Aspey, R., Rutt, I., Nettles, M. and Baugé, T., 2015. Dynamics of glacier calving at the ungrounded margin of Helheim Glacier,

List of References

- southeast Greenland. *Journal of Geophysical Research: Earth Surface*, 120(6), pp.964-982.
<https://doi.org/10.1002/2015JF003531>
- Muto, A., Anandakrishnan, S., Alley, R.B., Horgan, H.J., Parizek, B.R., Koellner, S., Christianson, K. and Holschuh, N., 2019. Relating bed character and subglacial morphology using seismic data from Thwaites Glacier, West Antarctica. *Earth and Planetary Science Letters*, 507, pp.199-206.
<https://doi.org/10.1016/j.epsl.2018.12.008>
- Nagler, T., Rott, H., Hetzenecker, M., Wuite, J. and Potin, P., 2015. The Sentinel-1 mission: New opportunities for ice sheet observations. *Remote Sensing*, 7(7), pp.9371-9389.
<https://doi.org/10.3390/rs70709371>
- Naruse, R., Fukami, H. and Aniya, M., 1992. Short-term variations in flow velocity of Glaciar Soler, Patagonia, Chile. *Journal of Glaciology*, 38(128), pp.152-156.
<https://doi.org/10.3189/S0022143000009679>
- Naruse, R., Skvarca, P. and Takeuchi, Y., 1997. Thinning and retreat of Glaciar Upsala, and an estimate of annual ablation changes in southern Patagonia. *Annals of Glaciology*, 24, pp.38-42.
<https://doi.org/10.3189/S0260305500011903>
- Naruse, R. and Skvarca, P., 2000. Dynamic features of thinning and retreating Glaciar Upsala, a lacustrine calving glacier in southern Patagonia. *Arctic, Antarctic, and Alpine Research*, 32(4), pp.485-491.
<https://doi.org/10.1080/15230430.2000.12003393>
- NASA Earth Observatory (2007). *Grey Glacier, Chile*. [online] Earthobservatory.nasa.gov. Available at: <https://earthobservatory.nasa.gov/images/7802/grey-glacier-chile>. [Accessed: 25th March 2021].
- Nick, F.M., van der Kwast, J. and Oerlemans, J., 2007a. Simulation of the evolution of Breidamerkurjökull in the late Holocene. *Journal of Geophysical Research: Solid Earth*, 112(B1).
<https://doi.org/10.1029/2006JB004358>
- Nick, F.M., van der Veen, C.J. and Oerlemans, J., 2007b. Controls on advance of tidewater glaciers: Results from numerical modelling applied to Columbia Glacier. *Journal of Geophysical Research: Earth Surface*, 112(F3). <https://doi.org/10.1029/2006JF000551>
- Nick, F.M., Vieli, A., Howat, I.M. and Joughin, I., 2009. Large-scale changes in Greenland outlet glacier dynamics triggered at the terminus. *Nature Geoscience*, 2(2), pp.110-114.
<https://doi.org/10.1038/ngeo394>
- Nick, F.M., van der Veen, C.J., Vieli, A. and Benn, D.I., 2010. A physically based calving model applied to marine outlet glaciers and implications for the glacier dynamics. *Journal of Glaciology*, 56(199), pp.781-794. <https://doi.org/10.3189/002214310794457344>
- Nie, Y., Sheng, Y., Liu, Q., Liu, L., Liu, S., Zhang, Y. and Song, C., 2017. A regional-scale assessment of Himalayan glacial lake changes using satellite observations from 1990–2015. *Remote Sensing of Environment*, 189, pp.1-13. <https://doi.org/10.1016/j.rse.2016.11.008>
- Nienow, P., 1994. *Dye tracer investigations of glacier hydrological systems* (Doctoral dissertation, University of Cambridge). [Accessed from: <https://ethos.bl.uk/OrderDetails.do?uin=uk.bl.ethos.282820>]
- Nienow, P., Sharp, M. and Willis, I., 1998. Seasonal changes in the morphology of the subglacial drainage system, Haut Glacier d'Arolla, Switzerland. *Earth Surface Processes and Landforms: The Journal of the British Geomorphological Group*, 23(9), pp.825-843. [https://doi.org/10.1002/\(SICI\)1096-9837\(199809\)23:9%3C825::AID-ESP893%3E3.0.CO;2-2](https://doi.org/10.1002/(SICI)1096-9837(199809)23:9%3C825::AID-ESP893%3E3.0.CO;2-2)
- Nienow, P.W., Sole, A.J., Slater, D.A. and Cowton, T.R., 2017. Recent advances in our understanding of the role of meltwater in the Greenland Ice Sheet system. *Current Climate Change Reports*, 3(4), pp.330-344. <https://doi.org/10.1007/s40641-017-0083-9>

- Nye, J.F., 1952. The mechanics of glacier flow. *Journal of Glaciology*, 2(12), pp.82-93.
<https://doi.org/10.3189/S0022143000033967>
- Nye, J.F., 1957. The distribution of stress and velocity in glaciers and ice-sheets. *Proceedings of the Royal Society of London. Series A. Mathematical and Physical Sciences*, 239(1216), pp.113-133.
<https://doi.org/10.1098/rspa.1957.0026>
- Nye, J.F., 1973. Water at the bed of a glacier. 225–238 in Hydrology of Glaciers (Symposium at Cambridge, 1969). *International Association of Hydrological Sciences Publication*, (95).
- O'Neel, S., Echelmeyer, K.A. and Motyka, R.J., 2001. Short-term flow dynamics of a retreating tidewater glacier: LeConte Glacier, Alaska, USA. *Journal of Glaciology*, 47(159), pp.567-578,
<https://doi.org/10.3189/172756501781831855>
- O'Neel, S., Pfeffer, W.T., Krimmel, R. and Meier, M., 2005. Evolving force balance at Columbia Glacier, Alaska, during its rapid retreat. *Journal of Geophysical Research: Earth Surface*, 110(F3).
<https://doi.org/10.1029/2005JF000292>
- OPUS., 2020. OPUS: Online Positioning User Service. [online]. Available at:
<https://geodesy.noaa.gov/OPUS/about.jsp#FAQ>. [Accessed: 24th September 2021].
- Palmer, S., Shepherd, A., Nienow, P. and Joughin, I., 2011. Seasonal speedup of the Greenland Ice Sheet linked to routing of surface water. *Earth and Planetary Science Letters*, 302(3-4), pp.423-428.
<https://doi.org/10.1016/j.epsl.2010.12.037>
- Parizek, B.R. and Alley, R.B., 2004. Implications of increased Greenland surface melt under global-warming scenarios: ice-sheet simulations. *Quaternary Science Reviews*, 23(9-10), pp.1013-1027.
<https://doi.org/10.1016/j.quascirev.2003.12.024>
- Parkes, D. and Marzeion, B., 2018. Twentieth-century contribution to sea-level rise from uncharted glaciers. *Nature*, 563(7732), pp.551-554. <https://doi.org/10.1038/s41586-018-0687-9>
- Paul, F., Bolch, T., Kääb, A., Nagler, T., Nuth, C., Scharrer, K., Shepherd, A., Strozzi, T., Ticconi, F., Bhambri, R. and Berthier, E., 2015. The glaciers climate change initiative: Methods for creating glacier area, elevation change and velocity products. *Remote Sensing of Environment*, 162, pp.408-426. <https://doi.org/10.1016/j.rse.2013.07.043>
- Paul, F., Bolch, T., Briggs, K., Kääb, A., McMillan, M., McNabb, R., Nagler, T., Nuth, C., Rastner, P., Strozzi, T. and Wuite, J., 2017. Error sources and guidelines for quality assessment of glacier area, elevation change, and velocity products derived from satellite data in the Glaciers_cci project. *Remote Sensing of Environment*, 203, pp.256-275.
<https://doi.org/10.1016/j.rse.2017.08.038>
- Pattyn, F., 2002. Transient glacier response with a higher-order numerical ice-flow model. *Journal of Glaciology*, 48(162), pp.467-477. <https://doi.org/10.3189/172756502781831278>
- Pavelka, K., Šedina, J., Matoušková, E., Hlaváčová, I. and Korth, W., 2019. Examples of different techniques for glaciers motion monitoring using InSAR and RPAS. *European Journal of Remote Sensing*, 52(sup1), pp.219-232. <https://doi.org/10.1080/22797254.2018.1559001>
- Pelto, M.S. and Warren, C.R., 1991. Relationship between tidewater glacier calving velocity and water depth at the calving front. *Annals of Glaciology*, 15, pp.115-118.
<https://doi.org/10.3189/S0260305500009617>
- Perkins, A.J. and Brennand, T.A., 2015. Refining the pattern and style of Cordilleran Ice Sheet retreat: palaeogeography, evolution and implications of lateglacial ice-dammed lake systems on the southern Fraser Plateau, British Columbia, Canada. *Boreas*, 44(2), pp.319-342.
<https://doi.org/10.1111/bor.12100>

List of References

- Piermattei, L., Carturan, L. and Guarnieri, A., 2015. Use of terrestrial photogrammetry based on structure-from-motion for mass balance estimation of a small glacier in the Italian Alps. *Earth Surface Processes and Landforms*, 40(13), pp.1791-1802. <https://doi.org/10.1002/esp.3756>
- Pimentel, S. and Flowers, G.E., 2011. A numerical study of hydrologically driven glacier dynamics and subglacial flooding. *Proceedings of the Royal Society A: Mathematical, Physical and Engineering Sciences*, 467(2126), pp.537-558. <https://doi.org/10.1098/rspa.2010.0211>
- Planet Team., 2017. Planet Application Program Interface: In space for life on Earth. San Francisco, CA.
- Pollard, D., 1984. Some ice-age aspects of a calving ice-sheet model. In: Berger, A., Imbrie, J., Hays, J., Kukla, G. and Saltzman, B., (eds). *Milankovitch and climate* (pp. 541-564). Dordrecht: Springer.
- Pope, A., Rees, W.G., Fox, A.J. and Fleming, A., 2014. Open access data in polar and cryospheric remote sensing. *Remote Sensing*, 6(7), pp.6183-6220. <https://doi.org/10.3390/rs6076183>
- Pritchard, H.D., Arthern, R.J., Vaughan, D.G. and Edwards, L.A., 2009. Extensive dynamic thinning on the margins of the Greenland and Antarctic ice sheets. *Nature*, 461(7266), pp.971-975. <https://doi.org/10.1038/nature08471>
- Purdie, H.L., Brook, M.S. and Fuller, I.C., 2008. Seasonal variation in ablation and surface velocity on a temperate maritime glacier: Fox Glacier, New Zealand. *Arctic, Antarctic, and Alpine Research*, 40(1), pp.140-147. [https://doi.org/10.1657/1523-0430\(06-032\)\[PURDIE\]2.0.CO;2](https://doi.org/10.1657/1523-0430(06-032)[PURDIE]2.0.CO;2)
- Quincey, D.J. and Luckman, A., 2009. Progress in satellite remote sensing of ice sheets. *Progress in Physical Geography*, 33(4), pp.547-567. <https://doi.org/10.1177%2F0309133309346883>
- Quincey, D.J., Luckman, A. and Benn, D., 2009. Quantification of Everest region glacier velocities between 1992 and 2002, using satellite radar interferometry and feature tracking. *Journal of Glaciology*, 55(192), pp.596-606. <https://doi.org/10.3189/002214309789470987>
- Radić, V. and Hock, R., 2011. Regionally differentiated contribution of mountain glaciers and ice caps to future sea-level rise. *Nature Geoscience*, 4(2), pp.91-94. <https://doi.org/10.1038/ngeo1052>
- Raup, B., Racoviteanu, A., Khalsa, S.J.S., Helm, C., Armstrong, R. and Arnaud, Y., 2007. The GLIMS geospatial glacier database: A new tool for studying glacier change. *Global and Planetary Change*, 56(1-2), pp.101-110. <https://doi.org/10.1016/j.gloplacha.2006.07.018>
- Redpath, T.A.N., Sirguey, P., Fitzsimons, S.J. and Kääh, A., 2013. Accuracy assessment for mapping glacier flow velocity and detecting flow dynamics from ASTER satellite imagery: Tasman Glacier, New Zealand. *Remote Sensing of Environment*, 133, pp.90-101. <https://doi.org/10.1016/j.rse.2013.02.008>
- Reeh, N., 1968. On the calving of ice from floating glaciers and ice shelves. *Journal of Glaciology*, 7(50), pp.215-232. <https://doi.org/10.3189/S0022143000031014>
- Rieg, L., Klug, C., Nicholson, L. and Sailer, R., 2018. Pléiades Tri-Stereo Data for Glacier Investigations—Examples from the European Alps and the Khumbu Himal. *Remote Sensing*, 10(10), p.1563. <https://doi.org/10.3390/rs10101563>
- Rignot, E.J., Gogineni, S.P., Krabill, W.B. and Ekholm, S., 1997. North and northeast Greenland ice discharge from satellite radar interferometry. *Science*, 276(5314), pp.934-937. <https://doi.org/10.1126/science.276.5314.934>
- Rignot, E., Buscarlet, G., Csatho, B., Gogineni, S., Krabill, W. and Schmeltz, M., 2000. Mass balance of the northeast sector of the Greenland ice sheet: A remote-sensing perspective. *Journal of Glaciology*, 46(153), pp.265-273. <https://doi.org/10.3189/172756500781832972>
- Rignot, E., Rivera, A. and Casassa, G., 2003. Contribution of the Patagonia Icefields of South America to sea level rise. *Science*, 302(5644), pp.434-437. <https://doi.org/10.1126/science.1087393>

- Rignot, E., Jacobs, S., Mouginot, J. and Scheuchl, B., 2013. Ice-shelf melting around Antarctica. *Science*, 341(6143), pp.266-270. <https://doi.org/10.1126/science.1235798>
- Rippin, D.M., Pomfret, A. and King, N., 2015. High resolution mapping of supra-glacial drainage pathways reveals link between micro-channel drainage density, surface roughness and surface reflectance. *Earth Surface Processes and Landforms*, 40(10), pp.1279-1290. <https://doi.org/10.1002/esp.3719>
- Riveros, N.C., Euillades, L.D., Euillades, P.A., Moreiras, S.M. and Balbarani, S., 2013. Offset tracking procedure applied to high resolution SAR data on Viedma Glacier, Patagonian Andes, Argentina. *Advances in Geosciences*, 35, pp.7-13. <https://doi.org/10.5194/adgeo-35-7-2013>
- Robertson, C.M., Benn, D.I., Brook, M.S. and Holt, K.A., 2012. Subaqueous calving margin morphology at Mueller, Hooker and Tasman glaciers in Aoraki/Mount Cook National Park, New Zealand. *Journal of Glaciology*, 58(212), pp.1037-1046. <https://doi.org/10.3189/2012JoG12J048>
- Robson, B.A., Nuth, C., Nielsen, P.R., Girod, L., Hendrickx, M. and Dahl, S.O., 2018. Spatial variability in patterns of glacier change across the Manaslu Range, Central Himalaya. *Frontiers in Earth Science*, 6, p.12. <https://doi.org/10.3389/feart.2018.00012>
- Röhl, K., 2006. Thermo-erosional notch development at fresh-water-calving Tasman Glacier, New Zealand. *Journal of Glaciology*, 52(177), pp.203-213. <https://doi.org/10.3189/172756506781828773>
- Rolstad, C., Amlien, J., Hagen, J.O. and Lundén, B., 1997. Visible and near-infrared digital images for determination of ice velocities and surface elevation during a surge on Osbornegreen, a tidewater glacier in Svalbard. *Annals of Glaciology*, 24, pp.255-261. <https://doi.org/10.3189/S026030550001226X>
- Rossini, M., Di Mauro, B., Garzonio, R., Baccolo, G., Cavallini, G., Mattavelli, M., De Amicis, M. and Colombo, R., 2018. Rapid melting dynamics of an alpine glacier with repeated UAV photogrammetry. *Geomorphology*, 304, pp.159-172. <https://doi.org/10.1016/j.geomorph.2017.12.039>
- Rossmann, H.L., 2015. *Modelling subglacial water using Navier-Stokes flow* (Doctoral dissertation, University of Bremen).
- Röthlisberger, H., 1972. Water pressure in intra-and subglacial channels. *Journal of Glaciology*, 11(62), pp.177-203. <https://doi.org/10.3189/S0022143000022188>
- Ruiz, L., Berthier, E., Masiokas, M., Pitte, P. and Villalba, R., 2015. First surface velocity maps for glaciers of Monte Tronador, North Patagonian Andes, derived from sequential Pléiades satellite images. *Journal of Glaciology*, 61(229), pp.908-922. <https://doi.org/10.3189/2015JoG14J134>
- Ryan, J.C., Hubbard, A.L., Box, J.E., Todd, J., Christoffersen, P., Carr, J.R., Holt, T.O. and Snooke, N.A., 2015. UAV photogrammetry and structure from motion to assess calving dynamics at Store Glacier, a large outlet draining the Greenland ice sheet. *The Cryosphere*, 9, pp.1-11. <https://doi.org/10.5194/tc-9-1-2015>
- Ryan, J.C., Hubbard, A., Box, J.E., Brough, S., Cameron, K., Cook, J.M., Cooper, M., Doyle, S.H., Edwards, A., Holt, T., Irvine-Fynn, T., Jones, C., Pitcher, L.H., Rennermalm, A.K., Smith, L.C., Stibal, M., and Snooke, N., 2017. Derivation of high spatial resolution albedo from UAV digital imagery: Application over the Greenland Ice Sheet. *Frontiers in Earth Science*, 5(40), pp1-13. <https://doi.org/10.3389/feart.2017.00040>
- Ryan, J.C., Hubbard, A., Stibal, M., Irvine-Fynn, T.D., Cook, J., Smith, L.C., Cameron, K. and Box, J., 2018. Dark zone of the Greenland Ice Sheet controlled by distributed biologically-active impurities. *Nature Communications*, 9(1), pp.1-10. <https://doi.org/10.1038/s41467-018-03353-2>
- Ryser, C., Luethi, M.P., Andrews, L.C., Hoffman, M.J., Catania, G.A., Hawley, R.L., Neumann, T.A. and Kristensen, S.S., 2014. Sustained high basal motion of the Greenland ice sheet revealed by

List of References

- borehole deformation. *Journal of Glaciology*, 60(222), pp.647-660.
<https://doi.org/10.3189/2014JoG13J196>
- Sakai, A., Nishimura, K., Kadota, T. and Takeuchi, N., 2009. Onset of calving at supraglacial lakes on debris-covered glaciers of the Nepal Himalaya. *Journal of Glaciology*, 55(193), pp.909-917.
<https://doi.org/10.3189/002214309790152555>
- Sakakibara, D., Sugiyama, S., Sawagaki, T., Marinsek, S. and Skvarca, P., 2013. Rapid retreat, acceleration and thinning of Glaciar Upsala, Southern Patagonia Icefield, initiated in 2008. *Annals of Glaciology*, 54(63), pp.131-138. <https://doi.org/10.3189/2013AoG63A236>
- Sakakibara, D. and Sugiyama, S., 2014. Ice-front variations and speed changes of calving glaciers in the Southern Patagonia Icefield from 1984 to 2011. *Journal of Geophysical Research: Earth Surface*, 119(11), pp.2541-2554. <https://doi.org/10.1002/2014JF003148>
- Sakakibara, D. and Sugiyama, S., 2018. Ice front and flow speed variations of marine-terminating outlet glaciers along the coast of Prudhoe Land, northwestern Greenland. *Journal of glaciology*, 64(244), pp.300-310. <https://doi.org/10.1017/jog.2018.20>
- Sam, L., Bhardwaj, A., Singh, S. and Kumar, R., 2016. Remote sensing flow velocity of debris-covered glaciers using Landsat 8 data. *Progress in Physical Geography*, 40(2), pp.305-321.
<https://doi.org/10.1177%2F0309133315593894>
- Sánchez-Gómez, P. and Navarro, F.J., 2017. Glacier surface velocity retrieval using D-InSAR and offset tracking techniques applied to ascending and descending passes of Sentinel-1 data for southern Ellesmere ice caps, Canadian Arctic. *Remote Sensing*, 9(5), p.442.
<https://doi.org/10.3390/rs9050442>
- Sanz-Ablanedo, E., Chandler, J.H. and Wackrow, R., 2012. Parameterising internal camera geometry with focusing distance. *The Photogrammetric Record*, 27(138), pp.210-226.
<https://doi.org/10.1111/j.1477-9730.2012.00677.x>
- Sanz-Ablanedo, E., Chandler, J.H., Rodríguez-Pérez, J.R. and Ordóñez, C., 2018. Accuracy of unmanned aerial vehicle (UAV) and SfM photogrammetry survey as a function of the number and location of ground control points used. *Remote Sensing*, 10(10), pp.1-19.
<https://doi.org/10.3390/rs10101606>
- Scambos, T.A., Dutkiewicz, M.J., Wilson, J.C. and Bindschadler, R.A., 1992. Application of image cross-correlation to the measurement of glacier velocity using satellite image data. *Remote Sensing of Environment*, 42(3), pp.177-186. [https://doi.org/10.1016/0034-4257\(92\)90101-O](https://doi.org/10.1016/0034-4257(92)90101-O)
- Schellenberger, T., Dunse, T., Kääh, A., Kohler, J. and Reijmer, C., 2015. Surface speed and frontal ablation of Kronebreen and Kongsbreen, NW-Svalbard, from SAR offset tracking. *The Cryosphere Discussions*, 8, pp.6193-6233. <https://doi.org/10.5194/tcd-8-6193-2014>
- Scherler, D., Leprince, S. and Strecker, M.R., 2008. Glacier-surface velocities in alpine terrain from optical satellite imagery—Accuracy improvement and quality assessment. *Remote Sensing of Environment*, 112(10), pp.3806-3819. <https://doi.org/10.1016/j.rse.2008.05.018>
- Scherler, D., Bookhagen, B. and Strecker, M.R., 2011. Spatially variable response of Himalayan glaciers to climate change affected by debris cover. *Nature Geoscience*, 4(3), pp.156-159.
<https://doi.org/10.1038/ngeo1068>
- Schild, K.M., Renshaw, C.E., Benn, D.I., Luckman, A., Hawley, R.L., How, P., Trusel, L., Cottier, F.R., Pramanik, A. and Hulton, N.R.J., 2018. Glacier calving rates due to subglacial discharge, fjord circulation, and free convection. *Journal of Geophysical Research: Earth Surface*, 123(9), pp.2189-2204. <https://doi.org/10.1029/2017JF004520>

- Schneevoigt, N.J., Sund, M., Bogren, W., Kääb, A. and Weydahl, D.J., 2012. Glacier displacement on Comfortlessbreen, Svalbard, using 2-pass differential SAR interferometry (DInSAR) with a digital elevation model. *Polar Record*, 48(1), pp.17-25. <https://doi.org/10.1017/S0032247411000453>
- Schomacker, A., 2010. Expansion of ice-marginal lakes at the Vatnajökull ice cap, Iceland, from 1999 to 2009. *Geomorphology*, 119(3-4), pp.232-236. <https://doi.org/10.1016/j.geomorph.2010.03.022>
- Schoof, C., 2005. The effect of cavitation on glacier sliding. *Proceedings of the Royal Society A: Mathematical, Physical and Engineering Sciences*, 461(2055), pp.609-627. <https://doi.org/10.1098/rspa.2004.1350>
- Schoof, C., 2010. Ice-sheet acceleration driven by melt supply variability. *Nature*, 468(7325), pp.803-806. <https://doi.org/10.1038/nature09618>
- Schroeder, D.M., Blankenship, D.D. and Young, D.A., 2013. Evidence for a water system transition beneath Thwaites Glacier, West Antarctica. *Proceedings of the National Academy of Sciences*, 110(30), pp.12225-12228. <https://doi.org/10.1073/pnas.1302828110>
- Schweizer, J. and Iken, A., 1992. The role of bed separation and friction in sliding over an undeformable bed. *Journal of Glaciology*, 38(128), pp.77-92. <https://doi.org/10.3189/S0022143000009618>
- Seaberg, S.Z., Seaberg, J.Z., Hooke, R.L. and Wiberg, D.W., 1988. Character of the englacial and subglacial drainage system in the lower part of the ablation area of Storglaciären, Sweden, as revealed by dye-trace studies. *Journal of Glaciology*, 34(117), pp.217-227. <https://doi.org/10.3189/S0022143000032263>
- Serco Italia SPA. (2018) *Glacier Velocity with Sentinel-1 – Peterman Glacier, Greenland*. [Offset Tracking Tutorial, V.1.2]. Retrieved from: <https://rus-copernicus.eu/portal/the-rus-library/learn-by-yourself/>
- Shahbazi, M., Sohn, G., Théau, J. and Menard, P., 2015. Development and evaluation of a UAV-photogrammetry system for precise 3D environmental modelling. *Sensors*, 15(11), pp.27493-27524. <https://doi.org/10.3390/s151127493>
- Shannon, S.R., Payne, A.J., Bartholomew, I.D., van den Broeke, M.R., Edwards, T.L., Fettweis, X., Gagliardini, O., Gillet-Chaulet, F., Goelzer, H., Hoffman, M.J. and Huybrechts, P., 2013. Enhanced basal lubrication and the contribution of the Greenland ice sheet to future sea-level rise. *Proceedings of the National Academy of Sciences*, 110(35), pp.14156-14161. <https://doi.org/10.1073/pnas.1212647110>
- Shannon, S., Smith, R., Wiltshire, A., Payne, T., Huss, M., Betts, R., Caesar, J., Koutroulis, A., Jones, D. and Harrison, S., 2019. Global glacier volume projections under high-end climate change scenarios. *The Cryosphere*, 13, pp.325-350. <https://doi.org/10.5194/tc-13-325-2019>
- Shapero, D.R., Joughin, I.R., Poinar, K., Morlighem, M. and Gillet-Chaulet, F., 2016. Basal resistance for three of the largest Greenland outlet glaciers. *Journal of Geophysical Research: Earth Surface*, 121(1), pp.168-180. <https://doi.org/10.1002/2015JF003643>
- Shepherd, A., Hubbard, A., Nienow, P., King, M., McMillan, M. and Joughin, I., 2009. Greenland ice sheet motion coupled with daily melting in late summer. *Geophysical Research Letters*, 36(1). <https://doi.org/10.1029/2008GL035758>
- Shepherd, A., Ivins, E., Rignot, E., Smith, B., van Den Broeke, M., Velicogna, I., Whitehouse, P., Briggs, K., Joughin, I., Krinner, G. and Nowicki, S., 2018. Mass balance of the Antarctic Ice Sheet from 1992 to 2017. *Nature*, 558, pp.219-222. <https://doi.org/10.1038/s41586-018-0179-y>
- Shreve, R.L., 1972. Movement of water in glaciers. *Journal of Glaciology*, 11(62), pp.205-214. <https://doi.org/10.3189/S002214300002219X>

List of References

- Shreve, R.L., 1984. Glacier sliding at subfreezing temperatures. *Journal of Glaciology*, 30(106), pp.341-347. <https://doi.org/10.3189/S0022143000006195>
- Shugar, D.H., Burr, A., Haritashya, U.K., Kargel, J.S., Watson, C.S., Kennedy, M.C., Bevington, A.R., Betts, R.A., Harrison, S. and Strattman, K., 2020. Rapid worldwide growth of glacial lakes since 1990. *Nature Climate Change*, 10(10), pp.939-945. <https://doi.org/10.1038/s41558-020-0855-4>
- Sigurdsson, O., Jónsson, T. and Jóhannesson, T., 2007. Relation between glacier-termini variations and summer temperature in Iceland since 1930. *Annals of Glaciology*, 46, pp.170-176. <https://doi.org/10.3189/172756407782871611>
- Sikonia, W.G., 1982. Finite element glacier dynamics model applied to Columbia Glacier, Alaska (No. 1258-B). <https://doi.org/10.3133/pp1258B>
- Skvarca, P., De Angelis, H., Naruse, R., Warren, C.R. and Aniya, M., 2002. Calving rates in fresh water: New data from southern Patagonia. *Annals of Glaciology*, 34, pp.379-384. <https://doi.org/10.3189/172756402781817806>
- Śledź, S., Ewertowski, M. and Piekarczyk, J., 2021. Applications of unmanned aerial vehicle (UAV) surveys and Structure from Motion photogrammetry in glacial and periglacial geomorphology. *Geomorphology*, p.107620. <https://doi.org/10.1016/j.geomorph.2021.107620>
- Smith, M.W., Carrivick, J.L., Hooke, J. and Kirkby, M.J., 2014. Reconstructing flash flood magnitudes using 'Structure-from-Motion': A rapid assessment tool. *Journal of Hydrology*, 519, pp.1914-1927. <https://doi.org/10.1016/j.jhydrol.2014.09.078>
- Smith, M.W., Carrivick, J.L. and Quincey, D.J., 2016. Structure from motion photogrammetry in physical geography. *Progress in Physical Geography*, 40(2), pp.247-275. <https://doi.org/10.1177%2F0309133315615805>
- Snavely, K.N., 2008. *Scene reconstruction and visualization from internet photo collections* (PhD thesis, University of Washington).
- Sole, A.J., Mair, D.W.F., Nienow, P.W., Bartholomew, I.D., King, M.A., Burke, M.J. and Joughin, I., 2011. Seasonal speedup of a Greenland marine-terminating outlet glacier forced by surface melt-induced changes in subglacial hydrology. *Journal of Geophysical Research: Earth Surface*, 116(F3). <http://doi.org/10.1029/2010JF001948>
- Sole, A., Nienow, P., Bartholomew, I., Mair, D., Cowton, T., Tedstone, A. and King, M.A., 2013. Winter motion mediates dynamic response of the Greenland Ice Sheet to warmer summers. *Geophysical Research Letters*, 40(15), pp.3940-3944. <https://doi.org/10.1002/grl.50764>
- Spetsakis, M. and Aloimonos, J.Y., 1991. A multi-frame approach to visual motion perception. *International Journal of Computer Vision*, 6(3), pp.245-255. <https://doi.org/10.1007/BF00115698>
- Steiner, J.F., Kraaijenbrink, P.D., Jiduc, S.G. and Immerzeel, W.W., 2018. Brief communication: The Khurdopin glacier surge revisited—extreme flow velocities and formation of a dammed lake in 2017. *The Cryosphere*, 12(1), pp.95-101. <https://doi.org/10.5194/tc-12-95-2018>
- Stenborg, T., 1969. Studies of the internal drainage of glaciers. *Geografiska Annaler: Series A, Physical Geography*, 51(1-2), pp.13-41. <https://doi.org/10.1080/04353676.1969.11879788>
- Stevens, L.A., Behn, M.D., Das, S.B., Joughin, I., Noël, B.P., van den Broeke, M.R. and Herring, T., 2016. Greenland Ice Sheet flow response to runoff variability. *Geophysical Research Letters*, 43(21), pp.11-295. <https://doi.org/10.1002/2016GL070414>
- Stibal, M., Box, J.E., Cameron, K.A., Langen, P.L., Yallop, M.L., Mottram, R.H., Khan, A.L., Molotch, N.P., Christmas, N.A., Quaglia, F.C., Remias, D., Smeets, C.J.P.P., van den Broeke, M., Ryan, J.C., Hubbard, A., Tranter, M., van As, D. and Ahlstrøm, A.P., 2017. Algae drive enhanced darkening of

- bare ice on the Greenland ice sheet. *Geophysical Research Letters*, 44(22), pp.11-463.
<https://doi.org/10.1002/2017GL075958>
- Stokes, C.R. and Clark, C.D., 2004. Evolution of late glacial ice-marginal lakes on the northwestern Canadian Shield and their influence on the location of the Dubawnt Lake palaeo-ice stream. *Palaeogeography, Palaeoclimatology, Palaeoecology*, 215(1-2), pp.155-171.
<https://doi.org/10.1016/j.palaeo.2004.09.006>
- Storrar, R.D., Jones, A.H. and Evans, D.J., 2017. Small-scale topographically-controlled glacier flow switching in an expanding proglacial lake at Breiðamerkjökull, SE Iceland. *Journal of Glaciology*, 63(240), pp.745-750. <https://doi.org/10.1017/jog.2017.22>
- Strozzi, T., Luckman, A., Murray, T., Wegmuller, U. and Werner, C.L., 2002. Glacier motion estimation using SAR offset-tracking procedures. *IEEE Transactions on Geoscience and Remote Sensing*, 40(11), pp.2384-2391. <https://doi.org/10.1109/TGRS.2002.805079>
- Stuefer, M., Rott, H. and Skvarca, P., 2007. Glaciar Perito Moreno, Patagonia: climate sensitivities and glacier characteristics preceding the 2003/04 and 2005/06 damming events. *Journal of Glaciology*, 53(180), pp.3-16. <https://doi.org/10.3189/172756507781833848>
- Sugiyama, S., Skvarca, P., Naito, N., Enomoto, H., Tsutaki, S., Tone, K., Marinsek, S. and Aniya, M., 2011. Ice speed of a calving glacier modulated by small fluctuations in basal water pressure. *Nature Geoscience*, 4(9), pp.597-600. <https://doi.org/10.1038/ngeo1218>
- Sundal, A.V., Shepherd, A., Nienow, P., Hanna, E., Palmer, S. and Huybrechts, P., 2011. Melt-induced speed-up of Greenland ice sheet offset by efficient subglacial drainage. *Nature*, 469(7331), pp.521-524. <https://doi.org/10.1038/nature09740>
- Sutherland, J.L., Carrivick, J.L., Gandy, N., Shulmeister, J., Quincey, D.J. and Cornford, S.L., 2020. Proglacial lakes control glacier geometry and behavior during recession. *Geophysical Research Letters*, 47(19), p.e2020GL088865. <https://doi.org/10.1029/2020GL088865>
- Szeliski, R. and Kang, S.B., 1994. Recovering 3D shape and motion from image streams using nonlinear least squares. *Journal of Visual Communication and Image Representation*, 5(1), pp.10-28.
<https://doi.org/10.1006/jvci.1994.1002>
- Szeliski, R., 2010. *Computer vision: Algorithms and applications*. London: Springer.
- Tahar, K.N., Ahmad, A., Akib, W.A.A.W.M. and Mohd, W.M.N.W., 2012. Assessment on ground control points in unmanned aerial system image processing for slope mapping studies. *International Journal Science and Engineering Research*, 3(11), pp.1-10.
- Tedstone, A.J., Nienow, P.W., Sole, A.J., Mair, D.W., Cowton, T.R., Bartholomew, I.D. and King, M.A., 2013. Greenland ice sheet motion insensitive to exceptional meltwater forcing. *Proceedings of the National Academy of Sciences*, 110(49), pp.19719-19724.
<https://doi.org/10.1073/pnas.1315843110>
- Tedstone, A.J., Nienow, P.W., Gourmelen, N., Dehecq, A., Goldberg, D. and Hanna, E., 2015. Decadal slowdown of a land-terminating sector of the Greenland Ice Sheet despite warming. *Nature*, 526(7575), pp.692-695. <https://doi.org/10.1038/nature15722>
- Thomas, R.H., 2004. Force-perturbation analysis of recent thinning and acceleration of Jakobshavn Isbrae, Greenland. *Journal of Glaciology*, 50(168), pp.57-66.
<https://doi.org/10.3189/172756504781830321>
- Tiwari, R.K., Gupta, R.P. and Arora, M.K., 2014. Estimation of surface ice velocity of Chhota-Shigri glacier using sub-pixel ASTER image correlation. *Current Science*, pp.853-859.

List of References

- Tomsett, C. and Leyland, J., 2019. Remote sensing of river corridors: A review of current trends and future directions. *River Research and Applications*, 35(7), pp.779-803.
<https://doi.org/10.1002/rra.3479>
- Tonkin, T.N., Midgley, N.G., Graham, D.J. and Labadz, J.C., 2014. The potential of small unmanned aircraft systems and structure-from-motion for topographic surveys: A test of emerging integrated approaches at Cwm Idwal, North Wales. *Geomorphology*, 226, pp.35-43.
<https://doi.org/10.1016/j.geomorph.2014.07.021>
- Trouvé, E., Vasilé, G., Gay, M., Bombrun, L., Grussenmeyer, P., Landes, T., Nicolas, J.M., Bolon, P., Petillot, I., Julea, A. and Valet, L., 2007. Combining airborne photographs and spaceborne SAR data to monitor temperate glaciers: Potentials and limits. *IEEE Transactions on Geoscience and Remote Sensing*, 45(4), pp.905-924. <https://doi.org/10.1109/TGRS.2006.890554>
- Truffer, M. and Motyka, R.J., 2016. Where glaciers meet water: Subaqueous melt and its relevance to glaciers in various settings. *Reviews of Geophysics*, 54(1), pp.220-239.
<https://doi.org/10.1002/2015RG000494>
- Trüssel, B.L., Motyka, R.J., Truffer, M. and Larsen, C.F., 2013. Rapid thinning of lake-calving Yakutat Glacier and the collapse of the Yakutat Icefield, southeast Alaska, USA. *Journal of Glaciology*, 59(213), pp.149-161. <https://doi.org/10.3189/2013JOG12J081>
- Tsutaki, S., Nishimura, D., Yoshizawa, T. and Sugiyama, S., 2011. Changes in glacier dynamics under the influence of proglacial lake formation in Rhonegletscher, Switzerland. *Annals of Glaciology*, 52(58), pp.31-36. <https://doi.org/10.3189/172756411797252194>
- Tsutaki, S., Sugiyama, S., Nishimura, D. and Funk, M., 2013. Acceleration and flotation of a glacier terminus during formation of a proglacial lake in Rhonegletscher, Switzerland. *Journal of Glaciology*, 59(215), pp.559-570. <https://doi.org/10.3189/2013JoG12J107>
- Tsutaki, S., Fujita, K., Nuimura, T., Sakai, A., Sugiyama, S., Komori, J. and Tshering, P., 2019. Contrasting thinning patterns between lake-and land-terminating glaciers in the Bhutanese Himalaya. *The Cryosphere*, 13(10), pp.2733-2750. <https://doi.org/10.5194/tc-13-2733-2019>
- Tulaczyk, S., Kamb, W.B. and Engelhardt, H.F., 2000. Basal mechanics of ice stream B, West Antarctica: 1. Till mechanics. *Journal of Geophysical Research: Solid Earth*, 105(B1), pp.463-481.
<https://doi.org/10.1029/1999JB900329>
- Ullman, S., 1979. The interpretation of structure from motion. *Proceedings of the Royal Society of London. Series B. Biological Sciences*, 203(1153), pp.405-426.
<https://doi.org/10.1098/rspb.1979.0006>
- van de Wal, R.S., Boot, W., van den Broeke, M.R., Smeets, C.J.P.P., Reijmer, C.H., Donker, J.J.A. and Oerlemans, J., 2008. Large and rapid melt-induced velocity changes in the ablation zone of the Greenland Ice Sheet. *Science*, 321(5885), pp.111-113. <https://doi.org/10.1126/science.1158540>
- van den Broeke, M., Box, J., Fettweis, X., Hanna, E., Noël, B., Tedesco, M., van As, D., van de Berg, W.J. and van Kampenhout, L., 2017. Greenland ice sheet surface mass loss: Recent developments in observation and modelling. *Current Climate Change Reports*, 3(4), pp.345-356.
<https://doi.org/10.1007/s40641-017-0084-8>
- van der Sluijs, J., Kokelj, S.V., Fraser, R.H., Tunnicliffe, J. and Lacelle, D., 2018. Permafrost terrain dynamics and infrastructure impacts revealed by UAV photogrammetry and thermal imaging. *Remote Sensing*, 10(11), pp.1-30. <https://doi.org/10.3390/rs10111734>
- van der Veen, C.J. and Whillans, I.M., 1989. Force budget: I. Theory and numerical methods. *Journal of Glaciology*, 35(119), pp.53-60. <https://doi.org/10.3189/002214389793701581>
- van der Veen, C.J., 1996. Tidewater calving. *Journal of Glaciology*, 42(141), pp.375-385.
<https://doi.org/10.3189/S0022143000004226>

- van der Veen, C.J., 1998a. Fracture mechanics approach to penetration of bottom crevasses on glaciers. *Cold Regions Science and Technology*, 27(3), pp.213-223. [https://doi.org/10.1016/S0165-232X\(98\)00006-8](https://doi.org/10.1016/S0165-232X(98)00006-8)
- van der Veen, C.J., 1998b. Fracture mechanics approach to penetration of surface crevasses on glaciers. *Cold Regions Science and Technology*, 27(1), pp.31-47. [https://doi.org/10.1016/S0165-232X\(97\)00022-0](https://doi.org/10.1016/S0165-232X(97)00022-0)
- van der Veen, C.J., 2002. Calving glaciers. *Progress in Physical Geography*, 26(1), pp.96-122. <https://doi.org/10.1191/2F0309133302pp327ra>
- van der Veen, C.J., 2007. Fracture propagation as means of rapidly transferring surface meltwater to the base of glaciers. *Geophysical Research Letters*, 34(1). <https://doi.org/10.1029/2006GL028385>
- Vaughan, D.G., Comiso, J.C., Allison, I., Carrasco, J., Kaser, G., Kwok, R., Mote, P., Murray, T., Paul, F., Ren, J., Rignot, E., Solomina, O., Steffen, K., Zhang, T., 2013. Observations: Cryosphere. In: *Climate Change 2013: The Physical Science Basis* (pp.317-382). Contribution of Working Group I to the Fifth Assessment Report of the IPCC. Cambridge and New York: Cambridge University Press.
- Venteris, E.R., 1997. Evidence for bottom crevasse formation on Columbia Glacier, Alaska. *Byrd Polar Research Centre Report, No. 15*, pp. 181–185.
- Verhoeven, G.J., Loenders, J.O., Vermeulen, F. and Docter, R., 2009. Helikite aerial photography—a versatile means of unmanned, radio controlled, low-altitude aerial archaeology. *Archaeological Prospection*, 16(2), pp.125-138. <https://doi.org/10.1002/arp.353>
- Verhoeven, G., 2011. Taking computer vision aloft—archaeological three-dimensional reconstructions from aerial photographs with photostan. *Archaeological Prospection*, 18(1), pp.67-73. <https://doi.org/10.1002/arp.399>
- Verhoeven, G., Doneus, M., Briese, C. and Vermeulen, F., 2012. Mapping by matching: A computer vision-based approach to fast and accurate georeferencing of archaeological aerial photographs. *Journal of Archaeological Science*, 39(7), pp.2060-2070. <https://doi.org/10.1016/j.jas.2012.02.022>
- Vericat, D., Brasington, J., Wheaton, J. and Cowie, M., 2009. Accuracy assessment of aerial photographs acquired using lighter-than-air blimps: Low-cost tools for mapping river corridors. *River Research and Applications*, 25(8), pp.985-1000. <https://doi.org/10.1002/rra.1198>
- Vieli, A., Funk, M. and Blatter, H., 2000. Tidewater glaciers: Frontal flow acceleration and basal sliding. *Annals of Glaciology*, 31, pp.217-221. <https://doi.org/10.3189/172756400781820417>
- Vieli, A., Funk, M. and Blatter, H., 2001. Flow dynamics of tidewater glaciers: A numerical modelling approach. *Journal of Glaciology*, 47(159), pp.595-606. <https://doi.org/10.3189/172756501781831747>
- Vincent, C. and Moreau, L., 2016. Sliding velocity fluctuations and subglacial hydrology over the last two decades on Argentière glacier, Mont Blanc area. *Journal of Glaciology*, 62(235), pp.805-815. <https://doi.org/10.1017/jog.2016.35>
- Voytenko, D., Dixon, T.H., Howat, I.M., Gourmelen, N., Lembke, C., Werner, C.L., De La Peña, S. and Oddsson, B., 2015. Multi-year observations of Breiðamerkurjökull, a marine-terminating glacier in southeastern Iceland, using terrestrial radar interferometry. *Journal of Glaciology*, 61(225), pp.42-54. <https://doi.org/10.3189/2015JoG14J099>
- Wagner, T.J., James, T.D., Murray, T. and Vella, D., 2016. On the role of buoyant flexure in glacier calving. *Geophysical Research Letters*, 43(1), pp.232-240A. <https://doi.org/10.1002/2015GL067247>

List of References

- Walder, J.S., 1986. Hydraulics of subglacial cavities. *Journal of Glaciology*, 32(112), pp.439-445.
<https://doi.org/10.3189/S0022143000012156>
- Walder, J.S. and Fowler, A., 1994. Channelized subglacial drainage over a deformable bed. *Journal of Glaciology*, 40(134), pp.3-15. <https://doi.org/10.3189/S0022143000003750>
- Warren, C. R., 1991. Terminal environment, topographic control and fluctuations of West Greenland glaciers. *Boreas*, 20, pp.1-15. <https://doi.org/10.1111/j.1502-3885.1991.tb00453.x>
- Warren, C.R., Benn, D.I., Winchester, V. and Harrison, S., 2001. Buoyancy-driven lacustrine calving, Glacier Nef, Chilean Patagonia. *Journal of Glaciology*, 47, pp.135-146.
<https://doi.org/10.3189/172756501781832403>
- Warren, C.R. and Kirkbride, M.P., 2003. Calving speed and climatic sensitivity of New Zealand lake-calving glaciers. *Annals of Glaciology*, 36, pp.173-178.
<https://doi.org/10.3189/172756403781816446>
- Watson, C.S. and Quincey, D., 2015. Glacier movement. In Cook, S.J., Clarke, L.E. and Nield, J.M., (eds). *Geomorphological Techniques* (Section 3.4.5). London: British Society for Geomorphology.
- Watson, C.S., White, N.J., Church, J.A., King, M.A., Burgette, R.J. and Legresy, B., 2015. Unabated global mean sea-level rise over the satellite altimeter era. *Nature Climate Change*, 5(6), pp.565-568.
<https://doi.org/10.1038/nclimate2635>
- Watson, C.S., Kargel, J.S., Shugar, D.H., Haritashya, U.K., Schiassi, E. and Furfaro, R., 2020. Mass loss from calving in Himalayan proglacial lakes. *Frontiers in Earth Science*, 7(342), pp.1-19.
<https://doi.org/10.3389/feart.2019.00342>
- Weertman, J., 1957. On the sliding of glaciers. *Journal of Glaciology*, 3(21), pp.33-38.
<https://doi.org/10.3189/S0022143000024709>
- Weertman, J., 1964. The theory of glacier sliding. *Journal of Glaciology*, 5(39), pp.287-303.
<https://doi.org/10.3189/S0022143000029038>
- Weertman, J., 1972. General theory of water flow at the base of a glacier or ice sheet. *Reviews of Geophysics*, 10(1), pp.287-333. <https://doi.org/10.1029/RG010i001p00287>
- Weertman, J., 1983. Creep deformation of ice. *Annual Review of Earth and Planetary Sciences*, 11(1), pp.215-240.
- Wegmuller, U., Werner, C., Strozzi, T. and Wiesmann, A., 2006, July. Ionospheric electron concentration effects on SAR and INSAR. In *2006 IEEE International Symposium on Geoscience and Remote Sensing* (pp.3731-3734). IEEE. <https://doi.org/10.1109/IGARSS.2006.956>
- Welch, R., Jordan, T.R. and Thomas, A.W., 1984. A photogrammetric technique for measuring soil erosion. *Journal of Soil and Water Conservation*, 39(3), pp.191-194.
- Westoby, M.J., Brasington, J., Glasser, N.F., Hambrey, M.J. and Reynolds, J.M., 2012. 'Structure-from-Motion' photogrammetry: A low-cost, effective tool for geoscience applications. *Geomorphology*, 179, pp.300-314. <https://doi.org/10.1016/j.geomorph.2012.08.021>
- WGMS, 2020. Fluctuations of Glaciers Database. World Glacier Monitoring Service, Zurich, Switzerland.
<https://doi.org/10.5904/wgms-fog-2020-08>
- Whitehead, K., Moorman, B.J. and Hugenholtz, C.H., 2013. Brief Communication: Low-cost, on-demand aerial photogrammetry for glaciological measurement. *The Cryosphere*, 7(6), pp.1879-1884.
<https://doi.org/10.5194/tc-7-1879-2013>
- Wigmore, O. and Mark, B.G., 2017. Monitoring tropical debris-covered glacier dynamics from high-resolution unmanned aerial vehicle photogrammetry, Cordillera Blanca, Peru. *The Cryosphere*, 11, pp.2463-2480. <https://doi.org/10.5194/tc-11-2463-2017>

- Willis, I.C., Sharp, M.J. and Richards, K.S., 1990. Configuration of the drainage system of Midtdalsbreen, Norway, as indicated by dye-tracing experiments. *Journal of Glaciology*, 36(122), pp.89-101. <https://doi.org/10.3189/S0022143000005608>
- Willis, I.C., 1995. Intra-annual variations in glacier motion: a review. *Progress in Physical Geography*, 19(1), pp.61-106. <https://doi.org/10.1177%2F030913339501900104>
- Willis, M.J., Melkonian, A.K., Pritchard, M.E. and Ramage, J.M., 2012. Ice loss rates at the Northern Patagonian Icefield derived using a decade of satellite remote sensing. *Remote Sensing of Environment*, 117, pp.184-198. <https://doi.org/10.1016/j.rse.2011.09.017>
- Winsvold, S., Kääb, A., Nuth, C., Andreassen, L.M., van Pelt, W. and Schellenberger, T., 2018. Using SAR data time-series for regional glacier mapping. *The Cryosphere*, 12(3), pp.867-890. <https://doi.org/10.5194/tc-12-867-2018>
- Wittmann, M., Groot Zwaafink, C.D., Steffensen Schmidt, L., Guðmundsson, S., Pálsson, F., Arnalds, O., Björnsson, H., Thorsteinsson, T. and Stohl, A., 2017. Impact of dust deposition on the albedo of Vatnajökull ice cap, Iceland. *The Cryosphere*, 11(2), pp.741-754. <https://doi.org/10.5194/tc-11-741-2017>
- Xue, Y., Jing, Z., Kang, S., He, X. and Li, C., 2021. Combining UAV and Landsat data to assess glacier changes on the central Tibetan Plateau. *Journal of Glaciology*, pp.1-13. <https://doi.org/10.1017/jog.2021.37>
- Yang, W., Zhao, C., Westoby, M., Yao, T., Wang, Y., Pellicciotti, F., Zhou, J., He, Z. and Miles, E., 2020. Seasonal Dynamics of a Temperate Tibetan Glacier Revealed by High-Resolution UAV Photogrammetry and In Situ Measurements. *Remote Sensing*, 12(15), p.2389. <https://doi.org/10.3390/rs12152389>
- Zemp, M., Frey, H., Gärtner-Roer, I., Nussbaumer, S.U., Hoelzle, M., Paul, F. ... and Bajracharya, S., 2015. Historically unprecedented global glacier changes in the early 21st century. *Journal of Glaciology*, 61(228), pp.745-762. <https://doi.org/10.3189/2015JoG15J017>
- Zemp, M., Huss, M., Thibert, E., Eckert, N., McNabb, R., Huber, J. ... and Cogley, J.J., 2019. Global glacier mass changes and their contributions to sea-level rise from 1961 to 2016. *Nature*, 568(7752), pp.382-386. <https://doi.org/10.1038/s41586-019-1071-0>
- Zwally, H.J., Abdalati, W., Herring, T., Larson, K., Saba, J. and Steffen, K., 2002. Surface melt-induced acceleration of Greenland ice-sheet flow. *Science*, 297(5579), pp.218-222. <https://doi.org/10.1126/science.1072708>

